Synthetic Cell Aspirations

A Toolbox for Building a Membrane Container from the Bottom Up

van Buren, L.

DOI
10.4233/uuid:d0b7e1e5-7836-4914-993d-ff83e446a43f

Publication date
2022

Document Version
Final published version

Citation (APA)
van Buren, L. (2022). *Synthetic Cell Aspirations: A Toolbox for Building a Membrane Container from the Bottom Up*. [Dissertation (TU Delft), Delft University of Technology]. https://doi.org/10.4233/uuid:d0b7e1e5-7836-4914-993d-ff83e446a43f

Important note
To cite this publication, please use the final published version (if applicable).
Please check the document version above.

SYNTHETIC CELL ASPIRATIONS

A TOOLBOX FOR BUILDING A MEMBRANE CONTAINER FROM THE BOTTOM UP

SYNTHETIC CELL ASPIRATIONS

A TOOLBOX FOR BUILDING A MEMBRANE CONTAINER FROM THE BOTTOM UP

Proefschrift

ter verkrijging van de graad van doctor
aan de Technische Universiteit Delft,
op gezag van de Rector Magnificus prof. dr. ir. T. H. J. J. van der Hagen,
voorzitter van het College voor Promoties,
in het openbaar te verdedigen op DATE om TIME

door

Lennard VAN BUREN

Master of Science in Biotechnology, Wageningen University & Research, Nederland
geboren te Leerdam.

Dit proefschrift is goedgekeurd door de promotoren:

Prof. dr. G. H. Koenderink
Dr. M.E. Aubin-Tam

Samenstelling promotiecommissie:

Rector Magnificus,	voorzitter
Prof. dr. G. H. Koenderink,	Technische Universiteit Delft, promotor
Dr. M.E. Aubin-Tam,	Technische Universiteit Delft, tweede promotor

Keywords: Bottom-up reconstitution, giant unilamellar vesicles, synthetic cell, encapsulation, membrane mechanics, membrane fusion, image analysis

Printed by: PRINTSHOP

Front & Back: NAME

ISBN 000-00-0000-000-0

An electronic version of this dissertation is available at
http://repository.tudelft.nl/.

Everyone then who hears these words of mine
and does them will be like a wise man who built his house on the rock.
And the rain fell, and the floods came, and the winds blew and beat on that house,
but it did not fall, because it had been founded on the rock.
And everyone who hears these words of mine
and does not do them will be like a foolish man who built his house on the sand.
And the rain fell, and the floods came, and the winds blew and beat against that house,
and it fell, and great was the fall of it.

Matthew 7:24-27

PREFACE

'Build your house on the rock, not on the sand.' This old biblical expression has neither given in on power nor on accuracy in the past two thousand years. This is not a comfortable wisdom for a Dutchman, with the majority of our houses built unpleasantly below sea level on a soggy mix of sand and clay, and a rising sea luring greedily at our cities. Fortunately, climate change is beyond the scope of this work.

A broader interpretation is that a firm foundation is indispensable for the success and impact of any project. This also extends to the domain of science. Looking back at my PhD journey, I know that doing innovative research can sometimes feel like building on sand, whether it is a house or a synthetic cell. For example, I recall that after almost two years of intensive protocol optimization, in the cold and (still) cosy winter of 2020, we finally managed to produce good looking vesicles with the cDICE technique. What a relief! However, come summer, the quality of produced samples dropped tremendously for a reason that was not obvious to us at all. We had to get back to the drawing table once more, pausing our experimental progress in building a synthetic cell indefinitely. After long and thorough screening of many of our experimental input parameters, we finally identified what affected vesicle production so badly: humidity of the ambient air, which changes drastically over the seasons. Once we gained control over humidity during our formation runs, we drastically improved reliability of the method, paving the way for more advanced experiments.

Only by critically evaluating our own work, transparently reporting our results and methods, and taking effort to expand on the available methodologies, we can build a rock solid foundation for follow-up research. I truly hope that the work presented in this thesis will have a modest contribution to the progression of the field, and, who knows, to the construction of a synthetic cell.

Lennard van Buren
Delft, February 2022

SUMMARY

Everything that we consider alive, be it plants, dogs, bacteria or humans, is composed of the same microscopic building blocks: cells. While cells between and even within these organisms can look and behave very differently, they all share the same key functionalities: they can grow, they can divide to proliferate, they can eat and metabolise to fuel internal processes, and they carry a genetic blueprint which they can process to know what to do and how to do it. Since the first notion that cells form the universal building blocks of life [1], biologists have been intrigued by the fact that across the wide diversity of living organisms, all these constituent cells share the same fundamental characteristics. In the process of understanding how cells are capable of executing the key functionalities of growth, division, metabolism and information processing, biologists have identified the set of molecular components that constitute cellular life, and have broadly related components to specific cell functions. Despite the growing knowledge on *what* there is inside the cell, a crucial question remains largely unanswered: *how* do the molecular components of a cell give rise to these life-giving processes?

Answering that question that is easier said than done. Cells consist of thousands of different components that are in continuous interaction, can take over each other's function, or have multiple functions. Extracting a mechanistic understanding of how these components actually work together to make the cell alive, is almost impossible in such a complex soup. Even if we can list the minimal set of components that are vital to cellular life, we gain little understanding in how these ingredients function to make non-living matter alive.

Instead, for this purpose it might be more insightful to try to rebuild the cell with a minimal set of components: to build a *synthetic cell*. In such a bottom-up reconstitution approach, cell components and their interactions can be studied in a well-controlled chemical environment. Starting with a small number of components, complexity can step-by-step be increased while maintaining a fundamental understanding throughout the construction process. To achieve this goal of building a minimal cell, multiple research initiatives have been founded worldwide. As a unique interdisciplinary effort, synthetic cell research combines the expertise required to understand, rebuild and integrate all vital cellular functions *in vitro*.

In this project, being part of the Dutch synthetic cell research consortium BaSyC [2], we expand on the methodology essential for synthetic cell research. Specifically, we focus on the biophysical and analytical tools involved in the control and characterization of the physical compartment that houses the synthetic cell. While functional modules can in principle be developed independently, in the end they all need to be integrated in a single container. This makes the container a unique unifying aspect crucial to the successful development of a synthetic cell. We choose to work with lipid bilayer vesicles as containers, specifically giant unilamellar vesicles (GUVs), because they are cell-sized

compartments with a confining lipid bilayer membrane that closely resembles the biological plasma membrane.

We reduced the concept of 'container control' to three questions that are central to this thesis. First, how to build the synthetic cell container? While there are many techniques to produce GUVs, they are only recently being evaluated for their potential to allow synthetic cell research, which does not only involve formation of the compartment, but also requires encapsulation of complex reaction mixtures in the right stoichiometric ratios. Second, how to grow its surface area? Growth is a fundamental process of living cells and therefore one that we aim to reconstitute in the synthetic cells. Depending on the desired level of autonomy, membrane growth can be realized by synthesis of new membrane lipids inside the vesicle, or by external supply. Third, how to divide the synthetic cell? Cell division requires a protein machinery that is able to mechanically constrict the lipid envelope. A minimal machinery based on the eukaryotic actin cortex is a particularly interesting candidate, as this system is also used in our own body cells. To understand how to build such a machinery inside the container, we need not only to put in the ingredients, but also to understand how components give rise to structural and mechanical properties.

MAIN FINDINGS OF THIS THESIS

In this thesis, we explore the potential of using giant unilamellar vesicles as a functional compartment for the construction of an artificial cell. We carefully investigate each step of its life cycle as a synthetic cell, starting from its production, to the growth of its membrane, to division. However, a bottom-up synthetic cell is not built in a single PhD project. We therefore put a strong focus on evaluating the available methodology to reconstitute and characterize GUV-based systems, and expand on it wherever necessary. As such, we believe that this work contributes to a solid foundation for follow-up synthetic cell research, and thereby to unravel how biological cells fulfil their life-giving functionalities.

In **chapter 1**, we introduce the topic and scope of this thesis. Then, in **chapter 2**, we present a literature review on the state-of-the-art research on reconstituting a minimal actin-based division machinery. We identified two major pathways for building an actin machinery capable of dividing the synthetic cell, and we concretely pinpointed the outstanding challenges along the way.

After having set the long-term ambitions, we move on to the practicalities of producing a synthetic cell in the lab. In **chapter 3**, we show that a double-emulsion technique called continuous Droplet Interface Crossing Encapsulation (cDICE) [3] is well-capable of producing defect-free GUVs encapsulating a wide range of complex biochemical systems, thus being a powerful candidate for synthetic cell formation. In particular, we show that formation of high-quality vesicles and encapsulation of components therein can be done more reproducibly by tightly controlling environmental conditions and carefully tuning the lipid-in-oil dispersion.

However, we found a major drawback of cDICE to be that filamentous proteins could not be reliably encapsulated, while these proteins are essential for the construction of cytoskeletal networks that we want to employ for cell shaping. We circumvent this problem by making small adjustments to the original cDICE protocol, giving birth to a technique

that we call emulsion Droplet Interface Crossing Encapsulation (eDICE) that we present in **chapter 4**. Along with a number of other techniques ranging from bulk to microfluidic methods, we evaluate eDICE and cDICE for their ability to reconstitute an actin cortex inside GUVs in this chapter, based on our own experiences with these protocols. Because reconstitution of an actin cortex is a complex process, requiring controlled encapsulation of protein mixtures, producing membranes of the right lipid composition, and working in the right physiological buffers, this comparison serves as a broader basis to characterise production protocols for synthetic cell formation. We found that gel-assisted swelling is a convenient protocol to make membranes of various lipid compositions in all sorts of buffers. Furthermore, we demonstrate that eDICE can be successfully employed to encapsulate components required for the formation of a synthetic actin cortex. The power of both gel-assisted swelling and eDICE is that they are easy protocols while allowing reconstitution of versatile and complex systems. Besides only comparing GUV formation methods, we demonstrate that the process of lipid monolayer formation, a key step in emulsion-based GUV production techniques, can be studied isolated from the complex context of GUV formation by using pendant drop tensiometry. Interestingly, we found that the presence of actin affects the kinetics of lipid monolayer formation, stressing the need for more research on the effect of solutes on GUV formation and, in general, illustrating the limited understanding of the fundamental processes involved in vesicle production.

Increasing the complexity of reconstitution experiments requires analysis to be done at the population level to reveal if experimental conditions have statistically significant effects. To accommodate the need for quantitive analysis, we present in **chapter 5** 'DisGUVery', a new open-source software for automated detection and analysis of GUVs in microscopy images. We show that the three vesicle detection algorithms that DisGUVery accommodates together allow for accurate identification of GUVs in different image types, with varying intensity profiles, irrespective of their shape. Furthermore, we demonstrate that the software can be used to do otherwise time-intensive analysis in an efficient and automated manner, such as population-level quantification of membrane fluorescence or measuring the efficiency of encapsulation of a fluorescent protein. By allowing accessible high-throughput analysis, we believe that DisGUVery will aid synthetic cell research to develop to a more quantitative data description.

The shape of the synthetic cell container is determined by active deformation forces on the one side, and the mechanical resilience of its membrane on the other. In **chapter 6**, we show how GUV membrane mechanics can be determined by means of two well-established but challenging techniques: vesicle fluctuation analysis (VFA)[4, 5] and micropipette aspiration (MPA)[6, 7]. We provide detailed workflows for both experiments supplemented with practical fixes for typical challenges in their implementation. We validate the quality of our protocols by a series of benchmark measurements of bending and stretch moduli of model membranes, which agree well with literature values. Finally, we describe how VFA and MPA can be employed in future to determine mechanical properties of reconstituted cortices, thereby offering a way to understand and direct actin cortex reconstitution efforts.

To generate growth of the synthetic cell, we demonstrate successful implementation of an external membrane feeding mechanism in **chapter 7**. Our feeding protocol is based

on programmable membrane fusion of large unilamellar vesicles (LUVs), typically one hundred times smaller than GUVs, with GUVs by means of complementary membrane-anchored DNA linkers[8, 9]. We characterize large GUV populations at individual steps in the fusion process using the DisGUVery software presented in chapter 5. This analysis enables us to perform a thorough screening of the parameter space involved in DNA-mediated LUV-GUV fusion, thereby providing handles for efficient implementation of this membrane growth protocol. Our assay results in detectable membrane fusion in up to 30% of the GUVs, with the exact fusion rate being strongly dependent on the concentration of the DNA linker. We show that fusion works robustly for various GUV membrane compositions and for GUVs produced with different production techniques (gel-assisted swelling and eDICE), which underlines the potential of this supply-on-demand method for generating membrane growth in complex systems.

Finally, in **chapter 8** we outline next steps that can be taken to recreate division of the synthetic cell container based on the results of this work. In addition, we provide extra recommendations for further maturation of the synthetic cell field as whole.

CONTENTS

1

INTRODUCTION

All life is built up of cells, which in turn are composed of an overwhelmingly complex set of molecules. To understand how molecular components are spatiotemporally organized to create life, researchers aim to rebuild a minimal version of a living cell from scratch. A crucial aspect in developing such a synthetic cell is the construction and design of its container. Giant unilamellar vesicles (GUVs) are a popular model system to be used as a container, because they are cell-sized and confined by a lipid bilayer membrane, just like living cells. Using GUVs for synthetic cell reconstitution, experimental challenges lie ahead: how to build, grow, and divide them? These questions form the basis of this thesis. This chapter serves as an introduction to the work presented in this thesis, covering a background on synthetic cell research, the basic properties of lipid bilayer membranes, and presenting the scope and outline of this thesis.

1.1. BUILDING A SYNTHETIC CELL

Everything that we consider alive, is composed of the same microscopic building blocks: cells. Cells, in turn, are the smallest entities that we consider to be alive. Despite being the smallest universal building blocks, cells still show a bewildering complexity at the molecular level. A central question that has intrigued researcher for centuries, is: how do all these molecular parts work together to make a cell alive?

In the past centuries, biology has made tremendous progress in identifying the molecular components that constitute cellular life. However, we still know relatively little about how these components are spatiotemporally organized to give rise to vital cellular processes [10]. The classical top-down biological approach, where components are studied by their modification in the biological context, has a severe limitation with respect to unravelling mechanistic working principles. The biological context is so overwhelmingly complex (human cells have 20000 genes [11], typical number density is 0.2 to 4 million protein molecules per cubic micron [12]), that the function of an individual component can barely be isolated. For example, modification of a component can lead to a cascade of other effects, or its function can be taken over by other back-up molecules (redun-

1

dancy). Even more difficult than learning how single components function, is to understand how cooperation between molecules can give rise to complex emergent processes such as cell division and migration [10].

Instead, to obtain a mechanistic understanding of cellular parts and processes, it is often more insightful to isolate the components of interest and study them in a well-defined chemical environment [13]. This approach, called bottom-up synthetic biology, cell-free biology, or cellular reconstitution [14, 15], has gained significant interest over the past three decades. In concert with technological advances, scientists have been able to reconstitute cell processes with increasing complexity (reviewed in [10, 15–17]). Encouraged by the rapid progress in reconstitution studies, a new question arises: can we build an entire cell from the bottom up (fig. 1.1)?

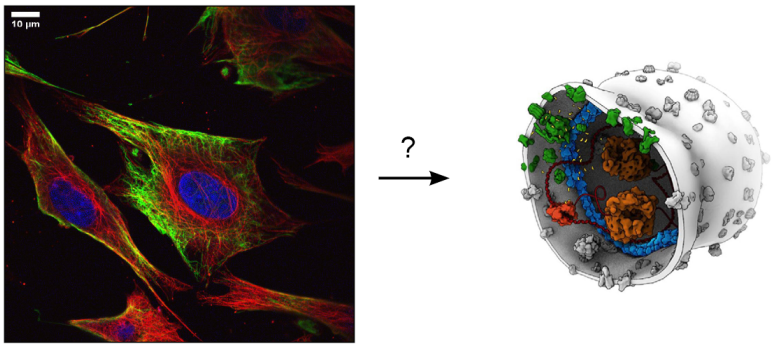

Figure 1.1: **How to build a minimal cell from the bottom up?** (left) Eukaryotic cell (3T3 fibroblast). Visible are the nucleus (blue), microtubules (red), and vimentin (green). Image courtesy: Michal Shemesh. (right) Conceptual minimal cell by Graham Johnson. The cell is cut open for visualization of the three basic processes: cell fuelling (green), DNA processing (red/orange), and cell division (blue).

To answer this question, a number of national and international research initiatives has been founded around the world (BaSyC, the Netherlands [2]; MaxSynBio, Germany [18]; Build-a-cell community, USA [19]; European Synthetic Cell Initiative, worldwide [20]; reviewed in [21]). Joined by these initiatives, researchers from all sorts of disciplines collaborate to synthesize the cellular modules and finally integrate them. Besides providing fundamental knowledge of cellular functioning, the route to building a synthetic cell holds potential in medical applications, for instance artificial blood cells and smart drug delivery vehicles [22, 23]. In addition, reconstitution of a living cell provokes important philosophical questions: what is life, and how does it work[24]?

Note that the definition of a synthetic cell is ambiguous. In fact, under different terms, a synthetic cell has been created by the Craig Venter institute from a top-down approach[25]. In their study, Gibson et al. implanted a synthesized genome into a DNA-free bacterial shell. Although this top-down synthetic cell has been a great technological advancement that provides valuable insights in vital genes [25, 26], it offers limited understanding of how life is assembled from its parts (reviewed in [27]).

The work presented in this thesis is part of the BaSyC project [2], where the goal is to build a cell from the bottom up using chemical and biological components. The ma-

jor challenges that have been defined are cell fuelling, DNA processing, and cell division (fig. 1.1). It is important to know that within the BaSyC programme, we are not trying to rebuild a specific cell type. Instead, modules from across all biology and even engineering approaches can be combined to engineer the synthetic cell. Many design choices thus need to be made, which will be motivated throughout this thesis.

1.2. CHOOSING A CELL CONTAINER

Arguably, the first step in building a synthetic cell is the construction of its container. The container, an aqueous compartment with a deformable envelope to allow cell division, creates a distinct chemical environment in which all reconstituted cellular processes take place. While proteins and metabolites are kept inside, the container should allow for selective transport of nutrients to allow feeding. Upon a first assembly of the container, requiring not only the formation of the compartment, but also the encapsulation of essential ingredients, the container needs to be able to grow and divide.

Let us first settle on the most fundamental design choice: what type of container are we using? There are various ways to create aqueous compartments [28, 29], which can be either membrane-less (coacervation[30]), or be confined by membranes composed of polymers (polymersomes[31]), proteins (proteosomes[32]), or lipids (liposomes[33, 34]). Of these compartmentalization strategies, liposomes are the closest mimic to cells and therefore the most obvious choice if the goal is to understand biological systems. Given that all life as we know it is compartmentalized by lipid membranes, across all kingdoms of life [35, 36], these envelopes have proven to be effective compartmentalization strategies. The use of liposomes also ensures compatibility with other biological building blocks, such as membrane-bound enzymes and transporters. In particular, giant liposomes, or Giant Unilamellar Vesicles (GUVs), are a close biological mimic, given that their size (5 to 100 μm) is comparable to the size of eukaryotic cells [33]. Furthermore, their size allows for easy visualization by optical microscopy. These properties make GUVs the perfect chassis for building a synthetic cell.

1.3. LIPID BILAYERS

As lipids, lipid membranes and GUVs are key players in this thesis, it is useful to take a moment to introduce them. As mentioned above, lipid membranes are omnipresent in biology. All cells are enveloped by a plasma membrane, which is essentially an envelope of phospholipids in which other functional and structural components are embedded, such as membrane proteins and sterols (reviewed in [37]). The architecture of the phospholipid membrane is remarkable. As phospholipids are amphiphatic molecules, with a hydrophilic head and two hydrophobic tails, they self-assemble into double layers with their heads facing outwards, hydrated by the surrounding aqueous solution, and their tails facing inwards, creating a hydrophobic core (fig. 1.2). These double layer membranes are called lipid bilayers, or shorter, bilayers. Exposure of the hydrophobic core to the aqueous environment comes with a high free energy penalty, meaning that bilayers are generally closed, giving rise to the spherical compartments which we call liposomes or lipid bilayer vesicles. We know liposomes with single bilayers (unilamellar), with multiple bilayers stacked (multilamellar), and liposomes encapsulating other

1

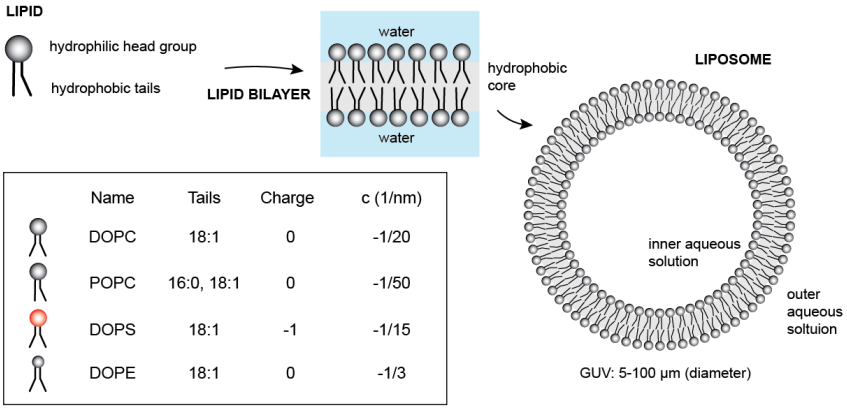

	Name	Tails	Charge	c (1/nm)
	DOPC	18:1	0	-1/20
	POPC	16:0, 18:1	0	-1/50
	DOPS	18:1	-1	-1/15
	DOPE	18:1	0	-1/3

Figure 1.2: **From lipids to giant unilamellar vesicles.** Schematic representation of basic properties and self-assembly mechanisms of lipids. Bottom left: overview of main lipids used in this thesis and their properties. Head group charges are at neutral pH. Tails represent length of the carbon chain and number of unsaturated bonds. In case only a single combination is given, both tails are identical. Intrinsic curvatures (c) were obtained from ref. [38, 39]. Large curvatures (e.g. DOPE) indicate a conical molecular shape.

liposomes (multivesicular) (reviewed in [33]). We typically consider unilamellar vesicles for simplicity. Henceforth, the terms lipid vesicle, vesicle, liposome and GUV are used interchangeably.

Lipid bilayers have unique physical properties, which has made them a topic of interest for researchers from biophysics and physical chemistry. Before going to the questions addressed in this thesis, we first need to discuss some of the most important features.

Permeability. Because of their hydrophobic core, lipid bilayers are permeable to hydrophobic molecules and small uncharged polar molecules such as water, but non-permeable to protons and ions, and large uncharged polar molecules such as proteins and sugars [40, 41]. Since water can move across the membrane, but solutes can not, lipid bilayer vesicles are subjected to osmosis. *In vivo*, permeation of ions and large molecules is upregulated by the use of membrane proteins like transporters and channels [42, 43].

Fluidity. Lipids in bilayers are kept together by non-covalent interactions. These relatively weak interactions allow lateral displacement of lipids through the membrane, giving rise to lateral diffusion of lipids and making the bilayer a fluid material [44]. In cells, lateral mobility of both proteins and lipids in the plasma membrane is of vital importance for many membrane-associated processes [45, 46].

Tension. Similar to liquid interfaces, forces acting to expand membranes are counteracted by a surface tension, the membrane tension. However, for fluid-fluid interfaces, extra surface area can easily be generated by recruitment of molecules from both bulk phases. Because lipids have minimal solubility in water, the number of lipids in a membrane is essentially fixed. This means that, while surface tension is a material property

dependent on the nature of both interfaces, membrane tension is a bilayer property that depends on the applied strain [47]. This, in turn, gives rise to membrane elasticity (see next). In cells, membrane tension is actively regulated to control cell processes that involve shape changes. In animal cells, membrane tension is generated by adhesion of the underlying cytoskeleton [48–50], while in plant and bacterial cells, tension originates from high internal osmotic pressure.

Elasticity. Lipid membranes are primarily deformed by stretch and curvature deformations as first described by W. Helfrich [47]. Membranes have a low bending modulus of $10-30k_BT$[51, 52], and can therefore easily bend out-of-plane, which is not surprising considering the small bilayer thickness ($\sim 6nm$ [53]). In fact, bilayers can already spontaneously bend by thermal fluctuations of the surrounding solvent. Bending of lipid membranes is of particular importance *in vivo* for cell shaping, such as the formation of thin protrusions as seen in neurons [54], and for inter- and intracellular communication mediated by small vesicles [55]. Contrary to bending, bilayers are strongly resistant against stretch deformations. Stretch moduli of bare lipid membranes are typically reported between 100-300 mN/m [56]. Due to its fluid nature, a local stretching of the bilayer is quickly equilibrated over the entire membrane. While bending deformations dominate at negligible membrane tensions, the membrane deforms by stretching at high tensions[7]. When membrane tension exceeds the lysis tension (between $4-10mN/m$, or 4-10% strain, dependent on bilayer composition[57, 58]), membranes rupture.

Asymmetry. In biological membranes, the inner leaflet is always different in composition from the outer leaflet, a property that is vital for cell functioning, differentiation and growth [59]. Transmembrane asymmetry exists because lipids can not easily transfer from one leaflet to the other [60], a process called flip-flop. In turn, compositional asymmetries give rise to spontaneous curvature effects, leading to membrane deformations like the formation of lipid nanotubes [61]. Besides from a compositional asymmetry, spontaneous curvature can also be generated by an asymmetry of the presence of membrane-interacting solutes such as sugars [62], ions [63] and proteins [64].

Diversity. Lipids are highly diverse in structure and properties [65, 66]. While they all share the common property of having a hydrophilic head and two hydrophobic tails, which ensures their self-assembly into bilayers, they vary in head group size and charge (which depends on pH), length of hydrocarbon tails, and saturation of the tails. As such, lipid properties determine interactions within the bilayer, thereby determining elasticity and fluidity, as well as interactions with the external environment, such as electrostatic interactions with proteins and ions. An important property arising from the lipid structure is its molecular shape, or intrinsic curvature, which determines the monolayer spontaneous curvature [67, 68]. If the head group of a lipid has a similar preferential molecular area in the bilayer as the tails, the lipid has an approximately cylindrical shape. Self-assembly of cylindrical lipids leads to the formation of a flat bilayer. In contrast, when the lipid head group is smaller than the tails, the molecular shape is conical, and self-assembly will naturally lead to a curved membrane. As a brief summary, a schematic overview of the main lipids used in this work is present in fig. 1.2. Besides lipids, plasma membranes contain other molecules. Of particular interest is cholesterol, a hydrophobic organic molecule with a small hydrophilic head group which is a key component in animal cell membranes. Cholesterol integrates in the bilayer where it modulates lipid

packing, thereby providing an important tool for animal cells to control fluidity, permeability and elasticity (reviewed in [69, 70]).

Shape. Altogether, the properties of GUVs and lipid membranes in general allow them to undergo drastic shape transformations in response to changes in for example membrane tension, area-to-volume ratio, or leaflet asymmetry. While these spontaneous shape transitions can be exploited for synthetic cell engineering applications, for example to reconstitute spontaneous curvature-driven division[71], cells need tight control over their shape. Therefore, most organisms have mechanisms to actively control membrane shaping, being able to switch between stable and dynamic states whenever necessary. Bacteria and plant cells juxtapose their deformable membrane with a rigid stable shell, the cell wall, while animal cells control their shape from the inside by means of a dynamic membrane-bound cytoskeleton [72].

1.4. THE THREE CONTAINER QUESTIONS

The unique properties of lipid membranes have accommodated the evolution of cellular life to its rich complexity and diversity that we see nowadays. Now, the question becomes: which of the aspects that cell containers have developed over the past million years, are essential? How can we rebuild the core functionalities of the cell container with a minimal set of ingredients? In practice, this boils down to three major, general questions that lie at the heart of this thesis (see fig. 1.3).

1. How to build the container? Over the past fifty years, a wide range of GUV production methods has been developed. Currently, there exist more than twenty different techniques that gave offspring to hundreds of protocols. Formation methods range from simple bulk assays[73–76] to sophisticated microfluidic assembly lines[77–79]. Despite the multitude of methods that has been developed (and is still being developed), there is still not a single technique that accommodates all criteria required for synthetic cell formation. It is not sufficient to just construct a lipid bilayer container. Fabrication additionally needs to allow for producing clean membranes of various compositions in physiological buffer. Maybe even more important, the essential building blocks for the synthetic cell, including proteins, DNA, and metabolites, need to be encapsulated in the right stoichiometric ratios without compromising their functionality [16, 34, 80]. A crucial challenge for synthetic cell research thus lies in the convergence to using a single GUV production platform for encapsulation of all modules that are now being developed independently.

To obtain answers to the next two questions, we can take inspiration from how cells grow and divide *in vivo*. The answer to this question, however, demands an engineering approach, because new cells only originate from living cells, and have so far never been constructed by mankind. Or quoting the famous biologist Rudolf Virchow (1855): *Omnis cellula-e cellua ('All cells (come) from cells')*. This imposes a grand technological challenge: how would the engineer build a cell, based on research, rationale, and available technology?

2. How to grow the container? After successful production of the container, it needs to grow. Cell size homeostasis is only obtained when the container doubles in volume

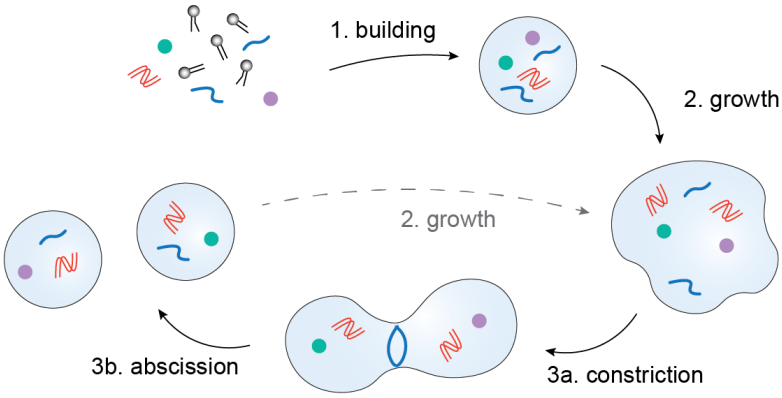

Figure 1.3: **Schematic representation of the container life cycle**. In this schematic, we assume division to be executed by the eukaryotic actomyosin machinery. To initiate the cycle, the container is assembled from the individual components (step 1), including lipids (grey), a division machinery (actin, blue), the genome (red), and solutes such as ions, energy sources and other proteins (green and purple). After assembly, the container needs to grow in membrane area and volume to ensure cell size homeostasis throughout the cell cycle (step 2). Once the cell has sufficiently grown, cytokinesis commences with the self-assembly of the contractile machinery, whose contraction leads to controlled membrane constriction at the cell mid-plane (step 3a). Finally, membrane abscission at the cytokinetic furrow gives rise to the formation of two physically separated daughter cells (step 3b). To go through multiple life cycles, the daughter cells should be capable of growing (step 2, dashed line).

and area before division. *In vivo*, membrane growth is regulated by synthesis of lipids via endogenous pathways [81]. In addition, cells have a large number of internal vesicles (endosomes) which can fuse with the plasma membrane to allow a membrane addition on-demand. Such a supply-on-demand system is for instance used in the final stages of cytokinesis [82], and for the formation of elongated neuronal contact sites [83]. In vitro, new membrane area has previously been generated by *de novo* lipid synthesis from precursors using non-enzymatic reactions [84, 85], with purified proteins [40, 86, 87], or with proteins produced from synthetic genes in vesicles [88]. Alternatively, area growth can be realised by external supply of new membrane material in the way of fusion of small vesicles [89–91]. While multiple methods thus exist for membrane production *in vitro*, there has been minimal attention for their compatibility with other synthetic cell modules. What area increase can be achieved? How can membrane production be temporally coordinated with cytokinesis? A synthetic cell requires not only expansion of its membrane, but also of its volume (reviewed in [92]). The volume of a vesicle is the result of a continuous, delicate balance between the concentration of ions inside and outside. As such, container volume can be increased by changing the osmotic gradient, for example by active influx of solutes [93, 94]. Volume growth is beyond the scope of this work.

3. How to divide the container? Understanding and reconstitution of cell division is a hot topic in synthetic biology, as it is such a fundamental process shared by all cellular life. Current reconstitution efforts have been excellently reviewed in ref. [16, 17, 95]. Cell division can be divided in two major steps. First, a division machinery mechanically constricts the cell membrane at the midpoint to create a dumbbell-like shape. Constriction is then followed by the final cleavage of the membrane at the neck region, which generates two physically separated daughter cells. The final abscission step is under current investigation by others using the eukaryotic ESCRT machinery [96, 97] or bacterial dynamin [98], but is not part of this thesis. We henceforth refer to constriction as division.

In vivo, constriction is typically carried out by a designated protein machinery. Division of bacteria mainly relies on the polymeric FtsZ protein which forms a cytokinetic ring (Z-ring) [99, 100], a large fraction of archaea divide using the Cdv system [101–103], and yeast and animal cells make use of the contractile actomyosin machinery [104, 105]. It is important to note that the exact mechanistic working principles of all cell division processes is to date still unknown. In bacteria and archaea, cell division involves the synthesis and remodelling of the cell wall. This extra component complicates reconstitution, especially because the cell wall is notoriously difficult to rebuild. We therefore choose to work with the eukaryotic machinery relying on actin and myosin. An additional reason to use the eukaryotic system for reconstitution is that it is the closest mimic to the division machinery that divides the cells in our own bodies, thus being of great interest for biomedical applications. Note that while cell division can also be reconstituted following an engineering approach, based on non-biological components or non-physiological processes[71, 92, 95], that is not the aim of this work.

Actin is a dynamic, filamentous protein which is able to form a wide variety of networks by its interaction with actin-binding proteins (reviewed in [105, 106]). While it is common knowledge that myosin motor proteins are able to contract actin networks, it remains elusive how actin and myosin are organized on the molecular level to establish cell division. In fact, acto-myosin based division strategies vary between eukaryotic cell types (reviewed in [107]). Much is also still unknown about the role of other actin-binding proteins and how actin network deformations result in controlled remodelling of the cellular membrane. Previous studies have demonstrated successful reconstitution of actin networks inside GUVs [108–111]. Membrane-bound actin networks could even be deformed by myosin activity [112–114]. However, none of these studies have shown constriction of the GUV membrane. Altogether, reconstitution studies suggest that vesicle division by actin and myosin requires a fine interplay between contractility of the actomyosin network, dynamic filament turnover, and adhesion of the network to the GUV membrane (for details, see chapter 2). The precise relation between these has yet to be reconciled, and requires a detailed molecular picture as well as an understanding of the mechanics of the actin-membrane composite structure.

1.5. AIM AND OUTLINE

The aim of this thesis is to develop a toolbox to reconstitute and thereby understand the container life cycle, as a prerequisite for building a synethtic cell from the bottom up.

In particular, we are interested in rebuilding an actomyosin machinery as is found in animal cells which is capable of dividing but also mechanically stabilizing the synthetic cell. Essential parts of this toolbox, we considered to be: (i) a GUV formation method that is capable of encapsulating cytoskeletal components, (ii) image analysis methods to quantitatively characterize large populations of GUVs throughout the cell cycle, (iii) membrane mechanical measurements to evaluate the mechanical effect of reconstituted cytoskeletal systems, and (iv) a mechanism to generate membrane growth. Starting from these requirements, the outline of this thesis is as follows.

First, in **chapter 2**, we describe the current state-of-the art of reconstituting actin-mediated division of synthetic cells. Based on a literature survey, we summarize the conceptual requirements for actin-mediated division, we discuss reconstitution work that has been done so far, and we lay out a roadmap for future research. Importantly, we take a systems view on synthetic cell division: besides the contractile actomyosin network, we acknowledge the roles of compartmentalization and the membrane.

Then, we start addressing the topic of synthetic cell fabrication in **chapter 3**. As discussed above, the success of recreating an autonomous cell relies heavily on the formation of its container and the controlled encapsulation of functional components therein. We show how the GUV formation technique known as continuous Droplet Interface Crossing Encapsulation (cDICE) [3] can be used to reliably produce vesicles while encapsulating a wide range of synthetic cell modules. We took a quantitative approach to map the effect of input parameters on vesicle production. Interestingly, we found that cDICE is highly sensitive to environmental conditions such as air humidity, which affected the membrane quality and yield of the produced vesicles. By performing sensitive preparation steps in the glove box, we show that high-quality vesicles can be robustly produced. Furthermore, we demonstrate that encapsulation of functional proteins and complex mixtures can be boosted by slight modifications in the formation protocol such as inclusion of sterically active lipids.

While cDICE provides a good basis for complex reconstitution, encapsulation of polymeric proteins remained challenging in our hands. This severely limits its applicability for reconstitution of a filamentous cytoskeleton. Therefore, in **chapter 4**, we take a bird's-eye view on GUV formation. Based on our personal experimental efforts, we compare a number of classical and new methods based on their potential to perform cytoskeletal reconstitution. In addition, we introduce a new GUV formation method by making a small but important change to the original cDICE protocol. We show that this new method, called emulsion Droplet Interface Crossing Encapsulation (eDICE), effectively by-passes encapsulation problems of cDICE. Using eDICE, we managed to encapsulate the cytoskeletal polymeric proteins actin and septin, which takes reconstitution in GUVs to a next level.

A crucial aspect of synthetic cell research is robust, quantitative analysis of samples. In **chapter 5**, we introduce the new open-source versatile software DisGUVery which allows for automated high-throughput analysis of GUVs in microscopy images. We describe the three vesicle detection algorithms that our software encapsulates, as well as a number of pre-defined analysis modules. With a careful performance analysis, we show that our software is compatible with a wide range of microscopy images and synthetic cell experiments. Our software therefore facilitates quantitative analysis of large GUV

populations, independent of their polydispersity, imaging conditions, or the desired application. This makes DisGUVery a powerful tool, for example to obtain size distributions of produced GUV samples, to measure encapsulation efficiencies, to determine membrane colocalization of a fluorescent protein, to classify vesicles based on lipid-lipid phase separation, or to quantify vesicle deformations.

Division of a synthetic cell requires a mechanical interplay between the cytoskeletal structure and the enveloping membrane. In **chapter 6**, we propose pipelines for two measurements that are often used to probe cell surface mechanics. First, micropipette aspiration (MPA) is a technique to actively deform cells or vesicles and measure the elastic response [7]. Second, membrane bending rigidity can be extracted from spontaneous fluctuations by vesicle fluctuation analysis (VFA) [4, 5]. For both methods, we explain how we implemented them in our lab, and we provide a clear workflow of how to perform the experiments as well as their analysis. As a validation of our new experimental setup and the entire workflow, we conclude the chapter with a set of benchmark measurements on model membranes. Outcomes of MPA and VFA measurements agree with each other, and correspond to literature values, together validating our workflow. We anticipate that these workflows lay a firm basis for the mechanical characterization of cytoskeleton-containing GUVs of increasing complexity.

In **chapter 7**, we focus on membrane growth of the synthetic cell. Using membrane-anchored DNA [8, 9], we show that small vesicles can be fused to GUVs, thereby establishing an external membrane feeding mechanism. To explore if this fusion assay can be used for synthetic cell membrane growth, we perform a thorough characterization of experimental input parameters. We study the individual steps in the fusion process by quantitive image analysis of large populations using the DisGUVery software. We show that fusion occurs in up to 30% of the GUVs analyzed, and we propose ways to further enhance this fraction. Importantly, we demonstrate fusion in vesicles produced with eDICE, which opens up a wide range of possibilities to integrate membrane growth with the reconstitution of cytoskeletal division machineries.

We conclude this work in **chapter 8** with an outlook on synthetic cell endeavours. We show how this work forms a basis for future reconstitution efforts and give both concrete and ambitious directions for follow-up research. In our opinion, the most important next steps lie in integration of different modules that are so far typically being developed independently. In addition to follow-up experiments, we present our view on the status-quo of the field of GUV research, and recommend general advancements in terms of vesicle fabrication and analysis.

2

ACTOMYOSIN-DRIVEN DIVISION OF A SYNTHETIC CELL

One of the major challenges of bottom-up synthetic biology is rebuilding a minimal division machinery. The animal cell division apparatus is mechanically the simplest, in which an actin-based ring constricts the membrane, as compared to microbes and plant cells where a cell wall is involved. Furthermore, reconstitution of the actin division machinery helps to understand the physical and molecular mechanisms of cytokinesis in animal cells and thus our own cells. In this review, we describe the state-of-the-art research on reconstitution of minimal actin-mediated cytokinetic machineries. Based on the conceptual requirements that we obtained from the physics of the shape changes involved in cell division, we propose two major routes for building a minimal actin apparatus capable of division. Importantly, we acknowledge both the passive and active roles that the confining lipid membrane can play in synthetic cytokinesis. We conclude this chapter by identifying the most pressing challenges for future reconstitution work, thereby laying out a roadmap for building a synthetic cell equipped minimal actin division machinery.

This chapter was written by Lucia Baldauf, Federico Fanalista and Lennard van Buren with equal contributions and is currently being prepared for submission.

2.1. INTRODUCTION

Bottom-up synthetic biology is an emerging field at the interface of cell biology, (bio)-chemistry and (bio)physics. Several national and international initiatives have been founded recently, which aim at reconstituting synthetic cells that can autonomously grow and divide [21]. As a chassis, usually giant unilamellar vesicles (GUVs) are used, which are cell-sized (5-50 µm) containers enveloped in a lipid bilayer [16, 28]. One of the key functions that a synthetic cell must be able to perform in order to be considered life-like is cytokinesis, a process in which a cell physically splits into two daughter cells. Various reconstitution strategies are being pursued, inspired by biological strategies employed by prokaryotic, archeael or eukaryotic cells [92, 95]. These biological systems have in common that cell division is accomplished by a cytoskeletal protein machinery, often ring-shaped, that assembles at the cell equator. In microbial cells (bacteria and yeast), this protein machinery collaborates with a cell wall synthesis machinery. By contrast, animal cells lack a cell wall and cytokinesis is entirely driven by the actin cytoskeleton. Actin-based cell division could thus be an ideal basis for engineering synthetic cell division.

Bottom-up reconstitution of actin-based cell division is interesting not only from an engineering perspective, but also as a means to understand how cytokinesis works at the molecular level in animal cells. Although cytokinesis is a well-studied cellular process, surprisingly many fundamental questions about its working principles remain unanswered [115]: how are forces generated and sustained? How much molecular complexity is needed to ensure that the actin cortex retains its structural integrity during cytokinesis? What are the requirements for cortex-membrane-interactions to promote furrow ingression? These questions are difficult to address in cell-based studies because of the enormous molecular complexity of cells and also because of substantial variations in cytokinetic mechanisms employed by different species and different cell types [116, 117].

In this review, we propose a roadmap towards reconstituting actin-driven cytokinesis in minimal cells. For brevity, we consider only the process of furrow ingression, neglecting other aspects such as membrane abscission and chromosome and cytoplasmic segregation [118]. Based on theoretical models of cytokinesis in animal cells, we first identify four central biophysical requirements for actin-driven furrow ingression. Next we review experimental insights obtained from recent efforts to reconstitute minimal actin systems. Finally we propose a roadmap towards building a molecular machinery that can successfully deform a minimal cell-like container. We also emphasize the importance of controlling the area of the synthetic plasma membrane to enable cell division.

2.2. BIOPHYSICAL REQUIREMENTS FOR MAKING A CELL DIVIDE

Cytokinesis in animal cells is a complicated process that involves many different molecular components (lipids and proteins) whose interactions and localization are tightly regulated. At a coarse-grained level, however, it is possible to formulate general biophysical requirements for cell division based on a consideration of the mechanical forces at play. Pioneering experimental work from the 1950s onward has demonstrated that cytokinesis is accompanied by membrane furrowing, cortical stiffening [6, 119] and the appearance of ordered filamentous structures in the cytokinetic ring [120, 121]. These ob-

servations have served as input for coarse-grained theoretical and computational models that describe cytokinesis as the shape evolution of a thin, viscoelastic and active shell around a (nearly) constant volume of cytoplasm. From the models, we can infer several key requirements that a cell, living or synthetic, must fulfil in order to successfully divide (fig. 2.1).

1. Cortical activity. The actin cortex driving cytokinesis in animal cells must be active. This means that it should include elements that hydrolyse adenosine triphosphate (ATP), an energy-carrying nucleotide, to generate contractile forces that produce cellular shape changes. The viscoelastic and active nature of the cortex can be described using the framework of active gel theory as proposed by Kruse et al. [122]. This formalism is usually applied in the viscous limit [123–126], as cytokinesis is slow (minutes) compared to the fluidization time scale (10 s) of the actin cortex [123]. The molecular origins of active force production are complex and depend on molecular detail, which will be addressed in section 2.3.

2. Cortical thickness. Cortex activity, at least when mediated by myosin motors, is roughly proportional to cortical thickness [123–125]. To maintain cortical activity, the cortex must consequently be of a controlled thickness. Cortical thickness is regulated by a balance of actin polymerization and depolymerization, or turnover, and cortical flows: cortical flows accumulate material in the cytokinetic furrow, whereas turnover redistributes actin throughout the cell. This suggests two requirements for synthetic cell division: Firstly, components of the cortex must be laterally mobile to be effectively redistributed by cortical flows [123, 125, 127]. Secondly, actin turnover rates must be low enough to allow some local actin accumulation and therefore increased contractility in the furrow region. If actin is removed too rapidly, furrow constriction slows down significantly and may be halted altogether [125]. On the other hand, complete lack of filament turnover in a 2D actomyosin cortex is theoretically predicted to lead to irreversible clustering of actin, inhibiting effective stress generation [128]. This prediction has yet to be reconciled with experimental evidence from yeast cells, which suggests that the persistent presence of filamentous actin, rather than turnover is key for successful contraction of the cytokinetic ring [129].

3. Cortical symmetry breaking. From the 1930s onwards, various models have been proposed to explain the mechanical basis of cytokinesis. The early models range from active expansion of the cell poles [130], through active pushing by the mitotic spindle[131], to spindle-mediated relaxation of the cell poles [127, 132] and finally active constriction of the cytokinetic furrow [121, 125, 133, 134]. While details vary widely between these models, they share a key characteristic: they all posit that there must be a difference in activity between the polar and equatorial regions to drive furrow ingression. After decades of research it is now widely accepted (reviewed e.g. in [135]) that the main driving factor of animal cell cytokinesis is actin-based constriction at the cleavage furrow. However, in vitro reconstitution may be the ideal tool to understand actin's role in molecular detail, and to assess to which extent other mechanisms [136, 137] also contribute.

4. Cell surface area and volume regulation. Consistent with observations in cells, models have generally assumed that the cytoplasm is very weakly, if at all, compressible [125, 127]. The apparent surface-to-volume ratio, however, changes dramatically during cytokinesis. It follows that the (visible) surface area must be changing. In theoretical

works this change in surface area is generally assumed to be energetically 'free', as living cells can regulate the available membrane area through a variety of processes like blebbing [138], or caveolae disassembly and membrane trafficking [139, 140]. This supply of membrane on demand is probably one of the most challenging aspects to recapitulate in a reconstituted system.

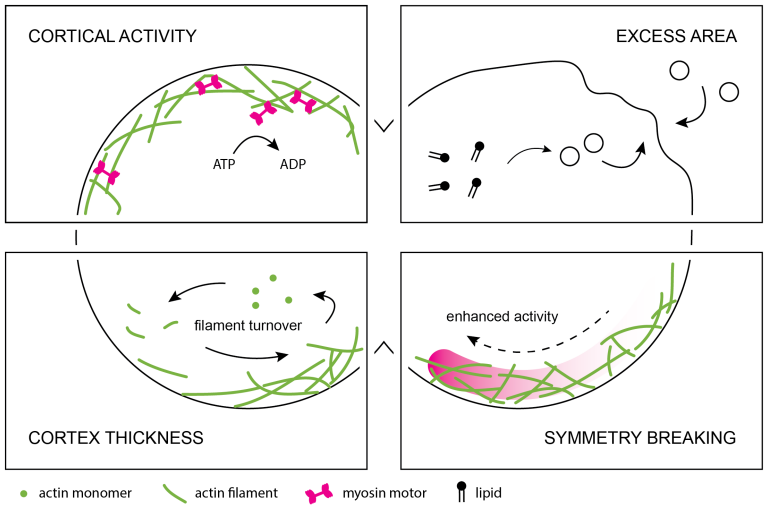

Figure 2.1: **Conceptual requirements for reconstituting synthetic cell division.** For cell deformation to occur, cortical activity is required (top left), which can for example be generated by myosin activity. Regulation of cortex thickness (bottom left) is essential for control of cortical activity and is determined by the rate of actin turnover versus cortical flows. For cortical activity to lead to cell deformation, the symmetry of the system needs to be broken (bottom right). Finally, to accommodate the drastic change in surface-to-volume ratio during division, excess membrane area needs to be generated prior to or during cytokinesis (top right).

2.3. ROADMAP TOWARDS ACTIN-DRIVEN CELL DIVISION IN VITRO

Cytokinesis of animal cells is a highly complex and tightly regulated process. Yet, fairly minimal computational models are able to recapitulate cytokinesis, suggesting that the underlying mechanisms may be recreated with simplified molecular mechanisms. Here, we propose a roadmap towards reconstituting actin-driven cell division by considering lessons from recent cell and *in vitro* studies. Basically, there are two routes for reconstitution of actin-driven cytokinesis (see fig. 2.2). First, cell division can be recreated via reconstitution of an actin cortex that is more contractile at the cell equator as compared to the poles upon symmetry breaking. This route is most close to cytokinesis in mammalian cells, and we therefore name it the naturalistic route. Second, by construction of a cytokinetic ring that anchors and contracts at the cell equator, coined the engineering route. We will first discuss the design of an actin-based machinery fit for driving cytokinesis in both scenarios, and in the next section consider the design of the lipid membrane envelope.

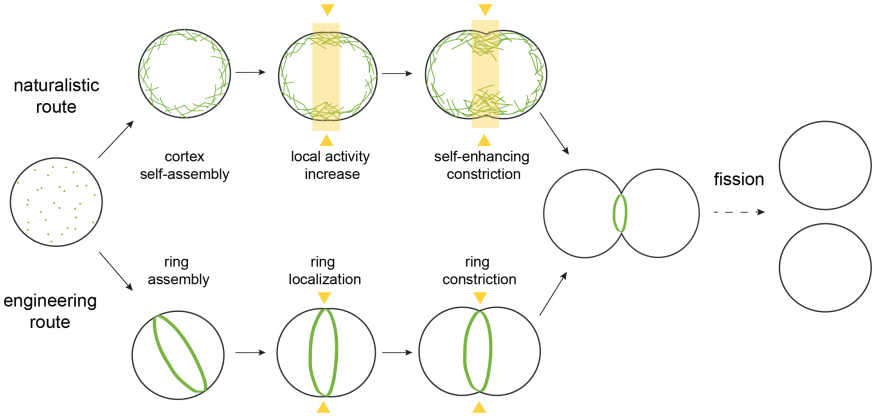

Figure 2.2: **Routes to actin-based synthetic cell division.** There are two main routes for achieving actin-driven division of a synthetic cell: by symmetry breaking of a reconstituted actin cortex, triggered by external or biochemical cues, which leads to self-enhanced furrow constriction (the 'naturalistic' route, top), or by construction of a contractile ring at the cell equator (the 'engineering' route, bottom). Yellow arrowheads indicate where contractile activity is concentrated. The final fission step is outside the scope of this review.

2.3.1. NATURALISTIC ROUTE: BUILDING A SELF-ASSEMBLING CYTOKINETIC RING

During interphase, mammalian cells have a continuous actin cortex that lines the plasma membrane [105]. When they enter mitosis, the cortex is remodelled and self-assembles into a contractile ring at the cell equator. Symmetry breaking and midplane localization of the cytokinetic furrow is initiated by biochemical signalling, which includes Rho-dependent myosin phosphorylation in the furrow region [125, 141]. The locally enhanced activation of myosin is thought to lead to cortical flows from the poles to the equator [127, 142], which further accumulates contractile elements in the furrow and drives furrow ingression [125]. Such a complex self-assembling system has not been built to date, but steps have been taken along the road (fig. 2.3).

RECONSTITUTION OF ACTIVE ACTIN NETWORKS

Both cell-free experiments and theoretical models of cortex-like disordered actin networks have been used to elucidate why disordered actomyosin networks are contractile in the first place. The detailed mechanisms are reviewed elsewhere [143–145], but they broadly comprise two scenarios. Actin filaments are semiflexible polymers with a thermal persistence length of 10-15 µm, of the same order as their contour length. The first contraction scenario, relevant for well-connected networks of long filaments, is that the anisotropic mechanical force-extension response of actin filaments causes them to buckle and break under motor-induced compressive stress [146, 147]. The second scenario, relevant for networks with short actin filaments, is that the structural polarity of actin filaments in combination with the tendency of myosin II motors to dwell at the plus end before detachment causes contraction via polarity sorting [124, 148, 149]. In the actin cortex of mammalian cells there may be a combination of both mechanisms, since there are distinct populations of short and long filaments present [150].

Notably, the combined effect of contractile motor activity and actin turnover remains poorly explored. Theoretical models generally assume that the cytokinetic cortex does undergo actin turnover [123, 125, 151], and have even indicated that turnover is key for sustained stress generation during furrow ingression [128]. Experimentally, besides one study with a cell extract [152], only one minimal in vitro study has so far combined actin turnover and myosin activity [153]. This work showed that myosin activity alone can be sufficient to induce turnover in minimal actin networks (see (fig. 2.3, purple). Myosin-driven compaction and fragmentation of Arp2/3-nucleated actin led to the removal of actin from the network, and subsequent redistribution and re-incorporation of network components, creating a cortex in dynamic steady state. Strikingly, actin turnover rates were observed to be much slower here than typical rates in cells [154, 155], with actin turning over within tens of minutes rather than tens of seconds. This is likely due to the absence of dedicated actin severing proteins in the minimal system. More rapid turnover has been observed in vitro in volume-spanning entangled actin networks where filaments were severed by cofilin and polymerization was driven by formin [156]. Combining more rapid turnover with motor activity in vitro may open a rich field of network behaviours, with complex implications for both the regulation of cortical thickness and of stress propagation and relaxation [157].

To build and control a system that allows actin to turn over, we can turn to the growing body of work studying the functions of various actin regulators on the single molecule or filament level. Research into the two key nucleators of cortical actin, Arp2/3 and formins [150, 159, 160] has uncovered new complexities in recent years. Both the processivity and the actin filament elongation rate of different formins have been shown to be regulated by the physicochemical environment, the presence of profilin, and mechanical stress [161–163]. Even more complex co-regulation of formin with other barbed-end binding proteins is emerging [164]. Regulation of Arp2/3 by profilin [165, 166] as well as by actin filament curvature [167] has been known for a number of years, but the true diversity and complexity of the various isoforms of Arp2/3 is only just emerging [168]. Spire, the most recently identified type of actin nucleator [169], remains barely used in reconstitution experiments and may offer another route towards reconstituting a minimal dynamic cortex. Actin depolymerization can equally be controlled by various factors. Disassembly of filamentous actin in vitro is usually mediated by proteins of the ADF/cofilin family [170]. The activity of ADF/cofilin proteins has been shown to depend on cooperation with other proteins [171, 172] and on actin crosslinking [173]. ADF/cofilin also facilitates debranching in actin networks nucleated by Arp2/3 [170], which is furthermore sensitive to force and actin filament age [174].

RECONSTITUTION OF ACTIN CORTICES INSIDE GUVS

Controlled actin encapsulation in GUVs has proven to be a challenge. Over the years, many different methods have been explored for protein encapsulation, either based on lipid swelling [109] or on emulsion transfer [108, 113, 175] (reviewed in [16] and see chapter 4). Of these, emulsion transfer is currently the most used method, although the encapsulation efficiency and the ability to upscale the number of encapsulates remain to be characterized [175]. Most prior GUV studies focused on the effect of crosslink proteins and myosin motors on bulk-nucleated actin. By contrast, membrane-nucleated actin networks with turnover in GUVs remain poorly explored. Early works from the

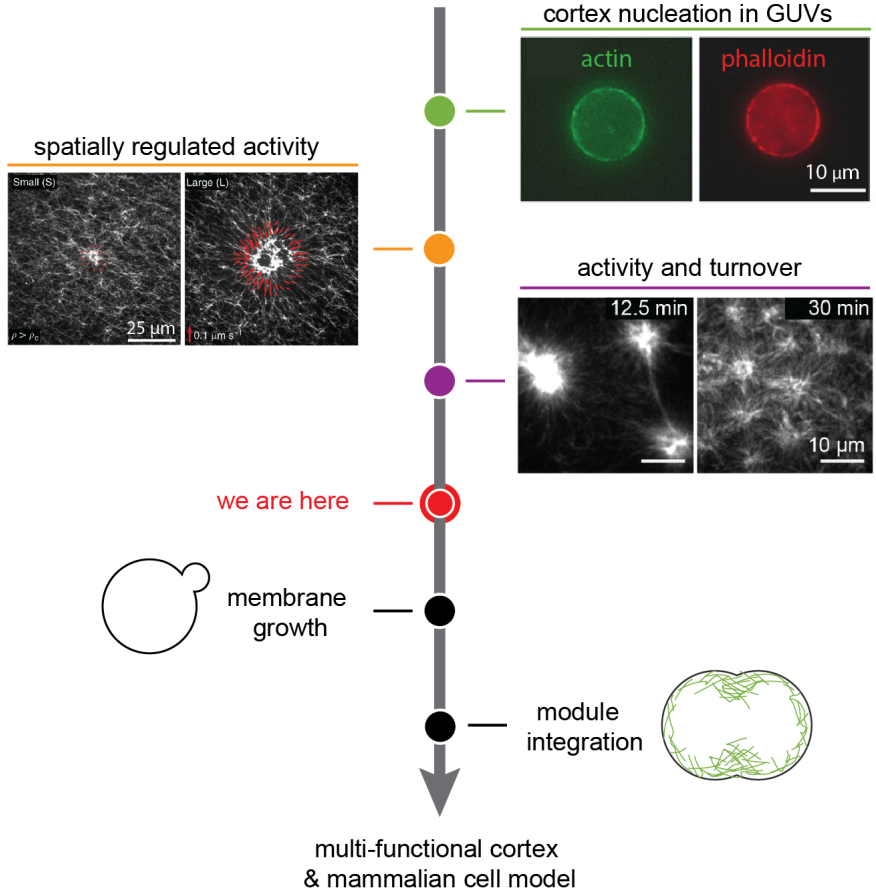

Figure 2.3: **Roadmap to division with an actin cortex.** Green: successful nucleation of an actin cortex inside GUVs [108]. Filament formation of actin (green) is confirmed by co-localization of the filament-binding peptide phalloidin (red). Orange: spatiotemporal control of myosin activity by light-induced inactivation of the myosin inhibitor blebbistatin was used to generate network contraction over different length scales, from small (left) to large (right) [158]. Purple: combination of myosin activity with actin filament turnover generates sustained network contraction [153]. In the coming time, steps need to be taken to engineer membrane growth, and finally to integrate the different modules inside a GUV.

Sykes lab [108, 176] demonstrated that Arp2/3 nucleated cortices can be reconstituted at the inner leaflet of GUVs (fig. 2.3, green), and that such cortex-bearing vesicles reproduce aspects of the mechanics of living cells. Recently, Dürre et al. demonstrated that Arp2/3 nucleated cortices can induce local deformations of the GUV membrane by either polymerization forces alone or in combination with contractility induced by non-muscle myosin-II [112].

More extensive work, especially with myosin-driven cortices, has been performed with stable actin filaments anchored to the membrane by streptavidin or actin-binding membrane proteins. In such systems, cortical tension was shown to depend on the ratio

of active versus passive crosslinkers [177] and excessive cortical tension was shown to cause full or partial detachment of the cortex from the membrane [177, 178]. Recently, Litschel et al. demonstrated the formation of actomyosin rings in GUVs [113]. However, these structures were unable to deform the GUV membrane on large length scales because they slipped on the membrane. Based on our understanding of cell division, this is likely due to (at least) three missing factors: cortex turnover, symmetry breaking between the poles and equator of the synthetic cell, and a severely limited supply of extra membrane area. Symmetry breaking is likely necessary for productive and sustained membrane deformations. There are several artificial means by which symmetry breaking could be triggered in synthetic cells. Myosin activity could, for instance, be locally light-activated by targeting either the light-sensitive myosin inhibitor blebbistatin [158, 179, 180] (see (fig. 2.3, orange) or myosin-II directly [181]. Similar approaches could be used to locally modulate the crosslink density of the actin cortex or the interaction strength of the cortex with the synthetic cell membrane. Finally, it would likely help to make GUVs shape-anisometric, for instance by using microfluidic channels [182].

Conceptually, building a dynamic actin cortex and pushing it towards self-assembly of a cytokinetic furrow is very attractive. Such a system would mimic many core attributes of the cortex of living animal cells. Further, the continuous nature of such a cortex would allow it take on a dual function, both as a mechanoprotective module for the synthetic cell and as a division apparatus, which sets it apart from other cytoskeletal systems such as FtsZ [183]. A life-like actin cortex offers the opportunity to test existing theoretical models of cell division and to tease out the essential functions needed for cytokinesis in living cells. On the other hand, a dynamic actin cortex will necessarily comprise more proteins and hence a higher level of complexity than one composed of stable actin filaments. Especially sustained actin turnover in combination with motor activity will require fine control over stoichiometry and activity of cytoskeletal components.

2.3.2. ENGINEERING ROUTE: BUILDING AN ISOLATED CONTRACTILE RING

A more engineering-type approach to synthetic cell division may also be interesting: instead of building a cortex that self-organizes into a ring, one could build an isolated ring directly (fig. 2.2, bottom). This would fulfil the requirement for different activities in polar and equatorial contractility easily, as by definition the poles are not contractile in such a case. If a sufficient supply of long actin filaments throughout furrow ingression can be ensured, the need for controlled turnover may be diminished and the complexities of such regulated filament assembly and disassembly may be avoidable. This approach will need to address three key challenges: 1) to build an actin ring, 2) to make it contractile, and 3) to control its position such that membrane invagination rather than ring slippage occurs.

HOW TO BUILD AN ISOLATED RING?

Actin filaments can be bundled and bent into ringlike structures in various ways (fig. 2.4, green). Most simply, ring formation can be induced by entropic effects through macromolecular crowding [184] or by cross-linking with multivalent ions [185]. Alternatively, proteins can be used to bend actin into rings. Septins spontaneously bend actin into

ringlike structures [186] and are recruited to the cytokinetic ring, where they cooperate with anillin in actin-membrane binding [187–190]. Anillin itself also promotes the formation of actin rings [191]. Further, the IQGAP fragment 'curly' has recently been shown to bend actin into rings on model membranes [192]. The fact that all three of these proteins are enriched in the cytokinetic furrow [193] suggests that these ring-forming capabilities may provide a cellular mechanism to promote successful cytokinesis.

Confinement of actin filaments inside spherical droplets or vesicles tends to promote the formation of actin rings because the confinement forces the semiflexible filaments to the periphery so the bending energy is minimized [197]. Entangled or crosslinked actin networks inside droplets or vesicles form peripheral cortex-like networks [111, 198–200], while bundled actin forms one or more closed rings [109, 194, 200]. Single rings form when the container size is smaller than the persistence length of the actin filament or bundle. Recent theoretical [201] and experimental work [113] has shown that ring formation is further enhanced by introducing actin-membrane adhesion. It should be noted, however, that ring formation requires a subtle balance of filament-filament and filament-wall adhesion, as well as size and stiffness of the confinement, and is not trivial to precisely control experimentally.

HOW TO CONTRACT AN ISOLATED RING?

Contracting a once-formed actin ring can again proceed in different ways (fig. 2.4, orange). The classical purse-string model posits a well-organized cytokinetic ring that closes by myosin-mediated translocation of actin filaments [121, 202]. Although this model does not appear to hold in all cell types [203–205], recent superresolution and electron microscopy showed convincing evidence that it does apply at least in some cell types [206, 207]. Contracting actin-myosin rings have been succesfully reconstituted on supported lipid bilayers [192] and inside water-in-oil droplets [194] and GUVs [113]. The closure efficiency is likely determined by the orientation and arrangement of the actin filaments in the ring, which can be tuned by crosslinker composition and concentration [111, 147, 208–210].

Alternatively, ring contraction may be driven by mechanisms that do not require molecular motors. For instance, anillin was recently shown to drive actin bundle contraction even though it is a passive crosslinker [191]. Contraction was attributed to an energetically driven process whereby actin filaments increase their overlap as long as energy can be gained by accumulating diffusible crosslinkers in the overlap region [191]. This mechanism was enhanced when anillin was combined with actin depolymerization. Since contraction driven by passive crosslinkers does not consume energy from an external energy source such as ATP, it can only bring the system into a configuration of minimal free energy, at which point rearrangement will stop [211]. Intriguingly, recent theoretical modelling [212] suggests that a crosslinker that consumes ATP to unbind from actin filaments, but does not actively translocate them like myosin, could in principle induce contraction indefinitely. In this case, the consumption of an energy carrier breaks detailed balance in the system, and in combination with the asymmetric mechanical properties of actin, overall contractile forces can arise.

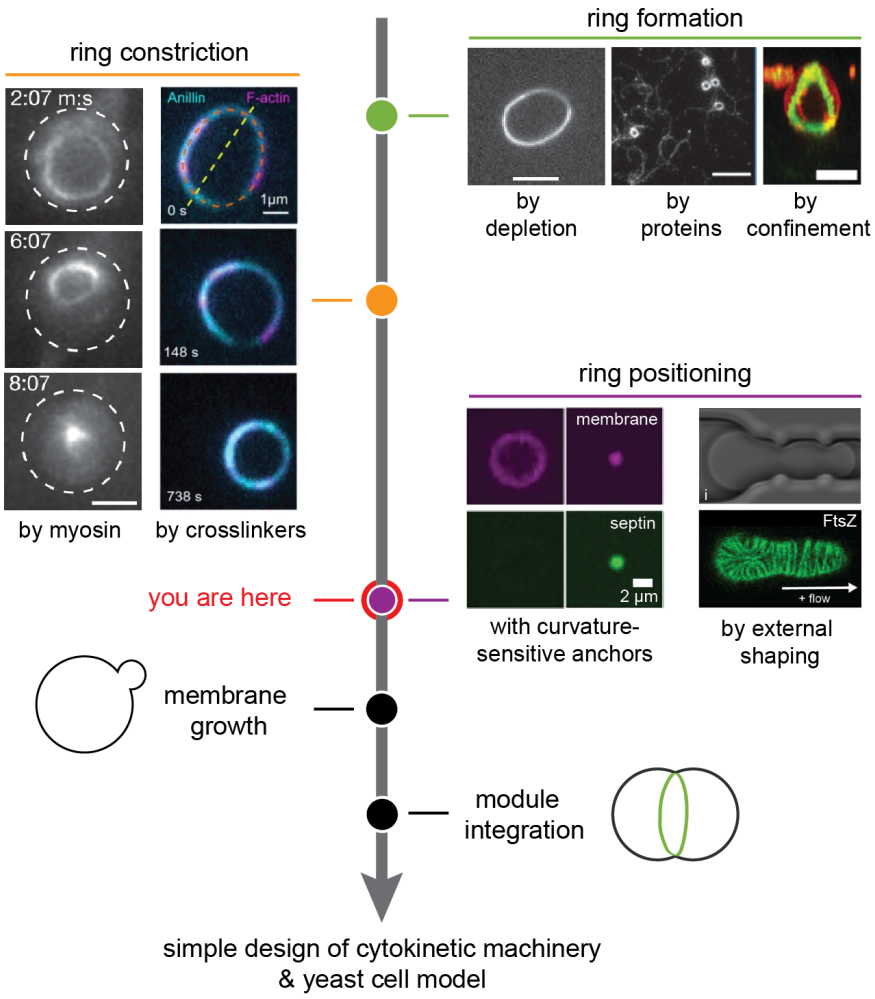

Figure 2.4: **Roadmap for division with contractile actin ring.** Roadmap towards synthetic cell division using a contractile actin ring. Green: actin rings can be formed by depletion interactions using macromolecular crowders [184], by proteins that combine actin binding with curvature generation such as curly [192] or simply by confinement of actin bundles [109]. Orange: constriction of actin rings can be executed using myosin motors [194] or using actin crosslinkers like anillin [191]. Purple: the actin ring can be positioned using curvature-sensing anchors (left: septin binds preferentially to membranes of higher curvatures as shown with membrane-coated beads [195]) or by mechanical deformation (right: microfluidic traps deform GUVs leading to rearrangement of FtsZ rings [196]). In the next steps towards achieving synthetic cell division, membrane growth needs to be reconstituted, and all separate modules have to be integrated.

HOW TO KEEP AN ISOLATED RING IN PLACE?

Although contractile actin rings have been successfully reconstituted inside GUVs, so far none of these efforts have yielded anything close to membrane invaginations. The rings either detached or slipped along the membrane upon myosin activation [113, 177,

178, 194], at best producing rare instances of slight membrane deformation [113]. In cells, positioning of the cytokinetic ring is ensured by a complex and poorly understood interplay between the actin and microtubule cytoskeleton, local changes in lipid composition, and soluble signalling molecules [213, 214]. Reconstituting this interplay in GUVs seems too technically challenging to be expected in the coming years. We therefore expect that simpler, if less biological, solutions may be more promising. To the best of our knowledge, no such efforts have been reported so far. However a few options present themselves (fig. 2.4, purple): curvature-sensing or –inducing scaffolding proteins such as septins [195] or I-BAR-domain proteins [215, 216] may help in templating a furrow and inhibiting slippage of contractile actin rings. They may have to be combined with more engineering-type solutions designed to deform GUVs from the outside, either by confinement in traps [182, 196] or by membrane-binding complexes [64, 217, 218].

Building an isolated contractile actin ring in principle offers an elegant way to drive synthetic cytokinesis. Formation of such a ring requires only few components and tuning ring contractility is certainly subtle, but most likely achievable. The biggest technical challenge in this approach is to localize the ring at the equator and keep it in place during contraction so as to foster productive membrane deformation. On a more conceptual level, reconstituting isolated contractile rings likely will not bring us much insight into the mechanisms of cytokinesis in animal cells. It may however be a valid strategy for understanding mechanisms in yeast cytokinesis, in tandem with top-down work on yeast cell ghosts [219].

2.4. INVOLVING THE MEMBRANE

So far, we have largely ignored an important assumption in the key requirements set out in section 2.2, which is that the GUV membrane and actin cortex are intrinsically coupled. However, it is far from trivial that actomyosin contraction is followed by deformation of the cellular membrane. While actomyosin networks and membranes have separately been thoroughly investigated by biophysicists, their interplay has received much less attention and presents a crucial challenge to address in the coming years.

2.4.1. MEMBRANE-CORTEX ANCHORING

In vivo, a multitude of cytoplasmic proteins is known to be involved in actin-membrane adhesion, many of which have binding sites for both actin and membrane lipids. These proteins include ERM (ezrin, radixin, moesin)-proteins, myosin1b, anillin and septins [223–226]. How these proteins cooperate in adhesion and how they are spatially organized at the membrane remains elusive. Electron microscopy and superresolution microscopy have revealed that the distance between the filamentous actin and the plasma membrane is surprisingly large, ranging from 10 to 20 nm in the cell cortex of animal cells [227] and from 60 to 160 nm in the cytokinetic ring of fission yeast [228, 229]. It is unclear how this large gap, which is often wider than the distance that known linker proteins span, arises. There is evidence that the actin cortex itself is stratified, with myosin filaments being restricted towards the cytoplasmic side of the cortex due to steric exclusion from the dense cortex [230]. Interestingly, a recent in vitro reconstitution study showed that actin-myosin networks on supported lipid bilayers spontaneously self-organize into

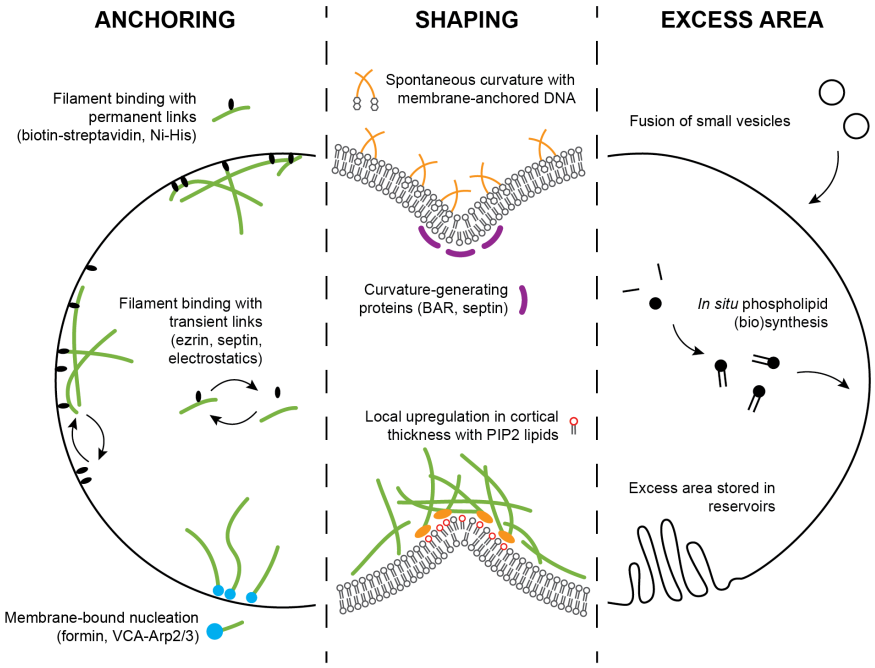

Figure 2.5: **Membrane engineering for synthetic cell division.** Schematic overview of possibilities for membrane design. Anchoring of the actin cortex (left) can be done either via filament nucleation from the membrane, or via filament binding to the membrane. Binding can be done using strong permanent linkers, or using weaker transient links. Membrane shaping (middle) can be done by generating spontaneous curvature, for example with membrane-bound DNA nanostars [220] or by physiological curvature-generating proteins such as BAR proteins [221] or septin [222]. Otherwise, when lipids can be spatially separated, local elevation of PIP2 levels can increase cortical thickness via regulating actin nucleation and severing proteins. To provide excess area during cytokinesis (right), new membrane area can be added by fusion of small vesicles (see chapter 7) or by *in situ* synthesis of phospholipids. Alternatively, membrane area could be stored in reservoirs that become accessible upon furrow ingression.

radial actin structures (asters) with myosin at the core and layered atop to relieve steric constraints [231].

Mechanical measurements on cells indicate that the cortex is adhered to the membrane via a high density of weak links. With optical tweezers, one can pull membrane tubes from cells with membrane-bound beads. These tubes can easily be moved over the cell surface [232], indicating that the membrane easily zips off the cortex and quickly rebinds. Various tube pulling experiments have shown that the force required for tube extrusion is dependent on the levels of ezrin [233] and PIP2 lipids [234]. PIP2 lipids specifically interact with many actin-binding proteins including ezrin (reviewed in [235]). In *S. Pombe* cells, PIP2 depletion causes sliding of the cytokinetic ring, indicating that PIP2-dependent actin-membrane adhesion is essential for anchoring of the ring[236]. Although PIP2/protein interactions are individually weak, their high density collectively

causes a tight yet dynamic seam between bilayer and cytoskeleton.

In stark contrast with the reversible actin-membrane binding observed in vivo, in vitro reconstitution efforts have mostly relied on anchoring interactions with unphysiologically high binding affinity (fig. 2.5, left). Many studies used either direct coupling of biotinylated actin filaments to biotinylated lipids via streptavidin [113, 177, 237] or indirect coupling using His-tagged actin-binding proteins coupled to Ni-NTA lipids [178, 238]. These bonds are virtually permanent and unbreakable [239–241]. As described above, actin-myosin cortices anchored in this manner typically detach from the membrane upon myosin activation [177, 178]. In two studies with high anchor density, the acto-myosin cortex did remain attached to the membrane upon contraction, but it slid towards one side so the membrane was only minimally deformed [113, 177]. Cortex slippage is likely due to the fluid nature of the lipid bilayer membrane. Actin and microtubule gliding assays with motors proteins anchored onto supported lipid bilayers have shown that motor activity is accompanied by lipid slippage [242, 243]. The interplay between the dynamics of the actin cortex and the dynamics of the lipids is complicated. Adhesion to the actin cortex slows down lipid diffusion [244, 245], while myosin-driven actin cortex contraction can actively cluster lipids into microdomains [246–251]. Altogether, it remains poorly understood what conditions are necessary for the actin cortex to remain stably anchored and cause sustained membrane deformation.

Dynamic actin-membrane linkage has so far been reconstituted only on supported lipid bilayers. Using ezrin recruited to the bilayer via PIP2 lipids, indeed a dynamic actin network was created that could be remodelled by passive filament cross-linkers [252]. Bead tracking microrheology showed that ezrin serves as a dynamic cross-linker for the membrane-attached actin layer with the network stiffness being controlled by the pinning point density [253]. Ezrin-anchored actin filaments could diffuse over the membrane but longer filaments were immobilized, being pinned by a larger number of actin-membrane links [254]. This indicates that collective binding with transient links can fix cytoskeletal structures in place on top of a fluid membrane. Other promising candidates for in vitro transient actin binding are septins and anillin. Septins themselves can bind to membranes and self-assemble into filamentous scaffolds [255]. Membrane binding is curvature-sensitive [222, 256], which renders septins interesting candidates for spatially controlling actin organization in synthetic cells. In solution, septins can bind and crosslink actin filaments into curved bundles [186]. This could explain the role of septins in the formation and stabilization of contractile acto-myosin rings observed in vivo [186]. However, the simultaneous interplay of septins with lipid membranes and actin has yet to be reconstituted in vitro. Like septins, also anillin possesses both actin-binding and membrane-binding domains. Anillin has been shown by reconstitution to be able to anchor actin filaments to lipid membranes in a RhoA-dependent manner [257]. In combination with anillin's ability to bundle and constrict actin rings via condensation forces [191], it would be interesting to explore anillin's ability to promote synthetic cell division. Besides protein-based binding, actin filaments can also be bound to lipid membranes by electrostatic interactions and interactions can be tuned by the choice of ions, offering an alternative route for studying and modulating transient actin-membrane binding [258].

Besides actin-membrane linkers, also membrane-localized actin nucleation contri-

butes to cortex-membrane adhesion. The main nucleators of cortical actin filaments in vivo are Arp2/3 and formin [159]. Arp2/3 in combination with membrane-bound nucleation promoting factors such as WASP are responsible for the formation of branched actin filament arrays, whereas formins nucleate linear filaments. Actin nucleation has been successfully reconstituted in vitro both with formins, often for simplicity with constitutively active mutants [259], and with Arp2/3, often with WASP fragments such as VCA [108, 260, 261]. Actin turnover can be introduced by addition of severing proteins such as ADF/cofilin [262].

It is unknown how filament nucleation in conjunction with actin-membrane anchoring by dynamic linker proteins such as ezrin will influence the ensemble mechanics of the actin-membrane composite. Tailoring actin-based division machineries towards synthetic cell division will require careful tuning of the cortex itself, the anchoring strategy, and also the membrane physico-chemical properties.

2.4.2. MEMBRANE ENGINEERING

The membrane should not be considered just a passive player in cytokinesis. In contrast, membrane properties can be exploited to aid cytokinesis, for example by shaping the contractile network (fig. 2.5, middle). In vivo, the plasma membrane in the cleavage furrow has a distinct lipid composition that is thought to contribute to cytokinesis by biochemical signalling and perhaps also by induction of spontaneous curvature [263]. Elevated PIP2 levels at the cleavage furrow probably contribute to furrow ingression by recruiting anillin, septins and ERM-proteins [264]. Also, PIP2-mediated signalling promotes the formation and maintenance of a stable actin cortex by promoting actin nucleation and slowing down actin filament severing via actin regulatory proteins [265]. Other membrane compontents such as ganglioside GM1 and cholesterol also accumulate in the cleavage furrow, where they regulate and bind the cortex [264]. In addition, the distribution of PE lipids over the two bilayer leaflets changes significantly during cell division: while PE lipids reside in the inner leaflet during interphase, they are exposed in the outer leaflet of the cleavage furrow during cytokinesis [266]. This asymmetric distribution of PE lipids has been shown to be important for disassembly of the contractile ring after cytokinesis [266]. It is possible that the specialized lipid composition of the cleavage furrow also directly affects cytokinesis by changing the mechanical properties of the membrane, but this remains to be shown.

For engineering artificial cell division, it could be useful to exploit known mechanical effects of lipids. An important characteristic of lipid bilayers is that asymmetries over the two membrane leaflets give rise to membrane spontaneous curvature. Asymmetries can be generated in many different ways (reviewed in [267]), such as by different lipid compositions or different numbers of lipids in the two leaflets [268], proteins binding to one leaflet[64], membrane-anchored DNA oligo's inserting into one leaflet[220], or different solutes on both sides of the membrane [63]. In the context of actomyosin-based synthetic cell division, spontaneous curvature effects could be exploited for spatial control and symmetry breaking. Binding of proteins to the outer leaflet of vesicles can be used to make vesicles dumbbell-shaped and to constrict and even split the neck [64]. Generation of negative membrane curvature could be used to locally recruit septins, which selectively bind to membrane areas with micrometric curvature [195, 222]. In addition,

membrane-binding proteins that not only sense, but also generate curvature could be used, such as BAR-domain proteins. I-BAR proteins were shown to directly bind to actin in fission yeast [216] and are therefore interesting candidates for promoting actomyosin-driven membrane invagination. Interestingly, I-BAR domain proteins promote ezrin enrichment in negatively curved membrane protrusions [215], providing further prospects for boosting membrane invagination in vitro.

2.4.3. ADDITION OF NEW MEMBRANE AREA

To create two daughter cells from a single mother cell, assuming spherical geometry, the cell surface area has to increase by 28% [269]. In vivo, this extra membrane area is delivered to the cleavage furrow by targeted endosomal transport [82]. This mechanism does not only lead to a local area increase, but also allows fast and localized delivery of specific lipids and regulatory proteins (reviewed in [270]). For reconstitution of cell division, various strategies can be followed to increase the membrane area (fig. 2.5, right). First, GUV membranes can be grown by external addition of small unilamellar vesicles (SUVs) that can be forced to fuse with the GUV using fusogenic peptides, DNA (see chapter 7), or charge-based interactions [89–91, 271]. Second, lipid membranes can be grown by in situ synthesis of lipids from their precursors. Examples are non-enzymatic reactions from synthetic reactive precursors [84] or enzyme-catalysed biosynthesis using either purified proteins [87] or in vitro transcription-translation [88]. Although there is evidence that mammalian cells do not use area reservoirs, such as microvilli, to supply extra membrane area for division [272, 273], this mechanism could be exploited for engineering division in a synthetic cells. Asymmetries between the two leaflets of the bilayer generated by different means (see preceding section) can be used to store excess area in membrane tubes and buds [63, 64, 274, 275]. Low forces suffice to access these reservoirs [63, 275]. To achieve synthetic cell division, it will be important to match timing of membrane areal growth with the timing of actin-driven constriction. To achieve multiple cycles of division, it will moreover be important to build in a mechanism to maintain lipid homeostasis.

2.5. CHALLENGES AHEAD

In the past decades, our knowledge of cell division and its molecular actors has increased tremendously. To understand the physical mechanisms governing actomyosin-driven cell division, focus is put increasingly on bottom-up reconstitution experiments. Bulk and SLB experiments have helped us to understand mechanics of active actomyosin networks in 3D and 2D. However, translating these insights to the process of cell division is not trivial. To summarise, we list here the critical challenges that need to be overcome before we can reconstitute a minimal version of actin-driven cell division.

First, we need to understand how network contraction is sustained to drive division all the way. This will require myosin activity working in concert with actin turnover. While activity and turnover have been studied to great extent individually, we still have minimal understanding how they together govern actin network mechanics and contractility. Not only is this a challenging system to understand from a physical and biological perspective, also from an experimental perspective it is difficult to recapitulate

as it involves a large number of components whose concentration and activity need to be tightly controlled. More in vitro work in this direction, both in 3D and 2D, will be essential to explore the parameter space.

Second, it remains elusive how the actomyosin network should be anchored onto the membrane in order to achieve membrane deformations. A multitude of anchoring strategies has been developed and investigated, but only minimally in combination with a deformable membrane. Combined with our limited understanding of cortex-membrane molecular organization in vivo, this might prove one of the most important challenges. Future studies need to focus on understanding the influence of linker density and strength, as well as membrane composition and organization. In addition, the respective roles of filament-membrane linkers and membrane-bound nucleators need to be investigated.

Third, attention must be paid to the supplying of extra membrane area during constriction. Additional area can be present in membrane reservoirs, be synthesized, or be added by fusion of small vesicles. However, none of these approaches have to our knowledge been co-reconstituted with actin-driven contraction and resulting membrane deformation.

Fourth, there is to date only a minimal body of work on contractile actomyosin networks in GUVs. Confining the system in GUVs requires that all components need to be encapsulated in the right concentration and stoichiometric ratio, while preserving functionality. Although there are numerous GUV formation techniques, they have been minimally characterized for their potential to encapsulate complex mixtures of biochemically active components. More work in this direction is crucial to perform controlled reconstitution in GUVs, but also to be able to extrapolate findings from bulk and SLB experiments to vesicle systems.

Fifth, spatial and temporal control of the components and their activity are crucial. On the short term, some of these challenges may be by-passed by taking a semi-autonomous approach on synthetic cell division. For example, optogenetics, external mechanical or chemical cues, or fusion-based delivery of components with small vesicles provide handles to control the system even after encapsulation of the components inside GUVs. However, if the goal is to create a synthetic cell that divides fully autonomously, reconstitution will be more complicated and will require for example feedback loops, signalling molecules and internal clocks.

As a concluding remark, we note that the most pressing challenges to achieve in vitro actin-driven cell division require integration of modules. Only when actomyosin studies meet membrane biophysics, when myosin motor activity is combined with actin turnover, and when protein biochemistry becomes integrated in GUV formation, we can start thinking about reconstituting cell division. In the coming years, perspectives from experimental work, theoretical studies and simulations need to be combined to guide future work with the ultimate goal to develop a full understanding of actin-driven synthetic cell division.

3

OPTIMIZED CDICE FOR EFFICIENT RECONSTITUTION OF BIOLOGICAL SYSTEMS IN GIANT UNILAMELLAR VESICLES

Giant unilamellar vesicles (GUVs) are often used to mimic biological membranes in reconstitution experiments. They are also widely used in research on synthetic cells as they provide a mechanically responsive reaction compartment that allows for controlled exchange of reactants with the environment. However, while many methods exist to encapsulate functional biomolecules in GUVs, there is no one-size-fits-all solution and reliable GUV fabrication still remains a major experimental hurdle in the field. Here, we show that defect-free GUVs containing complex biochemical systems can be generated by optimizing a double-emulsion method for GUV formation called continuous droplet interface crossing encapsulation (cDICE). By tightly controlling environmental conditions and tuning the lipid-in-oil dispersion, we show that it is possible to significantly improve the reproducibility of high-quality GUV formation as well as the encapsulation efficiency. We demonstrate efficient encapsulation for a range of minimal systems including a minimal actin cytoskeleton, membrane-anchored DNA nanostructures, and a functional PURE (Protein synthesis Using Recombinant Elements) system. Our optimized cDICE method displays promising potential to become a standard method in biophysics and bottom-up synthetic biology.

This chapter is based on the publication *Optimized cDICE for Efficient Reconstitution of Biological Systems in Giant Unilamellar Vesicles* by L. van de Cauter*, F. Fanalista*, Lennard van Buren* et al., published in ACS Synthetic Biology **10**, 7 (2021) [175]. Lennard van Buren performed the tensiometry and absorbance measurements and co-wrote the article. *equal contribution

3.1. Introduction

Cellular life is enabled by countless interacting molecules and biochemical reactions with a high degree of interconnectivity and redundancy. Reconstituting cell biological processes using only their minimal functional units from the bottom-up is therefore greatly helpful to study cellular mechanisms on a molecular and mechanistic level [276–278]. The field of bottom-up synthetic biology has gained a lot of traction over the last decade, an evolution synchronised with the emergence of several different consortia worldwide to lead the journey towards functional reconstitution of all basic cellular functions, culminating in the creation of a minimal synthetic cell [2, 18–20].

In this synthetic cell community, giant unilamellar vesicles (GUVs) are widely used as cell-sized, lipid bilayer-enclosed reaction compartments that can be visualized by real-time microscopy and directly manipulated using biophysical tools [33, 279–281]. Using GUVs as a basis for a functional synthetic cell requires encapsulation of different biological modules in a precise stoichiometry, consisting of a variety of biomolecules ranging in size and charge. However, state-of-the-art GUV fabrication methods are still far from ideal in establishing complex reconstituted systems (see chapter 4). On the one hand, easy-to-implement and high-yield methods, such as natural swelling [73], electroformation [74, 282–284], and gel-assisted swelling [76, 285, 286], offer poor control over encapsulation efficiency and stoichiometry, and inconveniently contain the same solution on the in- and outside. On the other hand, emulsion-based techniques, in which GUVs are generated from water-in-oil droplets crossing an oil-water interface (using gravity, centrifugation, microfluidic devices or microfluidic jetting [77, 287–292]), offer more control over GUV content and size monodispersity, but at the cost of being less reliable and more technologically advanced and therefore less accessible.

A promising method that is increasingly being used for complex reconstitutions is continuous droplet interface crossing encapsulation (cDICE). This double-emulsion based technique relies on the continuous transfer of capillary-generated water-in-oil droplets across an oil-water interface using centrifugal force [3]. Requiring only easy-to-operate laboratory instrumentation, cDICE can in principle provide high yields while being less technologically demanding than microfluidic-based approaches and allowing for more control over size and encapsulated content than swelling methods [3, 293]. However, despite promising first outcomes, using cDICE for protein encapsulation has remained difficult, beyond a few specific cases [294–296]. At least in part, this is likely due to our lack in understanding of both the physical process of vesicle formation and of which parameters are essential to control tightly for the method to work robustly. Significant lab-to-lab variability and constant adaptations to the protocol devised by various labs [3, 293, 294, 296], have also made it hard to reproduce results across different institutions, leading to the technique being far from accessible.

Here, we aimed to gain a better understanding of the parameters influencing both vesicle formation and encapsulation efficiency in cDICE, allowing us to design an accessible, robust and reproducible workflow for different encapsulation needs. We show that control of environmental conditions is crucial for reliable formation of defect-free GUVs (i.e., the vesicular membrane is uniform at optical length-scales and does not contain visible lipid pockets) at high yields. Furthermore, we demonstrate different approaches for enhancing the encapsulation efficiency of cDICE by changing the composition of

the lipid-in-oil dispersion. We thus provide future users with a detailed protocol for GUV fabrication and a toolbox that can form a firm basis for further experiment-specific optimization. By reproducing key experiments across multiple labs in different locations and encapsulating a large variety of biological systems, from the encapsulation of purified proteins to the PURE *in vitro* transcription-translation system, membrane-anchored DNA origami, and bacteria, we show robustness and versatility of the method. Overall, we demonstrate that our improved cDICE protocol shows great promise for a wide range of complex reconstitution processes in the future, overcoming a major hurdle on the route towards functional minimal synthetic cells.

3.2. RESULTS

3.2.1. ENVIRONMENTAL CONTROL IS ESSENTIAL FOR PRODUCING DEFECT-FREE GUVS WITH EDICE

To improve the robustness of the cDICE method, we sought to systematically screen various experimental parameters that might influence GUV formation in cDICE. A typical cDICE set-up (fig. 3.1a) consists of a rotating chamber containing two concentric fluid layers, an inner, lower-density lipid-containing oil phase and an outer, aqueous layer. The aqueous solution to be encapsulated, is injected into the lipid-in-oil layer through a capillary, leading to the formation of water-in-oil droplets at the capillary orifice. As these droplets travel outward and traverse the interface of the oil with the outer aqueous phase, a bilayer is formed, yielding GUVs, collected in the outer layer of the system (fig. 3.1a). GUV formation is thus dependent on the properties of all phases and on other experimental parameters, such as rotation speed and capillary size [3]. When we sought to enhance the consistency of vesicle production in this inherently sensitive experimental system, the first striking improvement was made by using a chloroform-based lipid-in-oil dispersion [296] as oil phase and preparing it in a humidity-free environment, i.e., inside a glovebox. Without the use of a glovebox, GUVs were generated but the sample contained a lot of residual membrane material, such as free tubes and fluorescent aggregates, and the vast majority of GUVs showed visible fluorescent pockets or budding membrane structures (fig. 3.1b). In contrast, when the lipid-in-oil dispersion was prepared in a glovebox, samples were much cleaner with most GUVs having quasi-spherical shapes without visible lipid pockets or budding membrane structures (fig. 3.1c).

In line with this observation, preparation of the lipid-in-oil dispersion inside a glovebox also affected its macroscopic appearance: oil dispersions prepared in a humidity-free environment were transparent, while preparations outside a glovebox yielded visibly opaque dispersions, as quantified by turbidity measurements ($A_{350} = 0.10 \pm 0.05$ vs 0.42 ± 0.10, fig. 3.5). Furthermore, we analysed the lipid adsorption kinetics of the different oil dispersions using pendant drop measurements [297], where a drop of aqueous solution is suspended in a lipid-in-oil mixture, mimicking the process happening at the orifice of the cDICE capillary. Without humidity control, interfacial tension decreased much faster (fig. 3.6), indicating faster adsorption of lipids to the water-oil interface. In combination with the adverse effect on vesicle quality, our experiments suggest that presence of water in the lipid-in-oil dispersion interferes with vesicle formation and bilayer quality via changing the microscopic organization of the lipids and their adsorptive

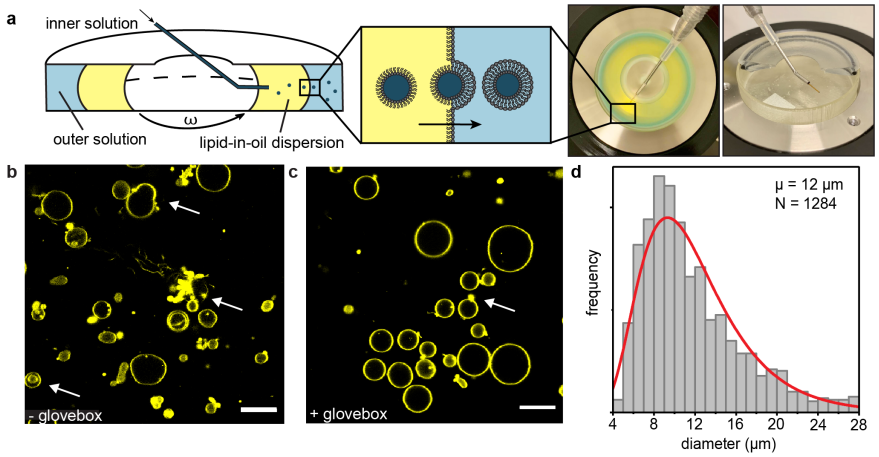

Figure 3.1: **General overview of the cDICE technique and influence of environmental conditions.** (a) Cross-sectional schematic of the cDICE method. The centre image displays the 3D printed rotation chamber, with the different fluid layers coloured differently for illustration purposes. The rightmost image displays the custom-built spinning device that accommodates the 3D printed rotation chamber. The capillary is inserted using an adjustable magnetic base to allow spatial flexibility upon insertion. During experiments, this set-up is connected to a syringe and syringe pump. (b) Representative field of view of GUVs formed using a chloroform-based lipid-in-oil dispersion prepared outside of the glovebox. ATTO 655 DOPE was used as a membrane stain and images were taken using confocal microscopy. Most GUVs contain artefacts in the lipid membrane, examples are indicated with arrows. Scale bar indicates $20\mu m$. (c) Representative field of view of GUVs formed using the final protocol including the use of a glovebox. ATTO 655 DOPE was used as a membrane stain and images were taken using confocal microscopy. Most GUVs are spherical and possess a clean membrane and only a small population of GUVs still shows artefacts, as indicated with an arrow. Scale bar indicates $20\mu m$. (d) d. Size distribution of GUVs made of DOPC lipids, obtained by the optimized protocol. The distribution is fitted to a log-normal function (red curve).

behaviour.

It is well known that humidity values change throughout the year, reaching highest values in summer. This seasonal dependency in daily relative humidity can be as large as several tens in percentage [298], equivalent to the range of 40 - 75% that we observed in the lab. Given the importance of humidity in preparation of the lipid-in-oil dispersion, we extended environmental control to regulating humidity in the room where the cDICE experiments were performed by using a dehumidifier. Indeed, dehumidification down to 30 - 40% resulted in smaller variability between lipid adsorption kinetics as measured in pendant drop experiments (fig. 3.6), indicating a more reproducible adsorption behaviour. In line with the lower variability found in lipid adsorption rates, dehumidification also proved to be essential for reliable production of clean vesicles throughout the year. Taken together, using a glovebox for preparation of the lipid-in-oil dispersion and storage of its components, and performing cDICE experiments in a continuously dehumidified room, resulted in a robust formation of clean GUVs.

In the original cDICE paper [3], as well as in other follow-up studies [178, 293, 294, 299], injection capillaries were pulled from glass tubes to final orifice diameters of a maximum of $20\mu m$. Since we found these narrow glass capillaries to be a significant

source of experimental variation and problems due to easy clogging of the orifice, we explored if using commercially available fused silica capillary tubing with larger diameters (25, 50 and 100 μm) would allow for even more consistent results, as previously used by Litschel et al. [296]. We found that using all three capillary sizes, our chloroform-based lipid-in-oil dispersion and optimized workflow led to high yields of GUVs with a mean diameter of $12\mu m$ and coefficient of variation of 47% for a capillary size of $100\mu m$ and rotation speed of 1900 rpm (fig. 3.1d). The size distributions of the GUVs did not significantly change across the different capillary sizes (fig. 3.7) and they were broader than the ones previously obtained for smaller orifice sizes [3]. However, the lack of control over GUV size is compensated by a much-improved reliability of encapsulation and GUV formation due to avoidance of clogging, in particular for $100\mu m$ fused silica capillaries. Other capillary materials were also successfully used, i.e., $100\mu m$ PEEK capillary tubing. Changes in rotation speed (1000 - 2900 rpm) neither altered the size distributions for the different orifice diameters (fig. 3.7). No precise control of rotation speed is thus needed in order to get robust GUV formation, with size distributions in an ideal range for bottom-up reconstitution of eukaryotic cells. In terms of yield, the absolute number of GUVs obtained using the optimized cDICE protocol is dependent on total encapsulation volume, flow rate, and characteristics of the used biological agents. From the average number of GUVs visible per field of view, we estimate the absolute number of GUVs to reach well over 1000 vesicles in a typical experiment ($100\mu L$ of inner aqueous solution and a flow rate of $25\mu L \text{min}^{-1}$).

3.2.2. UNILAMELLARITY OF CDICE-PRODUCED GUVS

Many reconstitution experiments require unilamellar lipid membranes, as this determines permeability and mechanical properties of the GUV and is needed for insertion of transmembrane proteins, including pore proteins, into the bilayer. Therefore, we next aimed to investigate if our GUV membranes were unilamellar by monitoring insertion of alpha-hemolysin, a protein that assembles a heptameric pore structure in the lipid membranes with a diameter of 14 Å, through which small molecules can pass and which is highly sensitive to the thickness of lipid bilayers [300, 301]. As a tracer, we encapsulated $5\mu M$ of the fluorescent dye Alexa Fluor 488 (643 Da) and we immobilized the GUVs within a polyisocyanide hydrogel [302] to aid long-term imaging [303]. After that, alpha-hemolysin was added to the chamber and fluorescent imaging was immediately started. Within minutes following alpha-hemolysin addition, all GUVs observed started to lose their fluorescent content and all had lost 50% of their content after ~ 20 minutes (fig. 3.2a, top row; fig. 3.2b, red curve). In stark contrast, when only alpha-hemolysin buffer was added to the GUVs as a control, fluorescent molecules were clearly retained within all GUVs (fig. 3.2a, bottom row; fig. 3.2b, blue curve). This indicated that loss of GUV content was due to pore formation and hence membrane unilamellarity. Furthermore, individual GUV membrane intensities normalised by the population's mean membrane intensity are consistently distributed around unity, indicating a homogenous lamellarity over the GUV population (fig. 3.2c). Taken together, our results clearly show that the cDICE method produces unilamellar GUVs.

3.2.3. Improvement of encapsulation efficiency

To allow for complex reconstitution experiments, it is essential to have control over the encapsulation of functional biomolecules in the right stoichiometric ratios. We probed the encapsulation efficiency of our improved cDICE protocol by encapsulation of the cytoskeletal protein actin, a broadly used protein in the synthetic biology field [16]. While all experiments using our optimized cDICE protocol resulted in successful encapsulation of monomeric actin in GUVs at high vesicle yields, automated analysis of actin fluorescence at the equatorial plane of the GUV from confocal fluorescence imaging surprisingly revealed a substantial fraction of GUVs with very low actin content, indicating that many of the formed vesicles were seemingly empty (23%, fig. 3.3a, fig. 3.8a). We tested if the encapsulation efficiency could be improved by using different lipid-in-oil mixtures. We reasoned that the encapsulation efficiency may depend on the lipid adsorption kinetics, as it has been reported earlier that the dispersion method of lipids had a strong effect on their adsorptive behaviour [304]. Therefore, we investigated the effect of lipid dispersion strategy on adsorption kinetics and on GUV formation and encapsulation efficiency for three lipid mixtures: lipids dispersed as aggregates in a 80:20 mixture of sil-

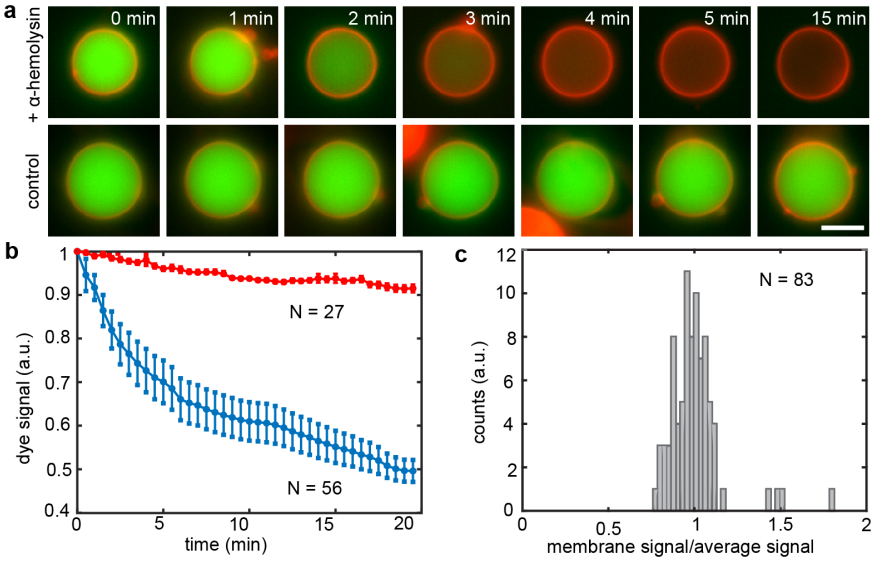

Figure 3.2: **Incorporation of alpha-hemolysin pore protein demonstrates unilamellarity of GUV membrane.** (a) Fluorescence microscopy images of single GUVs prepared using a chloroform-based lipid-in-oil dispersion showing different membrane permeability in presence (top row) or absence (bottom row) of alpha-hemolysin. When the pore protein is added to the lipid membrane (red, rhodamine-PE fluorescence signal), the encapsulated fluorescent dye (green, Alexa Fluor 488) is released in the outer environment within a few minutes. When only alpha-hemolysin buffer is added as a control instead, fluorescent molecules are retained within the GUV volume. Scale bar indicates $5\mu m$. (b) Quantitative analysis of GUV fluorescent content loss over time. In presence of alpha-hemolysin (blue curve), Alexa Fluor 488 signal intensity decreases down to 50% of the initial value within the first 20 minutes, while in absence of pores (red curve) only a minor decrease (< 10%), likely due to photobleaching, is detected. (c) c. Histogram showing GUV membrane fluorescence intensities compared to the overall GUV population.

icon and mineral oil using chloroform as mentioned above, a similar dispersion of lipid aggregates but using decane instead of chloroform, and a lipid-chloroform solution in mineral oil only. Chloroform and decane serve as good solvents for the lipids, while the lipids do not dissolve in the oil. This way, we aimed to produce different lipid-in-oil dispersions with various aggregation states, with the mineral oil dispersion having smallest aggregate size, and both chloroform- and decane-based lipid dispersions having larger aggregate sizes [304].

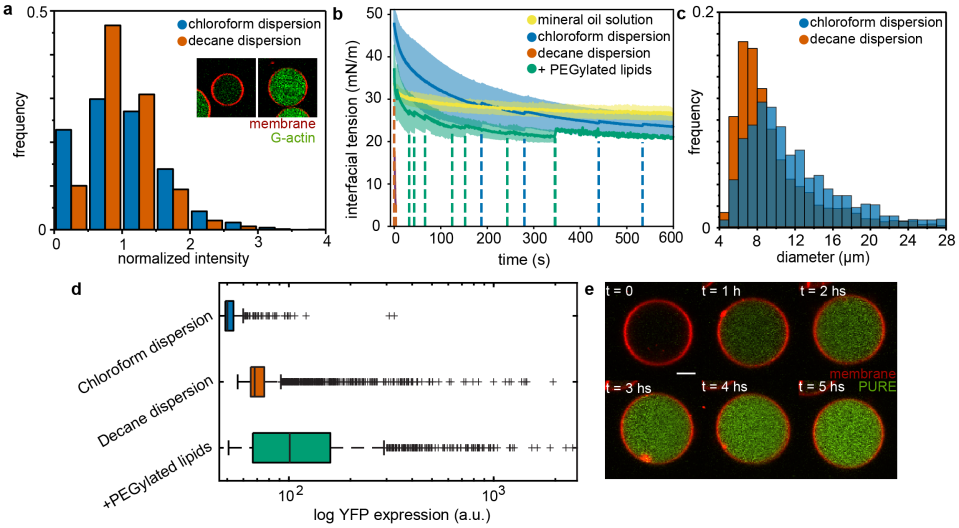

Figure 3.3: **Improved encapsulation by tuning of the lipid-in-oil dispersion.** (a) Encapsulation efficiency of G-actin using a chloroform-based lipid dispersion (blue) and decane-based lipid dispersion (orange). The first bin represents GUVs with very low fluorescence intensity, and represents 23% of the population for the chloroform-based lipid dispersion and only 10% for the decane-based lipid dispersion. (b) Interfacial tension decrease measured for a pendant droplet of G-buffer in different lipid-in-oil mixtures. Solid lines show averaged data with standard deviation for a lipid-chloroform solution in mineral oil only (yellow, n = 9), dispersed lipid aggregates using chloroform (blue, n = 13) or decane (orange, n = 7) in silicone oil:mineral oil 80:20 and a chloroform-based lipid-in-oil dispersion with 0.01 mol% of PEGylated lipids (green, n = 9). The dashed lines indicate individual events where the droplet fell off, which gave rise to apparent jumps in the averaged curves. When using the decane-based dispersion, all droplets detached within seconds. (c) Size distribution of GUVs made using a chloroform-based lipid dispersion (blue) and decane-based lipid dispersion (orange). (d) Box plots of the YFP expression after five hours of incubation in GUVs obtained using dispersed lipid aggregates using chloroform (blue), decane (orange), and a chloroform-based lipid-in-oil dispersion with 0.01 mol% of PEGylated lipids (green). The boxes represent IQR (25th–75th percentiles), the centre line indicates the median and the whiskers extend to the maximum and minimum value excluding outliers. Outliers are individually indicated using plus symbols. (e) e. Time-lapse images of YFP expression in a single GUV using a chloroform-based lipid-in-oil dispersion with 0.01 mol% of PEGylated lipids. Scale bar indicates $5\mu m$.

First, we confirmed the aggregation state of the lipids by absorbance measurements. Indeed, the mineral oil dispersion was much less turbid ($A_{350} = 0.03 \pm 0.01$) than the chloroform- or decane-based dispersion ($A_{350} = 0.10 \pm 0.05$ and $A_{350} = 0.20 \pm 0.12$ respectively, fig. 3.5), indicating that the latter two have a higher propensity to form aggregates. Pendant drop measurements showed that dispersing lipids as aggregates using chloroform resulted in fast lipid adsorption (fig. 3.7b, blue curve), indicating fast monolayer

formation. The decane-based lipid dispersion resulted in even faster adsorption, with all droplets detaching within several seconds (fig. 3.7b, orange curve). In contrast, lipids dispersed in mineral oil exhibited a slower and smaller decrease of interfacial tension (fig. 3.7b, yellow curve), meaning slow adsorption of lipids to the oil-water interface and a small coverage of the final interface. In line with the idea that faster stabilization of the oil-water interface by faster lipid adsorption leads to more robust monolayer formation, we observed no GUV formation when using lipids dispersed in mineral oil, whereas experiments using lipids dispersed as aggregates in a 80:20 mixture of silicon and mineral oil using chloroform or decane gave large GUV yields (fig. 3.8).

We then tested if the fast-adsorbing decane mixture could improve the encapsulation efficiency of cDICE. In stark contrast to the encapsulation of G-actin using chloroform as an organic solvent, using a decane-based lipid dispersion resulted in a significant decrease of the fraction of seemingly empty vesicles (10% versus 23%, fig. 3.3a, fig. 3.8). Although large differences in both adsorption kinetics and encapsulation efficiency can be observed between decane- and chloroform-based lipid-in-oil dispersions, they yield GUVs similar in size distribution, size polydispersity, and visual membrane cleanliness (fig. 3.3c, fig. 3.8). We also note that the lipid adsorption behaviour of the chloroform-based dispersion is highly variable, much more so than for decane-based lipid dispersions or lipids dispersed in mineral oil only (fig. 3.3b). Since the lipid dispersions are metastable mixtures and chloroform readily evaporates under ambient conditions, changes to their composition happen on timescales similar to the experimental runtime. Indeed, time-dependent absorbance measurements indicated a rapid change in oil turbidity, indicative of an increase in aggregate size, on the time scale of minutes, confirming the intrinsic instability of chloroform-based lipid dispersions (fig. 3.9).

Efficient encapsulation is particularly important for reconstitution of cell-free gene expression reactions (*in vitro* transcription-translation systems) within GUVs, as the relative stoichiometry of their components has to be rather closely retained for optimal functioning [305]. Functionality might further be affected by possible hydrophobic interactions of the protein components with organic solvents during encapsulation, although some groups already successfully encapsulated *in vitro* transcription-translation systems with emulsion-droplet transfer-[306–308] and microfluidic-based methods [309]. To our knowledge, functional encapsulation of a cell-free gene expression (e.g., the Protein synthesis Using Recombinant Elements (PURE) system [310]) has never been demonstrated for GUVs produced with the cDICE method. We therefore explored if we could encapsulate the PURE system using our improved cDICE protocol. To this end, GUVs encapsulating PURE*frex*2.0, a commercially available PURE system, along with a linear DNA construct coding for yellow fluorescent protein (YFP), were produced using both a chloroform-based lipid dispersion and a decane-based lipid dispersion. Gene expression in GUVs incubated at 37°C was monitored by imaging YFP production within the GUV lumen over time. We observed that the different dispersion strategies used for GUV fabrication influenced the level of gene expression: the distribution of luminal fluorescence intensity after five hours of gene expression employing decane-based lipid aggregates showed improved gene expression levels compared to the encapsulation using chloroform-based lipid aggregates, which barely yielded any YFP expressing GUVs at all. Nevertheless, both gene expression levels and numbers of YFP expressing GUVs

were still very low (fig. 3.3d and fig. 3.10).

In addition to the lipid dispersion strategy, the lipid composition of the bilayer membrane can also alter adsorption kinetics and hence improve encapsulation efficiency. In particular, PEGylated lipids, lipids with a flexible poly(ethylene) glycol (PEG) linker, are often proposed to boost robust vesicle formation for various protocols [285, 311–313]. We therefore investigated if doping the vesicular membrane with 0.01 mol% 18:0 PEG2000 PE could improve encapsulation of the PURE system when using cDICE. The presence of PEGylated lipids slightly increased the adsorption rate of lipids to the oil-water interface (fig. 3.3b, green curve). Interestingly, doping the membrane with 0.01 mol% PEGylated lipids greatly enhanced expression of the encapsulated PURE system and resulted in the highest gene expression levels and a large population of GUVs expressing YFP (fig. 3.3d, e and fig. 3.10). These results show that optimization of encapsulation efficiency both via lipid dispersion and lipid composition is crucial to allow for functional reconstitution of complex reactions such as the PURE system in GUVs made using cDICE.

3.2.4. PROOF-OF-CONCEPT EXPERIMENTS ILLUSTRATE VERSATILITY OF THE OPTIMIZED WORKFLOW

Finally, to investigate the broad applicability of our improved cDICE method, we aimed to reconstitute a wide range of minimal systems inside cDICE-made GUVs (fig. 3.4). First, we encapsulated a minimal, branched actin network. In eukaryotic cells, the actin cortex is the protein machinery responsible for cell division [107, 143]. Reconstitution of a functional actin cortex anchored to the inner leaflet of the GUV membrane therefore offers an attractive route to induce GUV constriction, and possibly membrane fission, in synthetic cells. Our minimal actin cortex consisted of actin together with the verpolin homology, cofilin, and acidic domain of the Wiscot-Aldrin Syndrome protein (VCA), the Arp2/3 complex, and profilin. The Arp 2/3 complex is an actin nucleator responsible for promoting formation of a branched actin network at the cell membrane [314, 315]. VCA was His-tagged to be able to bind to DGS-NTA(Ni) lipids in the membrane [153, 316]. Together with Arp 2/3, VCA promoted localized nucleation of a branched cortex at the membrane, while profilin was used to prevent actin polymerization in the lumen [317, 318]. Actin displayed a clear localization at the GUV membrane (fig. 3.4a *i*, fig. 3.11a), similarly to what was obtained using other GUV fabrication methods [108, 261]. In absence of membrane anchors and nucleators, actin was uniformly distributed within the GUV volume (fig. 3.4a *i*, fig. 3.11a).

As a synthetic mimic of the cellular actin cortex, we encapsulated DNA origami nanostructures [319] that are capable of lateral cross-linking at the vesicular membrane. These four-armed DNA assemblies diffuse freely in the lumen of the GUV but were efficiently recruited to the membrane upon co-encapsulation of a cholesterol-oligonucleotide membrane anchor that binds single-stranded DNA sites on the origami (fig. 3.4a *ii*, fig. 3.11b). Here, the monomeric DNA tiles freely diffuse in the membrane plane and form a pre-cortex. We also successfully encapsulated small unilamellar vesicles (SUVs, ~ 100 nm diameter), mimicking multicompartmental cellular systems (fig. 3.4a, *iii*, fig. 3.11c). In the future, these compartments could be designed to trigger or sustain intravesicular reactions, allowing control over biochemical reactions inside the GUV lumen [320–322].

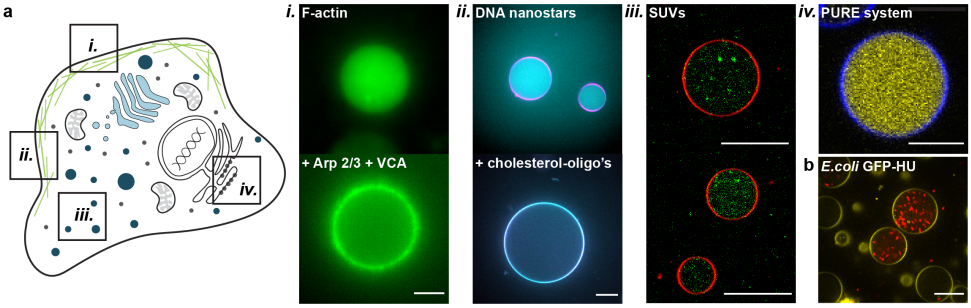

Figure 3.4: **Proof-of-concept experiments showing versatility of cDICE and its applicability for the synthetic cell community.** (a) Overview - GUVs as artificial membrane systems to mimic cellular membranes and membrane interactions. (*i*) Reconstitution of a minimal actin cortex inside a GUV, nucleated at the vesicular membrane by the Arp2/3 complex, the C-terminal VCA domain of WASp, and profilin. Scale bar indicates $5\mu m$. (*ii*). Encapsulation of DNA origami nanostructures, freely diffusing inside the GUV lumen and capable of membrane localization upon addition of $2\mu M$ of cholesterol-oligonucleotides. Scale bar indicates $15\mu m$. (*iii* Encapsulation of SUVs inside GUVs to form a multicompartmentalized system. Scale bars indicate $20\mu m$. (*iv*) Encapsulation of PURE*frex*2.0 and DNA encoding for YFP. Scale bar indicates $10\mu m$. (b) Encapsulation of GFP-HU expressing E. coli bacteria. A large number of bacteria could be observed inside the GUV lumen, clearly viable as evident from their motility. Scale bar indicates $20\mu m$.

Furthermore, as mentioned above, our cDICE method can be used to encapsulate a functional in vitro transcription-translation system (the PURE system), provided PEGylated lipids are included in the lipid mixture (fig. 3.4a *iv*). The broad applicability of cDICE is further demonstrated by the successful encapsulation of objects that are large compared to the GUV size, i.e. entire *E. coli* bacteria (fig. 3.4b, fig. 3.11d). Cylindrical in shape, with a length of approximately $3\mu m$ and a diameter of $1\mu m$ [323], these are several orders of magnitude larger than even many DNA origami structures. The bacteria were clearly mobile inside the GUVs (movie online), showing that the cDICE process does not significantly affect their viability. Encapsulating live bacteria inside synthetic cells could be a promising route to combine 'the best of both worlds', e.g., photosynthetic cyanobacteria could be repurposed as 'chloroplasts' for the synthetic cell, similar to a recent study which included chloroplasts isolated from plant cells [324].

Overall, the improved cDICE method is shown to be capable of encapsulating a variety of functional minimal systems related to cell mechanics, cell metabolism and gene expression, all required for the generation of a synthetic cell.

3.3. Discussion

A good understanding of the parameters influencing the GUV formation process in cDICE is crucial, especially for design of reconstitution experiments beyond first proof-of-concept experiments. Here, we showed that tight control over the lipid-in-oil mixture is key to successful and reproducible GUV formation. We found that membrane quality, which affects mechanical measurements and quantitative fluorescence analysis, was strongly improved by environmental control over preparation and handling of the lipid-in-oil dispersion, notably handling the lipid dispersion in a humidity-free environment (i.e., a glovebox) and decreasing humidity to 30% during vesicle formation. We hypothe-

size that air humidity affects bilayer formation by changing the microscopic aggregation state of the lipid-in-oil mixture, and thereby the lipid adsorption behaviour. Partial hydration of lipids could possibly lead to the formation of larger lipid aggregates, such as reverse micelles or lamellar structures, hindering proper mono- and bilayer formation. Yet, fully understanding the microscopic mechanics of this thermodynamically unstable, multicomponent system remains difficult [325, 326]. Importantly, we also demonstrated the unilamellarity of the formed GUVs by correct insertion of alpha-hemolysin to allow pore formation. Although the appearance of the GUV membranes was visibly improved upon environmental control, a common concern remains the possible presence of residual oil traces in the membrane. However, it was shown in previous work that cDICE-formed GUVs are unlikely to have large traces of oil persisting in the membrane [3, 293]. It is unknown whether transmembrane proteins are affected by the presence of residual oil in vesicular membranes but interestingly, recent work indicates that it does not significantly alter the static, mechanical membrane properties of the GUVs compared to electroformed GUVs [327–329]. Altogether, this makes vesicle formation with the improved protocol compatible with reconstitution experiments requiring clean unilamellar membranes, such as studies involving membrane mechanics or membrane permeability.

Furthermore, we showed that the dispersion state of the lipids is crucial for efficient GUV formation using cDICE. As other existing protocols show, many different lipid-in-oil mixtures can be used for GUV formation [3, 293, 294, 296, 304]. In particular, Claudet et al. [304] found lipids dispersed as aggregates in an oil phase to promote more efficient bilayer formation. We provide experimental evidence that indeed the lipid bulk aggregated state strongly influences adsorption kinetics and thereby vesicle formation, supporting and explaining the observations of Claudet et al. [304]. Our tensiometry findings also indicate that not solely adsorption speed is of importance for proper bilayer formation, but the structure and content of the lipid aggregates is just as crucial for mono- and bilayer formation. Hence, having lipids dispersed as aggregates alongside humidity control is essential for clean GUV formation. This indicates a non-trivial relation between lipid properties, lipid dispersion state, adsorption kinetics and the final membrane quality. Adsorption speed as measured by pendant drop experiments can therefore not be used as a stand-alone quantity to assess whether a given lipid-in-oil mixture will support GUV formation in cDICE. Future research into the molecular mechanisms of the lipid-in-oil dispersions could involve a systematic characterization of the lipid aggregates species via, for example, dynamic light scattering (DLS) or electron microscopy (EM).

By tuning the lipid-in-oil dispersion with different organic solvents or different types of lipids, the encapsulation efficiency of cDICE could be improved. Faster lipid adsorption when using a decane-based dispersion as compared to using a chloroform-based dispersion, led to a better G-actin encapsulation. For functional encapsulation of the PURE system on the other hand, the presence of PEGylated lipids proved to be crucial. This cell-free expression system has a complex molecular composition, and all the individual components need to be present in order to yield a functional readout. While addition of PEGylated lipids has proven to be very effective for encapsulation of the PURE system with cDICE, it should be noted that PEGylated lipids can have adverse effects on

protein functionality and membrane physicochemical behaviour, as the polymer chains introduce crowding and steric repulsion of components from the membrane as well as affect the membrane thickness [330]. In this case, our experiment suggest that depending on the encapsulated species, PEGylated lipids can be avoided and high encapsulation efficiencies can be reached instead by changing the solvent.

Our cDICE protocol robustly yields GUVs with an average diameter of $12\mu m$ and coefficient of variation of 47%. This size distribution was robust to changes in rotation speed and capillary diameters from 25 - 100 μm. This consistency over differences in these two central parameters implies that the workflow we have adopted lies in the jetting regime [331]. A jet at the capillary orifice is broken up into a polydisperse droplet population due to the Rayleigh instability in combination with the centrifugal force applied in cDICE [331]. A high degree of polydispersity can be advantageous for bulk assays to screen multiple conditions in one single experiment [109, 110], but undesirable for other applications. As Abkarian et al. [3] showed, decreasing the capillary diameter to values around $10\mu m$ or using an additional inner fluid layer to decrease shear forces are viable strategies to achieve more precise size control. However, using these small orifice sizes poses other problems, including fast clogging of small diameter capillaries, rendering the method much less reliable. Here, we demonstrate that to reproducibly encapsulate viscous solutions containing a high concentration of polymerizing protein, as when encapsulating concentrated actin solutions, it is advantageous to use a larger capillary.

Taken together, we have shown that humidity control is essential for reliable production of clean GUVs with cDICE. Furthermore, we found that the encapsulation of different biological systems can be modulated by tuning the lipid-in-oil dispersion and the membrane composition. As a result, the optimized workflow laid out in this research enables the generation of bespoke GUVs at good yields and with high encapsulation efficiency. We showed that encapsulation was compatible with molecular membrane anchors such as the cholesterol-oligonucleotide anchors used with DNA origami and a minimal actin cortex, while maintaining functionality even for complex systems like the PURE system. This renders a method that is robust and achieves reproducible results across many months and multiple labs. By conducting several proof-of-concept experiments, we were able to demonstrate the versatility of the cDICE method: from reconstitution of an actin cortex, to encapsulation of a cell-free expression system, membrane-anchored DNA nanostructures, and entire *E. coli* bacteria, these experiments open up a portal to generating GUVs with contents of ever-greater complexity. In the future, additional modifications by changing experimental parameters such as capillary size, rotation speed, chamber design, etc. can be made to further extend the possibilities of cDICE and perform experiment-specific optimization. This way, cDICE displays promising potential to become a standard method for the synthetic biology, biochemistry and biophysics communities in the future.

3.4. MATERIALS AND METHODS

3.4.1. DESIGN AND FABRICATION OF THE SPINNING DEVICE/ROTATIONAL CHAMBERS

The cDICE device was designed and developed in-house at AMOLF. A 15-Watt Maxon EC32 motor (5 wire version, part number 353399) served as the rotating component of the apparatus, providing a wide range of rotation speeds (from 200 rpm up to 6000 rpm) and allowing precise speed ramps for controlled speeding up and slowing down of rotation. This is especially important to avoid mixing of the solutions after experiments, which would lead to lipid debris in the outer aqueous solution, and to avoid disruption of the formed GUVs. Translucent, cylindrical chambers were designed and printed in-house (Stratasys Objet260 Connex3; Veroclear^{TM} printing material). The chambers measure 38 mm in diameter, have an inner height of 7.4 mm, and include a circular opening of 15 mm in diameter in the top to allow facile access to the solutions with the capillary. The respective designs for rotation chambers and cDICE device are available on GitHub (https://github.com/GanzingerLab). The other labs at TU Delft used similar devices.

3.4.2. GENERAL cDICE EXPERIMENTAL WORKFLOW

Synthetic fused silica capillary tubing (TSP 100/050/025 375, Molex) was employed due to its highly smooth inner surface, allowing a controlled flow of inner aqueous solutions. It was cut to a length of several centimetres using the supplied cutting stone and attached to a short piece of flexible microbore tubing (Microbore Tubing, 0.020″ x 0.060″ Cole-Parmer GmbH) using two-component epoxy glue (Bison) or instant glue (Pattex). Using a hollow piece of metal, the capillary tubing was then bent so it could be inserted horizontally into the rotational chamber. To inject the solutions, this set-up was connected to a 250μL glass syringe (SGE Gas Tight Syringe, luer lock, Sigma-Aldrich) using a shortened needle as connector (Hamilton Needle, Metal hub, needle size 22 ga. blunt tip, Sigma-Aldrich). PEEK capillary tubing (PEEK tubing, 1/32″ OD x 0.10 mm ID, BGB Analytik) was used in experiments when explicitly specified. The encapsulation solutions contained 18.5% v/v OptiPrep^{TM} (density gradient medium with a density of 1.320 gmL^{-1}) to increase the density. Unless specified otherwise, the outer aqueous phase was a solution of glucose in MilliQ water (concentration adjusted to reach a 10 – 20 mOsm higher osmolarity compared to the inner aqueous solution). In a typical experiment, the encapsulation solution was loaded into the syringe set-up, rotation was started, 700μL of outer aqueous solutions was inserted into the rotating chamber, followed by 5.5 mL of the lipid-in-oil dispersion. The capillary was then inserted horizontally in the oil layer, until it was visibly embedded.

The solution was injected using a syringe pump (KDS 100 CE, KD Scientific) at a rate of 25$\mu Lmin-^{-1}$, unless specified otherwise. The system was spun for a predetermined time depending on the encapsulation volume. Rotation speed ranged from 1000 rpm to 2700 rpm and the capillary diameter from 25 μm to 100 μm depending on the experiment type, with 1900 rpm and 100 μm being considered the default values. After every experiment, the chamber was tilted and excess oil was removed. The GUVs were then allowed to sink to the bottom of the rotation chamber for 10 minutes, after which they were harvested using a cut pipette tip and transferred to an observation chamber. Glass

coverslips were passivated using $1 mg mL^{-1}$ beta-casein in MilliQ water. Room humidity was kept around 30 - 40% using a dehumidifier (TTK 71 E Dehumidifier, Trotec). The other labs used a similar workflow, based on this main protocol.

3.4.3. Preparation of lipid-in-oil dispersion

1,2-distearoyl-sn-glycero-3-phosphoethanolamine-N-[methoxy(polyethylene glycol) -2000] (18:0 PEG2000 PE), 1,2-dioleoyl-sn-glycero-3-phosphoethanolamine-N-(lissamine rhodamine B sulfonyl (18:1 Liss Rhod PE), 18:1 1,2-dioleoyl-sn-glycero-3-phophocholine (DOPC), 1,2-dioleoyl-sn-glycero-3-[(N-(5-amino-1-carboxypentyl)iminodiacetic acid) succinyl] (nickel salt) (DGS-NTA(Ni)), and 1,2-dioleoyl-sn-glycer-3-phosphoethanolamine-N-(lissamine rhodamine B sulfonyl) (rhodamine-PE) were purchased from Avanti Polar Lipids. ATTO 488 and ATTO 655 labelled 1,2-dioleoyl-sn-glycero-3-phosphoethanolamine (DOPE) were obtained from ATTO-TEC. Stock solutions in chloroform were stored at - 20 °C. The lipids were mixed in the desired molar ratio in a 20 mL glass screw neck vial (Fisherbrand™ EPA Screw Neck Vial, Fisher Scientific and Fisherbran™ 24mm PP Screw Seal, Closed Top, 24-400 Thread, Assembled Septum, Fisher Scientific) to obtain a final concentration of $0.2 mg mL^{-1}$. After desiccation using a gentle nitrogen flow, the vial was brought inside a glovebox, where the lipid film was resuspended in $415 \mu L$ of chloroform (Uvasol®, Sigma-Aldrich) or n-decane (99+%, pure, Acros Organics). A mixture of 5.2 mL silicon oil (viscosity 5 cst (25 °C), Sigma-Aldrich) and 1.3 mL mineral oil (BioReagent, Sigma-Aldrich) was then added dropwise to the lipids while vortexing. For the lipid dispersion in mineral oil, 6.5 mL of mineral oil (BioReagent, Sigma-Aldrich) was used instead. After tightly closing the vial and securing the seal with Parafilm®, the lipid-in-oil dispersion was vortexed an additional 2.5 min and sonicated in a bath sonicator for 15 min while keeping the bath temperature below 40 °C. The mixtures were used the same day in experiments.

3.4.4. UV-VIS absorbance measurements

Turbidity measurements were performed by UV-VIS absorbance using a Denovix DS-11 spectrophotometer. Lipid-in-oil dispersions were prepared as described above and used directly for absorbance measurements. For each measurement, a cuvette (UV cuvette ultra-micro, BRAND®) was filled with $100 \mu L$ of lipid-in-oil dispersion and the absorbance at 350 nm was measured thrice. Prior to each measurement, a blank was taken using the corresponding oil or oil mix.

3.4.5. Pendant drop measurements

Pendant drop measurements were performed using a DSA 30S drop shape analyser (Kruss, Germany) and analysed with the Kruss Advanced software. For each measurement, a lipid-in-oil dispersion containing 100% DOPC was prepared in an identical manner as for cDICE experiments. Directly after vortexing, the mixture was divided over three glass 1.0 mm cuvettes (Hellma Analytics). In each cuvette, a $30 \mu L$ droplet containing G-buffer (5 mM tris(hydroxymethyl)aminomethane hydrochloride (Tris-HCl) pH 7.8 and 0.1 mM calcium chloride ($CaCl_2$)) and 18.5% v/v OptiPrep™ was formed with a rate of $5 \mu L s^{-1}$ using an automated dosing system from a hanging glass syringe with needle diameter of 1.060 mm (Hamilton). Immediately when the droplet reached its final vol-

ume, 100 frames of the droplets shape were first acquired at a frame rate of 5 frames per second after which another 500 frames were taken with 1 frame per second. The droplet contour was automatically detected and fitted with the Young-Laplace equation to yield the interfacial tension. For measurements in dehumidified conditions, a dehumidifier was switched on at least 1 hour prior to the measurement. The lipid-in-oil dispersion was continuously mixed during each measurement using a magnetic stirrer. In several experiments, interfacial tension decreased very rapidly causing the droplet to detach before the end of the measurement.

3.4.6. ALPHA-HEMOLYSIN

DOPC (97.4 mol%), DGS-NTA(Ni) (2.5 mol%), and rhodamine-PE lipids (0.1 mol%) were used for preparation of the lipid-in-oil dispersion as described earlier. GUVs encapsulating F-buffer (20 mM Tris-HCl pH 7.4, 50 mM potassium chloride (KCl), 2 mM magnesium chloride (MgCl2), 0.5 mM adenosine triphosphate (ATP) and 1mM dithiothreitol (DTT)), 18.5% v/v OptiPrep^{TM}, and 5μM Alexa Fluor 488 (Thermo Fischer) were produced in a 200 mM glucose solution. After production, 50 µl of GUV solution was collected from the bottom of the rotating chamber and deposited on a custom-built observation chamber. Separately, a buffered solution (80 mM Tris pH 7.4 and 240 mM glucose) was mixed with a $4 mg mL^{-1}$ 4 kDa polyisocyanide hydrogel solution [302] in a 1:1 volume ratio, and 50μL of the resulting solution was quickly added to the GUVs. The hydrogel was used to immobilize the GUVs, facilitating extended time-lapse imaging. After a few minutes, 2μL of 12μM alpha-hemolysin solution (100 mM Tris-HCl pH 7.5, 1 M sodium chloride (NaCl), 7.5 mM desthiobiotin (DTB)) was added to the observation chamber. Fluorescence intensity was analysed manually using ImageJ and results plotted with MATLAB. Alpha-hemolysin was purified in-house according to Stranges et al. [332].

3.4.7. G-ACTIN ENCAPSULATION

DOPC and ATTO 655 DOPE were mixed in a 99.9:0.1 molar ratio to prepare the lipid-in-oil dispersion. 100 µL of actin (4.4μM, 9% labelled with Alexa Fluor 488) in G-buffer (5 mM Tris-HCl pH 7.8, 0.1 mM $CaCl_2$, 0.02 mM ATP and 4 mM DTT) and 18.5% v/v OptiPrep^{TM} was encapsulated in every experiment, only varying rotation speed and capillary size. For a capillary size of 25μm, the flow rate was lowered to 2.5$\mu L \text{min}^{-1}$ to reduce the pressure in the capillary set-up. The encapsulated volume was reduced to 50μL in these experiments. GUVs were produced in an outer aqueous solution containing approximately 85 mM glucose in MilliQ water. Actin was purchased from Hypermol and Alexa Fluor 488-labelled actin was obtained from Invitrogen. All proteins were handled according to instructions provided by the manufacturer. GUVs were imaged in the outer aqueous solution using confocal microscopy, 50μL of GUV solution was deposited on a custom-made glass coverslip and covered. Microscopy was performed using a Nikon A1R-MP confocal microscope, using a Plan APO IR 60x water immersion objective. The 561 nm (laser power 1.0) and 488 nm (laser power 1.0) laser lines were used in combination with the appropriate emission filters to image the ATTO 655-labelled DOPE membrane and Alexa Fluor 488-labelled G-actin, respectively.

3.4.8. Data analysis of GUV images

GUV size and inner intensity (fig. 3.1d, fig. 3.3a, c, and fig. 3.7) were obtained from Z-stack images that were processed using custom-written Python software. The software performs feature tracking in each frame in three consecutive steps. First, the Canny edge detection algorithm [333] is applied, then filling of the detected edges is achieved by applying the binary hole filling function from the ndimage module of the SciPy package [334], and lastly these features in each frame are located using the measure module of the scikit-image package [335] for Python. The located features are linked together in a final step to group points belonging to the same GUV along the frame-axis. The radius of the GUVs was determined from the frame where the detected feature was largest and the inner intensity was also obtained from that respective frame and feature. User-based filtering was applied afterwards to discard multilamellar structures, aggregates or similar. The software is available on GitHub (https://github.com/GanzingerLab). The intensity was normalized to the mean of the distribution in fig. 3.3a.

3.4.9. PURE system encapsulation

The codon-optimized construct encoding for *meYFPco-LL-spinach* (enhanced yellow fluorescent protein) described in Van Nies et al. [336] was used. The sequence is codon-optimized for expression in the PURE system, and the template includes the T7 promoter and terminator. A linear DNA template was employed to observe fluorescence readout of the level of synthesized protein. The linear DNA construct was obtained by polymerase chain reaction (forward primer: GCGAAATTAATACGACTCACTATAGGGAGACC, reverse primer: AAAAAACCCCTCAAGACCCGTTTAGAGG). Amplification products were checked on a 1% agarose gel and were purified using the Wizard PCR clean-up kit (Promega). DNA concentration and purity were measured using a ND-1000 UV-Vis Spectrophotometer (Nanodrop Technologies). The full sequence of the *meYFPco-LL-spinach* linear construct can be found in [175].

DOPC and rhodamine-PE were used in a 99.9:0.1 molar ratio for the lipid-in-oil dispersion, 0.01 mol% of 18:0 PEG2000 PE was used when explicitly mentioned. PURE*frex*2.0 (GeneFrontier Corporation, Japan) was utilized following storage and handling instructions provided by the supplier. Linear DNA template was added at a concentration of 5 nM. Reactions of $40\mu L$ were assembled in test tubes and supplemented with 5% v/v OptiPrep^{TM} (higher ratios negatively interfered with the PURE reaction) and kept on ice. GUVs were produced in an outer aqueous solution composed of 220 mM glucose in MilliQ water. The flow rate was kept at $2.5\mu L\text{min}^{-1}$ for 8 minutes in total, given the limited availability of inner aqueous solution. After production, $25\mu L$ of GUV solution was transferred to the observation chamber, together with $25\mu L$ of additional outer aqueous solution composed of 35 mM glucose and 50% v/v PURE buffer. YFP expression was monitored at 37°C by confocal imaging using a Nikon A1R Laser scanning confocal microscope equipped with an SR Apo TIRF 100x oil-immersion objective. The 561 nm (laser power 5.0) and 488 nm (laser power 20.0) laser lines were used in combination with the appropriate emission filters to image the rhodamine-PE membrane and YFP, respectively. The software NIS (Nikon) was used for image acquisition and the settings were maintained for all experiments. Samples were mounted on a temperature-controlled stage maintained at 37°C during imaging up to five hours.

Image analysis was carried out in MATLAB version R2020b using the script published by Blanken et al. [337]. Briefly, the script reads the split-channel tiff files, identifies the GUVs, indexes them, and then stores the indexed variables in the data file. The script uses a sharpening filter on the rhodamine-PE image, the GUV lumen is determined by a flood filling step followed by a binarization phase with a cut-off of 200. An erosion step was conducted to filter segments relative to lipid aggregates and other sources of noise. Any segments with a circularity of less than 0.5 or greater than 2 have been excluded. For each GUV, average rhodamine-PE intensity, average YFP intensity and YFP intensity variance were determined. The box plots of the YFP intensity in the lumen were also generated in MATLAB version R2020b.

3.4.10. ACTIN CORTEX

GUVs were prepared using a mixture of DOPC and DGS-NTA(Ni) lipids in a 50:1 molar ratio. Actin (4.4μM, 9% labelled with Alexa Fluor 647), profilin (3.3μM), Arp2/3 (100 nM), and VCA (0.6μM) were added to a solution containing F-buffer (20 mM Tris-HCl pH 7.4, 50 mM KCl, 2 mM $MgCl_2$, 0.5 mM ATP and 1 mM DTT) and 18.5% v/v OptiPrep^{TM}. To minimize photobleaching, an oxygen-scavenger system [338] (1 mM protocatechuic acid (PCA) and 50 nM protocatechuate-3,4-dioxygenase (PCD)) was also added to the solution. GUVs were produced in an outer aqueous solution containing 200 mM glucose in MilliQ water. After production, 25μL of GUV solution was collected from the bottom of the rotating chamber and deposited on a custom-built observation chamber, to which an additional 25μL of a buffered solution (40 mM Tris pH 7.4 and 125 mM glucose) was added. Unless specified otherwise, all chemicals were purchased from Sigma-Aldrich. All proteins, except VCA, which was purified in-house, were purchased from Hypermol and dissolved according to instructions provided by the manufacturer. G-actin was dialyzed in G-buffer (5 mM Tris-HCl pH 7.8 and 0.1 mM $CaCl_2$) before storage at - 80 °C.

3.4.11. DNA ORIGAMI NANOSTRUCTURES ENCAPSULATION

The DNA origami design was adapted from Jeon et al. [319] by removing the 3′sequence 'sticky ends') mediating multimerization, thus keeping them monomeric. An additional 12 nt sequence was added at the 5′end to allow binding to the membrane via a cholesterol-oligonucleotide anchor. Nanostructures were folded by thermal annealing (from 95 °C to 23 °C, - 0.5 °C min^{-1}) and used at 1μM in buffered solution (50 mM Tris pH 7.0, 2 mM $MgCl_2$ and 200 mM sucrose). Right before encapsulation, 2μM of cholesterol-oligonucleotides were added to this buffer. As an outer aqueous phase, 50 mM Tris pH 7.0, 2 mM $MgCl_2$ and 200 mM glucose was used. Experiments were performed using PEEK capillary tubing.

3.4.12. SUV ENCAPSULATION

SUVs were prepared using DOPC and ATTO 488 DOPE in a 99:1 molar ratio. Under gentle nitrogen flow, chloroform was evaporated to obtain a homogenous lipid film. The lipid film was then desiccated for a minimum of three hours to remove any remaining solvent traces, after which it was rehydrated in phosphate-buffered saline buffer (PBS buffer) at 4$mgmL^{-1}$ by vortexing. Afterwards the solution was sonicated in aliquots of 20 µL for 2x 30 min. It was then diluted to 0.5$mgmL^{-1}$ for further use. DOPC and ATTO 655 DOPE

were used in a 99.9:1 molar ratio for the lipid-in-oil dispersion. For encapsulation, the SUVs were diluted 10x in PBS buffer and 18.5% v/v OptiPrep^{TM} was added. The outer aqueous phase consisted of 313 mM glucose in MilliQ water.

3.4.13. Bacteria encapsulation

We thank Paul Kouwer (Radboud University) for the kind gift of the polyisocyanide gel, and we thank Josef Melcr and Siewert-Jan Marrink for useful discussions. We acknowledge the financial support by the 'BaSyC - Building a Synthetic Cell' Gravitation grant (024.003.019) of the Netherlands Ministry of Education, Culture and Science (OCW) and the Netherlands Organization for Scientific Research (G.H.K., C. Dekker, and C. Danelon) and NWO-WISE funding (K.A.G.).

3.5. SUPPLEMENTARY FIGURES

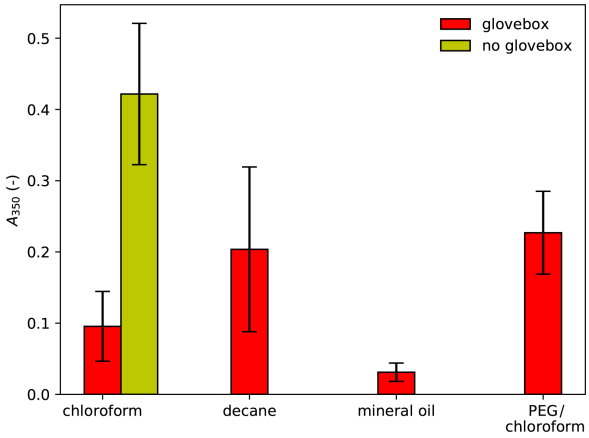

Figure 3.5: **UV-VIS absorbance of different lipid-in-oil mixtures as an indicator of the lipid aggregate size.** Absorbance at 350 nm of lipid-in-oil dispersions measured right after preparation. The different lipid-in-oil mixtures consist of: dispersed lipid aggregates using chloroform or decane in silicone oil:mineral oil 80:20, a lipid-chloroform solution in mineral oil only, and a chloroform-based lipid-in-oil dispersion with 0.01 mol% of PEGylated lipids. Red bars indicate dispersions that were prepared in the glovebox. The green bar shows the turbidity of the chloroform-based dispersion prepared outside of the glovebox. Data represents three measurements on at least two individual preparations with standard deviation.

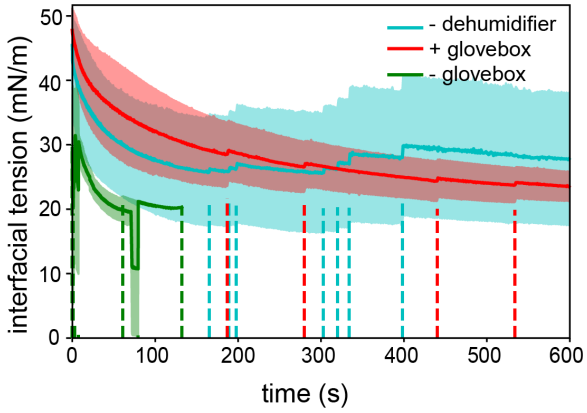

Figure 3.6: **Influence of environmental conditions on lipid adsorption kinetics.** Interfacial tension decrease measured for a pendant droplet of G-buffer in different lipid-in-oil mixtures. Solid lines show averaged data with standard deviation for a chloroform-based lipid-in-oil dispersion prepared inside a glovebox with dehumidifier in the experiment room (red, n = 13), outside a glovebox with dehumidifier in the experiment room (green, n = 9), and inside a glovebox without dehumidifier in the experiment room (blue, n = 11). The dashed lines indicate individual events where the droplet fell off, which gave rise to apparent jumps in the averaged curves.

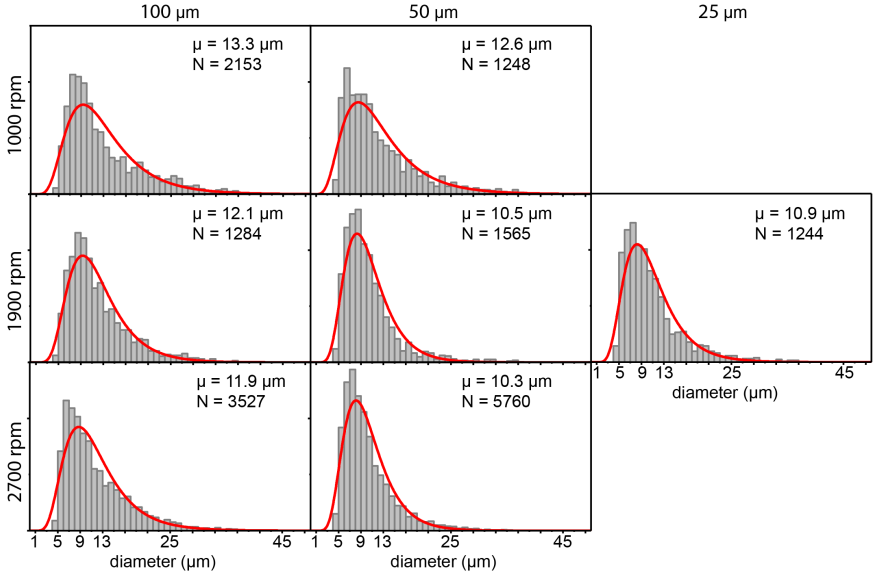

Figure 3.7: **Size distributions for different capillary sizes and rotation speeds.** Size distribution of GUVs made of DOPC lipids, using capillary sizes $25\mu m$, $50\mu m$, and $100mum$, and rotation speeds 1000 rpm, 1900 rpm, and 2700 rpm. The individual graphs represent pooled data for three experiments. The distributions are fitted to a log-normal function (red curves).

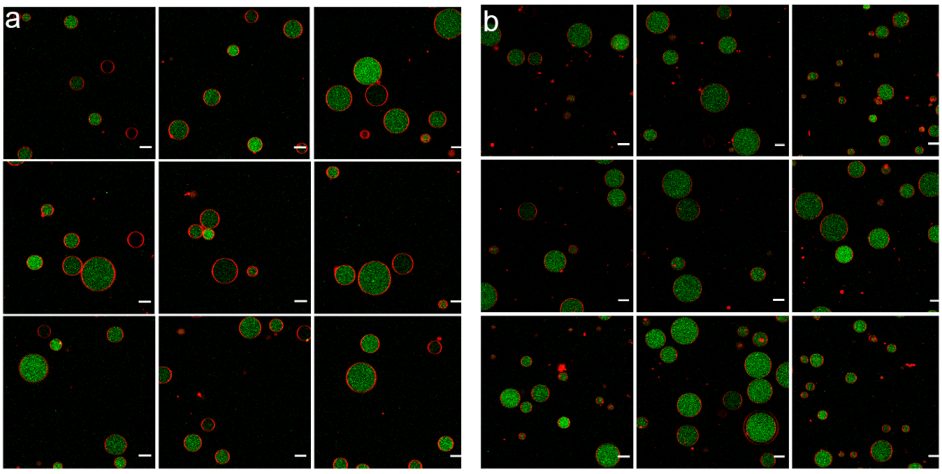

Figure 3.8: **Representative fields of view of GUVs encapsulating G-actin.** Membranes are shown in red, actin in green. Vesicles were formed with (a) a chloroform-based lipid in oil dispersion or (b) a decane-based lipid-in-oil dispersion. Scale bars indicate $10\mu m$. Images were acquired with identical imaging settings.

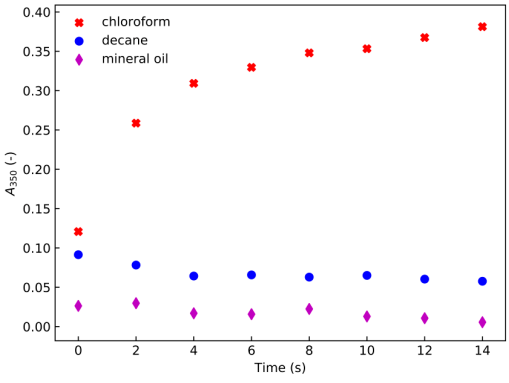

Figure 3.9: **Time traces of UV-VIS absorbance of different lipid-in-oil mixtures.** Absorbance at 350 nm of the lipid-in-oil dispersion was measured over ten minutes after opening of the vial. Measured samples include dispersed lipid aggregates using chloroform or decane in silicone oil:mineral oil 80:20 and a lipid-chloroform solution in mineral oil only. All samples were prepared in the glovebox.

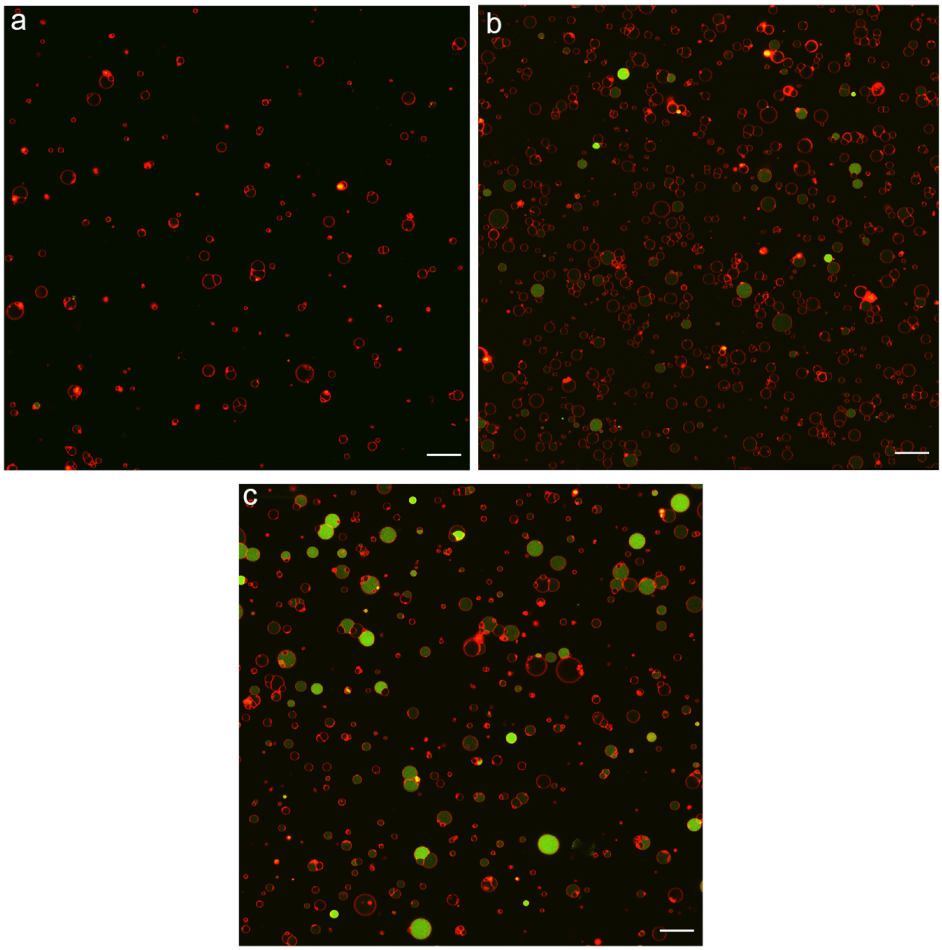

Figure 3.10: **Representative fields of view of GUVs encapsulating the PURE system.** In all images, GUVs (red) are produced encapsulating PURE*frex*2.0 and DNA encoding for YFP (green). Vesicles were formed using (a) a chloroform-based lipid-in-oil dispersion; (b) a decane-based lipid-in-oil dispersion, or (c) a chloroform-based lipid-in-oil dispersion and 0.01 mol% PEGylated lipids. All pictures have the same size (scale bars indicate 50μm) and were acquired with identical imaging settings.

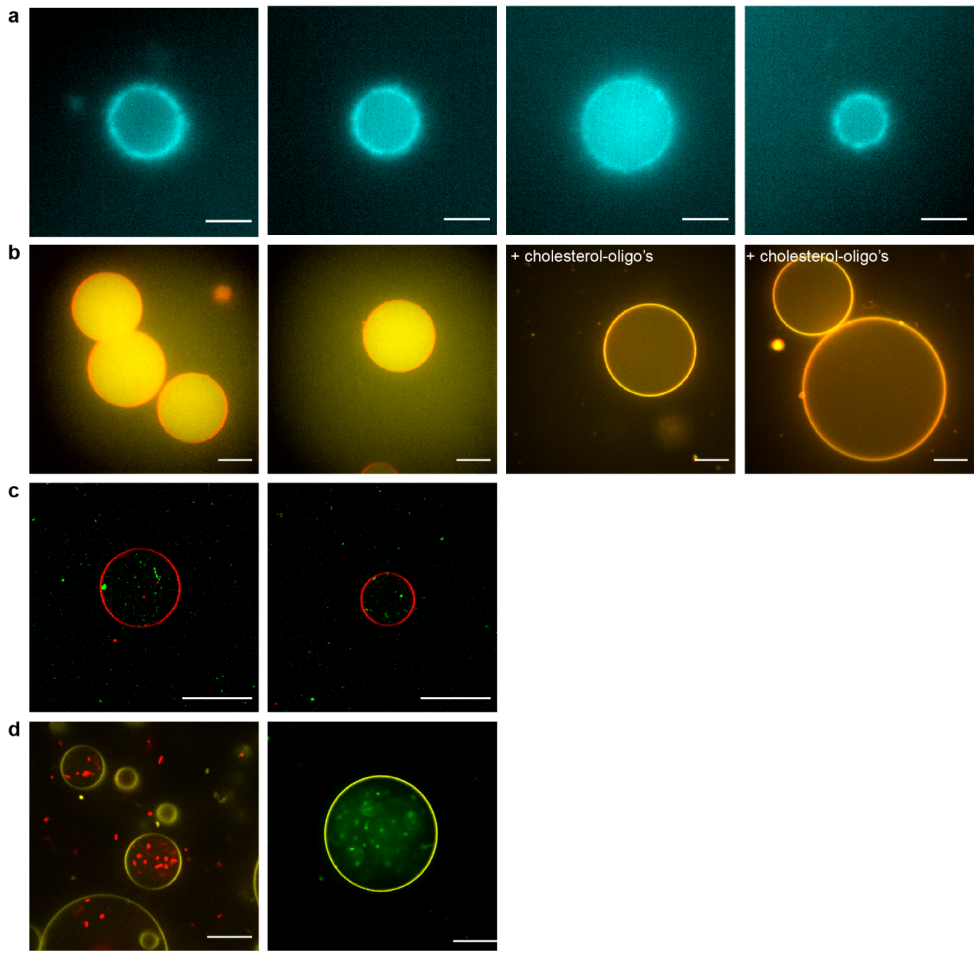

Figure 3.11: **Representative fields of view of proof-of-concept encapsulation experiments.** (a) Reconstitution of a minimal actin cortex (blue) inside a GUV, nucleated at the vesicular membrane by the Arp2/3 complex, the C-terminal VCA domain of WASp, and profilin. Scale bar indicates $5\mu m$. (b) Encapsulation of DNA origami nanostructures (yellow) inside GUVs (red), freely diffusing inside the GUV lumen (left) and capable of membrane localization upon addition of $2\mu M$ of cholesterol-oligonucleotides (right). Scale bar indicates $15\mu m$. (c) Encapsulation of SUVs (green) inside GUVs (red) to form a multicompartmentalized system. Scale bars indicate $20\mu m$. (d) Encapsulation of GFP-HU expressing *E. coli* bacteria (red, green) in GUVs (yellow). A large number of bacteria could be observed inside the GUV lumen, clearly viable as evident from their motility. Scale bar indicates $20\mu m$.

4

PICKING THE RIGHT CONTAINER ASSEMBLY METHOD

Giant Unilamellar Vesicles (GUVs) are a popular model system to study cell and membrane processes in vitro and provide a suitable compartment for building minimal synthetic cell. Sparked by their wide applicability, numerous protocols have been developed for GUV production, but to date there is not a one-size-fits-all protocol for establishing complex reconstituted systems. In this chapter, we test a large number of different formation methods in the specific context of building a synthetic cell with an actin cortex. We look for a protocol that works optimally with the required proteins, physiological buffers, and lipid composition. We show that gel-assisted swelling forms a solid basis for membrane reconstitution by allowing easy production of GUVs of varying lipid compositions in different buffers. For encapsulation of proteins with emulsion-based techniques, we found that the presence of actin negatively impacted vesicle formation. This effect likely originates from actin interfering with bilayer formation, as we showed with pendant drop tensiometry that actin changes lipid adsorption dynamics. Because encapsulation results with existing protocols were not satisfactory, either being too technologically demanding or unable to encapsulate filamentous proteins, we developed a new method which we called emulsion Droplet Interface Crossing Encapsulation (eDICE) by making minor modifications to the continuous Droplet Interface Crossing Encapsulation protocol reported in chapter 3. Using eDICE we efficiently encapsulated the cytoskeletal proteins actin and septin, both in monomeric and filamentous form, with control over membrane anchoring. We demonstrate the potential of eDICE by producing GUVs with different molecular mechanisms for membrane anchoring, highlighting its potential for complex reconstitution.

Actin encapsulation experiments with eDICE were performed by Lucia Baldauf and Iris Lambert. Data on septin encapsulation with eDICE was acquired by Britta Bor under supervision of Gerard Castro Linares and Lennard van Buren.

4.1. INTRODUCTION

The first step in building a synthetic cell is arguably constructing its container. The container separates the cellular content from its surrounding, thereby defining the entity that we call a cell. At the same time, it creates the chemical environment where all vital processes take place. In biology, the cell container is created by the cellular plasma membrane, which is primarily a lipid bilayer envelope enriched with proteins, fatty acids and sterols [37]. Synthetic biology offers multiple ways to form compartments, such as coacervates, polymersomes, proteosomes, and liposomes (reviewed in [28]). Of these compartmentalization strategies, liposomes are closest to their biological counterpart, as their membrane constitutes the same lipid bilayer as the plasma membrane matrix. In particular, giant unilamellar vesicles (GUVs) are frequently used, as they do not only match in membrane organization, but also their size (typically 5-30 µm) is comparable to that of eukaryotic cells. Due to their cell-mimicking properties, GUVs have been used for a wide range of research applications in biophysics, biomedicine and synthetic biology [33]. To accommodate the wide variety of applications and complexity of GUV research, significant effort has been spent on the development of GUV formation protocols. As such, GUVs can now be produced with controlled size [3, 77, 286**?**], with a wide range of phospholipid compositions [282, 329], using charged lipids [293, 339, 340] or sterols [341], with asymmetric bilayers [287, 342, 343], phase-separated membranes [344], in physiological buffers [285, 293, 339], and allowing encapsulation of proteins and other cargo inside vesicles [75, 175, 345]. There is no exact count of the number of different formation protocols, but while there are at least fifteen different formation techniques, the number of protocols must be well over a hundred. While the number of production techniques keeps increasing with over ten per year, the question arises: how to select the most suitable formation method?

Most of the production methods so far can actually be categorized in two groups: hydration of dried bilayers, called swelling approaches, or lipid adsorption to water-oil interfaces, called emulsion-based approaches. Swelling and emulsion based formation are typically used for different purposes.

In the past sixty years, swelling approaches have been employed abundantly to study membrane biophysical properties outside the cellular context, including bilayer elasticity [56, 346], lipid diffusion [347, 348], membrane lateral organization [344], and membrane permeability [349]. Initially, swelling was done simply by spontaneous hydration of the lipid film in an aqueous environment, called spontaneous swelling or gentle hydration [73]. Later, Angelova et al. showed that the swelling process could be promoted by application of an alternating electric field [74], introducing the electroformation method. While electroformation has been the golden standard for GUV formation since its invention, a major disadvantage has been its limited compatibility with producing vesicles with charged membranes and in physiological buffers. Porous hydrogels promote GUV swelling also in solutions of higher ionic strength [76, 109, 285, 311]. However, gel-swollen GUVs can be contaminated with gel polymers, thereby leading to altered membrane properties [350]. To produce clean membranes, more recent efforts have focused on changing the hydrogels physicochemical properties [76], cross-linking the polymers[286], or using other porous substrates such as textile [351, 352] or paper [353]. In the meanwhile, by changing the electroformation parameters, researchers

managed to produce GUVs also in physiological buffers [339, 354]. Altogether, a wide set of swelling-based GUV formation protocols have been developed to produce membranes of varying compositions, in buffers of different ionic strength (reviewed in ref. [355]).

While swelling-based formation techniques are useful to study lipid bilayer membrane properties, they have limited compatibility with more complex biological reconstitution experiments. In particular, encapsulation of large and charged water-soluble molecules is difficult by swelling [33]. Such encapsulation is interesting to study proteins and other biomolecules in cell-mimicking environments, and forms the basis of more recent endeavours to build a synthetic cell. When encapsulation is required, GUVs can better be formed from emulsion droplets by the inverse emulsion technique [75]. First, water droplets are dispersed in an oil phase containing lipids, which adsorb to the droplet water-oil interface to create a monolayer. Next, by spinning these droplets, typically by centrifugation, through another water-oil interface that is also covered with lipids, the droplets acquire a second monolayer as they transfer to the outer aqueous phase and transform into GUVs. Besides the ability to control the inner aqueous phase independently from the outer aqueous solution, an additional advantage of the inverse emulsion technique is that monolayers can be assembled one-by-one in this way, allowing the assembly of asymmetric bilayers [287, 299, 342, 343]. Many different biomolecular systems have been successfully encapsulated in this way, including Min proteins [296] and actin monomers that were triggered to polymerize in the cytosol [75] or at the membrane [108]. Furthermore, the working principle of inverse emulsion has given rise to a plethora of microfluidic assembly techniques (reviewed in [356–358]), which give an additional control over GUV size and allow for *in situ* observation of GUV formation. In addition, hybrid techniques have been developed, which combine the ease of bulk assays with enhanced control compared to inverse emulsion. An important example is called continuous Droplet Interface Crossing Encapsulation (cDICE) as is introduced in chapter 3, which has been successfully implemented for actin reconstitution experiments by various labs[113, 114, 175, 294, 359].

Even though a general guideline may be that swelling methods are more suitable for membrane research, and emulsion-based GUV formation is more suitable for controlled encapsulation, the variety in different methods is still overwhelming. Furthermore, which method works best depends on the molecular composition of the system of interest. In this chapter, we test a large number of different methods in the specific context of building a synthetic cell with an actin cortex. We look for a protocol that works optimally with the required proteins, buffer composition, and lipid composition of interest. First, we discuss swelling-based methods (electroformation [74], polyvinylalcohol-assisted swelling [76], spontaneous swelling [73] and swelling on paper [353]) and their potential for producing GUVs of the right lipid composition and with the right physiological buffers. Then, we explore four emulsion-based GUV formation techniques (inverse emulsion [75], octanol-assisted liposome assembly (OLA) [77], cDICE[3], and a modified version of cDICE that we invented, which we call emulsion Droplet Interface Crossing Encapsulation, or eDICE) and their compatibility with the reconstitution of an actin cortex. Altogether, our choice of GUV formation methods covers the entire range from bulk to microfluidic assays, from simple to difficult protocols, and from old to new

techniques. In addition, we use surface tension measurements to improve our general understanding of lipid monolayer formation in emulsion-based GUV formation. With this comparative testing, we aim to identify a method that is facile, has high yield, and high flexibility for choosing the lipid, ionic, and protein composition. Even though this review is specifically focused on making GUVs for the purpose of studying membrane mechanics and cytoskeletal reconstitution, we believe that, due to the wide scope of assays tested and our surface tension measurements on lipid monolayer formation, our results extend to general lessons on how to build a synthetic cell.

4.2. RESULTS

In this section compare our experimental work on eight different GUV formation strategies (**??**) in the light of the reconstitution of an actin cortex. We start by addressing the swelling methods, which are relatively easy to implement and produce vesicles with high yield. However, the main drawback of all swelling methods is that they provide limited opportunities for complex reconstitution experiments that involve encapsulation of one or multiple components. Therefore, we next discuss the emulsion method and specifically review their compatibility with protein encapsulation. Since we found that protein encapsulation affected GUV formation in multiple emulsion-based formation techniques, we conclude this chapter with a study on the effect of proteins on lipid monolayer formation using pendant drop tensiometry.

4.2.1. SWELLING METHODS

ELECTROFORMATION, THE GOLDEN STANDARD

With electroformation we were able to produce large numbers of vesicles, easily thousands per experiment. Membranes composed of only neutral lipids, such as DOPC or EggPC lipids, could easily be formed in a 200 mM sucrose solution both on a platinum wire (fig. 4.2a) and on an ITO slide (fig. 4.2b). Vesicles produced with ITO slides and platinum wires were qualitatively similar in number, size distribution and morphological features. After a formation phase at 10 Hz and 2 V_{pp} for one hour, GUVs were formed with diameters up to 100μm. In the absence of salts in solution, vesicle formation was followed by a detachment phase at lower frequency of 1 Hz still at 2 V_{pp} which aided physical detachment of vesicles from the conductive surface. During this detachment phase, vesicles could clearly be seen bouncing on the conductive surface with the field frequency. Vesicles could be successfully harvested and observed outside the electroformation chamber (fig. 4.2c).

Addition of ions to the swelling buffer required an adjustment of the electric field settings, in particular an increase in frequency [340, 354]. A combined experimental and finite element simulation study has shown that low frequencies in saline solutions lead to high electric field strengths at the electrode surface, thereby driving lipid oxidation [340]. By increasing the frequency, this problem is circumvented, and GUVs can be formed[339, 340, 354]. In fig. 4.2c, we show successful formation of POPC vesicles in a solution containing 100 mM NaCl without sugar and buffer using electric field settings 1000 Hz and 2.5 V_{pp}. However, vesicle growth was notably slower than in non-ionic solutions, even though we increased the temperature up to 35°C to promote membrane

fluidity and thereby vesicle growth [340]. After 2 hours, vesicles had diameters of maximally 10μm. When we tried to do the same experiment at room temperature, GUVs were barely visible after 2 hours, with a maximal diameter of about 2μm (data not shown). For these experiments, the formation time could be extended to yield larger vesicles, but note that this requires additional experimental precautions such as proper water-tight closure of the electroformation chamber. A detachment phase was not used in solutions of high ionic strength as this resulted in degradation of the vesicles (read below), visible as the formation of a fuzzy membrane carpet on the electrode surface. Also, note that addition of ions, even at low concentrations (10 mM), required electric field parameters to be adjusted. For example, when we tried to form DOPC vesicles in a solution containing 200 mOsm sucrose and 10 mM Tris-HCl at 10 Hz and 2 V_{pp}, we observed formation of a fuzzy fluorescent layer on the electrode after several minutes. In this case, successful vesicle formation required adjustment of the electric field parameters to 300 Hz and 2 V_{pp} (see also chapter 6). Table 4.3 contains an overview of electroformation parameters that successfully led to GUV formation in solutions of different salinity.

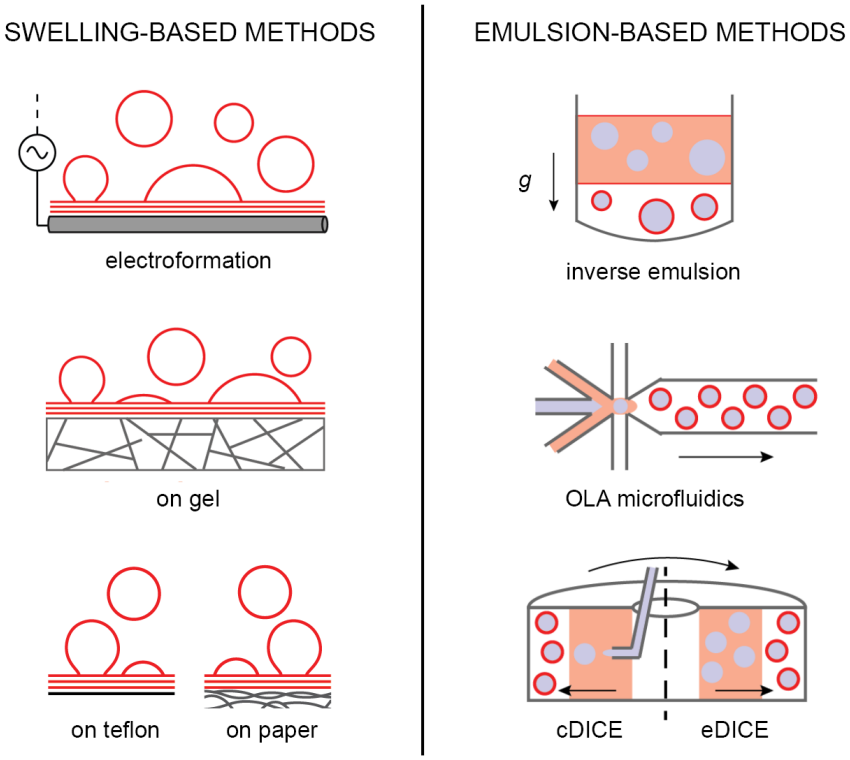

Figure 4.1: **Overview of GUV formation techniques.** Schematic overview of the GUV formation techniques discussed in this chapter. Left: swelling-based techniques. Right: emulsion-based methods.

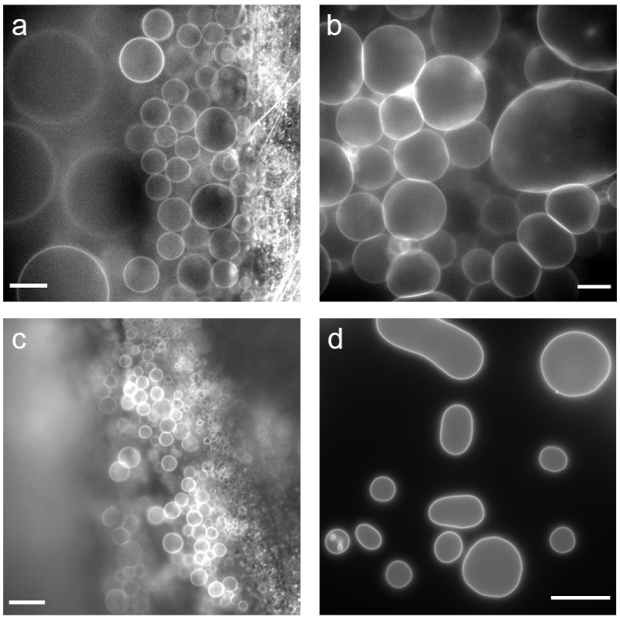

Figure 4.2: **Examples of successful electroformation.** All images are epifluorescence images. Scale bar is 20 µm in all images. (a) DOPC vesicles on a platinum wire (right side of the image) in 200 mM sucrose imaged in the formation chamber, after 1 hour formation time. (b)EggPC vesicles on an ITO slide in 200 mM sucrose imaged in the formation chamber after 1 hour formation time. (c) POPC vesicles on a platinum wire in a solution containing 100mM NaCl at 35 °C imaged in the formation chamber after 2 hours formation time. Note that GUVs are smaller than in image (a) and (b) due to modified electric field settings. (d) Harvested POPC vesicles after successful electroformation in 200 mM sucrose on Pt wires.

Several factors were critical for successful electroformation. First, we noticed that lipid spreading and vesicle detachment strongly determined the quality of the produced vesicles. When lipids were not spread evenly over the platinum wire, and when formation was not followed by detachment by mechanical agitation, the resulting vesicle sample exhibited a zoo of different appearances (see fig. 4.3a). The majority of the sample was multilamellar or multivesicular. The fraction of unilamellar vesicles notably increased when lipids were spread evenly over the wire or ITO glass using a glass syringe needle, and when vesicles were mechanically detached after formation, for example by tapping the closed chambers on a table.

Furthermore, vesicle formation had to be executed above the membrane melting temperature T_m. While GUVs from DOPC and POPC lipids could be formed at room temperature, electroformation of DMPC lipid films at room temperature led to randomly shaped multilamellar structures (fig. 4.3b). Since DOPC and POPC have a T_m well below room temperature, that is -17°C and -2°C respectively, these membranes are fluid at room temperature, but DMPC with a T_m of 24°C is below its phase transition temperature at room temperature[360]. Starting from the DMPC membranes shown in fig. 4.3b,

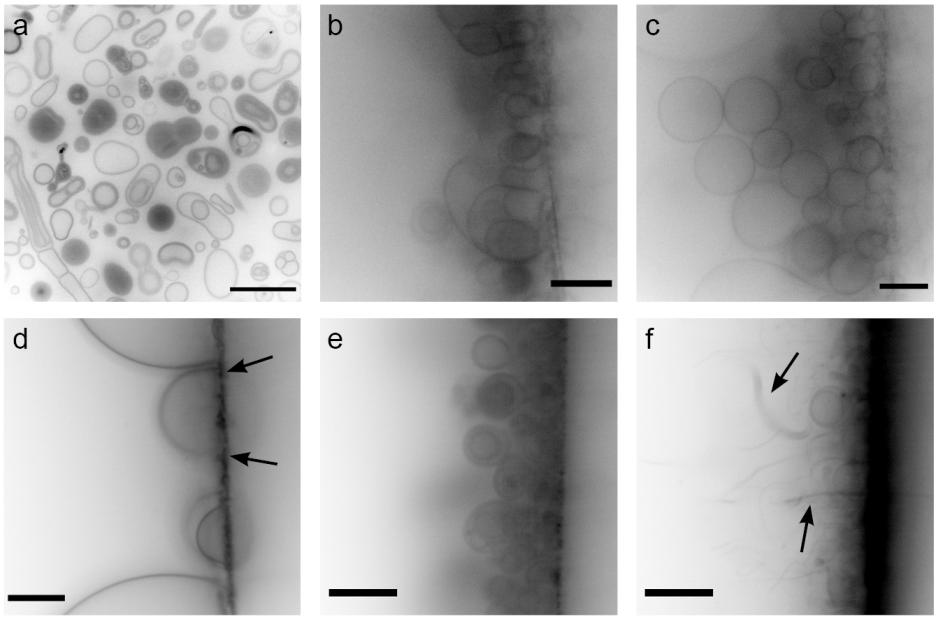

Figure 4.3: **Typical issues encountered with electroformation.** All images are confocal images with inverted contrast for better visualization. Scale bar is 20 µm in all images. In (b-f), vesicles are imaged during formation on a platinum electrode (oriented vertically and positioned on the right side of the image). (a) Harvested vesicles (here DOPC) were very polydisperse in size, morphology and lamellarity when the lipid film was not spread well over the platinum wire electrode and vesicles were not detached by mechanical agitation. (b-c) Formation of DMPC vesicles. (b) Initial swelling at room temperature led to multilamellar, non-spherical structures. (c) A subsequent increase in temperature to 30°C at the same electric field settings caused spherical vesicles to form. (d) Electroformation of DOPC:DOPS (80:20 mol/mol) GUVs in 200 mM sucrose resulted in pinning of the membranes on the electrode (indicated with arrows) (e-f) Electroformation using the charged *E. coli* polar lipid extract in 200 mOsm sucrose. Initial swelling at 10 Hz, 2 V resulted in multilamellar vesicles (e) while subsequent adjustment to 1 Hz, 2 V caused vesicles to disintegrate, resulting in membrane tubes as indicated with arrows (f)

when we increased the temperature up to 30°C while operating at the same electric field settings, membranes blew up to a spherical shape within minutes (fig. 4.3c).

Finally, we investigated electroformation of GUVs containing charged lipids using a lipid mixture containing 20% (mol/mol) DOPS and using the *E. coli* polar lipid extract. The bacterial polar lipid extract is a natural lipid extract from the *E. coli* inner membrane. It therefore naturally contains a wide variety of lipids, including 20 % lipids with a PG headgroup, contributing one negative charge per lipid, and about 10 % cardiolipin, carrying two negative charges per molecule [361]. To confirm the effective surface charge of this complex mix of lipids, we measured the zeta potential of the bacterial lipid extract. We first constructed a surface charge calibration curve using POPC LUVs doped with 0%, 5%, 15%, 20% and 40% DOPS. From fig. 4.16 (SI) it can be seen that the zeta potential becomes more negative upon addition of the negatively charged DOPS lipid, starting from -5 mV for 100% POPC vesicles, to -43 mV for POPC vesicles containing 40%

DOPS. We measured the zeta potential of the bacterial extract to be -37.6 ∓ 1.7 mV (average ∓ standard deviation), corresponding, based on the calibration curve (fig. 4.16), to about 30% negatively charged head groups. Thus, we confirmed an increasing negative surface charge upon DOPS addition, and we measured the *E. coli* polar lipid extract surface charge to be strongly negative.

When we included 20% (mol/mol) DOPS in the DOPC:Cy5-PE lipid mix for electroformation, we did not observe any formation of spherical GUVs, but instead the membrane was pinned on the electrode (see fig. 4.3d). Thus, although the membrane could be swollen, pinning prevented the formation of closed, detached vesicles. To our knowledge, membrane pinning has not been reported before in the context of GUV electroformation. However, pinning was reminiscent of electrostatic membrane adhesion to charged surfaces as reported by Steinkuhler et al.[362] and could therefore potentially be modulated by changing the surface charge of the electrode. Otherwise, membrane adhesion could be prevented by steric repulsion by addition of PEGylated lipids, but we did not pursue this further.

Another remarkable observation was the effect of a low-frequency detachment phase on charged membranes. In fig. 4.3e we show the growth of (multilamellar) vesicles consisting of the highly charged *E. coli* polar lipid extract. Lowering the frequency to $1Hz$ did not lead to vesicle detachment from the electrode, but instead caused degradation of vesicles, turning them into tubes while the fluorescent signal on the wire increased in brightness. While a low-frequency detachment phase clearly resulted in GUV separation from the wire or ITO slide in non-ionic solutions and neutral membranes, this could not be applied to charged membranes.

FACILE AND VERSATILE GUV FORMATION BY GEL-ASSISTED SWELLING

Swelling membranes on top of hydrogels proved to be a much more robust GUV formation method as compared to electroformation, where electric field parameters had to be tuned according to membrane composition and content of the swelling solution. The process of GUV formation by gel-assisted swelling is shown in fig. 4.4a-c for EggPC vesicles in 200 mOsm sucrose. Before addition of a swelling solution, the dried lipid film is visible on top of the hydrogel (fig. 4.4a). Irrespective of whether the dried lipids formed an inhomogeneous layer with brighter and darker patches as in fig. 4.4a, or if they formed a film with uniform intensity, in both cases GUVs could be formed successfully. After careful addition of a swelling solution so as not to disturb the lipid film, vesicles started to grow immediately (fig. 4.4b), reaching diameters up to 50μm within minutes (fig. 4.4c).

Essential for harvesting the produced vesicles was to detach them from the gel, which could be done either by tapping the bottom of the swel-ling chamber or by flushing swelling solution over the tilted gel. Vesicles could be harvested after several minutes, but we waited for 1 hour as longer swelling times generally reduced the presence of secondary membrane structures on vesicles (see fig. 4.6b-c, indicated with white arrows). High production yields could be obtained by gel-swelling, as shown for DOPC vesicles in 200 mOsm sucrose including 10 mM Tris-HCl (fig. 4.4d). GUVs could also be formed successfully from the strongly negatively charged *E. coli* polar lipid extract with only minor adjustments (fig. 4.4e). First, we changed the swelling buffer to 100 mOsm sucrose,

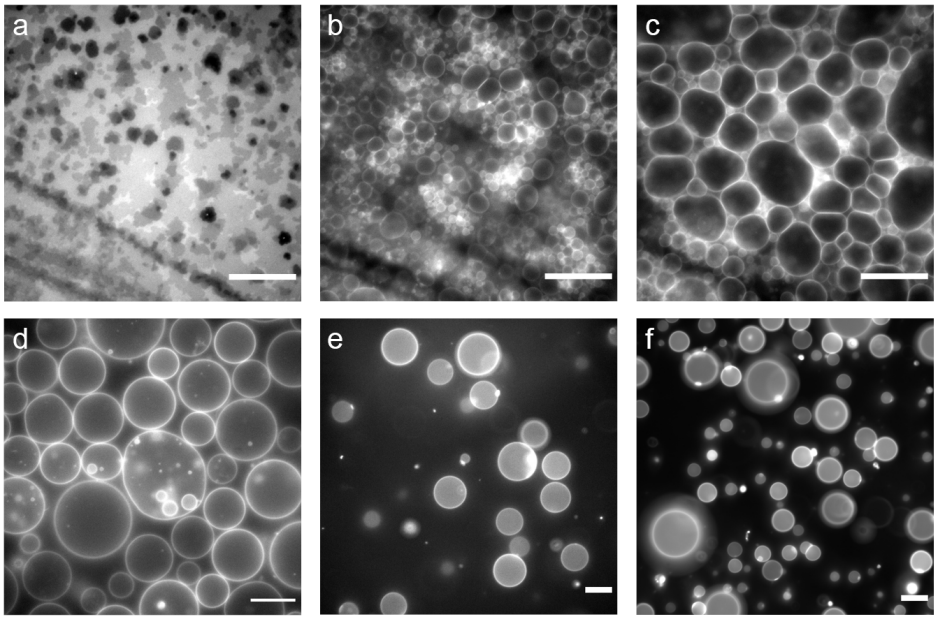

Figure 4.4: **Examples of successful gel-assisted swelling experiments.** All images are epifluorescence images. (a-c) Formation of EggPC vesicles. Scale bar is 20 µm in all images. (a) After drying the lipids on top of the hydrogel, a flat film is visible that is either patchy (shown) or homogeneous (not shown). (b) Immediately after addition of the swelling buffer containing 200 mOsm sucrose and 10 mM Tris-HCl at pH 7.4, vesicles start to grow. (c) After several minutes, GUVs have grown to diameters up to 50 µm. (d-f) GUVs obtained after harvesting from the gel, scale bar is 20 µm. (d) DOPC vesicles swollen in 200 mOsm glucose and 10 mM Tris at pH 7.4. (e) GUVs made from *E. coli* polar lipid extract swollen at 37°C in 100 mOsm sucrose, 100 mM KCl and 10 mM Tris at pH 7.4. (f) GUVs made from an Archaeal *P. furiosus* lipid extract containing mainly diether lipids, produced at 37°*C* in a swelling solution containing 100 mOsm sucrose, 100 mM KCl and 10 mM Tris at pH 7.4.

100 mM KCl and 10 mM Tris-HCl at pH 7.4, where we added KCl to increase electrostatic screening and create a more physiologically relevant environment. Second, we increased the swelling temperature to 37°C, well above the phase transition temperature of this bacterial lipid extract (25°C)[363]. With identical swelling conditions, we were also able to form vesicles from a lipid extract from the Archaeum *Pyrococcus furiosus* (fig. 4.4f). For above-mentioned lipid compositions, we obtained comparable yields.

Even though we found PVA-assisted swelling to be the most robust GUV formation method tested in this study, some experimental design considerations are worth noting. First, gel attachment to the supporting glass coverslip was essential for successful GUV formation. If the gel was not adhering well to the glass, or when the gel was too thick, we observed cracking and wrinkling of the gel upon addition of the swelling solution (fig. 4.5a). In the case of gel cracking, GUV formation was unsuccessful. This is similar to what has been reported by Souissi et al. [364], although they reported cracking to originate from high temperatures, which were not encountered in our study. In our case, we were able to prevent cracking with two adaptations. First, we activated the glass sur-

face by plasma treatment prior to PVA spreading. Second, the PVA solution was always brought to room temperature before application to make it less viscous, resulting in a thinner gel layer. Together, these measures ensured sufficient stability of the PVA layer during swelling.

Secondly, depending on the membrane composition, the swelling buffer and temperature had to be adapted. In particular, when working with charged membranes, we found that swelling in non-ionic solutions caused the lipid film to break off from the gel (fig. 4.5b) indicating the necessity to use buffers containing ions. Similarly, swelling the *E. coli* membranes at room temperature, which is below their T_m (25°C [363]), also resulted in detachment of the lipid film.

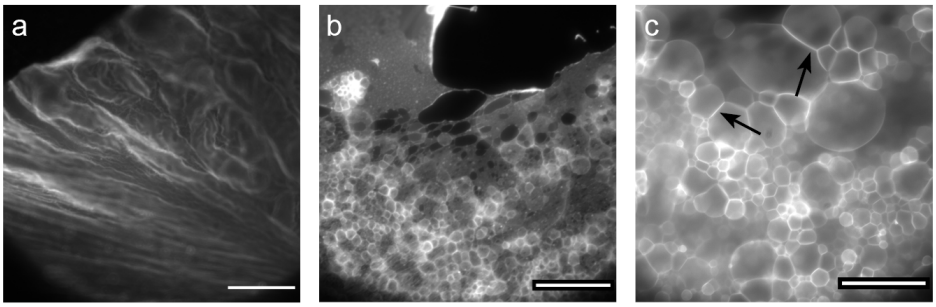

Figure 4.5: **Typical issues encountered during gel-assisted welling.** All images were taken while lipids and/or vesicles were still on the gel, so before harvesting. In all images, the signal signifies fluorescently labelled lipids. Scale bar is 50 µm in all images. (a) Cracking of a PVA gel that was too thick, because the PVA solution was initially spread over the glass support at a too low temperature. In addition to gel cracking, the lipid film detached. Similar detachment occurred when glass supports were not plasma-treated before applying the fluid PVA. In this example, swelling was performed with a mix of DOPC and Atto 655 DOPE in a molar ratio of 99.5:0.5 and a swelling solution containing 100$mOsm$ sucrose and 10mM Tris-HCl at pH 7.4. (b) The lipid film detached while GUVs were swelling when the swelling temperature was too low, or when the swelling buffer was chosen inappropriately. In this example, membrane were swollen with a lipid composition of DOPC:DOPS:Atto 655 DOPE in a molar ratio 69.5:20:0.5, in a swelling solution consisting of 100$mOsm$ sucrose and 10mM Tris-HCl at pH 7.4. (c) Adhesion between GUV membranes made of *E. coli* polar lipid extract. Black arrows indicate adhesion sites. In this example, membranes were swollen in a solution of 100$mOsm$ sucrose and 100mM KCl, without buffer.

Finally, when vesicles did swell properly, we sometimes observed adhesion between adjacent GUVs (fig. 4.5c, indicated with arrows) dependent on membrane composition and swelling buffer. In the example in fig. 4.5c, *E. coli* GUVs adhere in an unbuffered solution containing only 100 mM KCl and 100 mOsm sucrose. Addition of 10 mM Tris-HCl at pH 7.4 to the swelling buffer prevented GUV adhesion. Presumably, buffer addition shifted the solution's pH with respect to the isoelectric point of the lipids, thereby changing the lipid's net charge.

An important consideration for PVA-assisted swelling for GUV production is the presence of sugar during the formation process. We found that the GUV yield strongly increased with increasing concentrations of sucrose in the swelling solution (fig. 4.6a-d). In fact, at a concentration of 20 mOsm sucrose, barely any vesicles formed (fig. 4.6a), while

yields were extremely high at 500 mOsm sucrose in the swelling solution (fig. 4.6d). At the same time, the number of secondary membrane structures (see fig. 4.6b-c, indicated with arrows) seemed to decrease for higher sugar concentrations. While it is known that sugars affect membrane properties such as bending rigidity (reviewed in ref. [52]), sugar interactions with the membrane might also be beneficial for GUV formation. In addition, we found that the presence of sucrose in the PVA gel was crucial for successful GUV formation. When we dissolved PVA in milliQ water instead of in 200 mOsm sucrose solution, the resulting gels were not usable for GUV formation. Instead, upon addition of the swelling solution on these gels, the lipid film cracked and detached as in fig. 4.5a-b.

OTHER SWELLING METHODS

Although gel swelling is a robust method compatible with different membrane compositions and buffers, it has the drawback that PVA polymers could potentially remain associated with the membrane[365]. We therefore explored yet two other swelling-based GUV formation methods that potentially combine versatility with membrane cleanliness: spontaneous swelling [73] and swelling from tracing paper [353]. Both techniques use solid, rigid supports, and do not require an electric field for swelling, making them at first sight promising alternatives.

Figure 4.7a shows DOPC vesicles produced in 200 mOsm sucrose by overnight spontaneous swelling at room temperature of a dried lipid film on a teflon disk. Similarly, *E. coli* vesicles could be formed by overnight spontaneous swelling at elevated temperature (37°C) in the same swelling solution. In both cases, the produced vesicles are very polydisperse in appearance, with many vesicles being multilamellar or enclosing other vesicles. Moreover, the vesicles were limited in size up to 20 µm. The spontaneous swelling technique is easy to implement, but results in the formation of very polydisperse samples. Further optimization of the technique is difficult because of its limited programmability.

In addition, we followed a recently published protocol using tracing paper to swell GUVs [353]. Unlike the PVA hydrogel substrates, which consist of non-covalently linked polymers, tracing paper consists of large, immobile cellulose fibres that are less likely to contaminate the GUV membranes during the swelling process. Indeed, we found DOPC GUVs to grow on the tracing paper (fig. 4.7b) over the course of several hours in a swelling solution containing $200 mOsm$ sucrose and $10 mM$ Tris-HCl at pH 7.4. However, we did not pursue this method further since yields were low after harvesting, probably due to a combination of a low vesicle density on the paper and difficult detachment.

4.2.2. EMULSION-BASED METHODS

When encapsulation of complex (protein) solutions is required, emulsion-based vesicle formation strategies offer more control than the aforementioned swelling methods. In these methods, vesicles are produced with an inner aqueous solution (IAS) that can be different from the outer aqueous solution (OAS). This gives the opportunity to tune the vesicle content independently, simply by controlling the content of the IAS. We investigated the potential of several emulsion-based formation methods to produce vesicle containing cytoskeletal proteins. The covered techniques are the classical inverted emulsion technique[75], OLA microfluidics[77] and a new technique that we adapted

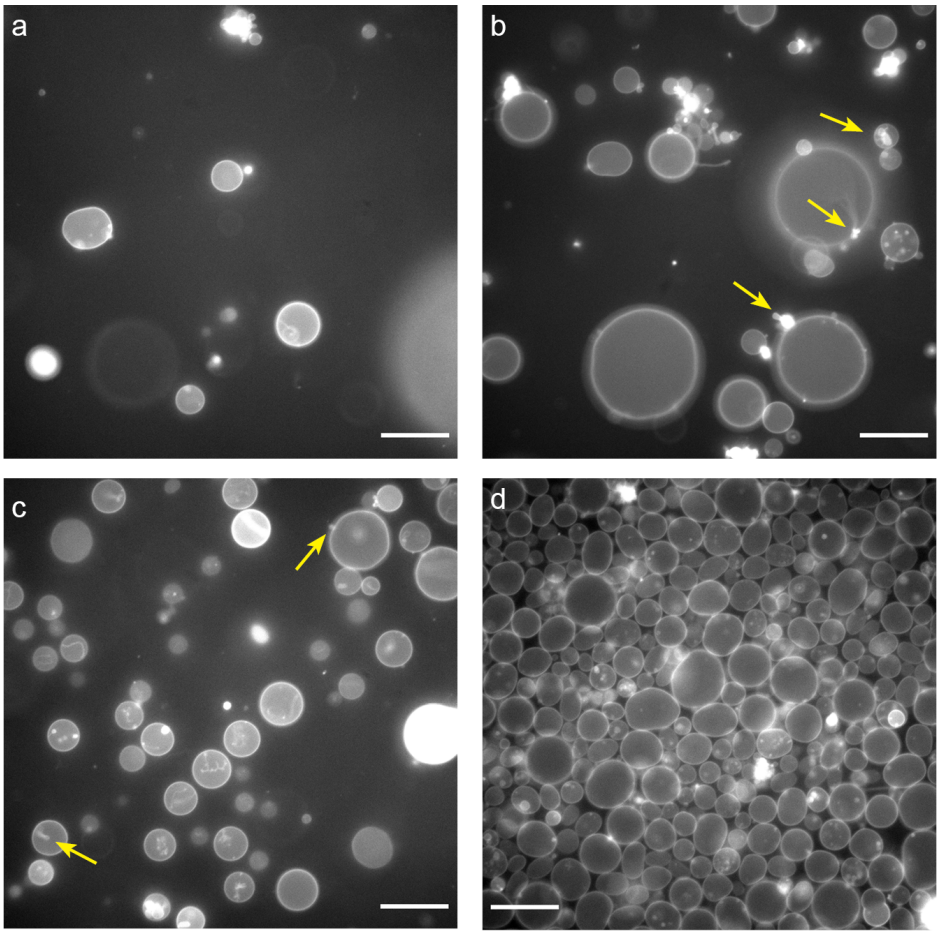

Figure 4.6: **Sucrose aids the formation of GUVs by gel-assisted swelling.** Harvested DOPC vesicles after formation by gel-swelling in solutions containing different concentrations of sucrose. In addition to sucrose, all swelling solutions contained 10 mM Tris-HCl at pH 7.4. Secondary membrane structures were sometimes seen on GUV membranes and are indicated with white arrows. Scale bar is 20 µm in all images. (a) 20 mOsm sucrose. (b) 100 mOsm sucrose. (c) 200 mOsm sucrose. (d) 500 mOsm sucrose.

from cDICE, which we call emulsion Droplet Interface Crossing Encapsulation (eDICE).

WHERE IT BEGAN: INVERSE EMULSION

We produced vesicles following the original emulsion-based formation method called inverse emulsion or droplet transfer method [75]. In this method, the IAS is dispersed into a lipid-oil solution (LOS) in one tube by rigorous pipetting. In another tube, the LOS is layered on top of the OAS. The emulsion is then placed on top of the LOS-OAS system and the IAS droplets are spun down to produce lipid bilayer vesicles.

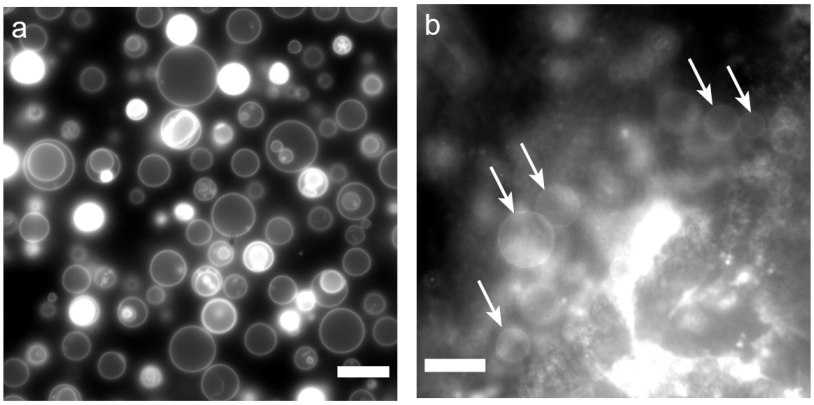

Figure 4.7: **GUVs formed with other swelling techniques.** Scale bar is 20 µm in both images. (a) DOPC vesicles doped with 0.5% (mol/mol) Atto 655 DOPE formed by spontaneous swelling overnight in $200mOsm$ sucrose. (b) GUVs comprised of DOPC:Atto 655 DOPE lipids at a molar ratio of 99.5:0.5 growing on tracing paper in $200mOsm$ sucrose with $10mM$ Tris-HCl at pH 7.4. White arrows indicate swollen vesicles, while the tracing paper can be seen below.

GUV formation by inverse emulsion was easy and quick, and often resulted in yields of hundreds of vesicles per sample with diameters typically ranging from 5 to 50 µm. In fig. 4.8a, we show a sample of DOPC vesicles encapsulating actin G-buffer, containing 0.2 mM $CaCl_2$ and 20 mM imidazole at pH 7.4. In fig. 4.8b, we show that the water-soluble HPTS dye dissolved in the IAS successfully gets encapsulated in the vesicles. The HPTS signal is noticeably higher inside the vesicles than in the surrounding outer aqueous solution. However, the GUVs have variable HPTS intensities in their lumen, pointing at a variable encapsulation efficiency between GUVs within the same sample.[1]

Furthermore, in many inverse emulsion experiments, we noticed to a varying degree the presence of small bright dots in vesicles (indicated with arrows in fig. 4.8a). We interpreted these to be small fluorescent lipid structures. The presence of these structures appeared to be related to the solubility of the lipids in the organic phase, as GUVs formed with lipids dissolved in warm oil contained structures fewer in number and smaller in size (fig. 4.8a, yellow arrows) than GUVs formed from lipids dissolved in room temperature oil (fig. 4.8c, yellow arrows). Some fluorescent structures were also visible in bright-field (fig. 4.8d, blue arrows), possibly indicating the presence of oil. While GUV formation by inverse emulsion resulted in high vesicle yields when the IAS was a sugar solution with or without G-buffer, the vesicle yield dropped tremendously when we tried to encapsulate actin F-buffer (without actin) or 10 µM G-actin in G-buffer. Actin F-buffer differs from actin G-buffer in its salt content: where F-buffer contains 50 mM KCl and 2 mM $MgCl_2$, and G-buffer contains only 0.2 mM $CaCl_2$. This indicates that either ionic strength, the concentration of divalent cations or the presence of Mg^{2+} ions specifically

[1] In epifluorescence imaging, larger GUVs are expected to show a higher signal due to of out-of-focus fluorescence. However, this cannot account for the variation since the observed variation is clearly size-independent.

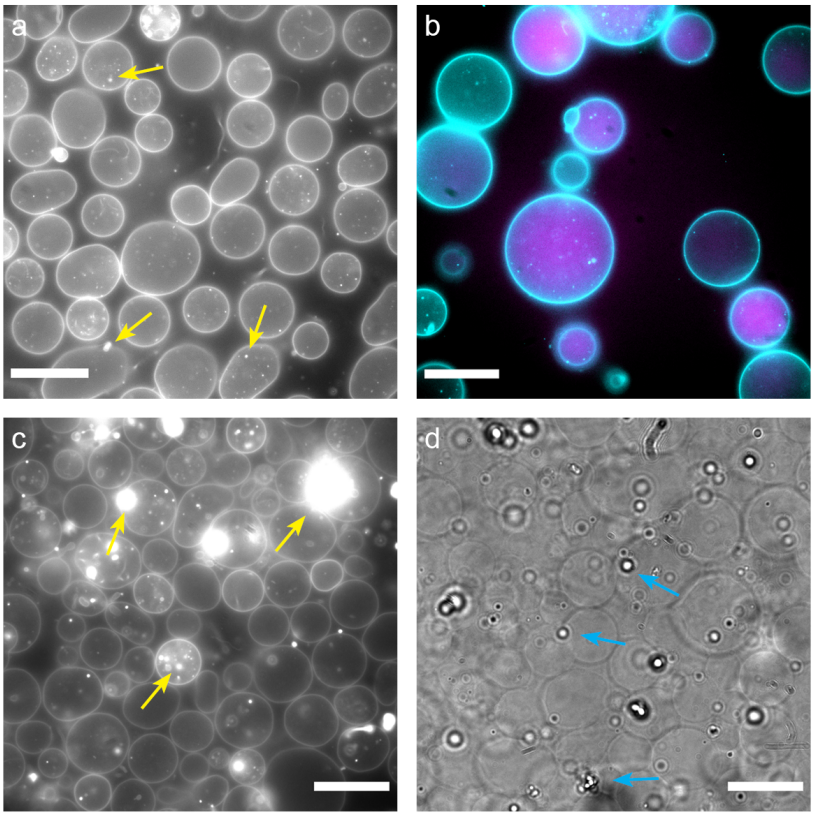

Figure 4.8: **GUVs formed with the inverse emulsion method.** Scale bar in all images is 20 µm. (a) DOPC vesicles encapsulating G-buffer containing 0.2 mM $CaCl_2$, 20 mM imidazole at pH 7.4 and an additional 190 mM sucrose. Outer solution is 190 mM glucose. Fluorescent lipid structures are indicated with arrows. (b) DOPC vesicles (cyan) encapsulating 4.8 mM HPTS (magenta) and 190 mM sucrose. Encapsulation efficiency varies between vesicles. (c) DOPC GUVs produced from an LOS where the dried lipids were suspended in oil at room temperature instead of at 80 °C. Bright fluorescent structures (arrows) are larger in size and in number as compared to panel a. (d) Brightfield image of the sample in (c) reveals stark optical contrast between structures (arrows) and aqueous solution.

interfere with vesicle formation by inverse emulsion. In addition, the presence of actin compromised vesicle formation.

While the inverse emulsion method proved to be a facile method for GUV production, the choice of vesicle content was severely limited because vesicle yield depended strongly on IAS composition. Furthermore, inverse emulsion is a coarse bulk method, where all droplets are produced simultaneously, and all droplets traverse the LOS/OAS interface at once. Colliding droplets or depletion of lipids from the LOS/AOS interface might affect the success rate of GUV formation. We therefore moved on to a microfluidics method, which should provide control over size and rate of droplet and vesicle production, while allowing the researcher to view vesicle production *in situ*.

OLA MICROFLUIDICS: HIGH RISK, HIGH GAIN?

Various microfluidic techniques have been published for the purpose of GUV production [356, 357]. We chose to follow the Octanol-assisted Liposome Assembly method [77], named OLA henceforth. In this technique, lipids are dissolved at high concentration in octanol, named the lipid-oil solution (LOS). Vesicle production is done in a microfluidic device, specifically at a six-way junction where one input channel of IA, two input channels of LOS, two input channels of OAS and one outlet channel meet (fig. 4.9a). A flow of IAS and LOS is pinched off continuously by incoming OAS at the junction, thereby forming droplets of IAS covered by a layer of LOS. As the double emulsion droplets travel through the outlet channel or maturation channel, lipids in the LOS shell self-assemble into monolayers on both water-octanol interfaces, eventually zipping together to form a lipid bilayer accompanied by dewetting and detachment of the octanol phase. The produced GUVs can be visualized in the chip or pipetted out of the outlet channel.

In fig. 4.9a, we show a successful OLA run using an LOS containing DOPC lipids and an IAS consisting of G-buffer. Double emulsion droplets are produced at the junction and travel upwards through the channel. Dewetting of the octanol phase is clearly visible, as droplets produced at the junction still have a sickle-shaped bright octanol phase (fig. 4.9a, inset below), while the octanol rounds up to form a pocket as the droplet matures (fig. 4.9a, inset above). Similarly, we managed to encapsulate actin at 10 μM in G-buffer in double emulsion droplets with OLA (fig. 4.9b). The actin is clearly confined in compartments, as can be seen from the discrete spherical shapes of high intensity.

Once a chip is operating successfully, OLA offers superb control over vesicle production. However, we found that a variety of practical issues severely restricted the success rate. We list here the typical problems that we encountered with microfluidic vesicle formation. First, the chip pretreatment with a PVA solution, essential to render the PDMS channels hydrophilic, was often unsuccessful. Pretreatment sometimes resulted in residual PVA either in the microfluidic channels (see fig. 4.9c) or in one of the inlet channels. PVA structures in the flow channel disturbed the laminar flow in the chip, causing vesicles to deform or burst. PVA clogging of the inlet channels prevented insertion of the fluid streams. Pretreatment also often failed, rendering the channels not sufficiently hydrophilic, and finally resulting in wetting of the post-junction channel by LOS during chip operation (see fig. 4.9d). When this happened, formation of double emulsion droplets was impossible. Second, When initializing the chip for GUV production, care should be taken for the inlet streams to arrive at the post-junction sequentially, being first OAS, then LOS, and finally IAS. No air bubbles should be trapped in one of the channels, nor should the LOS stream enter the IAS or OAS channel, or vice versa. Fluid control sometimes required the use of high pressures, which increased the risk of inlet streams abruptly flowing in the wrong direction. When the LOS mixed with IAS or OAS in one of the pre-junction channels, this often resulted in flow obstruction and channel clogging (fig. 4.9e). Third, Once the chip was initialized properly, the three inlet stream flow rates had to be tuned to be in the correct (jetting) regime for GUV production. During chip operation, the junction was prone to clogging, in particular in the lipid channels as seen in fig. 4.9b and fig. 4.9e, limiting the time a chip could be used for. Another general concern was chip leakage, which sometimes happened due to adhesion failure between the PDMS slab and the supporting surface.

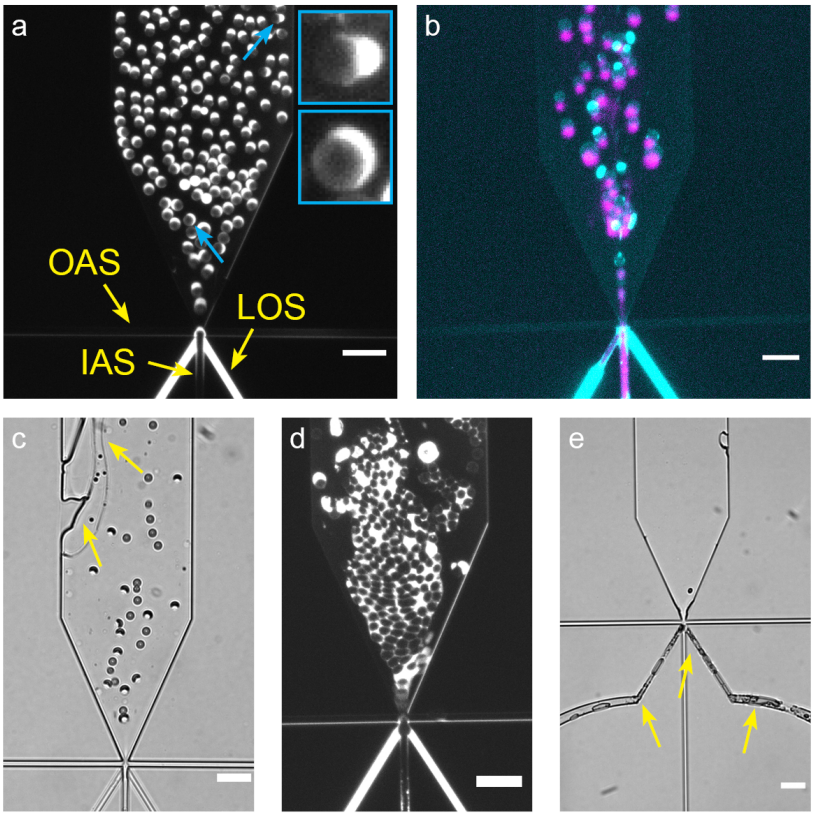

Figure 4.9: **Microfluidic production of GUVs with OLA.** Scale bar is 50 µm in all images. (a) Successful DOPC GUV production with OLA. The inner aqueous solution (IAS) flows in the lower vertical channel, the lipid-containing octanol (LOS) stream in the bright diagonal channels from both sides, and the outer aqueous solution (OAS) in the horizontal channels from both sides. Vesicles with bright octanol pockets form at the junction and mature as they flow downstream (upwards in the image). Two states of droplet maturation are indicated with blue arrows and shown in the inset: the lower droplet has a sickle-shaped octanol phase, the upper, older droplet a budding pocket. (b) Successful production of DOPC vesicles (blue) encapsulating monomeric actin (magenta) in G-buffer. Lipid and actin signals show a small spatial discrepancy due to the movement of the droplets between images. Note the clogging in the left lipid channel. (c) When PVA was not entirely washed out during chip pre-treatment, residual solidified PVA (yellow arrows) disturbed the flow of maturing GUVs. (d) Clogging of the lipid channels (yellow arrows) sometimes occurred when the flow rates were too low or when one of the aqueous solutions entered the lipid channel. (e) When PVA-treatment was not successful, double emulsion droplets could not flow freely into the maturation channel, but instead formed a water-in-oil emulsion sticking to the channel walls.

Since chips in almost all cases had to be discarded when one of the problems above occurred, the success ratio of these experiments turned out to be very low. Furthermore, operating these microfluidic chips requires months of practice. As the OLA method is time-intensive in general, taking in total 2-3 days to fabricate the chips, do the PVA treatment, and finally operate the chips, we did not pursue this method any further.

eDICE allows for efficient and versatile cortex reconstitution

In chapter 3, we have shown that cDICE can be efficiently employed to encapsulate a variety of proteins and other cargo in GUVs. However, for some reconstitution experiments, in particular with cytoskeletal proteins that polymerize, we needed to modify the cDICE protocol. The two major bottlenecks that we identified in the original cDICE protocol were the use of a thin capillary for injecting the inner aqueous solution, that was prone to clogging when filamentous proteins were flushed through, and the time between preparing the encapsulation solution and vesicle formation, which takes several minutes in the original cDICE protocol. To circumvent these problems, we did not inject the inner aqueous solution drop-by-drop using the capillary, but instead we first emulsified the IAS in $1\,mL$ of the LOS in a separate tube, and then we pipetted the emulsion directly into the spinning disk. We demonstrate here how we successfully employed eDICE to encapsulate filamentous actin and septin in GUVs, and furthermore how eDICE can be employed to perform a wide variety of reconstitution experiments. eDICE experiments generally gave a high production yield, as we easily located 100-1000 GUVs in imaging chambers.

Prepolymerized actin filaments were successfully encapsulated in GUVs using the eDICE method (fig. 4.10a). Since actin filaments have a diameter below the resolution limit, it is not trivial to distinguish filaments from monomers in epifluorescence images. We therefore performed two tests to confirm the filamentous nature. First, we visualized actin from the same solution that was encapsulated by injecting it in flow channels, followed by imaging with total internal reflection fluorescence (TIRF) microscopy. TIRF images clearly revealed that actin was filamentous (data not shown). Second, we co-encapsulated fascin in a 1:20 molar ratio (fascin:actin) with the actin using eDICE. Fascin is a protein able to bundle actin filaments[109]. Upon addition of fascin, we observed stiff actin bundles of several micrometers long (see fig. 4.10c), indeed confirming the existence of actin filaments in vesicles. In some vesicles, fascin-induced actin bundles were even capable of deforming the membranes into Φ-shaped vesicles similar to what has been published before [109]. Both tests independently confirm the filamentous nature of the actin, thus showing that eDICE is suitable for encapsulating micrometer-long filaments. It is worth mentioning that encapsulation of F-actin with eDICE was easy and quick, in stark contrast with cDICE where the capillary often clogged in seconds, leading to IAS leakage upstream and eventually requiring replacement of the capillary and redoing of the GUV formation. Furthermore, the severely reduced requirement for IAS volume makes encapsulation of typically precious proteins much more affordable. Lastly, by reducing the time of droplet formation well over 10 minutes to below 30 seconds, we are finally able to capture cytoskeletal dynamics such as actin nucleation.

Next, we encapsulated the cytoskeletal protein septin. Septin is an oligomeric protein that is able to form higher order structures[195, 366, 367], is capable of binding other cytoskeletal proteins such as actin and microtubules [368] (reviewed in ref. [367]), and has been found to bind to membranes containing the negatively charged lipids PS and PIP_2 [255, 369]. As such, septin is an interesting membrane anchor for the actin cortex. We encapsulated septin in DOPC GUVs using eDICE (fig. 4.10c). In these vesicles, we do not expect septin to bind to the membrane. Indeed, we saw either a homogeneous distribution of septin in the vesicle lumen (fig. 4.10), or we observed the forma-

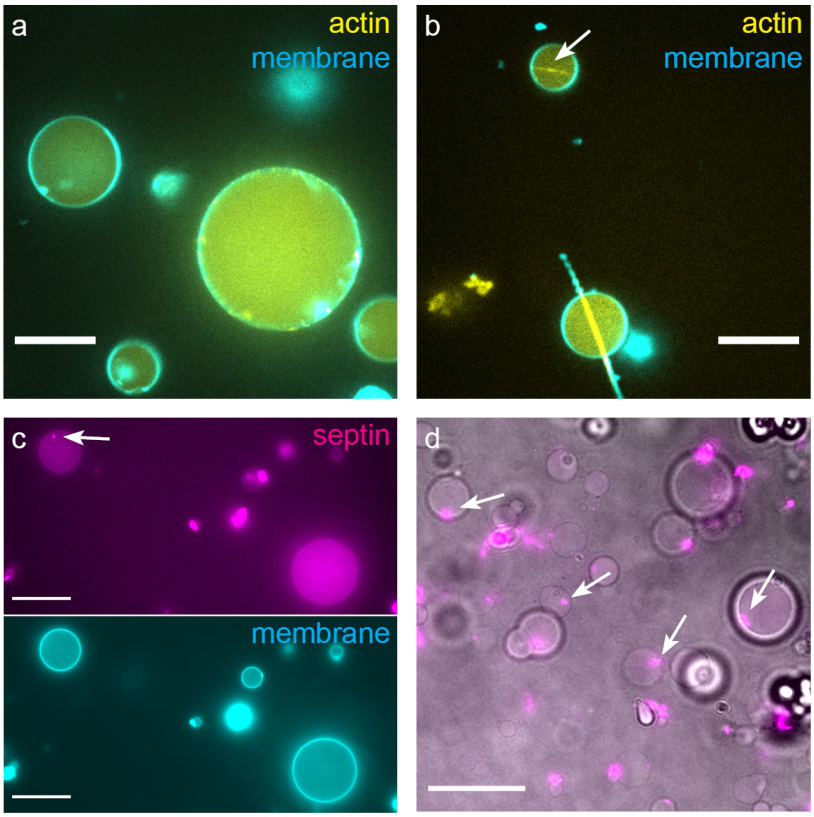

Figure 4.10: **eDICE effectively encapsulates filamentous proteins.** Encapsulation of the polymerizing cytoskeletal proteins actin and septin with eDICE. All images are epifluorescence images with scale bar of 20 µm. (a) Prepolymerized actin filaments (yellow) at a nominal concentration of 4.4μM in F-buffer, stabilized with phalloidin in a 1:1 ratio were successfully encapsulated in GUVs (cyan). Actin was labelled with 10% (mol/mol) AlexaFluor488-labelled monomers. Presence of filaments was confirmed in flow channels by TIRF microscopy (not shown). (b) Encapsulation of F-actin at a nominal concentration of 4.4μM in F-buffer together with fascin in a 20:1 molar ratio resulted in actin bundle formation inside GUVs (the arrow points to an example bundle). Actin polymerization was triggered at the same time when fascin was added by temperature increase, right before GUV formation. In some cases, the actin bundle deformed the vesicle membrane, leading to the formation of Φ-like structures (lower vesicle). (c) Encapsulation of 300 nM septin hexamers (magenta) in DOPC GUVs. Septin is distributed throughout the vesicle lumen. (d) Composite image of septin hexamers imaged at 488 nm (magenta) encapsulated at 300 nM in DOPC GUVs imaged in brightfield (greys). In some cases, septin formed bright, micrometer-sized structures (white arrows) at this concentration in DOPC vesicles.

tion of micrometer-sized bright septin structures, likely corresponding to septin bundles [186, 255, 370].

The possibility to encapsulate polymerized or polymerizing proteins with eDICE opens up new opportunities for synthetic cell reconstitution experiments. One important goal in this research field is to achieve synthetic cell division[92, 95], which requires control over the shape of the synthetic cell (see chapter 2). Following the mechanisms

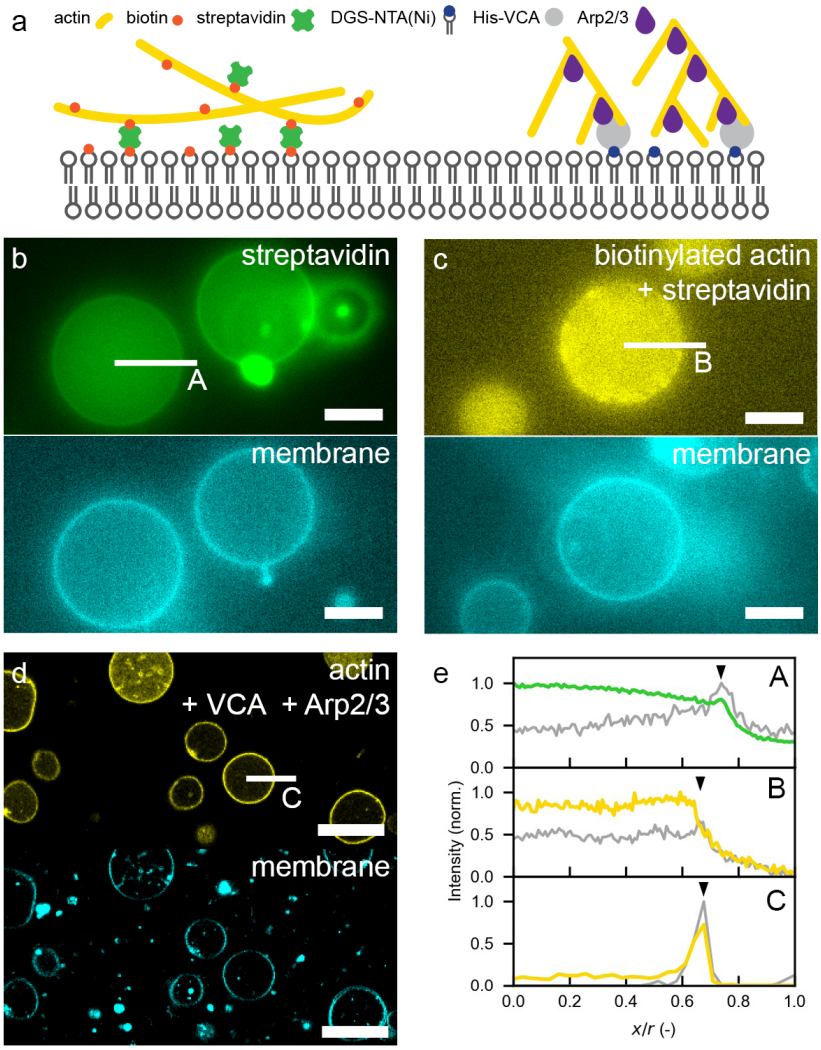
a
actin
biotin
streptavidin
DGS-NTA(Ni)
His-VCA
Arp2/3
b
streptavidin
A
membrane
c
biotinylated actin
+ streptavidin
B
membrane
d
actin
+ VCA + Arp2/3
C
membrane
e
A
B
C
Intensity (norm.)
1.0
0.5
0.0
0.0
0.2
0.4
0.6
0.8
1.0
x/r (-)

that animal cells employ for cell division, a cytoskeletal cortex bound to the membrane could be used for shape control. With the encapsulation of filamentous structural proteins such as actin and septin, we are one step closer to the reconstitution of such a cortex. Yet another important aspect is the ability to mechanically link these cytoskeletal proteins to the membrane. Using eDICE, we explored the potential of various membrane anchoring systems.

In current research endeavours to build minimal actin cortices, actin filaments are typically anchored to the membrane either via biotin-streptavidin binding[113, 177, 237], or by membrane localization of the actin nucleating factors VCA and Arp2/3[108, 153]. We show that eDICE is capable of reconstitution of both systems. By including 2.5% (mol/mol) biotinylated lipids in the membrane, encapsulated streptavidin clearly localized at the membrane (fig. 4.11b, e). As a next step in the formation of an artificial cortex, we co-encapsulated filamentous actin with 1% (mol/mol) biotinylated actin monomers. These filaments were encapsulated successfully and localized at the streptavidin-decorated membrane (fig. 4.11, c, e). Even though biotin-avidin linking is not the most physiologically relevant mechanism to study (see chapter 2), an important advantage of this system is that anchoring can easily be controlled by varying linker density[177].

A more physiological approach to the assembly of an actin cortex inside GUVs is by use of the actin nucleator Arp2/3, that is able to form branched actin networks at the cell membrane[371]. In this approach, actin nucleation is typically restricted to the membrane by addition of the His-tagged VCA domain of the Wiskott-Aldrich Syndrome protein (N-WASP) and incorporation of DGS-NTA(Ni) lipids in the membrane[108]. VCA binds to the nickelated lipids in the membrane, recruits Arp2/3, which in turn gives rise to the formation of a membrane-bound cortex. Using eDICE, we were able to encapsulate all the required components and to produce GUVs with a clear membrane-nucleated actin cortex (fig. 4.11d, e). Non-spherical GUVs with an a nucleated cortex showed no visible membrane fluctuations, suggesting enhanced stiffness imposed by the cortical actin.

Figure 4.11 *(preceding page)*: **Building an actin cortex with eDICE.** eDICE is compatible with the classical strategies to create minimal actin cortices. All images are epifluorescence images. (a) Schematic representation of two cortex formation methods: biotin-streptavidin mediated membrane binding of pre-formed actin filaments (left) and nucleation of a branched actin cortex with Arp2/3 and membrane-bound His-VCA (right). (b) DOPC GUVs (cyan) doped with 2.5% (mol/mol) biotin-PE encapsulating 88 nM streptavidin-AlexaFluor488 (green) in F-buffer. Streptavidin signal localizes at the membrane. Scale bar is 5 µm. (c) DOPC GUVs (cyan) doped with 2.5% (mol/mol) biotin-PE encapsulating 88 nM streptavidin and 4.4μM F-actin (yellow) in F-buffer. Actin filaments contained 1% biotinylated monomers and 10% AlexaFluor488-labelled monomers which resulted in membrane colocalization. Scale bar is 10 µm. (d) Epifluorescence images of actin (yellow) encapsulated at a nominal concentration of 8μM with Arp2/3 and His-tagged VCA in DOPC GUVs containing 2.5% (mol/mol) nickelated lipids. Actin signal is clearly enhanced at the membrane, indicating successful nucleation of filaments on the membrane. Deformed vesicles with a cortex were stiff, showing no observable membrane fluctuations. Scale bar is 20 µm. (e) Line intensity profiles for the GUVs annotated in panel a, b and c. Panels from top to bottom: streptavidin only, streptavidin and biotinylated F-actin, VCA/Arp2/3 nucleated-actin. The x-axis represents the relative distance to the GUV centre normalized to unity, the y-axis signifies the signal normalized to unity. Membrane signal is shown in grey, streptavidin in green, and actin in yellow. The membrane positions are indicated with black arrowheads. Note that aqueous dyes that do not localize, when encapsulated in a spherical compartment, would show a spherical cap-like intensity profile when imaged in epifluorescence mode.

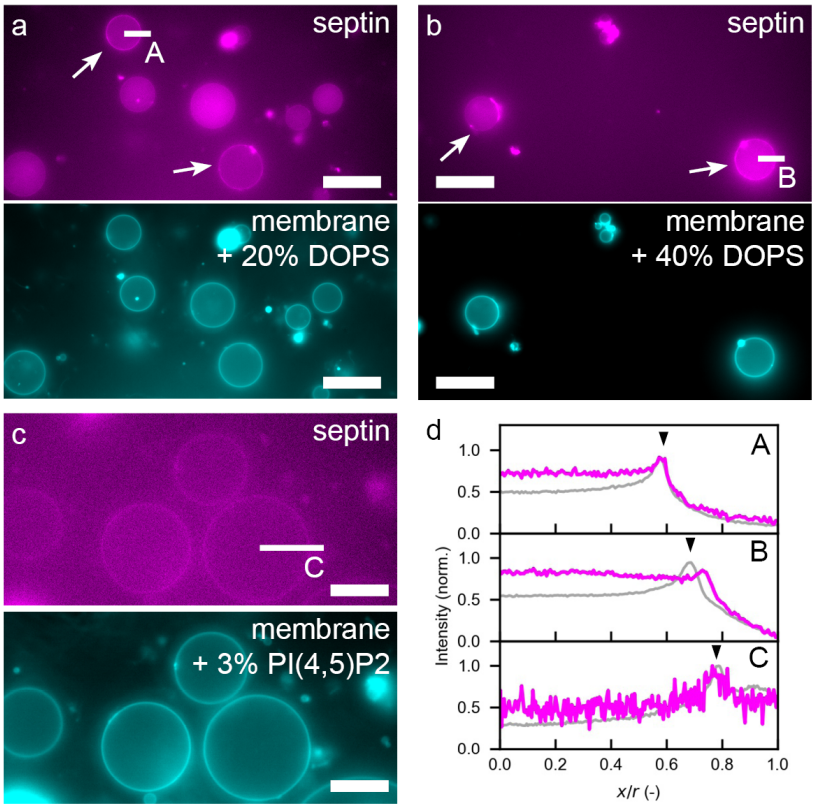

Figure 4.12: **Building septin cortices with eDICE.** eDICE can be employed to create GUVs with membrane-bound encapsulated septin. All images are epifluorescence images. (a) 300 nM septin hexamers (magenta) encapsulated in DOPC GUVs containing 20% DOPS. In the presence of DOPS lipids, septin signal localizes at the GUV membrane (indicated with arrows). Scale bar is 20 µm. (b) 300 nM septin hexamers (magenta) encapsulated in DOPC GUVs containing 40 % DOPS. Septin localization appeared to be stronger as compared to 20% DOPS, but the production yield was lower. Scale bar is 20 µm. (c) 300 nM septin hexamers (magenta) encapsulated in DOPC GUVs containing 3% PIP_2. Septin recruitment to the vesicle membrane shows that PIP_2 lipids are successfully incorporated in the GUV membrane. (d) Line intensity profiles for the GUVs annotated with white horizontal bars in panel a, b and c. Panels from top to bottom: 20% DOPS, 40% DOPS, and 3% $PI(4,5)P_2$. The x-axis represents the relative distance to the GUV centre normalized to unity, the y-axis signifies the signal normalized to unity. Membrane signal is shown in grey, septin in magenta. The membrane positions are indicated with black arrowheads. Note that aqueous dyes homogeneously distributed in a spherical compartment would show a spherical cap-like intensity profile when imaged in epifluorescence mode.

Next, we explored if charged lipids could be incorporated in the membrane using eDICE, and if we could use electrostatic interactions to anchor proteins. As septin is able to bind DOPS lipids [255], we encapsulated septin hexamers in DOPC vesicles doped with 20% DOPS and 40% DOPS (mol/mol). Addition of DOPS lipids indeed shifted septin localisation to the membrane (fig. 4.12a, b, d) as compared to its presence in the lumen in absence of DOPS (see fig. 4.10c). In addition, we tested if PIP_2 could be successfully incorporated in the membrane. PIP_2 is a signalling lipid involved in many intra-

cellular interactions, among which spatially defining the division mid-plane[265, 372, 373]. However, it is challenging to incorporate in membranes because of its high water solubility[374]. Addition of 3% (mol/mol) PI(4,5)P_2 resulted in recruitment of septin to the membrane, suggesting that eDICE can be employed to incorporate PIP_2 lipids in GUV membranes (fig. 4.12c, d) which is in line with results by Kelley et al.[375]. Possibly, the lipid dispersion strategy plays a role in the incorporation of PIP_2. Since lipids are dispersed as aggregates, their recruitment to the interface is governed by the adsorption of the aggregate rather than the solubility of the individual lipids[304]. This might improve the incorporation of PIP_2 in lipid monolayers. However, spontaneous desorption after bilayer formation still presents a problem [376].

Altogether, the combination of fast encapsulation, high vesicle yields, versatility of the method and robustness of the protocol, while being fairly easy to execute, make eDICE a powerful method in the realm of GUV reconstitution experiments.

4

ACTIN CHANGES LIPID ADSORPTION DYNAMICS

While eventually we developed robust protocols capable of protein encapsulation in GUVs, we were surprised by the sensitivity of many emulsion-based GUV formation techniques towards changing the content of the aqueous solutions. For example, vesicle production by the inverse emulsion method was strongly impeded when we added actin to the IAS, or when we encapsulated F-buffer instead of G-buffer. Likewise, in the process of developing a robust cDICE protocol, we noticed that vesicle production was sensitive to the presence of actin, ions and Tris-HCl in the aqueous solutions.

To acquire a better understanding of the effect of solutes on vesicle formation, we set up a pendant drop tensiometry experiment that allowed us to study lipid adsorption to water-oil interfaces. With this experiment, we could isolate the lipid monolayer formation step from the more complex process of GUV assembly. The formation of lipid monolayers is crucial to all emulsion-based GUV formation methods, for the assembly of both the inner and outer leaflet of the lipid bilayer. Studying this process in a controlled environment can help us to develop a more general understanding of emulsion-based GUV formation.

In the classical pendant drop experiment, a water droplet is dispensed from a needle positioned upside down, leaving the droplet hanging in air from the tip of the needle, thus creating a pendant droplet[297]. As the droplet hangs, the shape of the droplet is governed by an interplay between gravitational forces pulling the droplet down, deforming it into a pear-like shape, and surface tension forcing the droplet in spherical shape. A camera is placed perpendicular to the hanging drop to record the silhouette of the droplet. Using contour detection followed by fitting with the Young-Laplace equation, the surface tension is derived. In our experiments, we created a droplet of IAS, and we substituted the air by a cuvette filled with LOS. In this way, we measure not the surface tension of the droplet, but instead the interfacial tension of the water-oil interface. Over time, lipids from the LOS adsorb, which decreases the interfacial tension, in turn leading to an increasing pear-like shape of the droplet (see fig. 4.13a and fig. 4.13c).

In chapter 3, we have shown how the oil composition and preparation of the lipid-in-oil solution have a drastic effect on lipid adsorption kinetics. Here, we discuss how the composition of the aqueous solutions and the lipid composition affects lipid adsorption

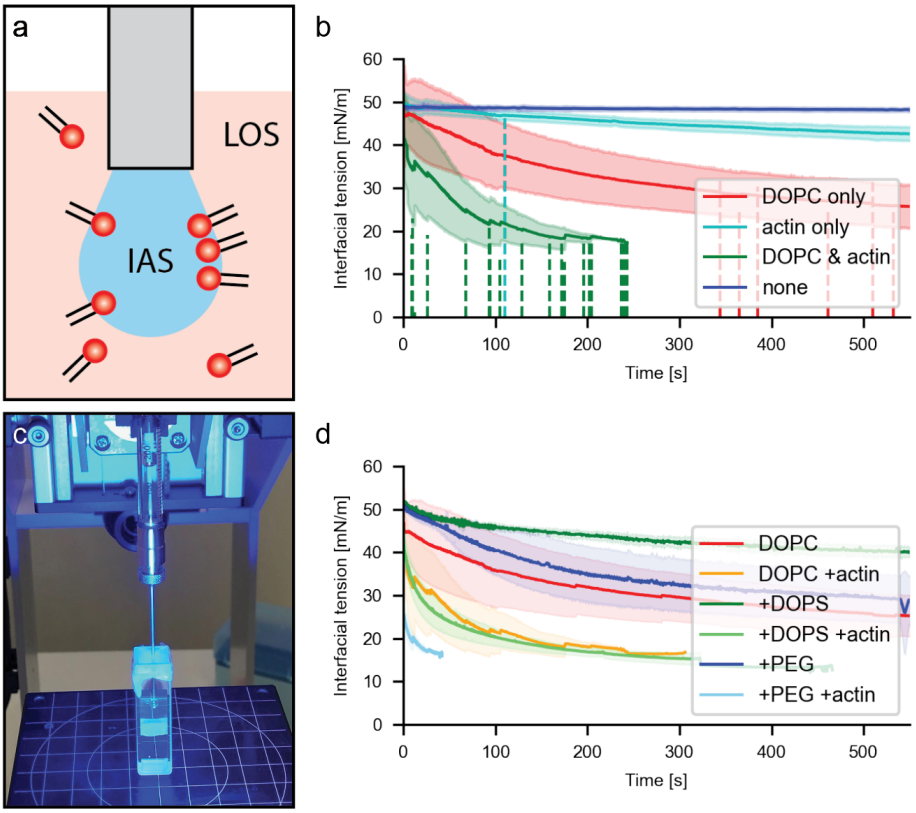

Figure 4.13: **Interfacial adsorption of lipids in absence and presence of actin.** (a) Schematic overview of the pendant drop experiment. A droplet of IAS is dispersed in LOS. Over time, lipids from the LOS adsorb to the water-oil interface. (b) Evolution of interfacial tension of a water-oil interface formed between an IAS composed of G-buffer and optiprep (18.5% v/v) in absence and presence of 4.4μM actin, and a chlorofom-based LOS with and without 0.2 mg/mL DOPC. Without actin, but with 0.2mg/mL DOPC only (red line, n=21), with 4μM G-actin only and without DOPC (cyan line, n=6), with both DOPC and G-actin (green line, n=19), and without lipids or actin (blue line, n=2). Each curve represents the average over n measurements with the shaded region being the standard deviation. (c) Photograph of the tensiometry experiment. A syringe with needle containing IAS is mounted vertically with the needle pointing downwards. The needle is inserted in a cuvette containing LOS. The cuvette is closed on top using parafilm. In the final experiment, a magnetic stirrer is placed underneath the cuvette. The droplet is illuminated from the viewer's side, and a camera is positioned behind the droplet to capture the silhouette. (d) Interfacial tension evolution with and without actin using different lipid compositions. Each curve represents the average over n measurements with the shaded region being the standard deviation. Only DOPC against IAS without (red line, n=21) and with (orange line, n=19) actin, DOPC with 20% DOPS against IAS without (dark green line, n=2) and with (light green line, n=3) actin, and finally DOPC with 5% PEG 2000 DOPE measured against IAS without (dark blue line, n=3) and with 0.4μM actin (light blue line, n=3).

behaviour. In fig. 4.13b, we show the average adsorption curve for DOPC lipids dispersed with chloroform in a 1:4 mineral oil:silicone oil (v/v) at a total lipid concentration of 0.2 mg/mL against an IAS composed of G-buffer and an additional 18.5% optiprep (red line),

thus mimicking solutions typically used in cDICE and eDICE experiments. Remarkably, when 4.4μM of actin was added to the IAS, the interfacial tension decreased substantially faster (green line). In addition, many droplets fell from the needle before the end of the experiment (indicated with dashed lines). Interestingly, this effect was similar for monomeric G-actin (in G-buffer) and filamentous F-actin (in F-buffer) (see fig. 4.17a). None of the solutes had an effect as drastic as actin (see fig. 4.17b). We then asked ourselves if actin by itself is surface-active, thereby speeding up interfacial stabilization. To answer this, we measured the interfacial tension development of IAS containing actin against an LOS that did not contain any lipids (cyan line). In this case, it turned out that actin only minimally affected interfacial tension compared to an experiment where actin nor lipids were included (blue). Furthermore, stabilization by actin alone occurred much slower than by actin combined with DOPC. These results together implicate that the rapid interfacial tension decrease in a system containing both actin and DOPC cannot be explained by the mere sum of the two components.

Given that the presence of actin in the IAS has such a strong effect on interfacial adsorption of lipids, this could affect the formation of lipid monolayers and bilayers in GUV formation experiments. To counteract this undesired effect, we investigated if actin could be repelled from the interface by electrostatic or by steric repulsion. Since actin is slightly negatively charged in solution, we added 20% (mol/mol) negatively charged DOPS lipids to the lipid mixture while keeping the total concentration of lipids constant. We measured the interfacial tension development with DOPS both with and without actin (fig. 4.13d, dark green and light green line, respectively). Compared to adsorption kinetics in absence of DOPS (fig. 4.13d, red and orange line), we did not see a substantial repulsion effect: both lipid compositions showed a similar increase in adsorption kinetics upon addition of actin. Also steric repulsion of actin by addition of 5% PEG-ylated lipids did not prevent actin from speeding up interfacial adsorption (fig. 4.13d, dark blue and light blue line); if anything, interfacial tension decreased even faster in presence of PEG-ylated lipids when actin was added, as compared to a sample without PEG-ylated lipids. Both strategies did thus not prove to be successful in preventing actin from changing lipid adsorption dynamics.

4.3. DISCUSSION

The number of GUV formation methods in the literature is large and still increasing. In addition, for each formation methods, the available experimental protocols keep diverging. We tested a selection of GUV formation techniques for their applicability to build a synthetic cell with an actin cortex, requiring encapsulation of proteins and physiological buffers while producing membranes of diverse lipid compositions. Swelling methods were easiest to set up, requiring only simple experimental equipment and minimal training of the experimentalist. In general, the total amount of lipids required to perform swelling assays (10 µg for gel-assisted swelling) is much smaller than what is needed for emulsion methods (2 mg for eDICE), which is of special importance when working with precious substances. In addition, we experienced that GUV samples produced with swelling methods generally showed a smaller day-to-day variability than GUVs produced with emulsion-based techniques. The influence of environmental conditions on cDICE vesicle production was already discussed in chapter 3. In table 4.1, we summarize

our experience with the four swelling-based methods that we tested: electroformation (EF) [74], gel swelling (GSW) [76, 285], spontaneous swelling (SSW) and paper swelling (PSW) [353].

	Electroformation	**Gel swelling**	**Spontaneous swelling**	**Paper swelling**
Publications	>500	>100	>100	less than 5
Recommended literature	[339, 340, 377, 378]	[76, 364, 379]	[355, 380]	[351, 353]
Difficulty	mediocre	easy	easy	easy
Implementation	2 months	2 weeks	1 week	2 weeks
Training[1]	2 months	1 month	2 weeks	2 weeks
Protocol optimization	for each condition	once	once	once
Production yield (est. no. GUVs)	>1000	>1000	>100	<100
Formation time	2-20 hours	1 hour	overnight	1 hour
Size (est.)	5-100 µm	5-100 µm	up to 20 µm	up to 20 µm
Lamellarity (est.)[2]	all unilamellar	mostly unilamellar	polydisperse	not reported
Membrane cleanliness	clean[365], oxidation possible[283, 381]	possibly polymer residues[3] [350, 365]	probably clean	probably clean
Physiological buffers	requires optimization	yes	N.A.	N.A.
Charged membranes	requires optimization	yes	yes	N.A.
E. coli membranes	no	yes	yes	probably
Archaeal membranes	no	yes	probably	probably

Table 4.1: **Comparison of swelling methods.** Summary of our experiences with swelling-based GUV formation methods.

[1] Time until a new user produces results at the state-of-the-art level.
[2] Estimated based on membrane fluorescence.
[3] Note that we measured similar stretch moduli for GUVs produced by GSW and EF, see chapter 6.

While these methods are typically being evaluated based on the characteristics of the vesicles they produce, we found their user-friendliness and accessibility an equally important criterium for guiding new users which method to use. In fact, we found big differences between methods to lie in their robustness towards changing experimental conditions, including buffer composition, buffer ionic strength, and membrane lipid composition. With GSW, it was particularly easy to vary both membrane composition, including charged lipids, and the ionic strength of the buffer. Versatility of GSW with minimal adjustments of formation parameters is also demonstrated in literature [61, 76, 109].

On the contrary, in EF, changing the fraction of charged lipids or the ionic strength of the buffer always required additional tweaking of the formation protocol. While there is a body of literature showing that electroformation of GUVs can be performed in a wide range of conditions[340, 354, 355], it was generally difficult to translate published protocols to our experimental systems. This was mainly caused by divergence of protocols: lipid deposition methods and electrical field parameters[340] (reviewed in ref. [355]) vary widely across publications. A time-intensive protocol optimization was therefore necessary whenever we tried to produce GUVs with a different lipid composition or in a different buffer. SSW and PSW were in this project not tested for a wider range of membrane and buffer compositions, but we expect them to be robust since both methods are based on non-specific osmotic effects.

Other considerations when selecting a GUV formation method are GUV size, sample polydispersity, membrane cleanliness and membrane lamellarity (see table 4.1). Lamellarity was only qualitatively assessed in our study based on membrane fluorescence, but was also shown quantitatively in ref. [382] to depend on formation method. In agreement with ref. [382], we noted that SSW vesicles showed most variation. A general concern with GUV formation is membrane cleanliness. For GSW, it is known that residual polymers from the swelling gel can end up in GUVs or their membranes [350] and that this can lead to altered membrane properties such as fluidity, permeability and mechanics [365, 383]. Note that polymer contamination of the membrane depends on the polymer physicochemical properties [76, 350] as well as on the degree and nature of crosslinking [286]. PVA-based swelling was found to lead to cleaner membranes as compared to agarose swelling [76, 350]. While Dao et al. reported the stretch modulus of PVA swollen GUVs to be lower than for electroformed vesicles [365], we found the bending rigidity of vesicles produced with both techniques to be similar (see chapter 6). From this we learn that it is important to assess the extent of membrane contamination for the specific GSW protocol that is used for GUV formation, but also that membrane contamination does not necessarily affect the membrane property of interest. Novel gel-assisted swelling techniques involving cross-linked hydrogels [286] or using other polymers [382] provide promising routes to make clean membranes with a robust method. Other swelling methods on porous solid substrates, next to tracing paper[353], involving for example textile [351], are interesting candidates for the future. However, these techniques are young, meaning that the formation parameter space is still relatively undiscovered, and their potential and accessibility have yet to be proven. SSW provides the cleanest membranes, the properties of which have been compared to other swelling techniques (reviewed in [355]) as well as to emulsion-based GUV formation [384]. While electroformed membranes are typically also considered clean membranes, one should be careful to avoid lipid oxidation [283, 381].

A crucial limitation of all swelling techniques is that there is minimal control over the encapsulation of content. While swelling approaches have been used in the past to encapsulate proteins[109, 311, 385] and other macromolecules[386, 387], this comes with significant disadvantages. First, vesicles show wide distributions of encapsulation efficiency[386, 387]. Especially for reconstitution with multiple components, encapsulation has to be done in the correct stoichiometric ratios. Second, the inner solution is identical to the outer solution, meaning that any protein or other molecule interact-

ing with the membrane inner leaflet, also interacts from the outside. To get rid of non-encapsulated material, vesicles can be washed during formation [388] or afterwards in a microfluidic channel [389, 390], but in both cases this presents an extra experimental challenge. Bound molecules could be removed with proteolytic enzymes, or might not be possible to remove at all.

Emulsion-based techniques are more suitable for encapsulation. An inner aqueous solution with the components of interest can be prepared separately from the outer solution. To accommodate the increasing interest in GUVs and encapsulation, the number of different emulsion-based GUV formation techniques has exploded, ranging from bulk to microfluidic methods [16]. While many of these techniques have been demonstrated to be capable of encapsulation of cargo, they are substantially different. Dependent on the application in mind, the right technique should be chosen carefully. Here, we summarize our findings on a number of emulsion-based GUV formation techniques in the light of reconstitution of cytoskeletal networks, in particular actin (see table 4.2). We compared Inverse Emulsion (IE) [75], OLA microfluidics[77], cDICE [3] and a modified version of cDICE that we invented, called eDICE.

Encapsulation of actin was not trivial with any of the methods. Robust and reproducible production of GUVs encapsulating monomeric actin was only achieved with cDICE and eDICE. While we have established a robust IE protocol for successful formation of GUVs in sugar solutions and G-buffer (no actin), vesicle yields dropped tremendously when we tried to encapsulate G-actin in G-buffer with the same protocol. Note that G-actin has been encapsulated by other groups using IE [108, 391]. With OLA we did manage to encapsulate G-actin with minimal modifications with respect to the original protocol [77]. However, success rates of OLA experiments were in our hands so low, that it was not feasible to continue down this line. In addition, OLA microfluidics is a time intensive experiment because of the time involved in chip fabrication, pretreatment and handling. This makes troubleshooting also time-intensive. Next to OLA, also cDICE proved to be well capable of encapsulating G-actin as reported by several other groups [110–113, 178, 294, 359, 375], albeit with a significant troubleshooting effort as reported in chapter 3. During the process of method optimization, we often noticed that GUV yields were substantially lower in presence of actin as compared to similar conditions without actin. We found the preparation of the lipid-in-oil phase, and in particular the low-humidity environment and the organic solvent used for lipid dispersion, to be the crucial determinants for successful GUV formation and actin encapsulation. Compared to OLA, cDICE is faster and simpler, meaning that once the method is established, multiple cDICE experiments can be prepared, executed, and imaged on a single day. Nonetheless, even with cDICE, encapsulation of filamentous proteins was cumbersome. Addition of prepolymerized and phalloidin-stabilized actin filaments to the IAS often resulted in clogging of the injection capillary and leakage of the IAS from the supply tube. Moreover, we noticed that the time between preparation of the IAS and GUV formation was often too long, resulting in premature polymerization of filaments. These issues were both solved with the eDICE method that we invented. By quickly emulsifying the IAS in LOD and directly adding it to the spinning chambers, GUVs could be formed within minutes without the use of a capillary. Besides actin filaments, we also

encapsulated septins, which appeared to form bundles inside GUVs.

It is interesting to note that the eDICE method, which in our hands turned out to be by far the most successful for cytoskeletal encapsulation, is in fact very similar to IE. In both methods, droplets of the IAS are dispersed in LOD by pipetting to produce a bulk w/o emulsion. Crucial differences may lie in the composition and preparation of the lipid-oil dispersion, as well as in the geometry of the system. The LOD was optimized for cDICE based on lipid adsorption behaviour (see chapter 3) and finally constituted a metastable complex mix of dispersed lipid aggregates[304]. We have not tested this LOD in the inverse emulsion protocol. Furthermore, the larger OAS-LOD interface provided by the spinning disk geometry allows many IAS droplets to traverse through the interface simultaneously without colliding.

Since we found actin to interfere with GUV formation both in IE and while optimizing cDICE, we set out to test if actin interfered with lipid monolayer formation. Proteins are known to be surface active compounds[392], a property widely exploited in food physics for the formation of foams and emulsions [393]. Their surface activity is dependent on their thermodynamic stability, flexibility, amphipathicity, molecular size and charge [394]. Moreover, many proteins show strong lateral interactions at the interface and unfold irreversibly upon adsorption [395]. To test if also actin is surface active, we monitored its adsorption to the IAS-LOD interface by pendant drop tensiometry. Actin on itself, in absence of lipids, was found to be only mildly surface-active, adsorbing much slower than lipids. However, when both actin and lipids were present, adsorption rates were drastically, also compared to lipids alone (fig. 4.13). We observed this behaviour both with F-actin in F-buffer, and G-actin in G-buffer (fig. 4.17a) which has previously been found to be less surface-active than F-actin [396].

The radical change in adsorption dynamics, which only occurs when both actin and lipids are present, points to a synergistic effect. Previous studies have indeed demonstrated interactions of actin with lipids. First, we have shown that electrostatic interactions can cause either F-actin adhesion or repulsion to a bilayer membrane depending on the lipid and buffer composition [258]. Moreover, in experiments with pre-formed lipid monolayers, actin was found to intercalate between phospholipids, an effect mediated by electrostatic interactions [397, 398]. Nonetheless, in our pendant drop assays, the adsorption behaviour did not qualitatively change upon addition of 20% of negatively charged DOPS lipids (fig. 4.13). As an alternative to electrostatic repulsion, we tested if actin could be repelled from the interface by inclusion of 5% PEG 2000 DOPE lipids, which has previously been shown to sterically hinder protein adsorption to lipid monolayers [399]. However, also steric repulsion did not lead to a change in adsorption. How can our adsorption results be different from previously published reports? A major difference is that in our study, we look at the effect of actin adsorption during instead of after lipid monolayer formation. Therefore actin does not only interact with lipid head groups, but also with lipid tails and the water-oil interface, thereby potentially disturbing the formation of monolayers. In addition, the lipid-oil dispersions used for cDICE, eDICE and tensiometry measurements were highly unstable (see chapter 3), making it complicated to disentangle effects of actin adsorption from LOD instability. To acquire a better understanding of the synergistic adsorption effect, future studies should test if the effect is specific for actin or generic for proteins. In addition, effects of protein

polymerization should be mapped. Actin accumulation at the interface could induce polymerization[400], which in turn can affect interfacial properties[398].

Even after optimization of the cDICE technique for actin encapsulation, the produced GUVs still showed a variation in encapsulated content for reasons we do not understand. While encapsulation efficiency has been characterized for swelling methods [386, 387], the physicochemical parameters influencing encapsulation in emulsion-based methods have not been established yet. In chapter 3, we demonstrated that variability in encapsulation could be reduced by a judicious choice of the lipid dispersion method in the LOD (using decane instead of chloroform) and by inclusion of a small fraction of PEG-ylated lipids. While addition of PEG-ylated lipids did not qualitatively change the combined lipid adsorption behaviour in presence of actin as measured by tensiometry (see above), it effectively narrowed down the distribution of encapsulated fluorescence (chapter 3). In addition, when actin was encapsulated, yields of GUVs produced with eDICE increased tremendously upon a small fraction of PEG-ylated lipids. This indicates a non-trivial relationship between lipid adsorption and encapsulation efficiency or may imply that monolayer formation is not the crucial step in preservation of encapsulated content. A possible source of variation could be the temporal opening of membrane pores during either the formation of GUVs or their travel through the OAS, which would lead to content transfer across the bilayer. Another source could be shear-induced splitting of GUVs after formation. When content is not homogeneously distributed throughout the GUV lumen, splitting would result in vesicles encapsulating different concentrations of solute as suggested by Stano et al. [401]. To test these ideas, it would be instructive to visualize droplets as they transfer from the oil phase to the OAS and to map the effect of shear forces, lipid composition and solute physicochemical properties on encapsulation.

We found an additional important selection criterium for emulsion-based GUV formation methods their day-to-day variability in produced samples. Especially with IE, we noticed that produced samples varied widely in terms of yield and presence of fluorescent structures (fig. 4.8). We experienced a similar day-to-day variability with cDICE before protocol optimization (see chapter 3). The extent to which conditions such as humidity and preparation of the lipid oil solution play a general role in emulsion-based vesicle formation has yet to be investigated. Thorough characterization of GUV formation methods and mapping their input parameters has gained attention only recently [175, 328, 340] and will be crucial to achieve reproducible GUV formation in future.

Altogether, we think that the most crucial aspects in the choice of emulsion-based GUV formation methods are their encapsulation potential, experimental difficulty and reproducibility. OLA microfluidics offer great potential for homogeneous encapsulation, but microfluidic techniques are in general demanding in terms of equipment, training, and time and have thus minimally been reproduced by other labs. The inverse emulsion method is easy to implement and conduct, but was in our hands not capable of robust actin encapsulation and showed a high day-to-day variability. cDICE provides a useful compromise, being able to encapsulate G-actin while being fairly simple. Compared to cDICE, eDICE is easier to execute, extends the encapsulation potential to filamentous proteins and time-sensitive systems, and reduced the amount of inner aqueous solution required. This makes eDICE an excellent candidate for cytoskeletal reconstitution.

	Inverse emulsion	**OLA microfluidics**	**cDICE**	**eDICE**
Publications	>50	<10	10-20	0
Recommended literature	[328]	[356, 357, 402]	[16, 175, 293]	This work
Difficulty	easy	difficult	mediocre	easy
Implementation	2 weeks	3 months	2 months	2 months
Training[1]	<1 month	3-8 months	1-2 months	1 month
Success rate	intermediate	low	high	high
Production yield (est. no. GUVs)	>100	>1000	>1000	>1000
Size (est.)	5-30 µm	5-30 µm	5-30 µm	5-30 µm
Size control	no	yes	no[2]	no
Lamellarity[3]	mostly unilamellar	unilamellar	mostly unilamellar	mostly unilamellar
Day-to-day variability	high	low	low after modifications[175]	low after modifications
Physiological buffers	problematic	yes	yes	yes
Encapsulation of monomeric proteins	problematic	yes	yes	yes
Encapsulation of filamentous proteins	problematic	likely problematic	no	yes

Table 4.2: **Comparison of emulsion methods.** Overview of our experiences with emulsion-based GUV formation methods.

[1] Time until a new user produces results at the state-of-the-art level.
[2] Unless small capillaries are used [3], the choice of which depends on what needs to be encapsulated.
[3] Estimated based on membrane fluorescence.

When size control and constant encapsulation efficiency are crucial, and time and budget is available, microfluidics might be considered.

We note that many GUV formation experiments in this chapter, both swelling and emulsion-based, have been performed at high sugar concentration. Presence of sugars can boost GUV formation by stabilizing membranes (fig. 4.6) and is required for inverse emulsion to establish a density gradient. However, high sugar concentrations can affect the biochemical properties of encapsulates. For example, we noticed that sugars and also optiprep influenced actin polymerization (data not shown). While Moga et al. [328] already showed for the inverse emulsion method that sugar can be replaced by polymers to create density differences, similar studies have yet to be conducted for other production methods to identify viable substitutes.

4.4. CONCLUSION

The number of different GUV formation techniques is large and still increasing, with tens of new protocols being published each year. The growing set of techniques allows for more and more versatility in GUV research, but it is becoming increasingly complex for researchers to identify which method suits their needs best. Several literature reviews have been written to guide researchers in choosing their methods [16, 355, 378]. Here, we presented an experimental review on a set of formation techniques based on our own experiences. This has the advantage that we evaluate methods not only on their theoretical potential, but also on pragmatism of their implementation and use.

We have evaluated a set of GUV formation techniques in the light of building a synthetic cell with an actin cortex. With GUV formation, it is important to note that there is not a one-size-fits-all method. Instead, the preferred method will strongly depend on the application of the study, required properties of the GUVs and content of the aqueous solution. As such, design parameters like lipid composition, membrane charge, buffer ionic strength, membrane cleanliness, encapsulation of solutes, and size monodispersity are crucial in choosing a formation method. While a production technique might on paper be compatible with these criteria, other, more pragmatic considerations are equally important. How much time will it take to implement the method? How much training does it take for someone to become sufficiently skilled with the method? Can one easily vary experimental conditions, for example membrane composition or buffer ionic strength, without having to go through a time-intensive protocol optimization each time?

We have compared four swelling-based techniques to produce GUVs with a wide range of membrane compositions and in different buffers. Gel-assisted swelling turned out to be the generally preferred method, as it requires only simple equipment, is easy to execute, and most importantly, allows for changing membrane composition, including charged lipid and complex lipid extracts from cells, and varying buffer ionic strength, without the need to modify the protocol. When membrane cleanliness is a must, electroformation and spontaneous swelling can be useful alternatives. However, electroformation requires time-intensive protocol optimization dependent on membrane charge and buffer ionic strength. Spontaneous swelling produces small (<20 µm diameter) liposomes that are polydisperse, showing many multilamellar and multivesicular vesicles. Swelling on solid porous substrates such as tracing paper might be a useful alternative

in the future to produce clean membranes in a facile manner, but is still a novel technique that needs to be re-established across labs.

In addition, we tested four emulsion-based GUV production methods for their ability to encapsulate a range of cytoskeletal proteins. Of those methods, we found cDICE to be well-capable of encapsulating monomeric actin while being fairly simple to execute. However, encapsulation of filamentous proteins remained difficult with cDICE. By modifying the original cDICE protocol, we managed to circumvent the use of a capillary for injection of the inner aqueous solution, which enabled us to encapsulate the filamentous proteins septin and actin. This new technique, which we called eDICE, is not only easier to use than cDICE, but also allows GUV formation to happen within minutes of preparation of the inner solution. Compared to eDICE and cDICE, producing GUVs by OLA microfluidics was significantly more demanding in terms of time and skills. While we demonstrated encapsulation of filamentous actin with OLA, we discontinued this method given a general low success rate in these experiments due to challenges in chip fabrication, pretreatment and operation. Lastly, we tested inverse emulsion experiments. This was the easiest method to implement and execute, but was prone to a high variability between experiments and was not suitable for encapsulation of actin, nor actin F-buffer.

Throughout this study, we found that emulsion-based GUV formation was sensitive to the composition of the aqueous solutions, in particular to the presence of actin. By using pendant drop tensiometry, we found that actin drastically changes the adsorption behaviour of lipids during their recruitment to the water-oil interface. This possibly implies that actin interferes with GUV formation by impacting the formation of the inner lipid monolayer. Future studies should point out if this effect is protein-specific and how it can be prevented.

GUV formation is an inevitable first step in any attempt to build an artificial cell, requiring one central technique that is compatible with encapsulation and functionality of all interconnected modules, which are nowadays usually developed independently. We identified two major hurdles that limit the field from converging to a single formation technique. First, our limited understanding of the physical mechanisms governing lipid monolayer and bilayer formation hinders reconstitution studies. Reliable encapsulation of solutes is currently challenging and time-consuming. For example, we found that the presence of actin influences lipid adsorption, showing us that the desired content of the GUV can effect the vesicle formation process itself. Future research should map the influence of solutes on bilayer formation, such that design parameters in GUV formation can be tweaked accordingly. Second, the field currently lacks characterization of methods and comparison between them. As such, it is difficult to assess a priori which of the large number of methods suits one's application best. To overcome this, transparency about formation methods should be improved. This starts with reporting properties of produced GUV samples on the population level, but extends to more practical aspects such as experiment success rate, difficulty and day-to-day variability. Note that we provide a software for accessible population-level quantitative characterization of GUV populations in chapter 5. Overcoming these two hurdles would greatly help researchers to efficiently select the best-fitting GUV production method for their research goal, thereby minimizing time-intensive troubleshooting and shifting the research focus

from GUV formation to their wide range of applications.

4.5. MATERIALS AND METHODS

4.5.1. CHEMICALS

Lipids. All of the following non-fluorescent lipids were obtained from Avanti: 1-palmitoyl-2-oleoyl-sn-glycero-3-phosphocholine (POPC), 1,2-dioleoyl-sn-glycero-3-phosphocholine (DOPC), 1,2-dioleoyl-sn-glycero-3-phospho-L-serine (DOPS), 1,2-dimyristoyl-sn-glycero-3-phosphocholine (DMPC), L-α-phosphatidylcholine (Egg, Chicken) (Egg PC), L-α-phosphatidylinositol-4,5-bisphosphate (Brain, Porcine) (PI(4,5)P_2), 1,2-distearoyl-sn-glycero-3-phosphoethanolamine-N-[methoxy-(polyethylene glycol)-2000] (PEG2000-DOPE), 1,2-dioleoyl-sn-glycero-3-phosphoethanolamine-N-(cap biotinyl), 1,2-dioleoyl-sn-glycero-3-phosphoethanolamine-N-(cap biotinyl) (biotin-DOPE) and 1,2-dioleoyl-sn-glycero-3-[(N-(5-amino-1-carboxypentyl)iminodiacetic acid)succinyl] (DGS-NTA(Ni)). Also fluorescent lipids DOPE-Cy5 and Rhodamine-DOPE were obtained from Avanti. Atto655-DOPE was obtained from ATTO-TEC GmbH, Germany. The *Escherichia coli* polar lipid extract was obtained from *E. coli* grown at 37 °C, and purchased from Avanti lipids. The Archaeal lipid extract from *Pyrococcus furiosus* was kindly given to us by the Arnold Driessen lab [403].

General chemicals and proteins. We obtained from Sigma-Aldrich all the following chemicals and proteins: sucrose, D-(+)-glucose, Tris(hydroxymethyl)aminomethane hydrochloride (Tris-HCl), imidazole, 8-Hydroxypyrene-1,3,6-trisulfonic acid trisodium salt (HPTS), chloroform (100-200 ppm amylenes as stabilizer, >99.5%), sodium chloride (KCl), calcium chloride ($CaCl_2$), magnesium chloride ($MgCl_2$), protocatechuic acid (PCA), protocatechuate dioxygenase (PCD), 6-hydroxy-2,5,7,8-tetramethylchromane-2-carboxylic acid (Trolox), dithiothreitol (DTT) and β-casein.

Method-specific chemicals. For inverse emulsion experiments, we used heavy mineral oil from Sigma Aldrich (product no. 330760). For cDICE and eDICE experiments, silicone oil (5 cSt), mineral oil (BioReagent) and chloroform (Uvasol) for preparation of the lipid-oil dispersion were obtained from Sigma-Aldrich, while *n*-decane (99+% pure) was purchased from Acros Organics. For OLA experiments, 1-octanol, glycerol and poloxamer 188 (P188) were obtained from Sigma-Aldrich. Polydimethylsiloxane (PDMS) for OLA chip fabrication was obtained from Dow Corning (Sylgard 184 silicone elastomer kit). We used two types of polyvinyl-alcohol (PVA) in this project: for surface treatment of OLA chips, we used a lower molecular weight of a lower hydrolysis rate (30-70 kDa MW, 87-90% hydrolyzed) obtained from Sigma-Aldrich, while for making gels for gel-assisted swelling, we used a higher molecular weight PVA (145 kDA, 98% hydrolysed, VWR, the Netherlands).

4.5.2. MICROSCOPY

All images shown in this chapter were taken using a Nikon Eclipse Ti microscope equipped with a spinning disk confocal module (X-Light, Crest), an LED light source for monochromatic illumination (wavelengths 395/25, 440/20, 470/24, 510/25, 550/15, 575/25, 640/30, Spectra X, Lumencor) and a digital camera (Orca-Flash 4.0, Hamamatsu). Microfluidic vesicle formation experiments were imaged with a 10x air objective (Plan Fluor, NA 0.3, Nikon), images of GUVs growing *in situ* during electroformation or gel-assisted swelling were taken with a 60x water immersion objective (CFI Plan Apochromat VS, NA 1.0, Nikon), and all other images were taken with a 100x oil immersion objective (CFI Plan Apochromat VC, NA 1.40, Nikon). Images of Arp2/3-nucleated cortices (fig. 4.11d) were acquired with a 63x glycerol immersion objective on a scanning confocal microscope (Leica Stellaris).

4.5.3. ELECTROFORMATION

Electroformation of GUVs was either done on platinum wires or on indium tin oxide (ITO) glass slides. ITO slides provide a larger surface for vesicle formation and thereby possibly a higher yield of produced GUVs. However, we found these chambers to be more fiddly, as they were only held together by vacuum grease (read below) which often resulted in leakage. In addition, platinum wires have been reported to work better for GUV formation in buffers with higher ionic strength (P. Bassereau, personal communication, 2020). We therefore compared both options for electroformation. For formation on platinum wires, we used both closed chambers and open chambers, which allowed *in situ* visualization of vesicle formation. All chambers used for electroformation are custom-made (fig. 4.14).

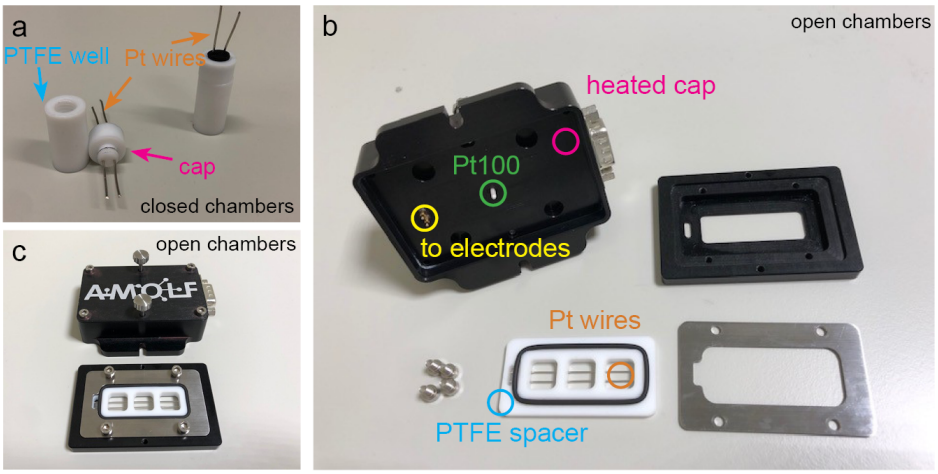

Figure 4.14: **Platinum-wired electroformation chambers used in this project.** (a) Closed electroformation chambers consisting of a PTFE well (blue) and cap (pink) including two platinum wires (orange). Wells are about 2 cm high and fit 100 μL. (b - c) Open electroformation chambers. (b) A teflon spacer (blue) was used to create three wells, each penetrated by two platinum wires. A voltage was applied via two electrodes (yellow) inserted in a cap (pink). Additionally, temperature in the electroformation chambers could be controlled via a Pt100 thermocouple (green) that was connected to an electrical heat resistance in the cap. The teflon spacer is approximately 7 x 3 cm (l x w) (c) Open electroformation chamber, bottom part assembled.

OPEN CHAMBER WITH PLATINUM WIRES

The open electroformation chamber was specifically designed for imaging GUV formation *in situ*. It consisted of a teflon (PTFE) spacer with three wells that could be used as electroformation chambers (see fig. 4.14). Two platinum wires (diameter 0.50 mm, Drijfhout, Amsterdam) ran through all three wells with 3 mm spacing between them. In addition, the open chamber had a built-in electrical resistance together with a Pt100 thermocouple for temperature controlled formation experiments. All parts were custom-made at the AMOLF mechanical workshop.

The open chamber was used as follows. Prior to use, the chamber was immersed in a beaker filled with 1% Hellmanex (Hellma Analytics, Müllheim, Germany) solution in milliQ water, which was placed in a sonicator bath and sonicated at room temperature for 15 minutes to remove any residual vacuum grease (see assembly below). This was followed by an additional sonication in milliQ water and then in ethanol (absolute grade). All sonication steps lasted 15 minutes. After blow-drying the electrodes with nitrogen gas, 5 µL of a lipid solution at 1 mg/mL in chloroform was

applied per chamber by spreading it over both electrodes using a 5 µL Hamilton syringe. Spreading of the lipid solution over the wire was found to be essential for GUV formation (fig. 4.3a). The electrodes were then dried for 30 minutes in a vacuum desiccator.

Next, the chambers could be assembled (see fig. 4.14b, c). We rinsed a glass slide (24x50 mm, no. 1, Menzel-Glaser) with water and ethanol and dried it with nitrogen gas. The slide was placed inside a metal holder that was designed to close and seal the open chamber, and to fit on the microscope stage. We then applied vacuum grease (Dow Corning, Midland, MI, USA) to the bottom of the teflon spacer around the well edges. The spacer was placed inside the metal holder and pressed firmly such that the grease formed a water-tight seal around the wells. A commercial rubber ring was placed around the chamber from the top for water-tight closure. Then, each well was gently filled with 300 µL of swelling solution, typically consisting of 200 mOsm sucrose in milliQ water (no buffer, pH 7). The chamber was then closed with the cap containing the temperature control units and electrical parts connecting to the electrodes. Bottom and top were firmly closed using four screws.

The chamber could then be placed on the microscope stage equipped with a 60x long working distance water immersion objective (2.0 mm working distance, Nikon). The electrodes were connected to a function generator (Rigol DG1032). When temperature control was used, we also connected the formation chamber to a custom-built temperature control box. We ran the formation experiments with the parameters as specified below. After formation, the chamber cap was unmounted. Vesicles were harvested by gently pipetting the solution around the electrodes up and down several times using a $1mL$ pipette tip. For these large pipette tips, we did not need to cut off the end. Vesicles were stored in the fridge and were typically used for further experiments within two days.

CLOSED CHAMBER WITH PLATINUM WIRES

While the open electroformation chamber was useful for monitoring vesicle growth and to tune the formation protocol, we mostly use the closed chambers once we had developed a successful protocol. The closed chambers were easier to assemble and prevented sample evaporation. Closed chambers were also custom-made, and consisted of a PTFE well and teflon cap with a rubber top for air-tight insertion of two platinum wires (0.5 mm diameter, Drijfhout, Amsterdam), 3 mm spaced apart (see fig. 4.14a).

The closed electroformation chambers were handled as follows. Chambers were cleaned by sonication for 15 minutes in milliQ water and then in ethanol (absolute grade) and dried with nitrogen gas. For each chamber, 5 µL of a 1 mg/mL lipid solution in chloroform was divided over both electrodes and carefully spread. After drying the lipids for 30 minutes in the vacuum desiccator, the bottom part of the electroformation chamber was filled with 100 µL of swelling solution, typically being 200 mOsm sucrose in milliQ water (no buffer) and the cap with electrodes was inserted. The electrodes were connected to the function generator and electroformation was performed using the field parameters specified below. After formation, we firmly tapped the chambers five times on a table to ensure GUV detachment from the wires.

ITO SLIDE

GUV formation on ITO slides was done as follows. We identified the conductive ITO side of two slides (25x75 mm, 30-60 Ohm, PSI supplies, West Chester, PA, USA) using a multimeter (15XL, Wavetek Meterman, Everett, WA, USA). Then, we cut two small pieces of copper tape to stick an electrical wire to the conductive side of each slide. We then spread 10 µL of lipid solution at a total lipid concentration of 1 mg/mL in chloroform over the ITO side of each slide using a 10 µL Hamilton syringe. Both slides were dried for 30 minutes in a vacuum desiccator. Afterwards, we applied vacuum grease to both sides of a U-shaped teflon spacer (20x20x3 mm (lxwxh), sawn out

of a sheet)) and formed a chamber by sticking it to the conductive side of both ITO slides. The chamber was filled with 300 µL swelling solution and placed with the open side facing up. After that, the slides were connected to the function generator using the electrical wires. Electroformation was executed using the field parameters specified below. When formation was finished, vesicles were harvested by gently pipetting the swelling solution up and down several times and then collecting the solution.

ELECTRIC FIELD PARAMETERS

Electric field parameters were chosen according to the swelling buffer used (see table 4.3) following [340, 354]. In general, for higher ionic strengths, the voltage and frequency were both increased according to previous reports [340, 354]. We confirmed the operation voltage by measuring the voltage directly on the wire using a multimeter, and adjusted it when necessary. We used the same parameters for electroformation on platinum wires and ITO slides. While the formation phase allows for swelling and growth of GUVs, a detachment phase characterized by a decrease in frequency was sometimes required to detach vesicles from the electrode. It should be noted that a detachment phase in some cases led to electric degradation of membranes, visible as the formation of a fuzzy, tubulated layer of membrane (see fig. 4.3f).

Table 4.3: **Field parameters used for electroformation.** Parameters below were successfully applied to produce neutral (DOPC and POPC) membranes. All waves have a sinusoidal waveform, with V_{pp} being the voltage (peak-to-peak) as measured with a multimeter.

Swelling solution	Formation phase	Detachment phase
200 mOsm sucrose in milliQ water (no buffer)	$2V_{pp}, 10Hz$ for 60 mins	$2V_{pp}, 1Hz$ for 15 mins
200 mOsm sucrose + 10 mM Tris-HCl at pH 7.4 in milliQ water	$2V_{pp}, 300Hz$ for 90 mins	None
100 mM NaCl in milliQ water (not buffered)	$2.5V_{pp}, 1000Hz$ for 4 hours	None

4.5.4. ZETA POTENTIAL MEASUREMENTS

We performed zeta potential measurements to measure the surface charge of vesicles made from the *E. coli* lipid extract. To this end, we first constructed a calibration curve using large unilamellar vesicles (LUVs) made of POPC lipids with varying molar fractions (0%, 5%, 15%, 20% and 40 %) of the negatively charged lipid DOPS. LUVs were made by transferring in total $1mg$ of lipids in chloroform in the desired ratio to 5 mL glass tubes (Pyrex). After drying the lipids in a vacuum desiccator overnight, we added $1mL$ of washing buffer ($100mM$ glucose, $100mM$ KCl and $10mM$ Tris-HCl buffered at pH 7.4) to yield a lipid mix at a total lipid concentration of $1mg/mL$. Addition of the washing buffer was done at $37°C$, which should be well above the lipid phase transition temperature (-17°C for pure DOPC[361], -11 °C for pure DOPS[361]), to ensure bilayers are fluid during hydration. We vortexed the tube for 1 minute, after which we extruded the LUVs 21 times through a polycarbonate membrane (Whatman) with a pore size of $100nm$ diameter using a commercial extruder (Avanti). Extrusion was done at room temperature for the POPC/DOPS LUVs, and at $37°C$ for the *E. coli* polar lipid extract LUVs. The extruded solution was diluted 10 times in washing buffer to yield an LUV suspension at a final lipid concentration of $0.1mg/mL$. We degassed this solution for 40 minutes in a vacuum desiccator to remove bubbles. Zeta potential measurements were carried out on a Zetasizer Nano ZS (Malvern Panalytical, Malvern, UK). 1 mL of LUV suspension was transferred to a special cuvette with two electrodes (DTS1070, Malvern Panalytical). During transfer, we made sure that no bubbles formed in the measurement cuvette

as bubbles can interfere with the electrophoresis measurement. The cuvette was then inserted in the machine and equilibrated to 21°C for all lipid samples measured. With each measurement cuvette, we ran three consecutive measurements, each consisting of 100 runs. For each condition, we produced one sample, which was transferred to two cuvettes for a total of six measurements per condition. Electrophoresis results were analysed with the Zetasizer software to finally yield the zeta potential.

4.5.5. GEL-ASSISTED SWELLING

For gel-swelling, we followed the protocol described by Weinberger et al. [76] with minor modifications. First a 5% (w/v) poly-vinyl alcohol (PVA, 145 kDa, 98% hydrolysed, VWR, the Netherlands) solution was prepared by adding the proper amount of PVA powder to a 200 mOsm sucrose solution in milliQ water (not buffered). The solution was then heated to 90°C on a hot plate while stirring continuously to dissolve the PVA powder. After a couple of hours, the solution was cooled down to room temperature. The solution was then filtered with a 200 nm filter (sterile, VWR, Amsterdam, the Netherlands) to remove any undissolved polymer. The resulting PVA solution could be used for months when stored in the fridge. To prepare a gel for GUV swelling, a 24x24 mm coverslip (no. 1, Menzel-Glaser) was first rinsed sequentially with ethanol, distilled water and ethanol and then blow-dried with nitrogen gas. The slide was then cleaned with a plasma cleaner (Plasma Prep III, SPI supplies, West Chester, PA, USA) for 30 seconds to ensure gel adhesion to the glass substrate. Then, 100 µL of PVA solution at room temperature was applied to the coverslip and spread by tilting the glass. Excess solution was removed with a tissue to minimize gel thickness. The slide was then baked for 30 minutes at 50°C, yielding a gel that was visibly solid. Then, 10 µL of lipid solution at 1 mg/mL in chloroform was spread on top of the gel with a glass syringe (Hamilton) and dried for 1 hour in a vacuum desiccator to remove any organic solvent. Afterwards, the coverslip was placed in a compartmentalised petri dish (4 compartments, VWR). 300 µL of swelling solution containing 200 mOsm sucrose and 10 mM Tris-HCl at pH 7.4 was carefully added on top of the gel. After swelling for 1 hour, vesicles were harvested by tilting the petri dish, pipetting up the swelling solution, flushing it once over the gel to promote vesicle detachment, and then collecting it. Vesicles were stored in the fridge for a maximum of two days.

4.5.6. SPONTANEOUS SWELLING

For spontaneous swelling of GUVs [73, 404], we followed the protocol in ref. [380] with minor adaptations. From a slab of teflon with a thickness of 2 mm, we cut several circular disks with a diameter of around 20 mm. These teflon disks served as supports for swelling of the lipid film. Then, we spread 10 µL of a lipid solution at a total concentration of 1 mg/mL lipids over a disk. Lipids were dried on the disk by first carefully flushing with nitrogen gas, and then transferred the disk to a 20 mL glass vial (VWR) that was placed open in a vacuum desiccator for 30 minutes. We carefully added 1 mL of swelling solution, typically consisting of 200 mOsm sucrose and 10 mM Tris-HCl at pH 7.4, to the vial without perturbing the lipid film. The vial was left overnight at room temperature to allow spontaneous swelling of the lipid film. GUVs were harvested the next day by gently pipetting the solution up and down and then collecting it. For the spontaneous swelling of GUVs from the *E. coli* polar lipid extract, lipids were dried in an oven at 50°C for 1 hour, and swelling was done at 37°C overnight.

4.5.7. SWELLING ON TRACING PAPER

For swelling on tracing paper, we followed the protocol in [353]. In short, we cut a piece of 1x1 cm of commercial tracing paper (Schoellershammer, Düren, Germany). The paper was cleaned by sequential rinsing with ethanol, water and ethanol, and then blow-dried with nitrogen gas. Then,

10 µL of a lipid solution at a total lipid concentration of 1 mg/mL was spread over one side of the paper using a Hamilton syringe. The lipids were dried in a vacuum desiccator for 30 minutes, after which we rolled up the paper with the lipid-coated side facing inwards and put it in an 1.5 mL Eppendorf tube. We added 1 mL of swelling solution, consisting of 200 mOsm sucrose and 10 mM Tris at pH 7.4. After 30 minutes swelling time, we transported the swelling paper to an observation chamber where we imaged the produced vesicles on the paper. We also tried to harvest the vesicles by pipetting up the swelling solution around the paper, but this repeatedly resulted in a very low number of vesicles.

4.5.8. INVERSE EMULSION

We produced vesicles by inverse emulsion following the protocol in [75]. We prepared three solutions: an inner aqueous solution (IAS) containing sucrose, an outer aqueous solution (OAS) containing glucose, and a lipid-oil solution consisting of 0.5 mg/mL lipids dispersed in heavy mineral oil. For vesicle formation without salts in solution, the IAS consisted only of 190$mOsm$ sucrose. For HPTS encapsulation, this IAS was supplemented with 4.8mM HPTS. For the G-buffer encapsulation experiments, the IAS consisted of 190mM sucrose, 0.2mM $CaCl_2$ and 20mM imidazole buffered at pH 7.4. In all inverse emulsion experiments, we used as OAS a glucose solution that matched the osmolarity of the IAS with a maximum difference of 10$mOsm$. To make the lipid-in-oil solution, we first added 0.5 mg lipids in chloroform to a small brown glass vial (1.5 mL with screw thread and septum closure, VWR) with a typical membrane composition of 99.5% DOPC and 0.5% Rhodamine DOPE (mol/mol). We removed organic solvent by placing the vial in a vacuum desiccator for 30 minutes. Then, we added 1 mL heavy mineral oil and placed the vial in the oven for 30 minutes at 80°C to promote lipid dissolution.

To produce vesicles, we first placed 300 µL OAS in a 1.5 mL Eppendorf tube, and 40 µL of IAS in another 1.5 mL Eppendorf tube. On top of the OAS, we gently layered 150 µL of the warm lipid-oil phase to create a two-layer system. To create the emulsion, we added 300 µL of the same warm lipid-oil phase to the IAS, and we quickly pipetted up and down vigorously with a 1 mL pipette tip until a homogeneous, turbid emulsion was obtained. The emulsion was layered on top of the oil layer in the other Eppendorf tube, after which we immediately centrifuged the tube at 1000 g for 10 minutes to promote travel of the IAS droplets into the OAS. We made sure that the total time between taking the oil out of the oven and starting centrifugation was less than 2 minutes, as we noticed that a cooled lipid oil solution negatively impacted yields and membrane quality of produced vesicles. After centrifugation, the top oil layer was carefully removed using a 200 µL pipette. Finally, the vesicles were harvested from the bottom of the tube.

4.5.9. OLA MICROFLUIDICS

Microfluidic vesicle production was done following the octanol-assisted liposome assembly (OLA) protocol described in [77, 402] with minor adjustments. For GUV production and imaging, we used the microscope described in section 4.5.2 with the 10x air objective. The chip and fluid flows were visualized in brightfield, and fluorescently tagged lipids and actin in epifluorescence mode. To control microfluidic pressure, we used three Fluigent pumps (MFCS-EZ, one pump of pressure range 0-7000 mbar, and two pumps of pressure range 0-2000 mbar, Fluigent) and flexible tubing (Tygon Microbore Tubing, ID 0.51 mm and OD 1.52 mm).

In short, the OLA microfluidic chip works as follows. The chip contains three inlet channels for an inner aqueous solution (IA), lipid-octanol solution (LO) and outer aqueous solution (OA), and one outlet channel (fig. 4.15). The LO and OA inlet channels are bifurcated and meet together with the IA channel in a six-way junction. At this junction, a continuous stream of IA and LO solution is pinched off by the OA solution to produce double emulsion droplets of IA solution with a lipid-containing LO shell. As the double emulsion droplets flow further downstream, a lipid bilayer

forms around the IA droplet and an octanol pockets buds off, resulting in the formation of GUVs. These GUVs can either be visualized on-chip or extracted from the device via the outlet channel.

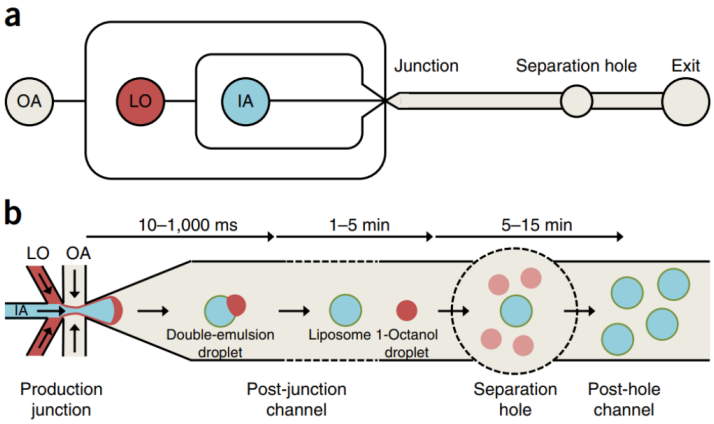

Figure 4.15: **Schematic overview of OLA microfluidics.** Image is copied from ref. [402]. (a) Schematic chip design. The chip contains three inlet channels for the outer aqueous solution (OA), lipid-octanol solution (LO), and inner aqueous solution (IA). The OA and LO streams are bifurcated and meet the IA at the six-way junction. After the junction, there is a separation hole to separate the lower mass density octanol droplets from the heavier GUV, and an exit hole where vesicles can be imaged or harvested. (b) Schematic working mechanism of OLA. A stream of IA and OA is continuously pinched off by OA at the six-way junction to form double emulsion droplets. As these droplets flow down the post-junction, the octanol buds of from the double emulsion, creating a GUV and an octanol droplet. The octanol droplets flow up into the separation hole, while the GUVs flow further down the post-hole channel and can be imaged and/or harvested.

For producing liposomes with actin F-buffer only, the IA solution consisted of 15% glycerol, 120 mM sucrose, 50 mM KCl, 2 mM $MgCl_2$ and 20 mM imidazole at pH 7.4, and the OA solution of 15% glycerol, 5% poloxamer 188, 120 mM glucose, 50 mM KCl, 2 mM $MgCl_2$ and 20 mM imidazole at pH 7.4. Sucrose and glucose were added in order to make the buffer composition similar as for the inverse emulsion protocol, but are not required for OLA vesicle formation [402]. For actin encapsulation in F-buffer, the inner aqueous solution was additionally supplied with 13.4 μ M actin monomers (rabbit skeletal muscle, Hypermol EK) in G-buffer, of which 12μ M dark actin monomers and 1.2μM Alexa488-labeled actin monomers. Furthermore, we added 2 mM PCA and 0.1μM PCD to minimize photobleaching [338], and 4 mM DTT to preserve protein integrity. To prepare the lipid-octanol solution, we first prepared 10% (w/v) lipids in ethanol at a typical molar ratio of 99.5% DOPC and 0.5% Rhodamine DOPE. This solution was stored at -20°C and diluted 1:50 (v/v) in 1-octanol prior to GUV formation.

Microfluidic chips were prepared from a fused silica wafer kindly given to us by Siddharth Deshpande. From a single wafer, four chips could be produced. We mixed PDMS (Dow Corning, Sylgard 184 silicone elastomer kit) in a 10:1 mass ratio (elastomer: cross-linker) and desiccated it for 30 minutes to remove bubbles. Then, we poured it on top of the wafer and again removed bubbles in a vacuum desiccator for 30 minutes. While desiccating, we cleaned the surface of four glass slides that would serve as the support for the chips by sequentially rinsing with milliQ, ethanol and milliQ sequentially. Next, we spin-coated a drop of PDMS on the clean glass slides at 200 rpm for 55 s followed by 1750 rpm for 60 s to create a thin and smooth layer. Both chips and slides were

baked in an oven at 100 °C for 1 hour to cure the PDMS. The resulting PDMS stamp was peeled off the wafer and the chips were cut out using a surgical knife. We covered the channels with tape to prevent contamination with dust. Inlet and outlet holes were pierced in the chip using a biopsy punch. Tape was removed from the chips and both chips and slides were cleaned with isopropanol and blow-dried with nitrogen gas. Then, both the slides and the bottoms side of the chips were activated using a portable corona discharger (Electro-Technic Products, Chicago, IL, USA) for several seconds. The chips were then carefully put on top of the slides and some pressure was applied to ensure adhesion between both plasma-treated sides. Chips were baked overnight at 100°C.

Before devices could be used for vesicle formation, a surface treatment was necessary to render the post-junction channel hydrophilic. A 2.5% PVA (30-70 kDa MW, 87-90% hydrolyzed, Sigma-Aldrich) solution in milliQ was flushed through the OA channels using the 7000 mbar pump, while keeping a positive pressure on the IA and LO channels using 2000 mbar pumps. In this way, the OA inlet channels and post-junction channel were coated with PVA solution for 5 minutes. Then, the solution was removed by exchanging the PVA inlet for air and increasing the air pressure on all inlet channels simultaneously. The high pressure pump was needed to remove all PVA from the OA channels. In addition, a vacuum pump was used to remove PVA solution from the device outlet. Directly after PVA removal, the chips were baked in an oven at 120 °C for 15 minutes to immobilize the hydrophilic PVA polymers on the PDMS surface. Surface-treated chips were used within a week.

With a surface-treated device, GUV formation was done as follows. IA, LO and OA solutions were prepared according to the recipes mentioned above. The three solutions were connected to the appropriate inlet channels. With a low but positive pressure, we first made sure that the OA reached the junction, then the LO, and then the IA, without capturing air in any of the channels, and while making sure that none of the solutions entered one of the other inlet channels. When all three inlets were flushed successfully through the device, we tuned the inlet pressures to achieve the jetting regime where water-octanol droplets were produced at the junction. These droplets could be observed in the post-junction channel to monitor their transformation into GUVs.

4.5.10. eDICE

For the encapsulation of the cytoskeletal proteins actin and septin in GUVs, we used the cDICE method described in chapter 3, but with one important modification. Instead of introducing the inner aqueous solution (IAS) in the spinning disk with a capillary, we emulsified the IAS in 1 mL of the lipid-oil dispersion (LOD) prior to adding it to the disk. In this way, we were able to circumvent the use of a narrow capillary that is easily clogged, and we also substantially reduced the time between preparation of the IAS and the formation of GUVs. This has the important advantage that it prevents premature polymerization of actin and septin. The adapted protocol we call eDICE henceforth: emulsion Droplet Interface Crossing Encapsulation. In addition, eDICE experiments require substantially less IAS volume: typical experiments were performed with 25μL IAS, which typically yields well over 1000 GUVs. Like with cDICE experiments, eDICE experiments were conducted in a low-humidity room, where a dehumidifier maintained a minimum air humidity between 35 and 40%. IAS, LOD and outer aqueous (OAS) solutions for eDICE encapsulation experiments were prepared as described in chapter 3, but with minor modifications dependent on the protein, as described below. After formation, GUVs were transferred to a solution buffered with 20 mM Tris-HCl at pH 7.4 (or 10 mM for actin encapsulation experiments) and imaged in imaging chambers passivated with β-casein.

SEPTIN ENCAPSULATION

For septin encapsulation, we dispersed lipids in the LOD by first mixing 50μL lipids in chloroform with 370μL decane. The lipid mix was then dispersed in a 1:4 (v/v) mixture of mineral oil:silicone

oil (see chapter 3 for a motivation and detailed description of the lipid dispersion strategy). The final LOD contained 50μL chloroform, 370μL decane, 1.3 mL mineral oil and 5.2 mL silicone oil, and a total lipid concentration of 0.2 mg/mL. We produced membranes composed of DOPC:DOPE-Cy5 at a molar ratio of 99.9:0.1, membranes with a net negative charge using a lipid mixture at a molar ratio of DOPC:DOPS:DOPE-Cy5 at a molar ratio of 79.9:20:0.1, and membranes containing PIP_2 lipids using a mixture of DOPC:PIP(4,5)P_2:PE-Cy5 in a molar ratio of 96.9:3:0.1.

Septins were purified in-house. Recombinant human hexamers bearing His6-N-terminally-tagged SEPT2, SEPT6 and Strep-tag-II-C-terminally-tagged SEPT7 were expressed in *E. coli* BL21 (DE3) and purified on a 5 mL HisTrap HP column (Sigma Aldrich) followed by a 1 mL StrepTrap HP column (Sigma Aldrich) (for details, see ref. [370]), after which septin was stored in septin buffer (50 mM Tris-HCl at pH 7.4, 5 mM $MgCl_2$, 300 mM KCl, 1 mM DTT). The final IAS contained 300 nM septin, which contained 90% (mol/mol) unlabelled hexamers and 10% hexamers tagged on the SEPT2 subunits with msfGFP[370]. In addition, the IAS contained 33 mM Tris-HCl at pH 7.4, 2.5 mM $MgCl_2$, 1 mM dithiothreitol (DTT), 45 mM KCl, 1 mM Trolox, 1 mM GTP, 1 mM protocatechuic acid (PCA), 0.05μM protocatechuate dioxygenase (PCD) and 18.5% (v/v) Optiprep. Trolox was added to prevent blinking of fluorophores[405]. PCA and PCD were added to prevent photobleaching[338]. Septin polymerization was triggered only right before GUV formation by decreasing the KCl concentration, by a 1:6 rapid dilution on ice to 45 mM KCl and a final septin concentration of 300 nM. The osmolarity of the final IAS was about 230 mOsm. The OA solution was composed of 240 mOsm glucose in milliQ water only, being about 10-20 mOsm higher than the IAS. We did not buffer the outer solution as we found that addition of 10 mM Tris-HCl buffered at pH 7.4 negatively impacted GUV production yields.

ACTIN ENCAPSULATION

For encapsulation of F-actin only (fig. 4.10a), F-actin with fascin (fig. 4.10b) and streptavidin with or without actin (fig. 4.11b, c), or was done with an LOD prepared by dispersing lipids diluted in chloroform in a 1:4 (v/v) mixture of mineral oil:silicone oil (see chapter 3). In these experiments, the final LOD contained 420μL chloroform, 1.3 mL mineral oil and 5.2 mL silicone oil at a total lipid concentration of 0.25 mM. However, we later found that dispersion with decane (as for septin, see above) drastically improved yields of produced GUVs. Encapsulation experiments with Arp2/3 (fig. 4.11d) were therefore performed with the same LOD as used for septin (but with different lipid compositions).

For the encapsulation of preformed F-actin stabilized with phalloidin, and pre-formed F-actin with fascin, we used a lipid mix of DOPC:DOPE-PEG2k:Cy5-DOPE (99.985:0.01:0.005 molar ratio). For the encapsulation of streptavidin and membrane anchoring of preformed biotinylated F-actin, we used a lipid mix of DOPC:DOPE-biotin:DOPE-PEG2k:Cy5-DOPE (97.485:2.5:0.01:0.005). For Arp2/3-mediated nucleation of actin cortices, we used a membrane composition of DOPC:DGS-NTA(Ni):DOPE-PEG2k:Cy5-DOPE (97.485:2.5:0.01:0.005 molar ratio). Note the inclusion of a small fraction of PEGylated lipids, which we found to be essential for successful GUV formation in presence of actin.

For all actin encapsulation experiments, we used rabbit skeletal muscle α-actin (Hypermol EK, product no. 8101-03). Actin was dissolved to 23.8μ M, left to depolymerize on ice for at least 2 hours, then cleared by centrifugation at 148.000 g for 1 hour, and finally snap-frozen and stored at -80°C. Actin was encapsulated at a nominal concentration of 4.4μ M (8μ M for fig. 4.11d), of which 10% Alexa 488-labelled monomers, in actin F-buffer consisting of 50 mM KCl, 2 mM $MgCl_2$ and 20 mM imidazole at pH 7.4. In addition, the IAS contained 6.5% (v/v) optiprep. Note that this concentration is lower than that is used in chapter 3 and for septin encapsulation, because we found that Optiprep influenced actin polymerization, both spontaneous and by actin nucleators. Unless mentioned otherwise, actin was kept on ice to prevent polymerization, and polymerization was

triggered upon transferring to room temperature right before GUV formation. For encapsulation of stabilized filaments, actin was polymerized for 1 hour at room temperature in a 1:1 molar ratio of phalloidin:G-actin prior to GUV formation. Phalloidin from *Amanita phalloides* (Sigma Aldrich, product number P2141-1MG) was dissolved at 1 mM in DMSO and stored at -20°C. From the stock, phalloidin was diluted in F-buffer to working stocks and stored at 4°C.

Co-encapsulation of F-actin with the actin bundling protein fascin was performed by addition of fascin in a 1:20 molar ratio to G-actin. After mixing, the IAS was encapsulated immediately to allow actin polymerization in the GUVs. Fascin was purified in-house from a GST-tagged murine fascin plasmid, gifted to us from the lab of R. Dyche Mullins. Recombinant fascin was expressed in T7 *E. coli* and purified according to Gentry et al [406]. Fascin was snap-frozen in liquid nitrogen and stored at -80°C.

For encapsulation of streptavidin, we added 88 nM streptavidin-AlexaFluor488 (Invitrogen, distributed by Thermofisher, cat no. S11223) in F-buffer. For co-encapsulation of streptavidin and biotinylated F-actin, we added actin to a total concentration of 4.4μM, of which 1% (mol/mol) biotinylated actin monomers (Hypermol EK, product number 8109-01) and 10% (mol/mol) AlexaFluor 488 labelled G-actin. Lyophilized biotin-actin was dissolved according to the supplier instructions, cleared by centrifuging for 1 hour at 148000 g, snap-frozen in aliquots and stored at -80°C. Actin was thawed on ice at least 2 hours before experiments.

For the nucleation of a minimal cortex, we followed the approach by Pontani et al. [108] using His-VCA bound to the membrane via nickelated lipids. Subsequent activation of the actin nucleator Arp2/3 by the membrane-anchored VCA resulted in cortex formation. 10xHis-VCA was purified in house [153] from murine N-WASP, the plasmid kindly given to us by Kristina Ganzinger. We used Arp2/3 from porcine brain (Hypermol EK, product no. 8413-01). The protein was dissolved according to the supplier instructions to a concentration of 2.3μM, snap-frozen and stored at -80°C. For GUV formation, we used an IAS containing 8μM actin monomers (10% labelled AlexaFluor488) in F-buffer, 5μM His-VCA and 50 nM Arp2/3. We found a higher actin concentration of 8μM to result in more reproducible membrane localization as compared to 4.4μM which we used for the other encapsulation experiments.

GUV FORMATION

Prior to GUV formation, 3D-printed cDICE disks were cleaned by sonication for 15 minutes in 100% ethanol and then rinsed with milliQ. Then, while spinning the disk at 1800rpm on a custom-built electrical spinner (see chapter 3), we first injected 700μL OAS, and then 5 mL of freshly prepared LOD. Separately, 1 mL of remaining LOD was placed in a 2mL Eppendorf tube. After the final preparation step of the IAS (either dilution for septin, or addition of actin to the IAS for actin), 40 µL IAS (25μL also worked fine) was placed also in the 2mL tube. The IAS was then quickly emulsified in the LOD by rubbing the tube 10 times over an Eppendorf rack. The emulsion was immediately pipetted into the rotation chamber, after which the disk was rotated for 90 seconds for solutions with 18.5% v/v Optiprep, or 3 minutes for IAS with 6.5% Optiprep. After that, excess oil was pipetted out of the chamber, and the chamber was left in tilted position for produced GUVs to settle in the lower corner of the disk. After 15 minutes, GUVs could be extracted by carefully pipetting 100 µL from the aqueous phase in the bottom edge of the disk using a 1 mL pipette. For actin experiments, we were worried about pH gradients across the membranes due to the absence of buffer in OAS. We therefore added buffer to the settling GUV solution immediately after removing excess oil, so that the pH mismatch was resolved within 5 minutes after starting spinning.

4.5.11. OSMOLARITY

All osmolarities were measured with a freezing point osmometer (Osmomat 010, Gonotec, Berlin, Germany). Unless mentioned otherwise, osmolarities between the GUV inner and outer solutions

were matched within $5 mOsm$ deviation.

4.5.12. IMAGING CHAMBERS

For all experiments where GUVs were first harvested, and then imaged, we used either large (200μL) or small (20μL) imaging chambers as described below. Large imaging chambers were assembled by first cutting glass coverslips (24x50 mm, no. 1.5H, Paul Marienfeld GmbH & Co. KG) to fit in a custom-made holder. Then, slides were cleaned with ethanol and MilliQ-water and dried under a stream of nitrogen gas. Chambers were made by cutting the bottom and lid of 0.2 mL PCR tubes (Thermo Fisher Scientific). The cut tubes were then glued on the cleaned slide with the bottom up using a two-component adhesive. To prevent membrane adhesion to the glass, chambers were passivated for at least 15 minutes with a 1 mg/mL β-casein solution in MilliQ water containing 10 mM Tris-HCl at pH 7.4. The chamber was then flushed twice with observation buffer to rinse out unbound β-casein, after which the GUVs could be transferred to the imaging chambers. In all experiments, GUVs had a higher density than the surrounding solution, leading to sedimentation of the vesicles, which in turn facilitated imaging. The chambers were closed with the cut-off lids to prevent evaporation for experiments that required imaging over longer times. Small imaging chambers were prepared by first cleaning glass coverslips (No. 1.5H, 24x50 mm, Thorlabs) sequentially with ethanol, water and again ethanol and then blow-drying with nitrogen. An 8-well silicone gasket (8-6 mm diameter x 1 mm depth, Grace Bio-Labs) was pre-wetted with isopropanol, dried with nitrogen gas and then placed on top of the glass. To each well, 15 µL of β-casein solution (1 mg/mL β-casein, 10 mM Tris-HCl pH 7.4) was added and left for 15 minutes to passivate the glass surface. The solution was removed with a tissue and the chambers were blow-dried with nitrogen gas. Vesicles were placed in the chamber which was closed from the top with a glass slide (1 mm thickness, Thermo Scientific) to prevent evaporation and minimize convective flow in the sample.

4.5.13. PENDANT DROP

Pendant drop experiments were performed as described in chapter 3. Measurements were performed with either 100% DOPC lipids, DOPC:DOPS (80:20), or DOPC:PEG2k-DOPE (95:5). In all experiments, lipids were dispersed using chloroform in a 4:1 (v/v) silicone oil:mineral oil mixture, to a final composition of 420μL chloroform, 1.3 mL mineral oil and 5.2 mL silicone oil at a total lipid concentration of 0.2 mg/mL. For aqueous solutions with G-buffer, we prepared solutions containing G-buffer (5 mM Tris-HCl at pH 7.8, 0.1 mM $CaCl_2$) and 18.5% (v/v) OptiPrep. For experiments with actin, we added monomeric actin to a final concentration of 4μM. For experiments with F-actin in F-buffer, we substituted the G-buffer for F-buffer (50 mM KCl, 2 mM $MgCl_2$ and 20 mM Tris at pH 7.8).

4.6. ACKNOWLEDGEMENTS

We thank Siddhart Dishpande for help with implementation of the OLA formation method, Wiebe de Gruijter for help with development of the electroformation protocol, François Liénard for help with development of the gel-swelling protocol, Migle Jakstaite for conducting preliminary actin cortex formation experiments, and Feng-Ching Tsai for useful discussions about the gel-swelling and electroformation experiments. We thank Anne-Sophie van Schelt and Sharon Bouw for help in development of the cDICE protocol, Britta Bor for septin encapsulation experiments with eDICE, and Iris Lambert, Lucia Baldauf, and Sohpie Sandy for encapsulation of actin. We thank the Amolf software department, engineering department and mechanical workshop who were indispensable for the development of our experimental setup. In particular, we thank Henk-Jan Boluijt for

designing the electroformation chambers, Tom Brouwer for producing the electroformation chambers, Dirk-Jan Spaanderman for development of the cDICE setup and Jan Bonne Aans

4.7. SUPPLEMENTARY FIGURES

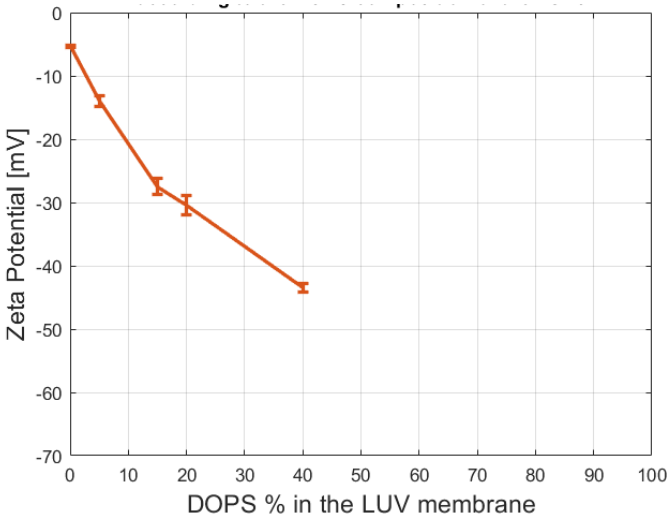

Figure 4.16: **Zeta potential measurements.** Zeta potential of POPC LUVs containing different fractions of DOPS. Error bars represent standard deviation between six measurements on two samples.

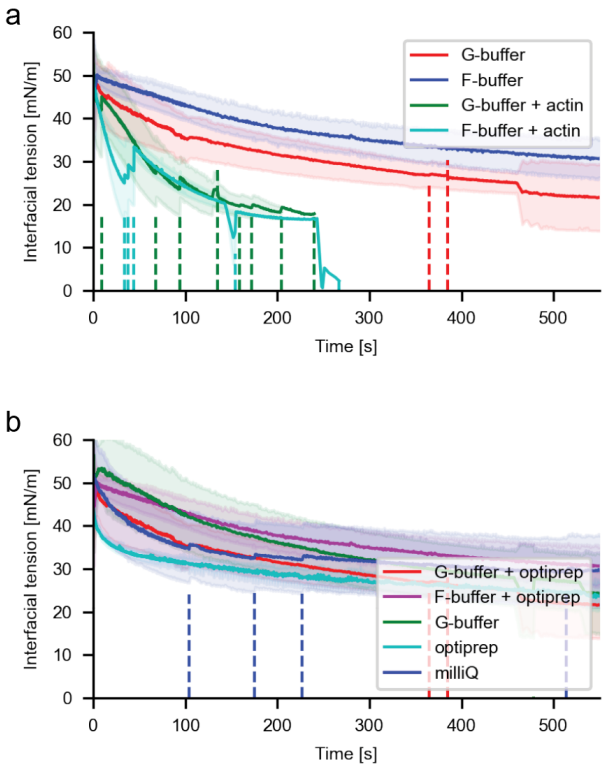

Figure 4.17: **Pendant drop measurements on eDICE inner solutions.** Interfacial tension measurements of lipid adsorption with the cDICE/eDICE aqueous and organic phases. Each curve represents the average over n measurements with the standard deviation between measurements illustrated by the shaded region. (a) Interfacial tension of the IAS-LOS interface comparing actin in G-buffer and F-buffer. Curves represent LOS against G-buffered IAS without actin (n=11, red line) and with actin (n=9, green line), and LOS against F-buffered IAS without (n=6, blue line) and with actin (n=5, cyan line). (b) Evolution of interfacial tension of the IAS-LOS interface measured for different compositions of the IAS. IAS consisted of G-buffer and 18.5 % (v/v) optiprep (red line, n=11), F-buffer with 18.5 % (v/v) optiprep (purple line, n=6), G-buffer without optiprep (green line, n=9), only 18.5 % optiprep (v/v) in milliQ water (cyan line, n=3), or pure milliQ water (blue line, n=12).)

5

DisGUVery: a versatile open-source software for high-throughput image analysis of Giant Unilamellar Vesicles

Giant Unilamellar Vesicles (GUVs) are cell-sized aqueous compartments enclosed by a phospholipid bilayer. Due to their cell-mimicking properties, GUVs have become a widespread experimental tool in synthetic biology to study membrane properties and cellular processes. In stark contrast to the experimental progress, quantitative analysis of GUV microscopy images has received much less attention. Currently, most analysis is performed either manually or with custom-made scripts, which makes analysis time-consuming and results difficult to compare across studies. To make quantitative GUV analysis accessible and fast, we present DisGUVery, an open-source, versatile software that encapsulates multiple algorithms for automated detection and analysis of GUVs in microscopy images. With a performance analysis, we demonstrate that DisGUVery's three vesicle detection modules successfully identify GUVs in images obtained with a wide range of imaging sources, in various typical GUV experiments. Multiple pre-defined analysis modules allow the user to extract important properties such as membrane fluorescence, vesicle shape and internal fluorescence from large populations. A new membrane segmentation algorithm facilitates analysis of spatially non-uniform intensities of membrane-bound species, and also correlate this with shape deformations. Altogether, DisGUVery provides an accessi-

This chapter is available on the bioRxiv preprint server under the name *DisGUVery: a versatile open-source software for high-throughput image analysis of Giant Unilamellar Vesicles* by Lennard van Buren, Gijsje H. Koenderink and Cristina Martinez-Torres (2022) [407].

ble tool to enable high-throughput automated analysis of GUVs, and thereby to promote quantitative data analysis in biophysical and synthetic cell research involving GUVs.

5.1. INTRODUCTION

Giant unilamellar vesicles (GUVs) are aqueous compartments enclosed by a lipid bilayer membrane [33]. Since their diameter is typically between 5 and 100 micrometers, which is comparable to the size of eukaryotic cells, and their membrane is composed of phospholipids just like plasma membranes, GUVs are considered a good model system for living cells. As such, GUVs have gained great interest from researchers in biochemistry, biophysics, synthetic biology and applied medicine.

One of the most classical applications of GUVs is in studying the physicochemical properties of biological membranes. Being larger than other biomimetic membrane systems such as large unilamellar vesicles (LUVs) and small unilamellar vesicles (SUVs), GUVs can be easily observed with optical microscopy. Accordingly, GUVs are extensively used to study a wide variety of membrane properties: mechanics[341], lipid diffusivity [408], permeability [349], as well as lipid order[409] and domain formation [410, 411]. Moreover, GUVs are often used to study the biophysical mechanisms that underlie important cellular events such as membrane growth[88], budding[64], fission[412] and fusion[413]. Furthermore, GUVs provide a suitable chassis in the endeavour of building synthetic or artificial cells[10, 16, 414]. In this emerging research field, cellular functionalities are being reconstituted from chemical or biological building blocks with increasing complexity, with the eventual goal to understand the minimal requirements for life at the cellular level[14]. Lastly, the biocompatibility of GUVs makes them also interesting in the context of targeted drug delivery[23]. They overcome size limitations of the SUVs that are typically used, offering a way to deliver more cargo per particle.

As GUVs are becoming a widely used tool in synthetic biology, also the possibilities for their production are growing. By now, numerous production methods have been developed to produce GUVs, ranging from simple and quick bulk methods with low-cost equipment to advanced microfluidic methods (see chapter 4). Two major pathways can be distinguished for the production. First, GUVs can be formed by hydration of a dried lipid film, either by spontaneous swelling on solid supports or porous substrates, or by application of an electric field [33, 74, 76, 415]. Second, GUVs can be templated from water-in-oil emulsion droplets, for example by the inverse emulsion method [75, 328], with microfluidics [77, 416] and by continuous Droplet Interface Crossing Encapsulation (cDICE, see chapter 3) [3, 175]. With the versatile options for formation, the design possibilities for GUVs have become legion: from simple membranes composed of a single lipid type to complex biological lipid extracts [282, 417], charged [90, 293] or biofunctionalized membranes [112], membranes with asymmetric leaflets [418] or including membrane proteins [419], in physiological buffers [293, 354], encapsulating functional protein [88, 175] or even active matter [295, 420].

By far the most widely used characterization technique for GUVs is optical microscopy. GUVs can be imaged in bright field or by fluorescence microscopy upon inclusion of dyes, either membrane-bound or encapsulated. While most studies with GUVs involve simple wide field or confocal microscopy, also superresolution microscopy [421] and bulk analysis with multi-well plate assays [328] and fluorescence-activated single

cell sorting (FACS) [422] have been employed. For all the GUV applications described above, it is crucial to evaluate the quality of the produced GUV samples because the success of GUV formation and the resulting vesicle properties can vary substantially dependent on experimental conditions. GUV analysis comes itself with the challenge that in most reconstitution experiments, the formed vesicles are polydisperse in size, shape, the presence of membrane structures and encapsulated content. The complex appearance of heterogeneous GUV populations therefore demands a quantitative characterization by accurate descriptors and robust statistics.

Despite the experimental ease of producing and imaging GUVs, their quantitative image analysis has received relatively little attention[378]. Typically, GUVs are either manually detected in the image and afterwards (manually) processed to extract data [89, 109, 112, 340, 359, 382, 391], or custom-made scripts are used to process specific data sets and generate a pre-defined set of output parameters [175, 328, 337, 423, 424]. Consequently, GUV image analysis is currently time-consuming and non-standardized, making it difficult to directly compare the outcome of different studies.

In the field of cell biology, analysis workflows do exist for automated characterization of cell or tissue image data, combining standardized detection modules with reporting a multitude of output variables[425, 426]. Unfortunately, these analysis workflows offer a limited compatibility with GUV data sets. While cells generally have a complex morphology, GUVs are typically near-spherical, highly symmetric 3D objects. Due to their often predictable shapes and intensity profiles, rapid and efficient detection and characterization of vesicles benefit from a simplified approach. Furthermore, irrespective of the application in which GUVs are used, the same set of descriptors are typically of interest, in particular vesicle size, shape, membrane intensity (lamellarity), and spatial intensity profiles of GUV membrane and content.

Some examples of openly available GUV analysis software do exist, laying the ground to make large-scale GUV analysis more accessible. However, they are all either geared towards specific, predefined analysis (membrane permeability [427], heterogeneity in membrane signal [428]) or they have limited compatibility with input data sets and vesicle types (confocal microscopy images [337], spherical vesicles [429]), requiring high signal-to-noise ratio of the membrane or predefined vesicle shapes for vesicle detection. In addition, most available software lacks a user-friendly interface that allows for interactivity during the detection and analysis procedures, in turn imposing a steep learning curve on new users.

To meet the requirement for accessible and flexible quantitative vesicle analysis, we have developed DisGUVery, an open-source software for the analysis of GUVs in microscopy images. Our tool encapsulates multiple algorithms for the detection of vesicles and the subsequent analysis of their morphology and content under a Graphical User Interface (GUI) based on Python. The software is designed to allow for maximal flexibility in data input, processing and analysis, enabling the user to work with a variety of imaging sources, to export variables of interest at any point during the processing, and to choose between a set of pre-defined detection and analysis modules. Our toolbox provides a general, fast, and user-friendly approach towards quantitative and high-throughput GUV sample characterization, which should be of broad use for the fields of membrane biophysics, cell biology, and bottom-up synthetic biology.

5.2. RESULTS AND DISCUSSION

The general workflow of DisGUVery is summarized in fig. 5.1A. The starting point is a microscopy image with GUVs visible either via fluorescent labelling (epifluorescence or confocal microscopy as shown in fig. 5.1B) or in bright field microscopy (phase contrast images). In case of multi-channel images, it is possible to select the channel that should be used for GUV detection, typically, but not limited to, a channel where a membrane dye is imaged, or a phase contrast channel in which vesicles are clearly visible. To allow for high-throughput analysis of large GUV data sets, images can be processed in batches both for vesicle detection and subsequent analysis. When processing is done, detection results can be inspected in the software, and erroneously detected vesicles or unsuccessfully processed images can be discarded before further analysis.

Prior to vesicle detection, background noise can be reduced by processing the input image using a Gaussian smoothing filter followed by an enhancement of the membrane signal (fig. 5.1C), both of which can be tuned according to the input image. After this optional preprocessing of the image, GUV detection can be done using one of three different methods, all of which yield the indexed locations and sizes of detected GUVs (fig. 5.1D). To optimize detection, input parameters can be varied in the GUI and the results can directly be inspected, and wrongly assigned vesicles can be manually discarded. Size distributions can at this point be directly computed and visualized, or other, more complex analysis can be pursued.

For many analysis purposes, such as obtaining vesicle shape descriptors of deformed GUVs [109] or probing membrane colocalization of fluorescent proteins [374], the precise membrane location is required. We have implemented a membrane segmentation algorithm that can track the membrane of non-spherical vesicles, detecting both the inner and outer edge of the membrane (fig. 5.1E). When high spatial accuracy is not required, users can also make use of the computationally cheaper basic membrane analysis feature, where the contour from vesicle detection is simply expanded with a certain width to create a ring that contains the membrane (fig. 5.1F, purple dashed lines). Regardless of the chosen method for membrane segmentation, the angular intensity profiles and the radially integrated intensity profiles can be extracted (fig. 5.1F), for example to retrieve the angular profile of membrane fluorescence [430, 431], the angular profile of a fluorescent membrane-binding molecule[178], or to quantify membrane localization of an encapsulated molecule[112] or an externally added membrane-binding protein[88].

Besides the radial and angular intensity profiles, which provide information about the spatial distribution of fluorescent probes, the average intensity of the vesicle lumen can also be extracted for detected vesicles using the Encapsulation Analysis module (fig. 5.1G). Analysis of internal fluorescence is essential for studying the efficiency of encapsulation of molecules and other components[175, 390], for permeabilization assays where transport of a fluorescent probe across the membrane is tested[345, 432, 433], and for fluorescence-based measurements of the activity of internal metabolic pathways[88, 434].

The analyses mentioned above are some of the methods that we have predefined in the software. However, we want to stress that the use of DisGUVery is not limited to these analyses. Since it is possible to export results from object detection, contour de-

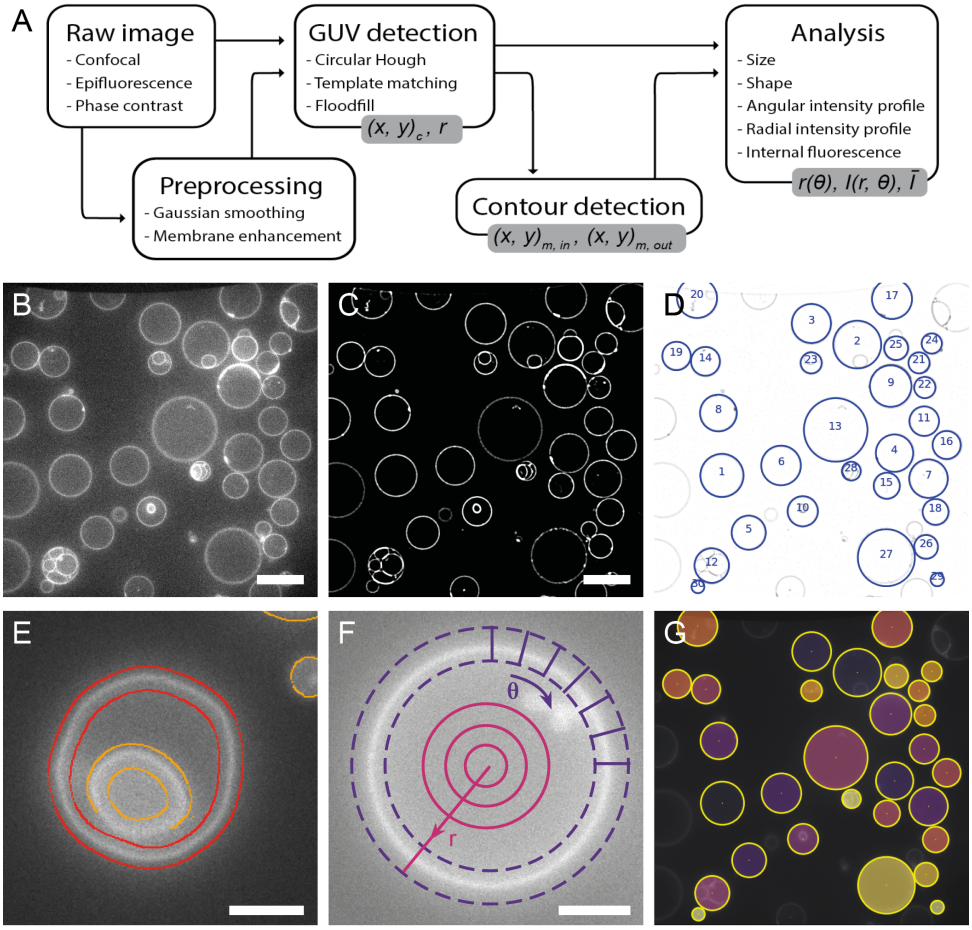

Figure 5.1: **General workflow of GUV detection and analysis by DisGUVery.** (A) Visual representation of the workflow. Output variables are shown in grey boxes. (B) Example of an unprocessed single-plane confocal fluorescence microscopy image of GUVs, used as input for the analysis. Scale bar is 20μm. (C) Processed image after enhancement of the membrane signal. (D) Vesicles detected by Circular Hough Detection indicated with blue circles and object index number. Contrast is inverted for visualization. (E) Refined contour detection distinguishes the enclosing membrane of a detected vesicle (red) from other fluorescent structures in the image (orange). Scale bar is 5μm (F) Radial (magenta) or angular (purple) intensity profiles can be extracted from detected GUVs. Scale bar is 5μm (G) Masks (colored) can be created from detected vesicles (yellow circles) to extract internal fluorescence of vesicles.

tection, and from the analyses at any point in the process, users can extract the relevant information and perform their own analyses outside the software.

5.2.1. VESICLE DETECTION

We have implemented three different methods for the detection of vesicles in microscopy images: Circular Hough Transform (CHT), Multiscale Template Matching (MTM) and Floodfill detection (FF). As the underlying principle for object detection is different for each of the methods, they allow detection of a variety of vesicle shapes and imaging sources. The first method, based on the circular Hough transform of the object edges [435], is commonly used in the detection of GUVs as it recognizes circular objects with little influence of the intensity profile [427, 429]. As a result, detection by CHT depends mostly on vesicle shape and not on image intensity, providing a robust method with a high selectivity towards circular vesicles. When the vesicle shape is not circular, but is predictable, for example, by having a population of similar looking vesicles in an image, detection can be done via the second method: template matching [436]. We have implemented a slight variation of this method, Multiscale Template Matching (MTM), by allowing the re-scaling of the template to multiple sizes. MTM works by the convolution of the image with a target object, or template, which can be an image of a typical vesicle. Regions in the image are then assigned as detected objects when this template matches the region, with the scaling of the template enabling the size-invariant detection of vesicles. The third method, Floodfill detection (FF), is based on an absolute intensity difference between membrane and background signals[437]. By thresholding the image, membranes can be distinguished from the background and closed membrane contours in the thresholded image are assigned as vesicles. Floodfill detects vesicles based on membrane fluorescence, regardless of their shape. Note that FF has been implemented previously for vesicle detection by Blanken et al. [337], but with a different starting point for the floodfill algorithm (the seed point). While their algorithm floods all the regions within GUVs by scanning a range of intensity thresholds and seed points, ours floods the surrounding background, which has the computational advantage of using only a single thresholding intensity and a single seed point.

We evaluated the performance of the three vesicle detectors on different types of microscopy images: fluorescence confocal, epifluorescence, and phase contrast. We focused on two main aspects to determine the quality of the detectors: how good are they at detecting vesicles within an image? And, how sensitive is this detection to different factors, e.g., detector parameters or image source? Detection outcomes of the software were benchmarked against human visual detection. We started by optimising the detector parameters on a single image. Figure 5.2A-C shows an example of the detection results for all detectors on a single confocal image. In this case, the optimal parameters are those which allow the detection of the highest number of vesicles in the image, regardless of their characteristics, while avoiding artefacts in the detection. Once this optimisation has been done, we explore the parameter space of each of the detectors and evaluate the F_1-score[438], defined as:

$$F_1 = 2\left(\frac{precision \times recall}{precision + recall}\right) \tag{5.1}$$

Here, $precision = \frac{TP}{TP+FP}$ and $recall = \frac{TP}{TP+FN}$ with TP, FP and FN being true positives, false positives and false negatives, respectively. In this study, true positives are detection results that correspond to vesicles, false positives are identified objects that are not vesicles, and false negatives represent GUVs that have not been detected. The reference human visual analysis was performed by a single observer by counting all GUVs in the images, regardless of vesicle size, type, appearance, or position in the image. GUVs at the edge of the image were included as long as a part of the membrane was visible.

We have chosen to use the F_1 score as an output metric to evaluate our detectors, because it is mainly penalized by false negatives and false positives, both of which are useful output parameters in object detection. As such, F_1 is amply used in object detection problems[439]. Since the F_1 score is the harmonic mean of precision and recall, both are weighed equally into a single output. While recall represents the fraction of objects in the image that are detected, precision denotes which fraction of detected objects are vesicles. Figure 5.2D-F show the F_1 scores as a function of pairs of critical parameters inherent to each of the detectors, with the exception of Floodfill (FF). For FF detection, we chose instead the size of the filter for membrane signal enhancing in the pre-processing step, as we have found it to be critical for the method performance (fig. 5.2F). We find that all detectors show a region within their parameter space in which the F_1 score is maximum and their performance is best. Note that the F_1 score only changes within 10% of its maximum value for a large set of parameters, suggesting that a precise optimisation of the parameters is not necessary, which facilitates batch-processing of data sets with similar images. Notably, CHT appears to be the least sensitive method to changes in the parameter choice of threshold values (fig. 5.2D), with performance dropping only at large thresholds ($\sim$ 50% increase from the optimal value). For MTM, the number of scales used to resize the template is the critical factor in achieving a good performance. This is strongly dependent on the dataset used, more specifically on the polydispersity in vesicle sizes. For the wide distribution of vesicle sizes in our sample, a large number of template scales allows precise matching of the template with GUVs of different sizes. To ensure that the size of the template prior to scaling does not play a crucial role in detection, for example due to pixelation effects, we tested templates of different sizes which resulted in similar performance (fig. 5.2E). As expected, FF detection depends greatly on the intensity threshold (fig. 5.2F), with higher values not allowing the vesicles to be properly segmented in the binary mask of the thresholded image. Interestingly, in the images tested, the pre-processing step of membrane enhancement is crucial for FF detection to succeed, as without it, FF detection simply fails to detect vesicles as is demonstrated in fig. 5.2F at the smallest edge filter size.

We then investigated the extent to which the imaging conditions impact the detection methods, for example, by changing the type of microscopy used to visualize the vesicles. We compiled a dataset of 5 images for each one of the three standard microscopy techniques mentioned above, resulting in a total of over 200 vesicles for each imaging method. For each dataset, we perform the detection using the parameters that were finely tuned for a random image within the set. To measure the performance of the detectors, we evaluate separately the precision and the recall. The reason for this split being that all detectors show a high precision value (between 0.9 and 0.99) for the different data sets (fig. 5.8), with any differences in the detection performance being represented

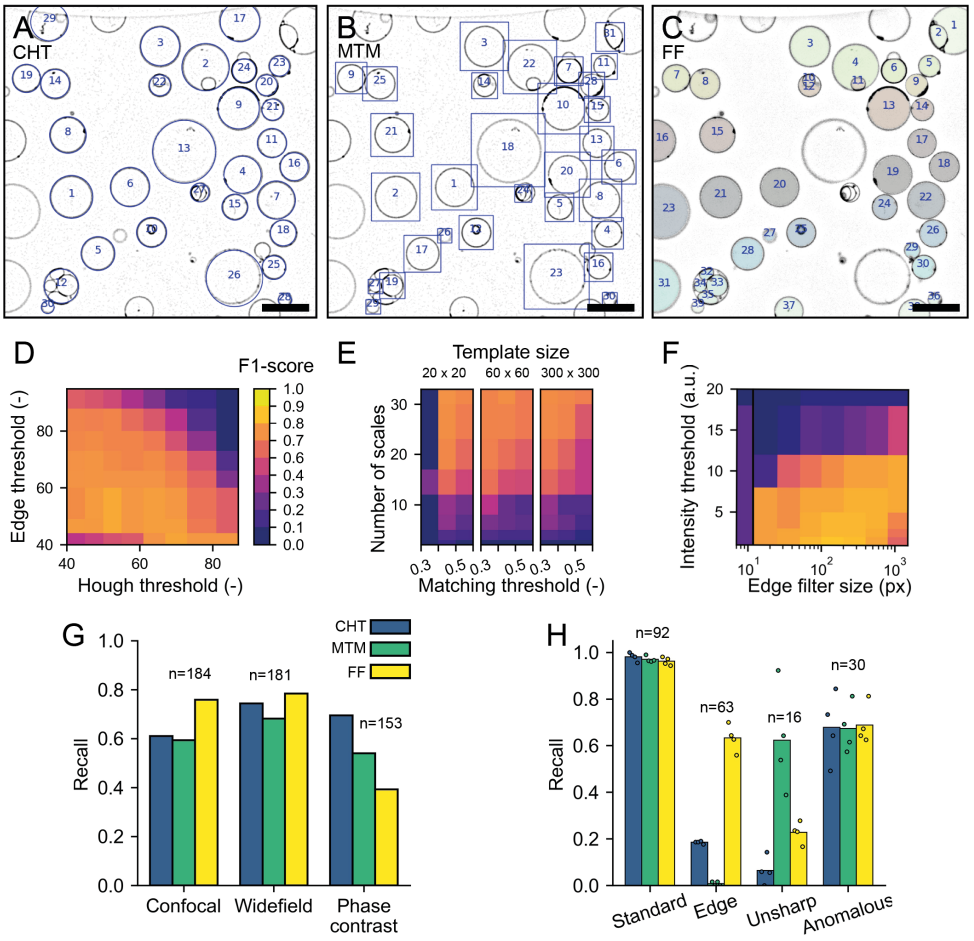

Figure 5.2: **Performance of Vesicle Detection.** (A-C) Detected vesicles with the Circular Hough Transform (A, blue circles), Multiscale Template Matching (B, blue bounding boxes) and Floodfill (C, colored objects). The contrast of the images has been inverted for visualisation purposes. Scale is $20\mu m$ in all images. (D-F) F_1-score of CHT (D), MTM (E) and FF (F) for different parameter values (see methods for details on the parameters). The color scale in (E-F) is the same as in (D). (G) Recall of vesicle detection for confocal fluorescence, widefield fluorescence and phase contrast images using the three different detectors. (H) Detection recall for different subcategories of vesicles as performed by four different human observers. See main text for more detailed explanation of the use of categories. Individual data points represent results of the individual observers, bars represent average recall values.

predominantly in the recall metric. In fig. 5.2G it can be seen that in both confocal fluorescence and epifluorescence images, all detectors are able to detect vesicles with a recall between 0.6 and 0.8, meaning that 60 to 80% of vesicles are properly detected. However, for phase contrast images, recall decreases, and significantly so for Floodfill detection (to 40%). The low performance of the FF detector in phase contrast is expected based on the intensity profile that vesicles show in this type of microscopy, where the GUV membrane does not represent an intensity maximum but instead the steepest intensity gradient. Furthermore, intensity variations either due to inhomogeneity of illumination or to the presence of surrounding objects interferes with detection based on an absolute intensity threshold. Unsurprisingly, CHT is the most robust method across imaging sources for the sample we investigated, emphasizing its dependence on vesicle shape over intensity profile.

Given that the detectors used target different types of objects, we next looked into what kind of vesicles were being detected by each method. We therefore manually divided all vesicles analyzed in fig. 5.2G into four categories: vesicles that were located at the edge of the image ('edge'), vesicles that were out of focus ('unsharp'), anomalous vesicles ('anomalous') and vesicles that do not belong to any of the first three categories which we called 'standard' vesicles. A gallery of example vesicles for all subcategories can be found in fig. 5.9. Anomalous vesicles could be vesicles with a bright membrane signal in their lumen, with very heterogeneous membrane signal, or vesicles that were stuck together in aggregates. Typically, the standard vesicles are those needed for further analysis. In fig. 5.2H, we can clearly see that while 'standard' vesicles are detected similarly by all methods, with recall being nearly 1.0, limiting cases such as vesicles on the edge of the image and those that are out of focus can be easily detected or filtered out depending on the method of choice. CHT and MTM filter out most vesicles at the edge. Furthermore, CHT also misses the unsharp vesicles, which are not detected by FF either. Interestingly, all detectors perform similarly for the anomalous vesicles, with more than 60% of them being detected. Together, these results show the robustness of the different detectors, allowing detection to be performed on a variety of vesicle types and imaging sources.

To illustrate the range of applications of the three detectors for synthetic cell research, we performed vesicle detection in a selection of proof-of-principle experiments. First, we investigated if our methods could be used to track GUV size and number during swelling-based GUV formation. GUV swelling methods include electroformation and gel-assisted swelling and are by far the most popular formation methods, as they are fast and easy and yield large numbers of GUVs[76, 355, 364, 378]. In these experiments, lipids are first dried on a surface, which can be a hydrogel, an electrode, glass, teflon or a porous material. Subsequent addition of a swelling solution leads to swelling of the lipid film and formation of large numbers of GUVs that are closely packed above the swelling surface (fig. 5.3A, top image). Using CHT detection, we efficiently detect spherical vesicles even at high surface coverage (fig. 5.3A, bottom image). By automated detection of GUVs during their formation, growth kinetics could easily be obtained. Since detection by CHT relies on vesicle shape rather than intensity, the method is largely insensitive to touching vesicles or high background fluorescence, both of which are more likely at high packing density. Furthermore, the ability to specify a minimum and maximum

GUV radius prevents detection of false positives in dense samples. In addition to GUV production by swelling, detection at high packing density is also relevant for studies on GUV-GUV adhesion[440] or while building multibody GUV tissues[441].

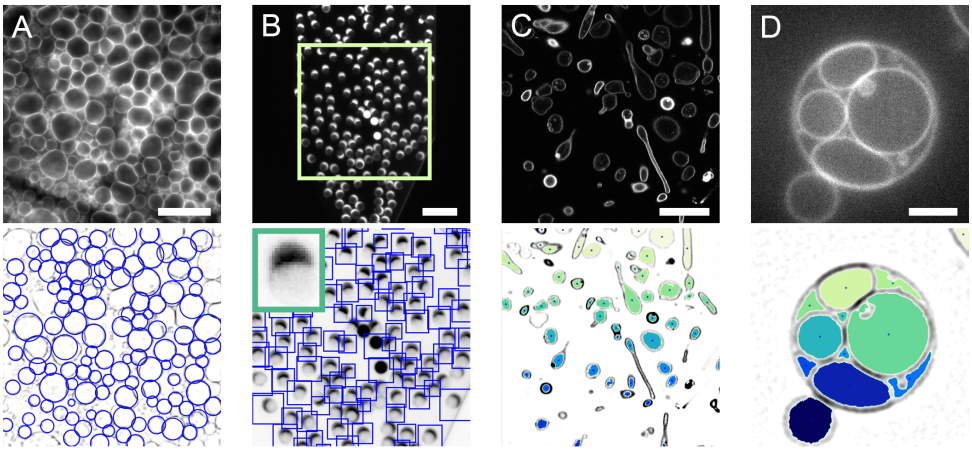

Figure 5.3: **Applications of vesicle detection methods.** Images at the top are the input fluorescence images, images at the bottom show the detection results. Contrast has been inverted for detection results to improve visualisation. (A) GUVs growing on top of a hydrogel following the gel-assisted swelling method are detected with CHT. Scale is 40μm. (B) Microfluidic production of GUVs imaged with a low magnification objective. MTM is employed to detect GUVs in the microfluidic channel. Produced vesicles contain a lipid-rich octanol pocket, visible as a bright cap. Scale is 100μm. Inset in bottom image is the template used for detection. (C) Encapsulation of stiff actin bundles in GUVs leads to deformation of the vesicles (data by F.C. Tsai, from [109]). The non-spherical vesicles can be detected with FF detection. Scale is 20μm. (D) A GUV formed by gel-assisted swelling contains large internal vesicles. FF detection on this multivesicular GUV leads to detection of the compartments rather than detection of the enclosing GUV. Scale is 5μm.

As an alternative to the classical swelling methods, microfluidic vesicle production is becoming increasingly popular, with multiple new techniques being published yearly (reviewed in ref. [357, 358]). Microfluidics offers superb control over vesicle formation, making it a powerful tool in the synthetic cell engineering field. Vesicles can be imaged *in situ* as they are being produced on-chip, using objectives with a large working distance with low magnification. This typically yields low-resolution images of vesicles. In line with MTM's ability to detect out-of-focus vesicles (fig. 5.2H), MTM also proves to be suitable for GUV detection in low-resolution images of microfluidic GUV fabrication, as we demonstrate with an octanol-assisted liposome assembly (OLA) experiment [77] (fig. 5.3B). Detection of vesicles on-chip enables users to extract GUV production rates and corresponding size distributions in microfluidic experiments. MTM detection does not require a sharp outline of the vesicle, but only a template that resembles the vesicles that need to be detected. Since the template can easily be picked from the image itself, MTM provides a versatile tool for vesicle detection even in low-resolution images. As alternative to MTM, CHT is also a useful detector in microfluidic experiments, since production by microfluidics often leads to spherical vesicles at high packing density with

a narrow size distribution[390].

While CHT and MTM are both shape-sensitive detectors, FF can detect vesicles of any shape. Having a detector that does not rely on vesicle shape is valuable, as shape control and GUV deformation are essential aspects of synthetic cell engineering[64, 109, 196, 296]. We demonstrate the use of FF on GUVs deformed by encapsulated stiff actin bundles (fig. 5.3C). In this experiment, filamentous actin is co-encapsulated with the bundling protein fascin, resulting in the formation of actin bundles up to tens of micrometers long[109]. Due to the high stiffness of these bundles, GUVs are deformed, resulting in elongated vesicles and actin-filled membrane protrusions. In fig. 5.3C, it can be seen that FF detects all vesicles irrespective of shape. In turn, detection by FF can be used as a starting point for vesicle deformation studies. Another application of the FF detector is found in the image segmentation of GUV internal compartments. Just like living cells contain numerous reactive compartments, GUVs can be compartmentalized to spatially separate cellular processes[78, 442]. Compartmentalization is becoming more popular in synthetic cell research, as distinct reaction environments are desired for reconstitution of increasingly complex processes. Due to its shape-insensitive detection, the FF method is suitable for detecting GUV compartments with random shapes and sizes as illustrated in fig. 5.3D. In this way, detection of compartments could be used to monitor internal activity of cellular processes.

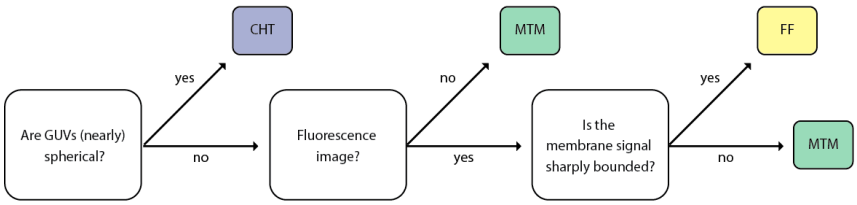

Figure 5.4: **Decision tree for GUV detection.** Decision tree for choosing one of DisGUVery's detection modules based on sample and image properties.

Altogether, the three vesicle detection methods make DisGUVery useful for a wide range of synthetic cell research applications. Based on properties of the sample inspected, such as image resolution and vesicle shape, the desired detection method can be chosen (fig. 5.4).

5.2.2. MEMBRANE ANALYSIS

Membrane detection and analysis are important for a wide range of GUV studies, as they allow vesicle shape characterisation and quantitative analysis of the membrane fluorescence and/or membrane-binding proteins or other molecules. We have implemented two modules to perform membrane analysis on the detected vesicles: Refined Membrane Detection (RMD) and Basic Membrane Analysis (BMA). We have developed RMD to enable the tracking of the membrane contours, facilitating the capture and quantification of any global and local deformations. This method is based on a Canny edge detector that we have combined with a directional search algorithm to assign the detected edges to the inner and outer contours of the membrane (fig. 5.5A-C, contours shown in

red). While the position of the detected contour can be affected by the choice of kernel size used with the edge detector (a predictable offset is introduced), the membrane position, taken as the midpoint between the inner and outer contour, will remain independent of the kernel size for confocal fluorescence images. Compared to RMD, BMA is a faster and simpler method to analyse the vesicle fluorescence signal, but at the expense of lower spatial accuracy. In BMA, a region of interest is created by a simple expansion of user-defined width around the boundaries of the detected vesicle. In case of CHT detection, this results in a circular ring as shown in fig. 5.5C.

After membrane segmentation, either by contour detection in RMD or by defining a region of interest in BMA, it is possible to extract the angular and radial intensity profiles of the entire vesicle. The intensity profiles are calculated by creating angular or radial slices, of size $d\theta$ or dr, and computing the corresponding descriptive metrics for each slice, thus taking into account all intensity values of the detected vesicle and reducing the effects of discretization associated to single linear profile extraction. For the vesicle in fig. 5.5C, the angular intensity profile using the mean membrane intensity from each angular slice is shown in fig. 5.5D (top). Note that, although the trend of the mean intensity profiles is similar for RMD and BMA, the values differ greatly. This is a consequence of the wider segmentation ring of BMA (fig. 5.5D, bottom), which, when used to compute the mean intensity values, introduces the influence of the background signal, unlike the contained segmentation done by RMD. Furthermore, it can be seen that the BMA profile shows a fluorescence increase from $\theta = 250°$ to 300°, while this effect is much weaker for RMD. We attribute this apparent increase in fluorescence to the fact that the membrane shows an outward deformation around $\theta = 250°$ (fig. 5.5D, bottom), causing a larger part of the BMA slices starting from that angle to be filled with membrane as compared to other slices. Since in RMD the ROI always tightly confines the membrane, extraction of fluorescence intensity is much less sensitive to membrane shape. Dependent on the nature of the data and the required analysis, the choice of descriptive metrics can have a significant contribution of imaging artefacts or other sample related noise (see SI). For example, while both the integrated intensity and the mean intensity are influenced by the background signal, the latter will also depend on the number of pixels within the slice. Polydisperse samples, where the vesicle size has a large variation, will thus require a careful interpretation of the results and likely, a different metric to analyse the data as compared to more monodisperse samples.

To further illustrate the applicability of both methods in the quantitative characterisation of GUV membranes, we show how RMD can be used to analyse the membrane and content of a deformed vesicle (fig. 5.5E), while we use BMA for an example on phase-separated membranes (fig. 5.5F). In the first example, a GUV is deformed to a prolate shape by encapsulated filamentous actin that is bundled by the bundling agent fascin[109]. We used RMD to track the membrane contour position, and additionally, we extracted the angular profile for the average actin intensity from the RMD contour (fig. 5.5E bottom). The plot clearly shows two peaks in membrane position around angles 150 and 340°, which correspond with the peaks in actin intensity. If desired, the obtained contour coordinates can be exported to compute other shape descriptors of interest. In this way, membrane deformation by fluorescent structures can be quantified in an automated way for vesicle populations, enabling an accessible and quantitative ap-

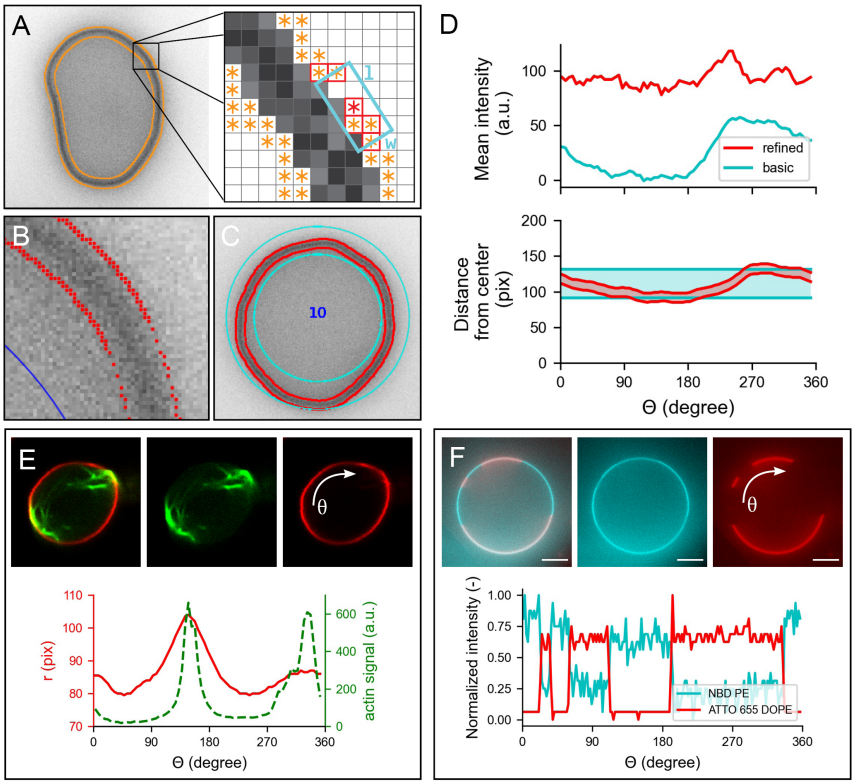

Figure 5.5: **Membrane analysis by DisGUVery.** (A) Schematic overview of the refined detection method. Left: epifluorescence image (inverted) of a GUV with all detected edges (orange). Right: edge points (orange) within the search box (cyan) of size l x w are connected (red border). (B) Zoom-in on membrane edges detected by refined detection (red), displayed on top of the inverted epifluorescence image of a GUV. (C) Segmentation of the membrane area as defined by basic membrane analysis (cyan) and refined membrane detection (red). (D) Angular profile of membrane properties from the vesicle in (C) extracted by basic membrane analysis (blue) and by refined membrane detection (red). Top: mean intensity per angular slice with an angular separation of 5°, and a ring width of 30 pixels for BMA. Bottom: radial distance to inner and outer boundary from the center of the vesicle. (E) Refined membrane detection on a non-spherical GUV deformed by actin bundles. Insets: composite confocal image of a GUV membrane (red) deformed by actin-fascin bundles (green) (data by F.C. Tsai, from Tsai et al. [109]). Plot: angular profile of the membrane's radial distance (red) and integrated actin intensity (green). (F) Basic membrane analysis of a phase-separated membrane containing DOPC:DPPC:cholesterol:NBD-DPPE:ATTO655-DOPE in a 31.8:48:20:0.1:0.1 molar ratio. Insets: image of vesicle labeled with NBD-DPPE (blue) and ATTO655DOPE (red). Plot: angular profile of both dyes extracted by basic membrane analysis, normalized to unity by subtraction of the minimum signal followed by division by the remaining maximum signal.

proach in GUV deformation studies. Besides its use in actin-mediated GUV deformation studies[109, 110, 113, 114, 359], this analysis is also valuable in other studies on global vesicle shape deformation, for example by other proteins involved in cytokinesis such as the bacterial division proteins FtsZ[443] and Min system[296], by other membrane-binding proteins [64], DNA origami[218], by microfluidic traps[182, 196], or by spontaneous membrane fluctuations [5]. Furthermore, RMD could be applied to characterize local membrane deformations, such as protrusions [444] or nanotubes[90, 430].

In cases where vesicles are rather spherical and their shape well characterised, BMA is a useful tool to study the fluorescence signal of the GUV membrane. In fig. 5.5F, we show a GUV composed of a lipid mix of DOPC:DPPC:cholesterol:NBD-DPPE:ATTO655-DOPE in molar ratio 31.8:48:20:0.1:0.1. In this ratio, the lipids form two spatially separated phases[344]: a liquid-ordered phase containing mainly DPPC lipids and cholesterol, and a liquid-disordered phase containing mainly DOPC lipids. While NBD-DPPE partitions preferentially into the liquid-ordered phase (blue), ATTO655-DOPE accumulates in the liquid-disordered phase (red). Using CHT detection followed by BMA, we obtained the angular profiles of both membrane dyes. The intensity profiles indeed clearly reveal that both dyes have a preferential presence in either one of the two phases. While here we show the example analysis for one single GUV, we would like to stress that BMA performs membrane analysis at high computation speed, enabling the analysis of membrane fluorescence for hundreds of vesicles within minutes. Next to lipid-lipid phase separation studies, BMA could be used for membrane quenching experiments[61], to probe the homogeneity of a reconstituted actin cortex [112], or for analysis of spectral images in lipid packing studies using polarity-sensitive probes[445].

5.2.3. POPULATION ANALYSIS

So far, we have demonstrated DisGUVery's working principles and the performance of detection and membrane analysis on single vesicles or single images. However, for the analysis of GUV experiments it is often desired to analyse large numbers or time-lapse series of vesicles. We implemented a batch-processing option that allows for the semi-automated analysis of multiple images, making population characterisation on large data sets accessible and enabling easy identification of statistical differences. We illustrate the potential of the batch-processing feature with two quantitative analyses: binding of small vesicles to GUVs using membrane-anchored oligonucleotides, and the encapsulation of a fluorescent protein inside GUVs.

In the first case, we utilise the membrane analysis module on a population of vesicles where we bound large unilamellar vesicles (LUVs) to GUVs by using membrane-anchored oligonucleotides (fig. 5.6A-E)[8, 91]. While GUVs have diameters of tens of microns (fig. 5.6A), the LUVs used in this study have a diameter of approximately 200 nm, close to the size of the diffraction limit. To generate specific binding between GUVs and LUVs, we incorporated one type of single-stranded DNA (ssDNA) in the GUVs, and the complementary ssDNA in LUVs. Here, we set out to test if the extent of LUV-GUV binding could be regulated by varying the DNA concentration. Therefore, we incubated vesicles either with $0.5\mu M$ DNA, $1\mu M$ DNA or no DNA at all prior to mixing LUVs with GUVs. LUVs were doped with a fluorescently tagged phospholipid for visualization and quantification. To allow vesicle detection that is not biased by LUV-binding, we inde-

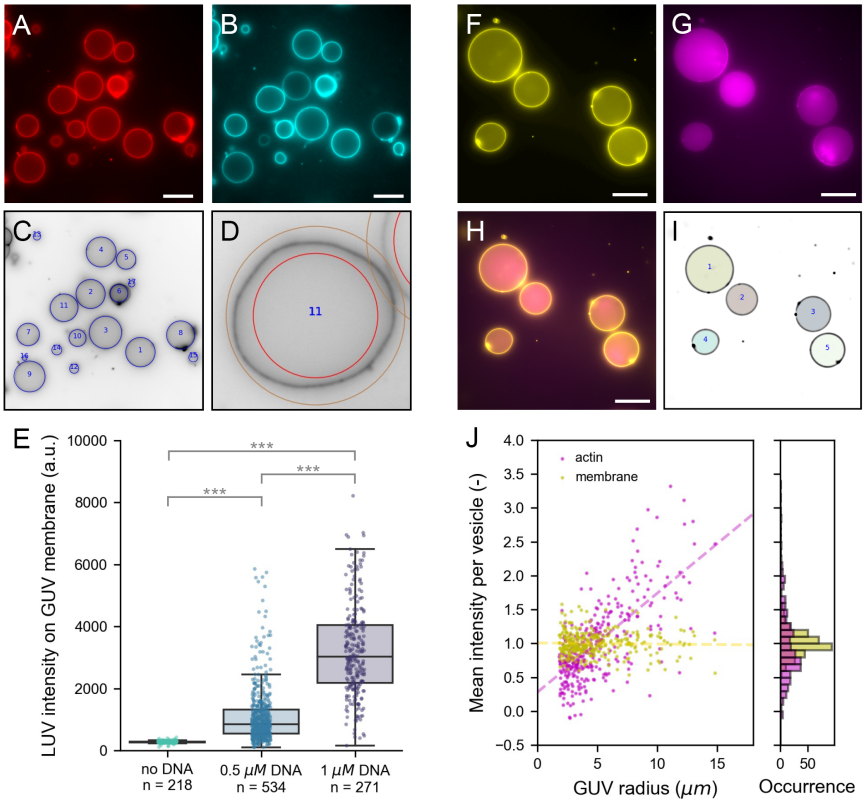

Figure 5.6: **Population analysis.** (A-E) Analysis of LUVs binding via membrane-anchored oligonucleotides to GUV membranes. (A) Atto 488 DOPE-labeled GUVs produced by gel-assisted swelling. (B) Atto 655 DOPE-labeled LUVs localize on GUV membranes when both are incubated with 1 μM cholesterol-DNA. (C) CHT detection in the Atto488-channel (inverted contrast). Detected vesicles are indicated with blue circles. (D) Example of the detection ring of 50 pixels width used for basic membrane analysis. (E) Bar plot of LUV intensity on the GUV membrane at different DNA concentrations. Each point represents the LUV intensity on an individual vesicle. *** indicates statistically significant difference with $p < 0.001$. (F-J) Analysis of fluorescent monomeric actin encapsulated in GUVs using cDICE. (F) DOPC GUVs labeled with 0.1% (mol/mol) 18:1 Cy5 PE. (G) Encapsulated actin of which 10% is labeled with Alexa 488. (H) Composite image of membrane and actin. (I) Results of FF detection. Masks represent detected vesicles. (J) Mean intensity normalised by population average of actin (magenta) and membrane (yellow) plotted against the GUV radius (left) and shown in a histogram (right). Dashed lines in the scatter plot are linear regression results for actin (magenta, slope is 0.15) and membrane (yellow, slope is 0.00). All images are epifluorescence images. Scale bar is 20 μm in all images.

pendently labeled GUV membranes with another fluorescent phospholipid. When both types of vesicles were incubated with 1μM of the complementary DNA strands prior to mixing, LUVs clearly localized on the GUV membranes (fig. 5.6B, fig. 5.10B), while we observed no colocalization in absence of DNA(fig. 5.10A). To quantify LUV binding, we first detected GUVs in the Atto488 channel using CHT detection (fig. 5.6C). Membrane fluorescence was analyzed using the basic membrane analysis because it is computationally light and our analysis did not demand a high spatial accuracy (fig. 5.6D). We chose a large (50 pixel) ring width to be able to extract membrane fluorescence also from non-spherical vesicles that were naturally present in the sample. While the software exports different intensity metrics from the angular slices, we performed our analysis using the intensity maximum per slice to minimize the effect of the background signal (see SI). Given that the maximum is sensitive to fluorescence outliers, for example caused by bright membrane structures or touching vesicles, we finally take the median of all angular maxima to represent the vesicle average. To correct for background intensity, we subtract the radial intensity average just outside the vesicle from the vesicle-average LUV intensity. In this way, we analyzed over 1000 GUVs in 50 different images. The results are plotted in fig. 5.6E. In absence of DNA, LUVs do not bind to GUVs, in line with what is seen the image (fig. 5.10). Upon DNA addition, membrane analysis shows a clear increase in membrane localization of LUVs. Furthermore, quantitative membrane analysis reveals that the LUV intensity is significantly higher when using 1 μM DNA than 0.5 μM DNA ($p<<0.001$). The data in fig. 5.6E underlines why population statistics can be essential for analyzing GUV data sets. While vesicles with similar LUV intensity exist in both populations, a statistical difference between the two populations can only be proven when a large number of vesicles is analyzed. In this way, high-throughput membrane analysis helps to quantitatively investigate the effect of experimental parameters on GUV membrane studies.

In the second example of population analysis, we perform an encapsulation analysis using the Encapsulation Analysis module in DisGUVery. Encapsulation of molecules, proteins, vesicles and even living cells inside GUVs is becoming more and more important as GUV-based reconstitution experiments are increasing in complexity[80, 92]. Besides controlling which type of molecules end up in the GUVs, also their concentration and stoichiometry often need to be regulated in order for them to function properly. It is essential to evaluate the quality of encapsulation, as this varies substantially between experiments, depending strongly on the way the GUVs are produced as well as on the molecule that needs to be encapsulated [16, 175, 276] (see also chapter 3 and chapter 4). When the encapsulated molecule can be visualized with fluorescence microscopy, the encapsulation efficiency can be determined as the distribution of internal fluorescence of the encapsulated molecule across the GUV population. To demonstrate this, we encapsulated monomeric actin in GUVs using the continuous Droplet Interface Crossing Encapsulation (cDICE) technique [3] following the protocol outlined in chapter 3. In this experiment, 10% of the actin monomers were labelled with Alexa 488 to allow for fluorescence visualization. Vesicles were imaged in epifluorescence microscopy to capture the signal of the entire vesicle volume in a single frame. From fig. 5.6F-H, it can be seen that the actin signal is strongly enhanced inside the GUVs as compared to the outer solution, and that the observed fluorescence varies among vesicles. To quantify the encapsulation

efficiency, we first detected vesicles based on the membrane signal by means of the FF detection method (fig. 5.6I). The advantage of using FF detection is that detected masks directly match the projected shape of the vesicle lumen, independent of vesicle shape and size. Using the output of the FF detection, we extracted the mean intensity of both the actin and the membrane signal for each vesicle. Furthermore, in each image, we determined the background signal for each imaging channel by taking the mode of the intensity histogram. Background signals were subtracted from the mean intensity per vesicle to finally yield the corrected mean intensity per vesicle. In total, we analyzed 329 vesicles in 22 images of one preparation. In fig. 5.6J we show the distribution of the corrected mean intensities for actin and the membrane. Note that in the epifluorescence imaging mode, the fluorescence emission from the entire focal volume is projected onto the imaging plane. Since the focal depth of the system is larger than the vesicle size, we expect a clear dependency on the vesicle size for any fluorescent molecule distributed in the volume of the GUV. In contrast, the membrane fluorescence signal is localized in the surface area of the vesicle, meaning that always the same volume of fluorescent membrane probes is projected onto the focal plane, independent of vesicle size. As a result, when we plot the mean intensity as a function of radius, we can easily distinguish encapsulated proteins from those that localize on the membrane. This offers an alternative route to probe fluorescence localization despite the lower depth-sectioning of epifluorescence imaging compared to confocal microscopy, enabling faster image acquisition and facilitating the screening of large datasets. We observe the expected linear trend for the intensity of encapsulated actin as a function of GUV radius (fig. 5.6J, dashed line) indicating that actin is distributed through the vesicle volume. The membrane mean fluorescence, on the other hand, shows no dependency on the vesicle radius, confirming that the fluorescent probe is membrane-bound. Furthermore, the mean intensity spread within the same vesicle size is larger for actin than it is for the membrane, reflecting the variability from protein encapsulation across vesicles. This analysis yields a relative measure of variations in encapsulation efficiency among GUVs, which, once combined with a calibration, could be used to evaluate absolute concentrations inside GUVs.

5.3. CONCLUSION

Giant Unilamellar Vesicles have become a widely used system for research in biophysics and synthetic biology. As the versatility and complexity of applications grow, and in concert the number of GUV formation methods, it becomes increasingly important to perform rigorous and standardised quantitative analyses. Here, we presented DisGUVery, an open-source software that we have developed for the high-throughput detection and analysis of GUVs in a wide range of microscopy images.

Since the detection of GUVs is the first step in any type of analysis, we have done an in-depth characterisation of the object detection algorithms that we have adapted and implemented. Our results show that each detector can be used as a filter for specific vesicle types, and that we are able to overcome the influence of imaging source by careful selection of the detector. By testing and demonstrating detection in a broad range of typical GUV samples, we show that DisGUVery fits in with many areas of GUV research. So far, the simplicity of GUVs combined with our hands-on experience in GUV research

have allowed us to develop lightweight algorithms with good detection performance. However, we note that with increased morphological complexity, it might be necessary to use more complex detectors, such as supervised machine learning. Even then, our software can serve as an accessible basis for generating training data sets for machine learning, thanks to the automated high-throughput segmentation algorithms.

As many GUV studies rely on shape and fluorescence of the membrane, we implemented a set of tools for membrane segmentation, which can be chosen depending on the spatial accuracy needed. Notably, we developed a membrane contour tracking method by coupling an edge detector with a directional search algorithm that takes advantage of the unique intensity profile of the membrane fluorescence. Furthermore, we showed how a contained membrane segmentation can easily identify local deformations and be less influenced by the background signal, when compared to a user-defined ROI that segments the membrane. Nevertheless, we illustrated how even a basic segmentation, in combination with high-throughput analysis, can identify statistical differences between GUV populations. Although we focused here on the intensity of the membrane, note that DisGUVery also allows to obtain the angular and radial intensity profiles of any imaging channel, allowing the user to study spatial distribution of encapsulated content. Altogether, the membrane analysis modules can be used to extract a wide range of vesicle properties, including GUV shape, internal fluorescence, membrane localisation of fluorescent proteins, or formation of internal structures. As such, the software can be used for all sorts of assays, such as membrane permeabilization studies, reconstitution of cytoskeletal networks, microfluidic vesicle production, GUV deformation studies, or membrane fusion assays. Although DisGUVery has been developed originally for detection and analysis of vesicles, the software might be equally useful for data analysis in other research domains involving similar types of microscopy data, such as colloidal and interfacial science.

Concluding, DisGUVery offers an accessible way to perform fast but thorough quantitative analysis of GUV microscopy images. By combining versatile vesicle detection and analysis algorithms, the software can robustly be employed for any type of GUV research. This makes DisGUVery a powerful tool that will help the field to progress towards a more quantitative, population-based research.

5.4. MATERIALS AND METHODS

5.4.1. SOFTWARE ALGORITHMS

IMAGE PREPROCESSING

DisGUVery includes two image preprocessing options to aid vesicle detection: smoothing and membrane enhancement. Image smoothing is performed by convolution of the original image with a 2D Gaussian function of user-defined kernel size. Membrane enhancement is based on the subtraction of a second smoothed image (the subtraction image) from the first smoothed image. To this end, the user specifies a kernel size (typically 10-20 times larger than the kernel used for smoothing the image) to create the subtraction image also based on Gaussian smoothing, which is used to eliminate large scale intensity variations. The subtraction image is then subtracted from the smoothed image and all pixels with negative intensity values are set to zero, creating the membrane enhanced image.

CIRCULAR HOUGH TRANSFORM DETECTION

We implemented a Circular Hough Transform detection method [435, 446] based on the `HoughCircles` function from the `OpenCV` package[447]. The procedure consists of two steps: edge detection and circle detection. First, edges are detected in an image of size $x \times y$ using a classical Canny edge detector. The user can pass an edge threshold to the detector to filter out low quality edges. Using the detected edges, the Circular Hough Transform is applied for circle detection. The method is well described in ref. [446]. In short, circle detection is done via a 'voting' procedure by voting in the Hough parameter space. To this end, the user passes the minimum and maximum radius for detection, after which the range is discretized into N radii. A three-dimensional accumulator array of the size (x, y, N) is created to record votes, where high numbers of votes represent the circle centers. Initially, the value of all cells in the accumulator matrix is set to zero, after which the voting procedure is done as follows. For each edge point (i, j) in the original space, a circle is formulated in the Hough parameter space centered at (i, j) with a certain radius r. For each point (a, b) in parameter space that the circle passes through, i.e. that fulfills $(i-a)^2 + (j-b)^2 = r^2$, the voting number is increased by one in the accumulator matrix in the corresponding point (a, b, r). In this way, the accumulator value increases for points where circles in Hough parameter space intersect, which correspond to the circle centers in original space. The procedure is repeated for all radii r. Finally, the local maxima in the matrix are detected to yield the circle center coordinates (x_c, y_c) and their radius r_v. By passing a Hough threshold to the detector, the user can selectively detect circles with the highest number of votes, corresponding to the highest quality circles. In addition, the user inputs a minimum radius between circles, which is used to prevent detection of multiple local maxima per GUV. Detected circles are drawn in the main display. It should be noted that detected radii and vesicle centers are approximations because of two reasons. One, the possible radii are discrete values, following from a discretization of the radii between r_{min} and r_{max} into N values. Two, the membrane signal in the input image represents an intensity maximum, meaning it provides two edges (an inner and an outer) for the Canny edge detector. Since both edges are close together, voting results from both edges might overlap, introducing an inaccuracy in the accumulator values. Refinement of spatial detection of GUV center and image can be done with Refined Membrane Detection.

MULTISCALE TEMPLATE MATCHING DETECTION

DisGUVery's Multiscale Template Matching detection is based on the `OpenCV` [447] function `matchTemplate` with an added template re-scaling option to enable size-invariant detection. First, a template needs to be selected: a template can be either defined manually from the input image, or a template image can be loaded. For template detection with a template of size $w \times h$ in an image of size $x \times y$, the function compares overlapped patches of size $w \times h$ of the image against the template. By default, the comparison method `cv2.TM_CCOEFF_NORMED` is applied where a high matching coefficient results in a high comparison value. A map of the comparison results is created by storing the comparison results in an array of size $(x-w+1) \times (y-h+1)$. Object detection is then performed by finding the local maxima in the comparison map. The user can pass a matching threshold to retain only high-quality results. Multiscale template matching is performed by resizing the template with a scaling factor a using `OpenCV` function `resize` to templates of size $aw \times ah$. Scaling factors are computed by the software from the user inputs minimum rescaling factor, maximum rescaling factor, and number of scales. The output generated by the software are the object locations x_c, y_c and the bounding boxes of size $aw \times ah$.

FLOODFILL DETECTION

Vesicle detection by Floodfill is implemented as follows. It is highly recommended to start with membrane enhancement for FF detection, as detection relies on absolute intensity differences.

The most important step for Floodfill detection is the binarization of the image. The image is first thresholded with a user-defined relative threshold value. The absolute threshold is computed by multiplying the input value with the median of all positive pixels (intensity higher than 0). Then, the absolute threshold is used to binarize the image, the result of which can be inspected in the GUI. Here, foreground pixels or membrane pixels have intensity value 1 (white), while background pixels have value 0 (black). DisGUVery's FF detection works by flooding background pixels in the outer solution which are connected using the `FloodFill` function of the `OpenCV` package. When pixels are flooded, their intensity is set to a different number. In this way, all background pixels in the exterior solution get a different value from background pixels in the GUV lumen and thus can the GUV interiors be distinguished. Flooding is started from a single point, the seed point, which must be located in the outer solution. After flooding, a binary mask of the size of the image is created where pixels belonging to the lumen of all GUVs are set to 1. The lumen masks will naturally contain holes, due to interior membrane structures or noise. These holes are filled by performing a second floodfilling step on the binary mask, flooding all pixels in the image except for the GUV interiors and the holes in the GUV masks. The filled GUV masks can then be collected by selecting all pixels with intensity value 0 and 1 and are stored in a second binary mask. All connected pixels are detected as a single GUV, after which objects smaller than the user input minimal area are discarded, and each separate GUV is labeled as a different object. Finally, DisGUVery creates as output the x, y matrix containing the labeled objects.

BASIC MEMBRANE ANALYSIS

Basic Membrane Analysis can be performed after vesicle detection. First, for each detected vesicle a region of interest (ROI) is created around the membrane based on the detection results. The ROI can be inspected in the image, after which angular and radially integrated intensity profiles are extracted from the ROI. The region of interest with a selected width w is defined differently dependent on the GUV detection method used. For a vesicle detected by CHT with radius r, two concentric circles are drawn from the vesicle center with $r_{in} = r - w/2$ and $r_{out} = r + w/2$ that together form a ring-like ROI. To obtain the angular intensity profile, the area confined by the inner and outer edge is divided into n_a angular slices calculated from the user input angular width per slice dθ (°). From each slice, various region properties for fluorescence intensity (minimum, maximum, average, background-corrected average and sum) are obtained. Furthermore, the radial distance of the ROI inner and outer edge, $r_{in}(\theta)$ and $r_{out}(\theta)$, respectively, can be extracted. Similar to extracting the angular intensity profile, the radial intensity profile is obtained by specifying the radial integration width dr (pixel), used to calculate the number of radial rings n_r. Integrating over all angles, the software then extracts region properties for all radial rings from the vesicle centre $r_0 = 0$ to $r_{out}(\theta)$. For each radial ring, various intensity metrics are obtained (minimum, maximum, average, background-corrected average and sum).

REFINED MEMBRANE DETECTION

The Refined Membrane Detection method consists of two steps: first all edges in the image are detected (the edge tracking step), then edge points are chained together and assigned to either the outer or the inner edge of a GUV membrane (the chaining step). Edges are tracked with a modified Canny edge detection algorithm with the wavelet transform (WT) as outlined in ref. [448]. By using the first derivative of a Gaussian in the WT, the 2D smoothed gradient of the image is computed [449]. In addition, for each point in the image the amplitude of the gradient (the WT modulus) and its direction (the WT argument) are obtained. These are passed to a modified Canny edge detector [333] in order to compute the edges. At each image coordinate, a point is considered to be an edge if the wavelet transform modulus is a local maximum, or the intensity in that point has the steepest gradient, when compared to its neighbouring pixels. The comparison is

made with the pixels that follow the argument of the wavelet transform at that point, that is, in the direction of the steepest gradient which is across the membrane. To distinguish 'true' edges from falsely detected edges, points are chained together and a double hysteresis algorithm is applied to connect weak with strong edges[333]. This process finally results in an edge mask that contains all the true edges of the entire image. For the second step, we developed a directional search algorithm to chain edge points and to assign them to either the inner or the outer edge of the membrane. The search occurs at each detected edge point, chosen at random, by chaining the neighbouring points contained within a defined search box centred around the point of interest and typically of aspect ratio > 2:1 (length: width). The orientation of the box is determined as orthogonal to the argument of the wavelet transform at the chosen point. Given that the WT argument will follow the direction where the gradient is steeper, thus across the membrane, its orthogonal direction will likely follow the points along the membrane. Lastly, all chains are measured by the number of points within, and the two longest chains will be assigned to the outer and inner edge of the membrane (fig. 5.5B). This directional search with a bounding box allows to chain points together without the need of them being connected. Furthermore, it enables the user to distinguish the enclosing GUV membrane, which is the membrane separating the inner from the outer solution, from internal membranes and secondary membrane structures such as tubes. Dependent on the membrane appearance, for example its thickness in the image, or the presence of secondary membrane structures, the user can define the length and width of the search box to fine-tune the tracking results. Finally, two lists of x and y coordinates are produced for the inner and outer edge of the GUV membrane. By calculating the centre of mass of the detected contours, the vesicle centre is refined. The angular profiles of radial distance from the vesicle centre to the inner and outer edge are calculated and can be exported. Furthermore, an ROI is defined between the two membrane edges, which can be used to extract angular and radial fluorescence profiles such as described above for BMA.

ENCAPSULATION ANALYSIS

The Encapsulation Analysis module uses masks of GUV interiors to collect all fluorescence intensities from under those masks. The user has various options to create the masks. First, the user can directly use the results from one of the three GUV detection methods as a mask. This yields circular masks for CHT, rectangular masks for MTM, and free shape masks for FF detection. Depending on the detection method chosen and the spatial accuracy required, the user can choose to perform an additional refinement step to refine the shape of the mask. In this refinement step, the image is first segmented using rectangular bounding boxes defined by the vesicle detection results. Then, for each GUV in its bounding box, FF detection is applied as described above to yield masks with fitting shape.

5.4.2. EXPERIMENTAL DATA

CHEMICALS AND PROTEINS

From Avanti Polar Lipids we obtained the lipids L-α-phosphatidylcholine (eggPC), 1,2-dioleoyl-sn-glycero-3-phosphocholine (DOPC), 1,2-distearoyl-sn-glycero-3-phospho-ethanolamine-N-[methoxy(polyethylene glycol)-2000] (PEG2000-DOPE), 1,2-dipalmitoyl-sn-glycero-3-phosphocholine (DPPC), 1,2-dioleoyl-sn-glycero-3-phosphoethanolamine-N-(Cyanine 5) (Cy5-DOPE), 1,2-dipalmitoyl-sn-glycero-3-phosphoethanolamine-N-(7-nitro-2-1,3-benzoxadiazol-4-yl) (NBD-DPPE) and 1,2-dioleoyl-sn-glycero-3-phosphoethanolamine-N-(lissamine rhodamine B sulfonyl) (Rhodamine-DOPE). The lipids ATTO 488 DOPE and ATTO 655 DOPE were obtained from ATTO-TEC GmbH (Siegen, Germany). All lipids were stored in chloroform at -20 °C under argon. The chemicals D-(+)-glucose, sucrose, Tris-HCl, KCl, 1-octanol, glycerol, Poloxamer 188, cholesterol, dithiothreitol (DTT), protocatechuic acid (PCA) and the proteins protocatechuate dioxyge-

nase (PCD) and β-casein were obtained from Sigma Aldrich. For gel-swelling, we used poly-vinyl alcohol (PVA) of 145 kDa, 98% hydrolysed, obtained from VWR, Amsterdam, the Netherlands. Actin for the encapsulation experiments was purified in house as described in ref. [450]. Alexa-488 labeling of actin was done in house following ref. [406].

GUV IMAGING

The protocols for GUV formation are described below. Depending on the formation method, produced GUVs were transferred to one of two types of imaging chambers: small $20\mu L$ wells assembled by using silicone gaskets, or $150\mu L$ wells made by using PCR-tubes. The small wells were used for samples of high GUV density, such as gel-swelling experiments, while the large wells were used to image GUVs produced at lower concentrations such as eDICE. For the preparation of small imaging wells, we first rinsed a 24x50mm cover glass (No. 1.5H, Thorlabs) with ethanol, water and ethanol, and then blow-dried it with nitrogen. Then, an 8-well silicone spacer (6 mm diameter x 1 mm depth, CultureWell^{TM}, Grace Bio-Labs) was pre-wetted with isopropanol, dried with nitrogen gas and placed on top of the glass. To each well, we added 15 μL of β-casein solution (1 mg/mL β-casein, 10 mM Tris-HCl pH 7.4) and let it rest to passivate the glass surface against membrane adhesion. After 15 minutes, the solution was removed with a tissue and the chambers were blow-dried with nitrogen gas. We added to each well first 15 μL of an isotonic glucose solution and then 5 μL of vesicle solution. Due to their higher density, vesicles sunk to the bottom of the chamber, which facilitated imaging. The chamber was then closed from the top with a glass slide (1mm thickness, Thermo Scientific) to prevent solvent evaporation and minimize flow in the sample. Large imaging chambers were made by gluing a PCR tube with a cut bottom upside down on a 24x50 mm coverslip that had been cleaned as described above. The chamber was passivated by treating it for 15 minutes with a 1 mg/mL β-casein solution in milliQ water containing $10mM$ Tris-HCl at pH 7.4, after which the chamber was rinsed with milliQ water and blow-dried. Then, $150\mu L$ of vesicle sample was added and the chamber was closed by placing the lid of the PCR tube on top.

All GUV images (except fig. 5.3C and fig. 5.5E, as described below) analyzed in this work were obtained using an inverted microscope (Nikon Ti Eclipse) with a digital CMOS camera (Orca Flash 4.0). The different objectives and imaging settings used for the respective experiments are specified below.

GUV FORMATION PROTOCOLS

The vesicles that were used to illustrate DisGUVery's workflow (fig. 5.1A), to test detection (fig. 5.2), the high density GUVs growing on top of a hydrogel (fig. 5.3A) and the compartmentalized vesicle (fig. 5.3D) have been produced by PVA(poly-vinyl alcohol)-assisted swelling following ref. [76] with minor modifications. In short, glass coverslips (24 x 24 mm, Menzel Glaser) were rinsed with water and ethanol, blow-dried with nitrogen, and plasma-treated for 30 seconds to create a clean and reactive surface. Then, $100\mu L$ of a viscous 5% (w/v) PVA solution was spread over the coverslip to create a thin layer. The coverslip was baked in the oven at 50 °C for 30 minutes to form a gel. After baking, $10\mu L$ lipids in chloroform at a total lipid concentration of $1mg/mL$ was spread over the gel using a Hamilton syringe. Typically, membranes consisted of 99.9% EggPC lipids and 0.01% fluorescent ATTO 655 DOPE. GUVs were swollen for 60 minutes in a swelling solution containing 200 mOsm sucrose and 10 mM Tris-HCl at pH 7.4. After formation, GUVs were harvested and transferred to a small imaging well (described above) containing an isotonic glucose solution (200 mOsm glucose, 10 mM Tris-HCl at pH 7.4). The images in fig. 5.1, fig. 5.2 and fig. 5.3D were taken using a 100x oil immersion objective with a phase ring (NA 1.45, Ph 3, Nikon) at an exposure time of $100ms$ for all imaging methods used. For epifluorescence imaging, the sample was illuminated with monochromatic LED light of $640nm$ (Lumencor Spectra Pad X), at 25% of the maximum

power. Confocal images were gathered on the same imaging set-up using a spinning disk confocal (Crest X-light) with pinhole size 70μm and illumination at 75% of full intensity. Phase contrast images were acquired with the microscope's DIA illuminator switched on at a voltage of 10.5V and using the corresponding phase mask in the microscope's condenser. For the image shown in fig. 5.3A, the coverslip with PVA gel and dried lipids on the microscope. The image was taken in epifluorescence mode using a 60x long working distance water immersion objective (CFI Plan Apochromat VS 60x WI, Nikon) 10 minutes after addition of the swelling buffer.

Actin-deformed GUVs shown in fig. 5.3C and also in fig. 5.5E were produced by F.C. Tsai as described in detail in ref. [109]. In short, GUVs of a lipid composition of DOPC:Rhodamine-DOPE: PEG2000DPPE in a molar ratio of 94.8:0.2:5 were produced by gel-assisted swelling on top of an agarose gel. Actin was encapsulated by adding it to the swelling solution at a concentration of 12μM, and at a 5:1 molar ratio with respect to fascin. 20-30 mol% of the actin was labeled with Alexa488 to allow fluorescence visualization. After formation, GUVs were harvested and imaged by confocal fluorescence microscopy. Images were taken with a Nikon Eclipse Ti inverted microscope equipped with a Nikon C1 confocal scanhead, a 100x NA1.4 Plan Apo oil immersion objective and lasers with wavelengths 488 nm and 543 nm.

Microfluidic vesicle production (fig. 5.3B) was done with the octanol-assisted liposome assembly (OLA) technique following ref. [77] (see chapter 4). Lipids were used in a composition of DOPC: Rhodamine DOPE in molar ratio 99.5:0.5. The inner aqueous solution consisted of 5% (v/v) glycerol in milliQ water, and the outer solution of 15 % (v/v) glycerol and 5% (w/v) Poloxamer 188. GUVs were imaged directly on-chip in the post-formation channel with a 10x air objective (Plan Fluor, NA 0.3, Nikon).

Phase-separated GUVs (fig. 5.5) were produced by gel-assisted swelling as described above, but with minor modifications. Lipids were dried in a mixture of DOPC:DPPC:cholesterol: NBD-DPPE:ATTO655-DOPE in molar ratio 31.8:48:20:0.1:0.1. In addition, swelling was done in a 37°C room to be above the membrane transition temperature, and thus to ensure proper mixing of lipids during formation. GUVs were imaged in the small imaging chambers.

DNA-mediated vesicle binding was performed following ref. [8] and ref. [91] . GUVs with a membrane composed of DOPC:ATTO 488 DOPE in molar ratio 99.5:0.5 were produced by gel-assisted swelling as described above in a solution containing 100$mOsm$ sucrose, 100mM KCl and 10mM Tris-HCl at pH 7.4. LUVs were produced by adding lipids in chloroform to a Pyrex glass tube, in a lipid composition of DOPC:ATTO 655 DOPE as 99.95:0.05 (mol/mol). After drying lipids for 1 hour in a vacuum desiccator, the dried film was resuspended by vortexing for 2 minutes in a solution containing 100$mMKCl$ and 10mM Tris-HCl at pH 7.4 to a final lipid concentration of 0.5mg/mL. To produce 200nm LUVs, the suspension was extruded (Mini Extruder, Avanti Polar Lipids Inc.) 21 times over a polycarbonate membrane with pore seize 200nm (Nuclepore, Whatman). To introduce specific binding between LUVs and GUVs, we used two complementary DNA strands (DNA1 and DNA1$'$) with a cholesterol moiety for membrane anchoring[8] (biomers.net, Ulm, Germany). The DNA strands were tagged with cholesterol on opposite ends to allow antiparallel binding, as is typically used for DNA-mediated membrane fusion assays [9]. The full sequences were taken from ref. [91] and read:

$$\text{chol-DNA1}: 5' - \text{TGGACATCAGAAAGGCACGACGA-cholesterol-TEG} - 3'$$
$$\text{chol-DNA1}': \text{cholesterol-TEG-}5'\text{TCCGTCGTGCCTTATTTCTGATGTCCA} - 3'$$

Note that the sequences do not fully overlap, which results from an error in the original publication (K. Jahnke, personal communication, 2021). For one hour, LUVs were incubated with 1μM of chol-DNA1, and GUVs with 1μM of chol-DNA1$'$. After DNA incbuation, GUVs and LUVs were mixed, left to bind for one hour, and finally imaged in the PCR tube imaging chamber in a solution containing 100$mOsm$ glucose, 100$mMKCl$

and 10mM Tris-HCl at pH 7.4. Images were taken in epifluorescence mode using a 100x oil immersion objective (CFI Plan Apochromat VC 100x oil, NA 1.40, Nikon) with an exposure time of 100 ms at 508 nm and 640 nm to image LUVs and GUVs, respectively.

Vesicles containing monomeric actin were produced as in ref. [175] . Lipids were mixed in a molar ratio of DOPC:PEG2000-DOPE:Cy5-DOPE 99.89:0.01:0.1. We encapsulated 4.4 μM actin in G-buffer of which 10% was labeled with Alexa-488 to allow fluorescence visualisation. The encapsulated solution also included 1mM dithiothreitol (DTT), 1μM protocatechuic acid (PCA) and 1μM protocatechuate dioxygenase (PCD). Epifluorescence images were taken with a 100x oil immersion objective (CFI Plan Apochromat VC 100x oil, NA 1.40, Nikon) at a wavelength 640 nm with 10% and 100 ms exposure time, and at 470 nm with 20% and 500 ms exposure time to visualise the vesicle membrane and actin content, respectively.

5.5. ACKNOWLEDGEMENTS

We thank Martin Depken for useful discussions on evaluation of vesicle detection performance, Britta Bor, Gerard Castro Linares and Lucia Baldauf for performance evaluation of vesicle detection, Tom Aarts and Lucia Baldauf for images on DNA-mediated vesicle binding and Jeffrey den Haan for protein purification and labeling. This project was partly funded by 'BaSyC - Building a Synthetic Cell' Gravitation grant of the Netherlands Ministry of Education, Culture and Science (OCW) and the Netherlands Organization for Scientific Research (NWO).

5.6. SUPPORTING INFORMATION

5.6.1. MEMBRANE ANALYSIS METRICS

DisGUVery's membrane analysis modules Refined Membrane Detection (RMD) and Basic Membrane Analysis (BMA) support the use of different metrics to extract membrane fluorescence. This section should serve as a guide to choose the right metric according to the imaging source and research goal.

ONE-DIMENSIONAL INTENSITY PROFILE

We consider a lipid bilayer membrane dyed with a fluorescent lipid. Since the membrane is thinner than the diffraction limit, the fluorescence intensity profile is given by the point spread function (PSF). We assume the PSF to be a Gaussian function, for a one-dimensional signal given by:

$$I(x) = Ae^{-\frac{(x-r)^2}{2\sigma^2}} \tag{5.2}$$

where x is the radial distance with respect to the GUV centre, r is the GUV radius, A is the amplitude of the signal and σ is the standard deviation, or the width of the point spread function. σ can be determined experimentally by fitting a Gaussian curve to the one-dimensional data.

In practice, fluorescence imaging is subjected to various sorts of noise (see fig. 5.7A). First, there is the camera read-out noise which contributes to a random noise in each pixel, $I_{cam}(x)$. Second, there is noise caused by out-of-focus fluorescence, ambient light and excitation light, which together add up to a minimum level of background fluorescence $I_{bg}(x)$. We split this background fluorescence in two contributions: a contribution $I_{bg,0}$ that is constant over the entire image, originating from e.g. excitation light and ambient light, and a varying contribution caused by out-of-focus fluorescence, $I_{bg,z}$. Considering the membrane signal $I(x)$ of a particular GUV, the most dominant contribution to $I_{bg,z}$ comes from the out-of-focus membrane fluorescence of that GUV, which is high in the GUV interior and low outside the vesicle. We therefore write $I_{bg,z}$ as a Heavyside step function, with the interior out-of-focus fluorescence depending on the z-resolution of the system c (between 0 and 1, where 1 means good z-resolution, e.g. scanning confocal microscopy) as well as the membrane signal as:

$$I_{bg,z}(x) = \begin{cases} (1-c)A, & \text{if } x < r \\ 0, & \text{otherwise} \end{cases} \tag{5.3}$$

Summing up, we obtain the total noise contribution:

$$I_{noise}(x) = I_{cam}(x) + I_{bg,0} + I_{bg,z}(x) \tag{5.4}$$

Including the noise in the experimentally obtained signal, we write:

$$I(x) = Ae^{-\frac{(x-r)^2}{2\sigma^2}} + I_{cam}(x) + I_{bg,0} + I_{bg,z}(x) \tag{5.5}$$

From the fluorescent signal, various metrics can be calculated to report a membrane intensity. The membrane is first segmented by an inner radius r_{in} and an outer radius

r_{out}. For a one-dimensional profile, the software can then obtain the sum of the signal $\sum(I(x))$ between r_{in} and r_{out}, given by:

$$\sum I(x) = \sum_{x=r_{in}}^{r_{out}} (Ae^{-\frac{(x-r)^2}{2\sigma^2}} + +I_{cam}(x) + I_{bg,0} + I_{bg,z}(x))´x \tag{5.6}$$

where $´x$ is the integration unit, typically the size of a pixel. Integration is done over a total number of N pixels, defined by $N´x = r_{out} - r_{in}$. Using N, we can simplify eq. (5.6) to:

$$\sum I(x) = NI_{bg,0} + \sum_{x=r_{in}}^{r_{out}} (Ae^{-\frac{(x-r)^2}{2\sigma^2}} + I_{cam(x)} + I_{bg,z}(x)))´x \tag{5.7}$$

The average signal $\bar{I}(x)$ can be calculated from eq. (5.7) by dividing over the number of pixels:

$$\bar{I}(x) = I_{bg,0} + \frac{1}{N}\sum_{x=r_{in}}^{r_{out}} (Ae^{-\frac{(x-r)^2}{2\sigma^2}} + I_{cam(x)} + I_{bg,z})´x \tag{5.8}$$

Since I_{cam} is random, when integration is done over a large number of pixels, or large N, $\sum_{x=0}^{N} I_{noise}(x) \to 0$ leaving:

$$\sum I(x) = NI_{bg} + \sum_{x=r_{in}}^{r_{out}} (Ae^{-\frac{(x-r)^2}{2\sigma^2}} + I_{bg,z})´x \tag{5.9}$$

$$\bar{I}(x) = I_{bg} + \frac{1}{N}\sum_{x=r_{in}}^{r_{out}} (Ae^{-\frac{(x-r)^2}{2\sigma^2}} + I_{bg,z})´x \tag{5.10}$$

As can be seen from eq. (5.9) and eq. (5.10), both the summed membrane intensity and average membrane intensity are influenced by the background signal I_{bg} and thus require background subtraction. In addition, we see the average signal is dependent on the number of pixels. This means that care should be taken when the number of pixels differs between vesicles, e.g. because vesicles have different sizes. Furthermore, it is important to note that when N is small, e.g. using a narrow membrane segmentation, I_{cam} can have a dominant contribution.

Another descriptor that is often used to quantify membrane fluorescence is the maximum intensity. While the maximum intensity is a parameter that is easy to extract, its value is affected by pixelation and noise effects. For a continuous signal without noise, the maximum is simply given by the signal amplitude A. However, because of pixelation in the image, we do not find the fluorescence intensity exactly at the membrane position, but at a position that is at maximum x_p separated from r, where x_p is the size of a pixel. For a signal without noise, the maximum intensity that is seen is given by:

$$I_{max} = Ae^{-\frac{x_p^2}{2\sigma^2}} \tag{5.11}$$

Assume we have a 100x objective with a pixel size of $60nm$ and a PSF of $240nm$, and assume that σ is half the width of the PSF, then $I_{max} = 0.9A$. However, for a typical 10x objective with a pixel size of $600nm$ and a PSF of $1.2\mu m$, $I_{max} = 0.6A$. Resolution can thus have a serious impact on the maximum intensity determined from a one-dimensional

profile. Moreover, random noise in the image can affect the measured membrane position. Suppose that we have 20% noise (with respect to A), we can calculate the possible shift in membrane position $\acute{}x$ due to addition of this noise. The signal with noise is given by:

$$I(\acute{}x) = Ae^{-\frac{\acute{}x^2}{2\sigma^2}} + 0.2A \tag{5.12}$$

We then find the shift in membrane position by identifying the $\acute{}x$ for which $I(\acute{}x) = A$, finally yielding $\acute{}x = 0.6\sigma$. For a noise level of 50%, this yields $\acute{}x = 1.2\sigma$. Assuming a σ of 2 pixels, noise can cause a shift of one or two pixels dependent on the imaging settings.

TWO-DIMENSIONAL INTENSITY PROFILE

When considering the two-dimensional intensity profile, two other effects of pixelation must be taken into account.

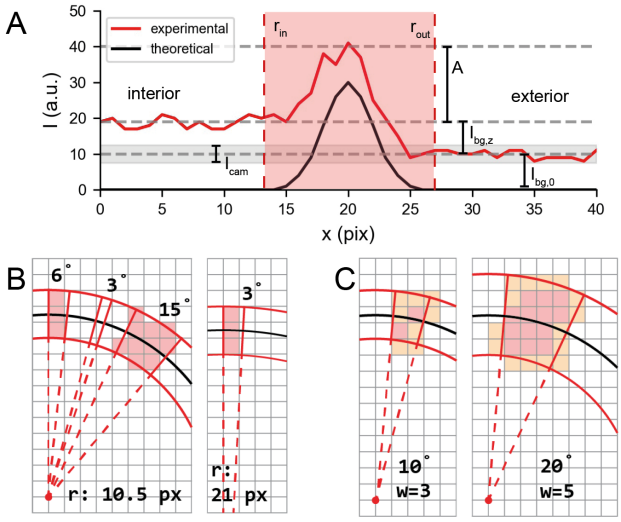

Figure 5.7: **Discretisation artefacts in membrane analysis.** (A) Theoretical (black) and predicted experimental (red) one-dimensional membrane intensity profile of a GUV. The experimental profile is calculated with eq. (5.5) and eq. (5.3). While the theoretical profile is a simple Gaussian, the experimental profile is subjected to noise of various origins. Here, the radius $r = 20px$, $\sigma = 2px$, $A = 30$, $I_{cam} = 5$, confocality factor $c = 0.7$, and $I_{bg,0} = 10$. The red shaded part denotes the segmented area based on $r_{in} = 13$ and $r_{out} = 27$. (B,C) Discretisation effects in two-dimensional signal analysis. Segmentation lines are shown in red, the GUV membrane in black. (B) The apparent GUV size in the image imposes a minimum angular separation for integration. Integration should not be done with slices smaller than the pixel size. For a small GUV with a radius of 10.5 pixels, the minimum θ is 6°(left), while a more precise angular separation of 3° can be used for a vesicle twice as large (right). (C) Edge effects impact intensity analysis. Pixels located at the edge of the segmentation area (yellow pixels) are more prominent for smaller segmentation areas (left) as compared to larger regions (right). The size of the segmentation area is defined by the width of the ring as well as the angular separation.

First, angular slices must have a minimal thickness to extract pixel intensities from the slice (fig. 5.7B). While thinner slices approach one-dimensional intensity profiles,

the slice thickness decreases when getting closer to the vesicle center. We compute the minimal angular separation θ where the slice thickness is larger than a pixel at a radial distance x. With the circle perimeter at a radial distance x given by $L = 2\pi x$, and the number of slices given by $N = 360/\theta$, the perimeter of an angular slice is $\acute{}L = \frac{2\pi x}{N}$. For $\acute{}L > 1$, we need $\theta > \frac{180}{\pi x}$. For a radial distance of 10 pixels, that is an angular separation of at least 6°. This effect is especially important for smaller vesicles or lower magnification images.

Second, the angular slice is drawn with four continuous lines, meaning that the edges of the mask run right through pixels(fig. 5.7C). This means that pixels that are partly outside the mask are weighed disproportionally into the average, while pixels partly inside the mask might be ignored. This effect is stronger for smaller slices. To get an idea of the number of pixels within the mask versus the number of pixels under the edge of the mask, we calculate the area and the perimeter of the angular mask. The area of the mask can be calculated by:

$$A_{slice} = \frac{\theta}{360}(A_{c,out} - A_{c,in}) \tag{5.13}$$

$$A_{slice} = \pi\frac{\theta}{360}(r_{out}^2 - r_{in}^2) \tag{5.14}$$

The perimeter, or the number of pixels at the borders of a slice can roughly be calculated by summing up the length of the four sides:

$$N_{edge} = 2(r_{out} - r_{in}) + \pi\frac{\theta}{360}(r_{out} + r_{in}) \tag{5.15}$$

Suppose we have a vesicle of $10\mu m$ radius. When imaged with an 100x objective with pixel size $60nm$ and a PSF of $240nm$, the membrane has an apparent thickness of 4 pixels, while the distance to the center of the vesicle is 150 pixels. Using an angular separation of 5 °and a total width of 12 pixels around the membrane, $r_{in} = 140$, $r_{out} = 160$, we obtain $A_{slice}/N_{edge} \sim 4$. This means that pixels at the edges have a relative small contribution, and thus that data can safely be extracted by integration. Problems arise when the size of the object in the image decreases. If we image the same vesicle with a 10x objective with pixel size $600nm$ and PSF $1.2\mu m$, we obtain a membrane width of 2 pixels and a radial distance of 15 pixels. Now, using a ring of 3 times the membrane width gives us $r_{in} = 12$ and $r_{out} = 18$, resulting in $A_{slice}/N_{edge} \sim 0.5$. Since edge pixels would weigh disproportionally large in this situation, it would be better to extract membrane intensities with one-dimensional extraction methods.

5.6.2. SUPPORTING FIGURES

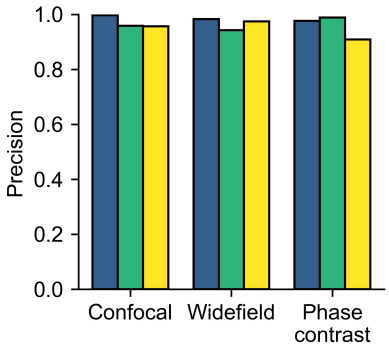

Figure 5.8: **Detection precision.** Precision of vesicle detection for different imaging types calculated from the same performance analysis results as shown in fig. 5.2G.

Category	Observer 1	Observer 2	Observer 3	Observer 4	average
Standard	93	84	103	89	92
Edge	59	59	63	68	62
Unsharp	17	13	14	18	16
Anomalous	15	61	13	32	30

Table 5.1: **GUV population sizes from detection classification.** Population sizes of vesicles in the different subcategories as counted by the four different observers in fig. 5.2H. The last column indicates the population size averaged over all observers.

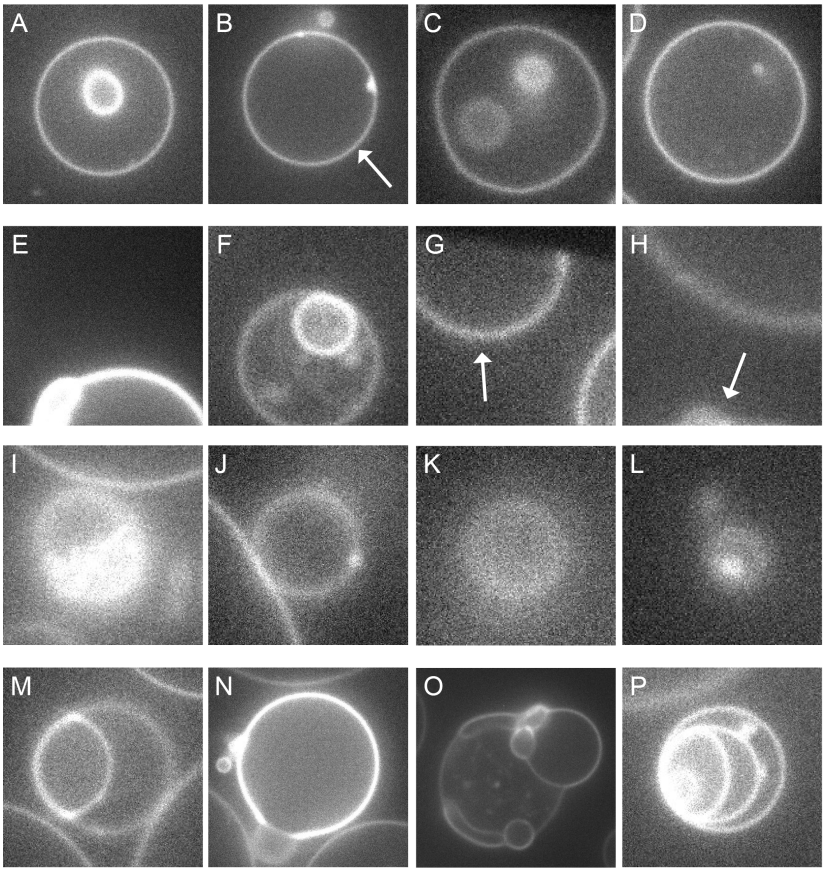

Figure 5.9: **Gallery of example vesicles from different subcategories.** In images containing multiple vesicles, the example vesicle has been indicated with an arrow. (A-D) Standard vesicles. (E-H) Vesicles at the edge of the image. (I-L) Vesicles that are out of focus. (M-P) Anomalous vesicles.

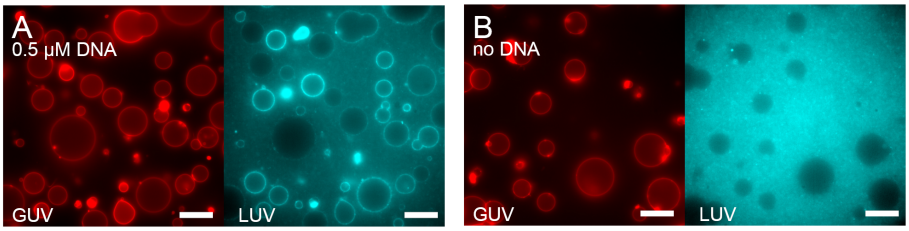

Figure 5.10: **Binding of LUVs at different DNA concentrations.** Images are epifluorescence images of Atto488 DOPE incorporated in the GUV membrane (red) and Atto 655 DOPE in the LUV membrane (cyan). Scale bar is 20 μm in all images. (A) At 0.5μM cholesterol-DNA, LUVs bound to the GUV membrane. (B) No membrane localization was observed in absence of cholesterol-DNA.

6

MEASURING MEMBRANE MECHANICS

Membrane reshaping is crucial for cellular functions like migration and cytokinesis. While we know that shaping of mammalian cells is primarily regulated by the membrane-anchored actin cortex, we still have a poor understanding of how the membrane and the underlying cortex together influence cell surface mechanics. A multitude of techniques has been developed for measuring membrane elastic moduli, of which the most popular are vesicle fluctuation analysis (VFA) and micropipette aspiration (MPA). Although these techniques have been amply employed, we found that their implementation can be rather challenging. In this chapter, we describe a detailed workflow for the experiments and analysis of both VFA and MPA measurements, while providing practical fixes for typical challenges in their implementation. We validate the quality of our new experimental setup and protocols by a series of benchmark measurements of bending moduli and stretch moduli of model lipid membranes. Finally, we describe how VFA and MPA can be employed in future to mechanically characterize synthetic cells with a reconstituted cortex, and in this way to gain a fundamental understanding of cellular shaping mechanisms.

Fluctuation data on GUVs encapsulating streptvidin and actin cortices was obtained by Sophie Sandy and Lucia Baldauf.

6.1. INTRODUCTION

Mammalian cells need to change their shape for many cellular functions. For example, during cell division, they first round up, and then deform to a dumbbell-shape, involving a progressive constriction of the neck region [451]. Migrating cells form actin-based membrane protrusions such as flat lamellipodia and thin finger-like filopodia at their leading edge [452, 453]. While cytokinesis involves membrane deformation on a length scale of micrometers, actin protrusions typically have dimensions on the order of nanometers. The mechanism by which cells are able to deform their surface over this wide span of length scales has fascinated biologists for decades.

Cell shape change involves a mechanical deformation of the cell surface. To measure and understand the mechanics of the cell surface, a multitude of techniques has been developed. The first device to measure cell surface mechanics was developed already in the 1950s by Mitchison and Swann [6]. This was only several years after the first microscopic film of cell division by Dr. Kurt Michel in 1943 [454]. Based on Michel's film, Mitchison and Swann developed the hypothesis that cell division was driven by mechanical expansion of the cell membrane. To test this hypothesis, they built a device that was able to deform the cell surface, coined The Cell Elastimeter [6]. By using a glass micropipette connected to a water reservoir, that was moveable in the vertical direction by a screw, they were able to apply a suction pressure and to draw in sea urchin eggs into the pipette. Upon further change of pressure using the screw, while following the egg deformation with an optical microscope, they were able to probe membrane deformation at a range of aspiration pressures. By aspiration, forces are primarily applied to the cell surface, allowing one to probe mechanics of the cell surface. Originating from this historic device, with remarkably little adjustments, the micropipette aspiration assay (MPA) was developed [7] that is still being used extensively nowadays. A major improvement has been more precise control of applied pressures and timing, for example by using a motorized stage for control of the water bath height [274, 455]. In addition, better microscopes are being used nowadays that give enhanced spatial resolution, such that MPA can be performed on cells that are much smaller than sea urchin eggs [456]. Furthermore, an interferometric technique was developed recently to provide real-time, sub-nanometer resolution of MPA measurements [457].

Over the years, MPA has been indispensable for the mechanical characterisation of cells [456], nuclei [458], and membranes of giant unilamellar vesicles (GUVs) [56]. Since the aspiration setup can be used to increase cell surface tension up to several mN/m, MPA can be employed to measure the membrane's mechanical response in different tension regimes. For example, one can measure the membrane's bending rigidity at low membrane tensions, the area compressibility modulus at higher membrane tensions, and even the membrane's lysis tension where the membrane ruptures [459]. Furthermore, MPA allows controlled cell deformation in combination with brightfield or fluorescence microscopy, which has opened up possibilities to study how cellular structures play a role in cell deformation [460, 461].

Despite the usefulness and wide versatility of the micropipette aspiration technique, a major drawback is the low throughput of the technique, as one typically measures one vesicle at a time. Moreover, MPA measurements require a complex experimental set-up, measurements are challenging to conduct, and interpretation can be difficult because

MPA operates in the non-linear regime. Lately, some microfluidic aspiration techniques have been developed to increase measurement throughput, where microfluidic chips allow aspiration of multiple cells simultaneously [462–464]. In addition, recent publications show automation of MPA measurements, possibly paving the way for more user-friendly experimentation [465, 466].

A much simpler technique to probe lipid membrane mechanics is called vesicle fluctuation analysis (VFA), which is based on observation and analysis of the spontaneous fluctuations of membranes. Since lipid bilayers have a thickness of only several nanometers [467], and bilayer lipids are solely linked by non-covalent interactions, membranes are remarkably soft and are even deformable by thermal fluctuations. These spontaneous deformations were first reported as the 'flickering' of red blood cells already back in 1890 [468]. Since then, membrane elasticity theories were developed that directly connect the amplitude of membrane fluctuations to the bending rigidity and membrane tension [4]. VFA is the most popular method to probe bending rigidity nowadays, as it is an easy, fast and non-invasive experimental technique that requires only a microscope and a digital camera. In this way, acquiring data on a single vesicle can be done in a couple of minutes. Furthermore, interpretation of VFA data is easier than for MPA, as mechanics are probed in the linear regime. In the past decades, VFA has been employed to characterize bending moduli of a wide range of membranes, including charged membranes [469], cell-derived plasma membrane vesicles [470] and membranes containing sterols [341, 471].

A major constraint of the VFA method is that the membrane should exhibit thermal fluctuations. This implies that VFA can not be employed to measure membranes at high tension or with high rigidity. While VFA can be used to measure mechanics of red blood cell membranes that are supported by a comparatively soft spectrin network [472, 473], membranes supported by a more rigid actin cortex are typically probed by active methods [474–478]. Otherwise, measuring thermal fluctuations with higher spatial and temporal resolution using quadrant photodiodes instead of cameras, opens up ways to measure spontaneous fluctuations in presence of an actin cortex [479, 480].

In addition to MPA and VFA, there are various other ways to measure membrane mechanics, which can be distinguished as either active or passive techniques [16, 51, 481, 482]. Other methods involving active membrane deformation include electrodeformation, where GUVs are being deformed by an electric field [471] or tube pulling, where lipid nanotubes are pulled from an aspirated vesicle [483]. In addition, mechanics can be probed using microrheology[474], indentation[476], or mechanical compressoin[475]. Otherwise, passive membrane mechanics measurements can be based on X-ray scattering on lipid bilayers [484]. It is good to note that not all techniques access the same properties. For example, while MPA and electrodeformation can be used to measure the membrane stretch modulus in addition to bending rigidity, VFA and tube pulling are limited to bending moduli. Furthermore, MPA can be used to probe lysis tension, a property inaccessible by passive techniques. In addition to experimental techniques, molecular dynamics simulations provide helpful insights [485].

Setting up a mechanical experiments requires a number of design choices. First, one should consider which technique to use, depending on the required sensitivity and the mechanical properties of interest (reviewed in [52, 486, 487]). Second, it is known that

membrane mechanics are sensitive to experimental conditions such as the presence of salts, sugars, and the pH of the surrounding medium (reviewed in [52, 481]). This may contribute to the large variation in modulus for the same membrane composition reported in different studies.

Since probing methods have complementary strengths and weaknesses, we set out to explore the applicability of MPA and VFA to GUVs with and without a cortex. We discuss in this chapter how we developed pipelines for performing both measurements. In addition, we address design criteria that we found to be essential for experiments and analysis of both techniques. We conclude this chapter with a set of benchmark measurements performed on model membranes to test sensitivity of our methods to changes in lipid composition. Lastly, we tested applicability of the techniques to GUVs bearing a cortex.

6.2. RESULTS

6.2.1. VESICLE FORMATION

Measuring the bending modulus of GUV membranes requires that the vesicle membrane exhibits measurable fluctuations, while measuring the stretching modulus requires there is no excess membrane area stored in tubes or other structures. We noticed that the chemical environment of the GUV affected the presence of stored excess membrane upon deflation of the GUVs, in line with previous studies investigating solute asymmetries over the membrane [61]. With GUVs containing 200 mOsm sucrose and suspended in an outer solution of 200 mOsm glucose, thin yet visible membrane tubes formed towards the GUV interior upon solvent evaporation (fig. 6.1a), while the outer surface retained a spherical shape. The solution pH was 5 for glucose, and 6 for sucrose. To compensate for the difference in acidity, we added 10 mM Tris-HCl buffered at pH 7.4 to both inner and outers solutions during the formation process. Formation of vesicles in buffered solutions both by gel-swelling and electroformation significantly decreased the fraction of GUVs with membrane nanotubes (fig. 6.1b).

Another experimental design parameter essential for mechanical measurements is the choice of the lipid dye. When using 0.5% (mol/mol) rhodamine labelled DOPE lipids in POPC membranes, vesicles got visibly deformed upon illumination with monochromatic LED light (fig. 6.1c-e). In contrast, vesicles consisting of fully saturated DMPC lipids that were labelled similarly did not undergo shape transformations (not shown), indicating a role for lipid tail saturation in membrane deformation. Following [488], we hypothesized that irradiation led to oxidation of the mono-unsaturated lipid tails in POPC membranes, which in turn caused the membrane area to increase. Substitution of rhodamine DOPE with a small fraction (0.1%) of the photostable ATTO 655 DOPE indeed abolished shape transformations at similar illumination conditions, while retaining sufficient intensity contrast in the images. We therefore used 0.1% ATTO 655 PE to label our membranes in all experiments discussed in this chapter, unless specified otherwise.

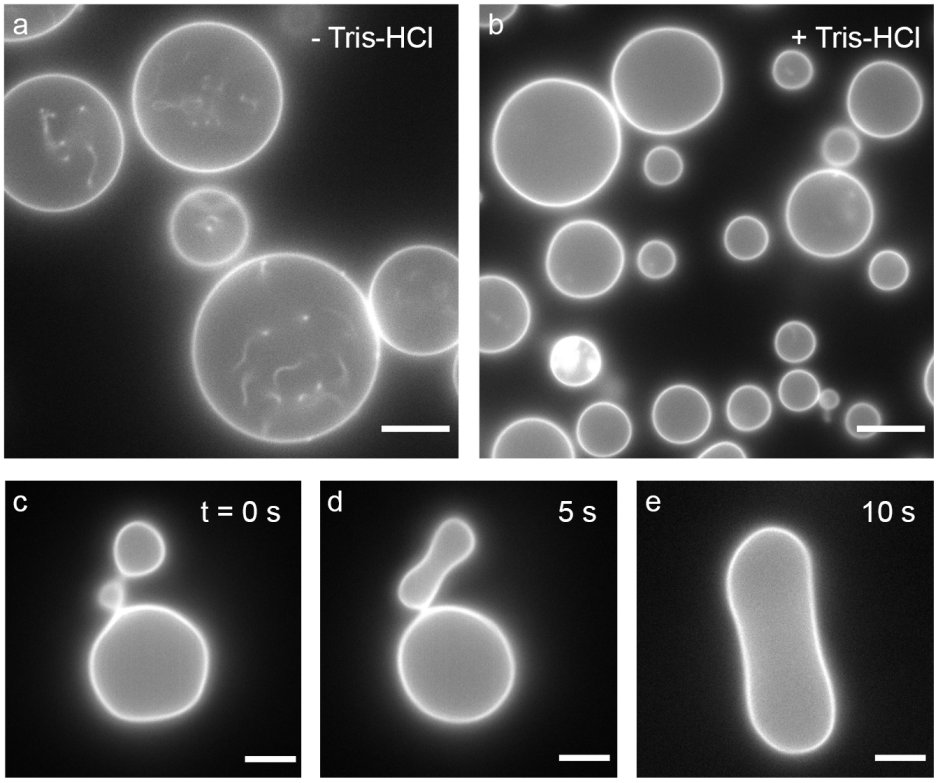

Figure 6.1: **Buffer and fluorescent lipids need to be chosen carefully for bending rigidity measurements.** Membrane conformation of electroformed GUVs was influenced by buffer addition and choice of fluorescent lipid dye. (a-b) Typical fields of view of EggPC vesicles with 0.1% ATTO-655 DOPE observed after sample evaporation for several minutes. Scale bar is 10 µm. (a) In absence of a pH-buffering component, thin inwards membrane tubes formed on the GUV membranes while vesicles remained overall spherical. (b) When 10 mM Tris-HCl at pH 7.4 was added to both inner and outer solutions, sample evaporation resulted in GUVs becoming quasispherical with fluctuating membranes. (c-e) Shape transformation of a single POPC vesicle with 0.5% rhodamine DOPE lipids upon illumination with 655 nm wavelength at high LED intensity. Initially, the vesicle showed two buds (c), which got incorporated one by one in the larger area during imaging (d,e). Scale bar is 5 µm.

6.2.2. MICROPIPETTE ASPIRATION (MPA)

PRACTICAL CONSIDERATIONS FOR ASPIRATION MEASUREMENTS

The ability to maintain a steady pressure is vital for doing reliable and reproducible elasticity measurements. Since bending rigidity is probed by pressure steps starting from ~0.002 mN/m, corresponding to ~0.1 Pa, while the entire measurement can take several minutes, the smallest pressure fluctuations in the measurement set-up can already hinder quantitative measurements. Several factors can influence the pressure that is applied in the pipette, including water evaporation from the sample chamber and/or water bath, flow of water out of the chamber, temperature differences, and the microscope objective

pulling at the sample chamber.

We found solvent evaporation from the chamber and water flow out of the chamber to have the strongest effect, in some cases leading to pressure changes of several hundreds of µm H_2O in a few minutes, corresponding to several pascals. Since both phenomena are intricately related to the design of the aspiration chamber, we investigated different chamber designs. Besides a constant pressure over time, additional design are an opening for the micropipette to enter and to move through the chamber to browse for vesicles, and handling space to exchange chamber content to wash out the β-casein solution.

We converged to a chamber that could be closed with an oil seal as it allows maximal flexibility for the pipette to move while preventing evaporation. However, deformations of the water-oil interface induced by movement of the oil affected the zero pressure. We attempted to solve this by pinning the water-oil interface using an aluminum spacer with small structures pointing into the sample compartment (fig. 6.2c). However, pinning was unsuccessful both with rectangular and wedge-shaped structures, leading to oil flow along the chamber opening. In addition, the sample and oil crept out of the chamber via the glass-spacer adhesion sites.

As an alternative approach, we made a chamber of a U-shaped silicone spacer sticking on top of a glass coverslip. The sample was placed in the chamber opening and the oil was layered on top of the sample (fig. 6.2b). In this design, the sample managed to flow out of the chamber via capillary attraction to the pipette during the washing steps after passivation. Once the sample had reached the coverslip edge, it was impossible to form a closing oil seal.

Then, we made a chamber consisting of a stainless steel spacer that held a top and bottom coverslip from two sides as used in [483]. We put enough sample as to entirely fill the volume between the coverslips, and we closed the chamber by spreading mineral oil along the open edges. By using a bottom coverslip 2-3 mm wider than the top coverslip, the oil did not flow down along the open edges. However, also with this design both sample and oil managed to escape the chamber via the glass-spacer adhesion sites. Furthermore, oil closure was often incomplete when the sample touched the glass edges along the open sides. We also tested different variants of mineral oil (heavy and light) as well as low-viscosity silicone oil, but this did not improve sealing.

The final iteration was made by increasing the distance between the spacer sites of the chamber shown in fig. 6.2c as well as the width of the glass coverslips. By doing so, the sample could be placed central in the chamber without touching either the edges on the long or short sides, even after the passivation and washing steps (fig. 6.2d-e). While the sample was fixed in position by capillary forces, the oil seal could be safely positioned around the sample, also without touching the spacer. With this configuration, the pressure showed a maximum change of 100 µm H_2O over the course of hours, corresponding to less than $1Pa$. This configuration was used for all data presented in this chapter.

Next to chamber design, we also noticed that the use of the microscope objective sometimes caused pressure changes. In particular, forces exerted on the sample chamber by changing focus with an oil objective hampered mechanical measurements. Retracting movements of the objective deformed the thin glass bottom coverslip via capillary action, resulting in pressure changes measured in the pipette. Using a long working

distance water immersion objective circumvented this problem.

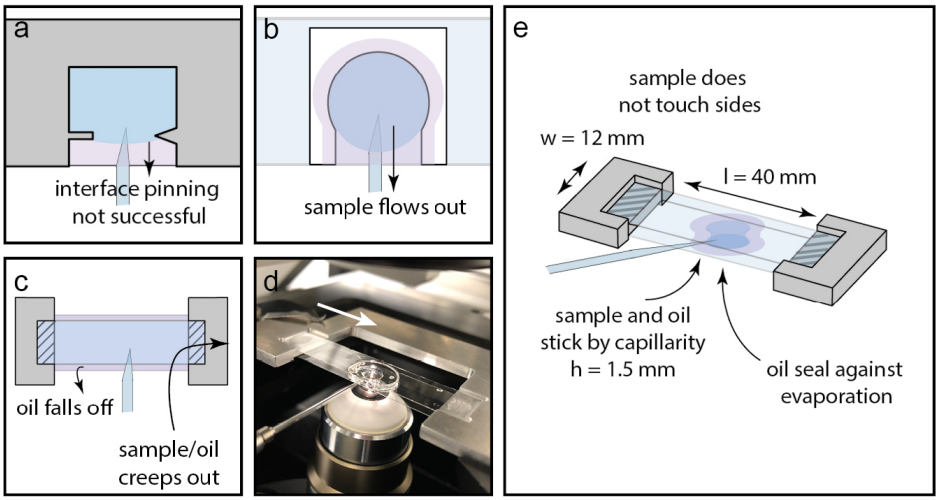

Figure 6.2: **Design of micropipette aspiration sample chambers.** The sample is shown in dark blue, oil in transparent purple, glass in transparent light blue, aluminium spacers in grey and the silicone spacer in white. (a) Pinning of the water-oil interface by chamber design using a rectangular (left) or triangular (right) structure. (b) A chamber open from the top created with a U-shaped silicone spacer. (c) Stainless steel spacer holding the chamber from two sides. (d) Image of the final chamber design. (e) Schematic of final chamber design used for mechanical measurements in this chapter. Both sides of the spacer are connected via a bridge (not shown here, but indicated in (d) with a white arrow).

During aspiration measurements, adhesion of the vesicle membrane to the aspiration pipette has to be minimised to allow quantitative interpretation. We explored different pipette coating agents: bovine serum albumin (BSA), polyethylene glycol (PLL-PEG) and β-casein. Of these components, only with β-casein we succeeded in coating the pipette such that vesicles could be repeatedly aspirated and released without leaving behind fluorescent membrane material on the pipette walls. The most efficient coating strategy proved to be a 30 minute incubation time with a 5 mg/mL β-casein solution of the chamber and pipette. Essential to a successful passivation was the addition of 10 mM Tris-HCl at pH 7.4 to the coating solution. Without buffer, the β-casein left a deposit on the pipette wall with a thickness increasing over time, reaching several µm in 30 minutes, thereby changing the pipette shape and narrowing the orifice from 5-8 µm to 3-5 µm.

ASPIRATION IMAGE ANALYSIS

In addition to existing image analysis methods that have been used for confocal fluorescence [483, 488] and bright field images [7], we provide a micropipette aspiration analysis pipeline compatible with epifluorescence images. Image analysis of image series recorded during micropipette aspiration was performed using a custom-written Python script (see fig. 6.3). First, circles were fitted to the tongue and vesicle to obtain radii and locations of both for all frames (fig. 6.3a-d). Detection of the tongue and vesicle circles

was automated and consisted of three main steps: image preprocessing, local maxima detection and circle fitting. In short, an unprocessed image I_0 as in fig. 6.3a was first smoothed with a Gaussian filter with small kernel size to create I_{sm}. Then, a second smoothed image I_{sub} was created from I_0 with a larger smoothing kernel size and this image was subtracted from the first smoothed image to yield the edge enhanced image I_{enh}. After thresholding to remove low-intensity noise, we obtained I_{thr} as shown in fig. 6.3b. The combination of a small and large kernel size for smoothing resulted in an effective noise reduction: after processing, membrane intensity showed a stark contrast with the background, while out-of-plane fluorescence from the vesicle lumen was filtered out. This processing is particularly useful for epifluorescence wide-field images, where contrast is small and where membrane intensity in the tongue is lower. We then applied a local maxima filter to retrieve a set of discrete coordinates representing membrane positions, as seen in fig. 6.3c. Since the signal of a labelled membrane represents an intensity peak in fluorescence images, we decided to use a local maxima detection rather than edge-based detection such as the classical Canny edge detector. Fitting of two circles to the local maxima yielded the vesicle centre $(x, y)_v$ and radius R_v and the tongue centre $(x, y)_p$ and radius R_p as displayed in fig. 6.3d.

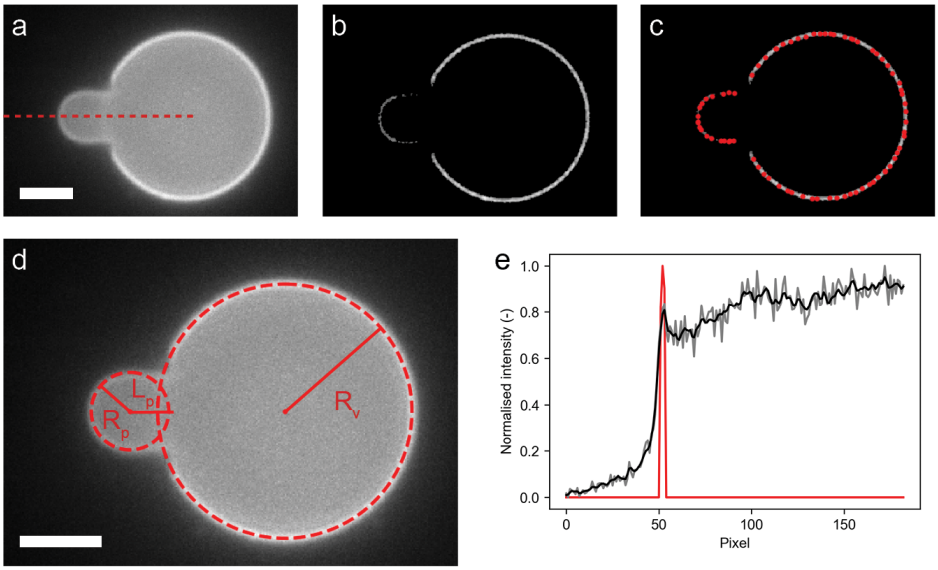

Figure 6.3: **Image analysis of micropipette aspiration measurements.** Scale bar is $5\mu m$ in all images. (a) Unprocessed epifluorescence image I_0 of an aspirated DOPC vesicle made by gel-assisted swelling imaged at the equatorial plane. The membrane was labelled with 0.1% (mol/mol) ATTO 655 DOPE. A red dashed line is drawn from where the intensity profiles in (e) are taken. (b) Processed image I_{thr} that is obtained after smoothing, edge enhancement and thresholding. (c) Detection of local maxima (indicated in red) in processed image. (d) Fitting two circles to the local maxima gives the vesicle radius R_v and the tongue radius R_p. From there, the tongue length L_p can be calculated. (e) Horizontal line intensity profiles drawn through the tongue centre from the raw image (grey), the smoothed image (black) and the processed image (red).

We then extracted the change in tongue length dL from all images. We first obtained

time-averaged radii and centre positions of the tongue and vesicle. Then, we extracted horizontal line intensity profiles through y_p (red dashed line in fig. 6.3a). From the thresholded line intensity profile, the tongue membrane position was identified as the maximum intensity, and dL could be calculated as the difference in tongue length between frames.

ASPIRATION ELASTICITY MEASUREMENTS

We used the micropipette aspiration technique to measure elastic moduli of synthetic lipid membranes. More specifically, we performed measurements in the low tension regime to probe the membrane's bending modulus κ and we measured at high tensions to obtain the membrane compressibility modulus or stretch modulus k_s. Here, we show the typical outcome and analysis of both a bending and stretching measurement performed on a GUV composed of DOPC lipids that was formed by gel-assisted swelling.

Bending moduli of these vesicles were probed by raising the membrane tension from 0 to 0.5 mN/m in a step-wise manner. The resulting increase of the projected membrane area can be seen in fig. 6.4a-c. From the calculated deformation of the membrane as a function of imposed tension (fig. 6.4d), the two deformation regimes can be clearly distinguished: at tensions below 0.5 mN/m, area increases logarithmically with tension, while at higher tensions there is a linear increase of membrane area with tension. The discrete dilation values are an effect of the pixel resolution of membrane detection, and were small compared to the large increase in tongue length in stretch modulus measurements. For bending modulus measurements, the increase in tongue length could be as small as ten times the pixel size. In these measurements, we minimized discretization effects by increasing the number of images (50 in total), leading to effective oversampling. The respective regimes were fitted with eq. (6.3) and eq. (6.4) to obtain the elastic moduli (for details see section 6.4). In this way, we obtained $\kappa = 16.9\ k_B T$ (fig. 6.4e) and a forward and reverse stretch modulus of respectively $k_{s,f} = 165$ mN/m and $k_{s,r} = 200$ mN/m (fig. 6.4f). The hysteresis in stretching and compression of the membrane was a general outcome of our measurements and will be discussed further in section 6.2.4.

6.2.3. VESICLE FLUCTUATION ANALYSIS (VFA)

While VFA is an established technique, there is not one universal image analysis protocol. Contour detection procedures differ between groups, and depend among others on the imaging method used (phase contrast [5, 469] versus fluorescence [469, 486, 489]) and the desired spatial accuracy [5, 469, 471, 489]. Detection methods have been developed that are based on either gradient-directed contour tracking [5] or radial intensity profiles [469, 471, 489]. In our analysis, we chose to detect based on radial intensity profiles with pixel precision, providing a straightforward and computationally cheap method. We discuss the workflow and analysis procedure which we have implemented in our lab. We demonstrate the analysis pipeline on an epifluorescence recording of a DOPC vesicle that was made by electroformation and that was recorded with an exposure time of 2 ms (fig. 6.5a).

We extracted the membrane positions from a fluctuating vesicle by pre-defining a collection of radial rays crossing the membrane and detecting the membrane position on these rays to obtain the radius r as a function of θ (fig. 6.5b). We explored different

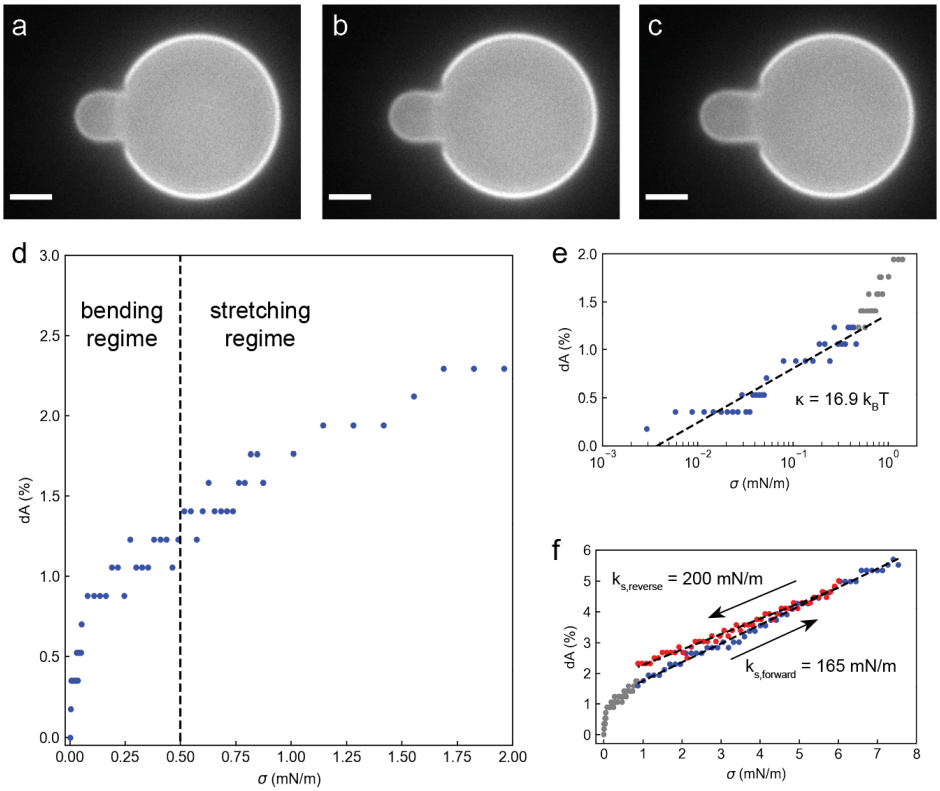

Figure 6.4: **Analysis of a typical aspiration measurement.** (a-c) Fluorescence wide field images of an aspirated DOPC vesicle at increasing aspiration pressure. The membrane was labelled with 0.1% (mol/mol) ATTO 655 DOPE and imaged at the equatorial plane. Scale bar is 5μm. (d) Stress-strain curve of the DOPC membrane shown in (a-c). A bending and stretching measurement have been combined to generate this plot. The dashed line indicates the cross-over tension between the two regimes at 0.5 mN/m. (e) Obtaining the bending modulus by fitting the low tension regime. The dashed line represents the fit with κ = 16.9 $k_B T$. Data that was not used for fitting is greyed out. (f) Obtaining the stretch modulus from fits to forward and reverse stretch measurements yielded $k_{s,f}$ = 165 mN/m and $k_{s,r}$ = 200 mN/m, respectively. Data that was not used for fitting is greyed out.

image preprocessing options: two-dimensional smoothing with a Gaussian before taking the intensity profile (2D), one-dimensional smoothing with a Gaussian after taking the intensity profile (1D), a combination of both smoothing options (2D + 1D) or no processing at all. The corresponding intensity profiles are shown in fig. 6.5c. In all cases, the membrane position was defined as the peak intensity on the one-dimensional signal. From fig. 6.5c it is clear that smoothing decreases ambiguity in peak detection, but also causes a shift in peak position towards the vesicle interior.

Completion of the membrane detection process with 2D smoothing for all angles yields a contour consisting of 360 membrane positions as shown in fig. 6.5d. As expected, the contour positions overlap with the membrane signal, albeit slightly shifted inwards

(inset of fig. 6.5d). Plotting $r(\theta)$ reveals the spatial profile of the fluctuating membrane (fig. 6.5e). As detection was performed with pixel precision, values of r are discretised. With the size of a pixel being 65 nm, we assume the amplitude of relevant fluctuations in the accessible mode range (typically up to $q \sim 20$, see section 6.4) to be larger than the pixel size, meaning that these modes are not affected by discretisation [5]. Note that we use q to denote the mode number and $q_x = \frac{q}{\langle R \rangle}$ to denote the wave number (m^{-1}) belonging to q. The membrane detection procedure was repeated for all frames

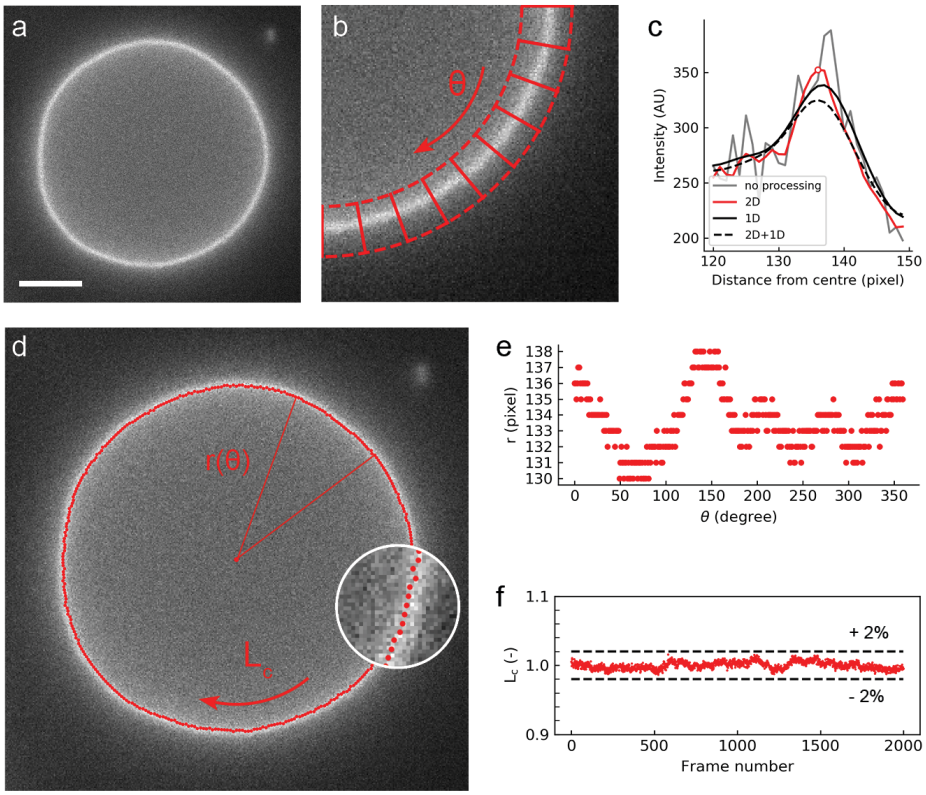

Figure 6.5: **Contour detection in VFA.** (a) Fluorescence wide field image of a fluctuating DOPC vesicle that was made by electroformation. The image was taken at the equatorial plane with an exposure time of 5 ms. Scale bar is 5 µm. (b) Radial intensity profiles were extracted around the membrane position with an angular separation of 1 degree. (c) Radial intensity profiles of the smoothed image (shown in black) were convolved again with a 1D-Gaussian (red line) before the membrane position (red circle) was identified as the maximum of the double smoothed profile. For comparison, also the unprocessed intensity profile is shown (grey). (d) The radial membrane position was determined for every angle, yielding an angular profile of the radius $r(\theta)$. From this, the contour length within the equatorial plane L_c could be calculated. Inset: zoom-in on detected membrane positions. (e) Angular profile of radius. Discretisation in values of r is an effect of detection performed at pixel resolution. (f) Plot of L_c normalized by the time-averaged contour length (red points), including 2% variation limits (black dashed line).

in the stack to extract $r(\theta, t)$. Calculation of the euclidian contour length in all frames and subsequent division by its time average following eq. (6.7) yields the normalized contour length L_c over time (fig. 6.5f). This length serves as a quality control for detection: if the membrane is detected correctly, the contour length stays constant over time. Frames where membrane positions have been falsely detected appear as deviating contour lengths. We chose to use a variation limit of 2%, and all videos with frames where the contour length exceeded this variation limit were excluded from the analysis. In this case, it can be seen that L_c stays within the 2% variation limit over the entire course of the video.

From the polar membrane coordinates, we calculated the spatial Fourier transform and finally the fluctuation spectrum using eq. (6.8) through eq. (6.11). Before we continue with fitting the Helfrich model (eq. (6.14)), we first select the mode regime to be used for fitting. We therefore compute the product of the variances and the cubic wave number, i.e. $\langle |\tilde{u}_q|^2 \rangle q_x^3$, which should show up as a plateau for an intermediate range of modes (see section 6.4.5 for a full explanation). Figure 6.6a shows the typical plateau plot with the different regimes. At low q, in this example $q \lesssim 3$, we see a large spread in variances, corresponding to the statistically under-represented modes that have not equilibrated during the time-lapse. These modes should therefore be excluded from fitting. For $q \gtrsim 20$, $\langle |\tilde{u}_q|^2 \rangle q_x^3$ increases linearly with q. In this high q regime, noise dominates the variance so this regime should also be excluded from fitting. For the intermediate modes, the variances scale with the inverse cube of the wave number, q^{-3}, thereby clearly forming a plateau. These modes are selected for fitting.

From the plateau plot, it is however difficult to precisely pick the lower and upper cut-off mode. We therefore use fig. 6.6a to assess the quality of the data and analysis, but we choose the cut-off modes differently. q_{high} is calculated using eq. (6.16) with an educated guess for κ. Instead of choosing one single q_{low}, we perform the fitting procedure with all values for q_{low} between 1 and q_{high}. In return, we retrieve κ as a function of the starting mode as shown in fig. 6.6b. From this plot, we can identify a region where κ minimally depends on the choice of q_{low}. We then compute our final value of κ by averaging over the values in this plateau (mode 5 to 11 in fig. 6.6b), yielding $\kappa = 20 k_B T$. Using the final κ and the first q_{low} belonging to the plateau, we once more perform the fit to get $\sigma = 2.6 \cdot 10^{-9} N/m$. The final results are plotted in fig. 6.6c. Note that the choice of q_{low} affects the fitting results: based on fig. 6.6a, one would choose $q_{low} = 3$ which would have resulted in $\kappa = 16 k_B T$ (fig. 6.6b). We found the choice of q_{high} to have less impact on the fitting results.

Then, we set out to investigate the effects of image preprocessing choices on the fluctuation analysis. As discussed above, we compared different combinations of smoothing options for membrane detection. While membrane detection was more robust when smoothing filters were applied, smoothing also caused the variance to drop at higher mode numbers when either a combination of 2-dimensional and 1-dimensional smoothing (2D+1D) or only 1-dimensional smoothing (1D) was applied (fig. 6.7a). In contrast, the scaled variance increased directly after a short plateau when no smoothing was applied. The longest plateau was observed for 2-dimensional (2D) smoothing only. In line with these results, 2D smoothing resulted in the most consistent outcomes of fitted κ values with varying q_{low} as can be seen from the long plateau in fig. 6.6c. No clear plateau

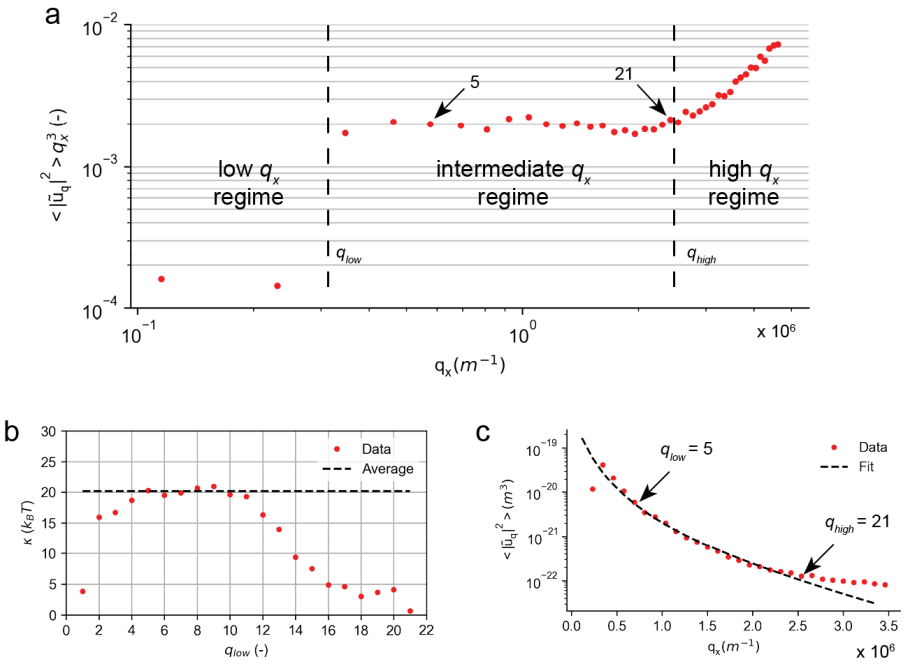

Figure 6.6: **Example VFA analysis for a DOPC vesicle.** Fluctuation spectrum and fitting for a DOPC vesicle with a radius of 8 µm made by electroformation and imaged in epifluorescence with 5 ms exposure time. (a) Scaling of the variances with wave number q_x reveals three different regimes: only the intermediate regime where variances scale with q_x^{-3} is used for fitting. The lower and upper cut-off modes, $q = 5$ and $q = 21$, are indicated. (b) Fitting results in values of κ as a function of q_{low}. It can be seen that from mode 5 to 11, κ minimally depends on q_{low}. Averaging κ over these modes yields $\kappa = 20 k_B T$ (black dashed line). (c) Final fitting results using $\kappa = 20 k_B T$, $\sigma = 2.6 \cdot 10^{-9} N/m$, $q_{low} = 5$ and $q_{high} = 21$.

was observed for 2D+1D and 1D preprocessing. As a result, also the fitted bending rigidities depend on image processing, ranging from $17 k_B T$ without smoothing to $27 k_B T$ with 2D+1D smoothing.

For choosing the optimal preprocessing settings, one should not only consider the scaled variance and fitted κ values, but also qualitatively inspect the detected membrane contours. While 2D smoothing resulted in visually correct detection (fig. 6.12a), detection without smoothing was noisy (fig. 6.12b) and caused larger variations in contour length (fig. 6.12c). Since convolution with a 2D Gaussian resulted in the longest plateaus both in the plateau plot and the plot of κ versus q, while ensuring robust membrane detection, we used this processing strategy for all videos analysed.

Another common concern while doing quantitative analysis of fluctuation measurements is the effect of camera exposure time τ. In our analysis, we implemented the theoretical correction proposed in [5]. To verify if we could indeed obtain a consistent κ independent of τ, we recorded time-lapses of a vesicle with three different exposure times 2, 5 and 10 ms. Figure 6.7b shows a typical measurement on a single vesicle im-

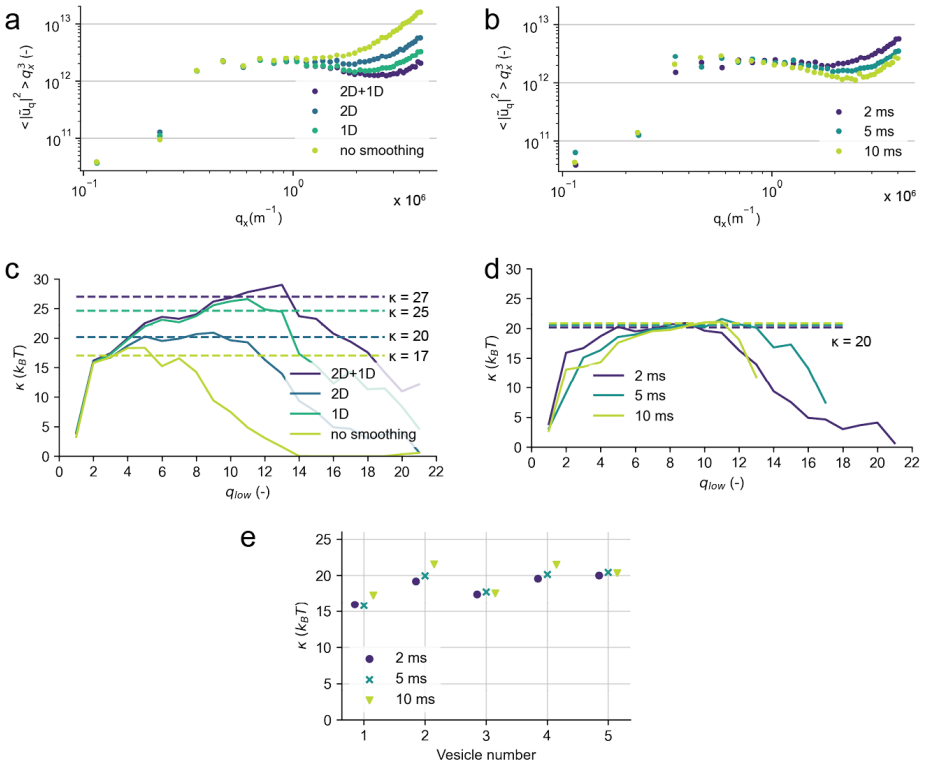

Figure 6.7: **Influence of image processing and exposure time on VFA.** (a) Plateau plot for one video of a fluctuating DOPC vesicle with a radius of 8μm imaged in epifluorescence with 2 ms exposure time, treated with different image processing options prior to membrane detection. '2D' is two-dimensional smoothing, '1D' is one-dimensional smoothing, '2D+1D' is both smoothing procedures combined, and 'no smoothing' means contour detection was performed in the unprocessed image. Values are plotted against the wave number. (b) Plateau plot for the same vesicle imaged with exposure times of 2, 5 and 10 ms, analysed with two-dimensional smoothing, plotted against the wave number. (c-d) Dependence of κ on q_{low} for the fluctuation spectrum in (a) and (b). Averaged values of κ obtained from the plateaus are indicated with dashed lines. Values are plotted against the mode number. (e) Bending rigidities obtained for five vesicles with radii between 6 and 9μm imaged with different exposure times. Values were shifted and placed arbitrarily on x-axis for ease of view.

aged with these exposure times. As expected, we obtain the longest plateau for $\tau = 2ms$, while longer exposure times cause a dip in the spectrum at higher modes. This is not a problem, as fitting with eq. (6.14) consistently returns the same κ for all exposure times used (fig. 6.7d). Note that q_{high} also depends on exposure time, in this example being 21, 17 and 13, for 2, 5 and 10 ms, respectively. Repeating these measurements on five different vesicles confirms that we indeed obtain a consistent κ per vesicle, independent of the exposure time used (fig. 6.7e).

Finally, we investigated how σ influenced the outcome for κ. For all VFA measurements presented in this study, we found values for σ between 10^{-10} and $10^{-8} N/m$ (see

table 6.3 for an overview of all results). Membranes with a higher tension did not fluctuate sufficiently to optically resolve the fluctuations. To explore the effect of σ on the fit outcomes for κ, we calculated the theoretical fluctuation spectrum with eq. (6.14) for a typical mode range from 5 to 25, for a vesicle with $R = 5\mu m$ using $\kappa = 15 k_B T$, $\sigma = 10^{-9} N/m$ and $\tau = 5ms$. We then performed a fit of eq. (6.14) to this theoretical spectrum to obtain κ, but with a range of fixed σ values between 10^{-10} and $10^{-8} N/m$. Within this range, results of κ were affected minimally by the choice of σ, changing at maximum $1 k_B T$ for a σ that was 10 times higher (fig. 6.13). These results confirm that σ does not substantially affect the fluctuation spectrum in this tension regime. At the same time, these results indicate that it is difficult to obtain a reliable measure for σ in this regime.

6.2.4. A BENCHMARK DATA SET

Having set up two independent techniques to measure membrane elasticity parameters, we performed a set of benchmark measurements on simple single-component membranes that have been well-characterized [7, 56, 341, 471].

Micropipette aspiration measurements on POPC vesicles tagged with 0.1 % (mol/mol) ATTO 655 DOPE, formed by gel-assisted swelling on PVA, yielded a bending rigidity of $(16.3 \pm 3.2)\ k_B T$ (average ± standard deviation, $n = 13$) (fig. 6.8a). As cholesterol is known to increase the bending rigidity of POPC membranes [341], we also performed measurements on membranes containing 70:30 POPC:cholesterol (mol/mol). The expected stiffness increase was captured with our micropipette aspiration setup, which gave κ $(23 \pm 5.5) k_B T$ ($n = 12$). VFA measurements on the same membranes yielded similar values as MPA for the bending rigidity, being 16.7 (n=3) without cholesterol and $24.1 k_B T$ (n=2) with cholesterol. Both the VFA and MPA results agree well with values reported in literature [481] and detect the expected increase in the POPC membrane's bending rigidity upon cholesterol addition, thereby providing a validation for both techniques.

We then used VFA to compare bending rigidities of different membrane compositions (for an overview, see table 6.3). Opposite to a stiffening effect on POPC, it has been shown that cholesterol does not change the bending rigidity of DOPC membranes [471, 490]. We therefore reconstituted membranes containing 100% DOPC and 70:30 DOPC: cholesterol (mol/mol) with the PVA-swelling method. Indeed, with VFA we measured bending rigidities that were identical between the two membranes (16.6 ± 1.8 (n=6) and $16.2 \pm 3.1 k_B T$ (n=4), respectively, see fig. 6.8a), and in addition similar to that of 100 % POPC membranes ($16.7 k_B T$).

Next, we investigated if the method used to produce vesicles affects the membrane's bending rigidity. Earlier work has shown that vesicles produced by gel-assisted swelling can display altered mechanical properties due to residual polymer in the membrane [350, 365]. To test this, we compared the bending rigidities of DOPC membranes formed by gel-assisted swelling to the typical model electroformed membranes. Interestingly, VFA measurements on both membranes showed a minimal difference, with κ (18.6 ± 1.8) $k_B T$ (n=10) for electroformed vesicles versus $(16.6 \pm 1.8)\ k_B T$ for gel-swollen vesicles (n=6). This indicates that formation artefacts are not universal, and may depend either on the exact execution of the production protocol or on the membrane property under investigation.

Furthermore, we checked if VFA could be performed with phase contrast imaging.

Using phase contrast time lapses for VFA experiments has the benefit that GUV membranes do not need to be fluorescently labelled, avoiding potential spectral cross-talk with other labelled structures. In addition, high intensity illumination can damage reconstituted proteins [113]. For contour detection in phase contrast images, the membrane position was defined by the maximum gradient instead of the maximum intensity as we used for fluorescence images. We directly compared epifluorescence and phase contrast measurements on EggPC (100%) and on EggPC:POPE (50:50 mol/mol) vesicles.

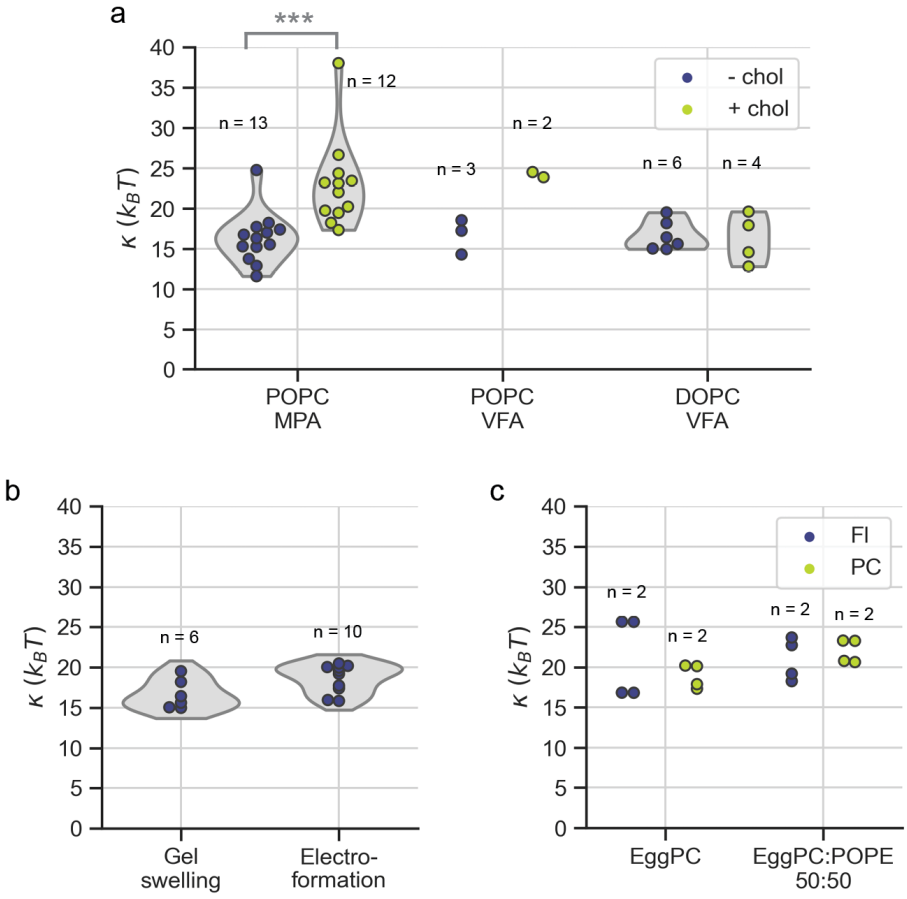

Figure 6.8: **Benchmark bending rigidity measurements.** Each data point represents a measurement on a single vesicle. All vesicles had a radius between 6 and 10mum. All VFA data is acquired with an exposure time of 2ms. (a) Comparison of MPA and VFA measurements on POPC and DOPC vesicles formed by gel swelling without (purple) and with 30% (molar ratio) cholesterol (yellow). Statistically significant differences (p<0.005) are indicated with stars, ***. (b) Comparison of VFA measurements on DOPC vesicles formed by gel-assisted swelling and electroformation. (c) Comparison of VFA performed with fluorescence (Fl) and phase contrast (PC).

In line with previous studies [491], bending rigidities were comparable between imaging methods for both membrane compositions tested (see fig. 6.8c), thus abolishing the requirement for membrane dyes.

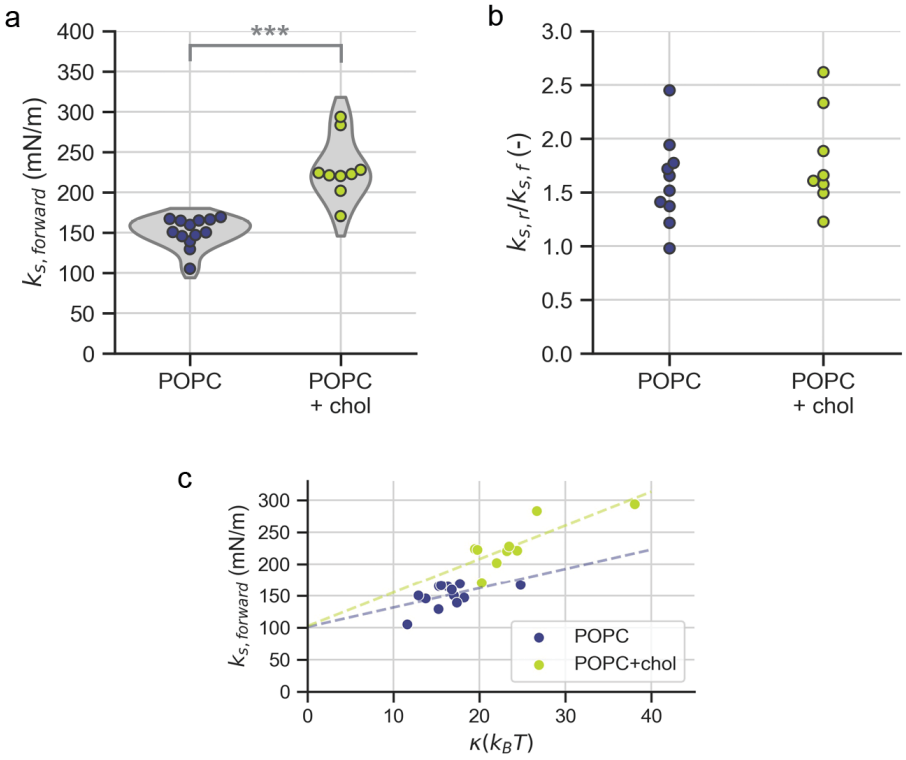

Figure 6.9: **Stretch elasticity measurements.** Stretch elasticity probed by MPA on POPC membranes formed by gel-assisted swelling without (purple) and with (yellow) 30% (mol/mol) cholesterol. Each data point represents a measurement on a single vesicle. (a) Stretch modulus of the forward measurement with increasing aspiration pressure. Statistical p-value is indicated with stars, ***p<0.005. (b) Ratio of k_s determined from the reverse and forward measurement. (c) Correlation between stretch moduli and bending rigidities for individual vesicles. Dashed lines are linear regression results with slopes 3 mN/m per k_BT and R^2 = 0.3 for POPC, and 5 mN/m per k_BT and R^2 = 0.7 for POPC+chol.

MPA measurements provide, in addition to the bending modulus, also the stretch modulus of vesicle membranes. Aspiration stretch measurements revealed an increased stretch modulus upon cholesterol incorporation in POPC membranes from (151 ± 18) mN/m (n=13) to (230 ± 40) mN/m (n=9) (fig. 6.9a). Our data is in line with previous studies, which have reported stretch moduli of POPC membranes between 160 and 220 mN/m [7, 365, 492] that increased upon cholesterol addition to 350 mN/m [7]. Interestingly, in our study the stretch moduli and bending moduli of individual vesicles were positively correlated. This indicates that the spread in results of both stretch and bending measurements as measured by MPA is not only a measurement error, but is also at

least partly caused by a natural variation between produced membranes (fig. 6.9c). Another interesting observation was that for almost all measurements, the membrane was more deformable during the first round of increasing aspiration pressure than in the subsequent round of decreasing aspiration pressure. The hysteresis between forward and reverse measurements, which we defined by $k_{s,f}/k_{s,r}$, ranged from 1 to 2.5 for POPC membranes and from 1.2 to 2.6 for 70:30 POPC:chol (mol/mol) membranes (fig. 6.9b). We did not find a clear correlation between vesicle size or bending rigidity with the hysteresis in compressibility.

6.2.5. FLUCTUATION ANALYSIS ON EDICE GUVS

While swelling techniques are useful to produce model membranes for benchmark mechanical measurements, they offer limitations with more complex reconstitution experiments that involve encapsulation of proteins or other cargo. In chapter 4, we demonstrated that emulsion Droplet Interface Crossing Encapsulation (eDICE) is a vesicle production technique which can efficiently encapsulate complex mixtures inside GUVs, such as components required to rebuild actin networks. To test if the eDICE formation method affects membrane mechanical properties, we measured bending rigidities by VFA.

DOPC GUVs produced with eDICE clearly showed membrane fluctuations. However, it was in general more difficult to perform VFA on these vesicles. While swelling techniques offered the luxury of choosing a GUV with a clean membrane, GUVs produced with eDICE often showed membrane tubes or other structures. Besides a possible mechanical effect that these structures might have, they also interfered with our contour detection algorithm both in phase contrast and epifluorescence recordings (fig. 6.10b, c). The effects of these structures was easily identified from the contour length quality control (fig. 6.10d, e), which showed sporadic peaks for frames with non-continuous angular contour profiles. Interference of membrane structures resulted in a flattened and elevated profile of the fluctuation spectrum especially at higher q values, indicative of a higher noise level at small wavelengths (fig. 6.10f). Other than by membranes structures, large variations in contour length were also caused by small sizes of GUVs (radius < $5\mu m$) and low signal-to-noise ratios.

Likewise, we observed fluctuations of GUVs encapsulating membrane-bound streptavidin (fig. 6.11a) or Arp2/3-nucleated cortices (fig. 6.11b). Vesicles in these samples also typically showed membrane structures, which hindered quantitative data extraction from time lapse videos. While the membrane structures in fig. 6.10 might be artefacts of the vesicle formation method (see chapter 3), in case of membrane-interacting proteins, such as streptavidin or His-tagged VCA, the formation of structures could result from the interactions themselves.

6.3. DISCUSSION

VESICLE QUALITY FOR MECHANICAL ASSAYS

We discovered that control of the pH of the vesicle inner and outer solution was important to obtain vesicles that are suitable for mechanical measurements. We observed formation of membrane tubes when trying to deflate vesicles, formed in 200 mOsm sucrose,

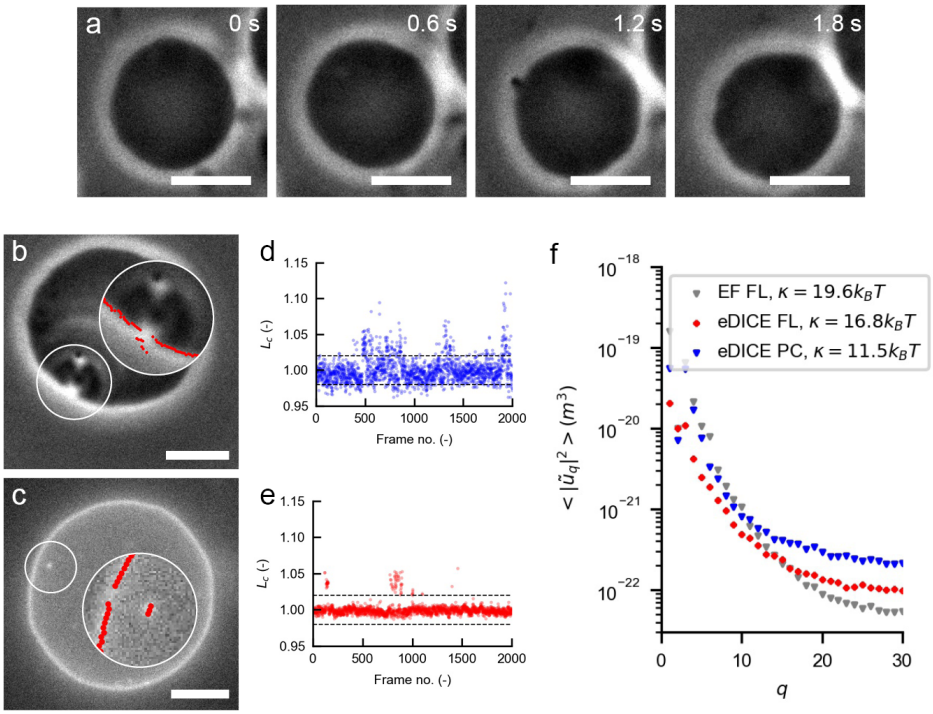

Figure 6.10: **VFA on GUVs produced with eDICE.** All vesicles are DOPC GUVs produced with eDICE. Scale bar is 5μm in all images. (a) Time lapse of a fluctuating DOPC vesicle in phase contrast. (b-c) Erroneous membrane detection in phase contrast (b) and epifluorescence (c) images due to the presence of random structures on GUV membranes. Detected membrane points are indicated in red. (d-e) Contour lengths L_c of videos belonging to images shown in panel b and c, respectively. Contour lengths are normalized by division by their time-average. The 2% variation limits are indicated with black dashed lines. Sporadic jumps in L_c are clearly visible and are indicate of erroneous membrane detection. (f) Fluctuation spectra as calculated from the phase contrast (shown in blue, belonging to panel b and d) and epifluorescence recording (shown in red, belonging to panel c and e). The fluctuation spectrum of an epifluorescence recording of an electroformed vesicle with a clean membrane is shown as a reference (grey), together with fitted κ for all three spectra. Erroneous membrane detection causes a shift in fluctuation spectra, especially at higher q values, and results in a decreased membrane bending rigidity.

by gradual evaporation of the outer aqueous solution, consisting of 200 mOsm glucose. When tubes formed, membranes did not start to fluctuate upon vesicle deflation, making them unsuitable for VFA measurements. In micropipette aspiration experiments, the tubes act as a membrane reservoir that gets incorporated into the main membrane when membrane tension is increased. Effectively, the membrane then appears to be softer than it actually is, and the measured elasticity is determined by the shape of the membrane rather than by its composition [274].

Tube formation in vesicles has been reported before as an effect of bilayer asymmetry [63]. There is a growing body of literature on this so-called 'spontaneous curvature' effect, which arises when lipids in both leaflets have a different equilibrium head group

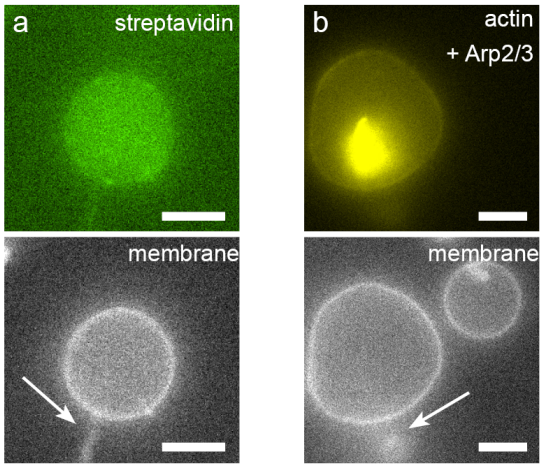

Figure 6.11: **GUVs encapsulating proteins displayed membrane structures.** Epifluorescence images of fluctuating vesicles. Vesicles were produced as described in chapter 4. Scale bar is $5\mu m$ in all images. (a) Biotin-PE functionalized GUV encapsulating $88nM$ streptavidin labeled with AlexaFluor488 (green). A membrane tube is connected to the GUV membrane (grey) as indicated with the arrow. (b) Two vesicles of which one contains an actin cortex (yellow) nucleated by Arp2/3 from membrane-bound VCA. A bright actin cluster can be seen in the GUV centre, as well as a membrane tube pointing outwards (indicated with arrow).

area. A higher fraction of negatively charged PG lipids can for instance cause more electrostatic repulsion and thus a larger area of one of the leaflets. The resulting curvature frustration is accommodated by bending of the membrane into a tube [61]. In our work, the only possible source of bilayer asymmetry could have arisen from the use of a different sugar in the inner and outer solution. As the sucrose and glucose solutions turned out to have a different pH of 5 and 6, respectively, we added 10 mM Tris-HCl at pH 7.4 to both solutions. This effectively helped to generate more fluctuating membranes and to reduce the number of vesicles with membrane tubes. It should be noted that addition of 10 mM Tris-HCl required a change in electric field parameters in the electroformation procedure, see section 6.4.2.

Another important design criterium for vesicle formation for mechanical assays was the choice of the fluorescent membrane lipid. Irradiation of fluorescent lipids can induce morphological changes of GUVs, driven by a surface area increase upon lipid peroxidation [488, 491, 493]. While we did observe such shape changes when doping the membrane with Rhodamine-labelled lipids, vesicle shapes were stable when using ATTO 655-labelled lipids, even under strong irradiation conditions. This shows that the latter dye is suitable for mechanical measurements.

BENCHMARK MEASUREMENTS

The mechanics of DOPC and POPC membranes have been studied intensively in the past decades, making these membranes ideal candidates for benchmark measurements when setting up a mechanical assay. In table 6.1, we summarize bending rigidity results from literature. Literature values range from 10 to 22.5 k_BT for DOPC and 19 to 38.5

Lipid	Technique	$\kappa(k_BT)$ -chol	$\kappa(k_BT)$ +30% chol	Reference
DOPC	Tube pulling	16 ± 2	15 ± 2	[496]
	Electrodeformation	26.7 ± 2.5	23 ± 1.3	[471]
	X-ray scattering	18.1	17.7	[490]
	NSE + NMRR	19.05 ± 0.65	30.34 ± 2.47 (20% chol)	[497]
	MPA	20.3 ± 2.4		[56]
	VFA	22.5 ± 2		[491]
	VFA	26.7 ± 2.5	23 ± 1.3	[471]
	VFA	16.6 ± 1.8	16.2 ± 3.1	This work
POPC	VFA	38.5 ± 0.8	86.8 ± 1.4	[341]
	MD simulation	22	50	[498]
	NSE	19 ± 2	25 ± 2	[499]
	MPA	16.3 ± 3.2	23 ± 5.5	This work
	VFA	16.7 ± 1.2 (n=3)	24.1 ± 0.3 (n=2)	This work

Table 6.1: **Overview of reported bending rigidities.** Measured for DOPC and POPC membranes with and without cholesterol. VFA is vesicle fluctuation analysis, NSE refers to neutron spin echo measurements, NMRR is nuclear magnetic resonance relaxation, MPA is micropipette aspiration, and MD is molecular dynamics.

k_BT for POPC membranes, in line with the values obtained in this work (18.6 k_BT for DOPC membranes, 16.3-16.6 k_BT for POPC, dependent on the measurement method). It is a striking observation that the range of bending moduli reported in literature is so wide, even for simple synthetic single-component membranes. There is consensus in the field that measured values do not only depend on membrane composition, but also on the measurement technique used [494]. In addition, the presence of salts and other solutes influences bending rigidity outcomes, as is reviewed in [481]. With respect to our work, it is in particular important to note that sugars, such as sucrose, can reduce the membrane's bending rigidity up to two-fold at a concentration of 200 mM [495]. Addition of sugar, however, does provide pragmatic benefits to experiments, as it improves GUV formation (see chapter 4) and facilitates visualisation of vesicles.

We set out to incorporate cholesterol in our model membranes as this molecule is a vital constituent of animal cell membranes, composing up to 50 mol% of the total lipids in animal plasma membranes [500]. The classical view on cholesterol is that it has a universal stiffening effect on membranes. Multiple studies on POPC membranes, using various techniques, indeed captured this stiffening effect [7, 498, 499, 501]. We found a similar stiffening behaviour of cholesterol on POPC bilayers with both measurement techniques used in this study, from 16 to 23k_BT with MPA and from 16.7 to 21.4k_BT with VFA. This universality of stiffening was, however, disputed a decade ago, when it was found that cholesterol did not increase the bending rigidity of DOPC membranes [471, 490, 496]. This finding was confirmed by multiple research groups by VFA, electrodeformation (ED), tube-pulling and X-ray measurements [471, 490, 496]. Also in our measurements, we did not observe any stiffening upon addition of cholesterol to DOPC

Lipid	Technique	$k_s(mN/m)$ -chol	$k_s(mN/m)$ +30% chol	Reference
DOPC	MPA	265 ± 18		[56]
	X-ray scattering	290	420	[490]
POPC	MPA	213 ± 5	354 ± 5	[501]
	MPA	161 ± 10		[365]
	MPA	198 ± 8		[492]
	MPA	151 ± 18	230 ± 40	This work

Table 6.2: **Overview of reported stretch moduli**. Measured for DOPC and POPC membranes in absence or presence of 30% (mol/mol) cholesterol.

membranes ($16.6k_BT$ and $16.2k_BT$ without and with 30% cholesterol, respectively). The general view is that cholesterol influences membrane mechanics by changing the molecular packing of the lipids. The cholesterol molecule has a smooth and a rough side, where straight saturated acyl chains pack well against the smooth side [490]. This packing leads to a condensation of chains, accompanied by an increase of orientational order of the lipids and an increase in membrane thickness [490, 499]. Unsaturated chains are thought to have weaker interactions with cholesterol, making them less susceptible to condensing. Since POPC has one saturated and one unsaturated chain, while DOPC has two unsaturated tails, this provides an explanation for the mechanical effect of cholesterol on POPC but not DOPC membranes. Interestingly, recent neutron spin echo (NSE) and nuclear magnetic resonance relaxation (NMRR) measurements have shown an increase in DOPC bending rigidity upon the addition of cholesterol [497]. This controversy emphasizes that bending modulus measurements should be interpreted carefully, especially when based on different techniques (see [485] for a comparison and [494] for a critical discussion). While VFA, ED, tube pulling and X-ray measurements are static measurements, NSE and NMRR sense relaxations which are influenced by medium viscosity, leaving interpretation of the new outcomes under discussion by the scientific community [502, 503].

Next to bending moduli, we also measured stretch moduli for POPC membranes with and without cholesterol (table 6.2). The stretch modulus of POPC membranes measured in this work ($151mN/m$) is close to literature values [7, 365]. Upon cholesterol addition, we observe a stiffening effect to $230mN/m$. An elevated stretch modulus of POPC membranes upon cholesterol addition is in line with previously reported values [7].

EXPERIMENTAL DESIGN CONSIDERATIONS FOR MPA MEASUREMENTS

Over the past decades, the original GUV micropipette aspiration protocol [504] has been adopted and published by various research groups [7, 56, 455, 459, 488] including recent videographic publications [483, 505]. With the number of published aspiration protocols increasing and the number of applications growing, the consistency between protocols and labs decreases. We found little consideration of the differences between methodologies and their effect on experimental outcomes in the literature. In this work, we therefore made a systematic investigation of experimental design parameters for MPA measurements that should aid experimentalists new to the method to make design choices

while setting up the measurement assay.

Essential to performing reproducible micropipette aspiration measurements was the ability to precisely control pressure in the pipette. This was strongly influenced by aspiration chamber design. In many designs tested in this work, the pressure was affected substantially over time by water evaporation or flow of the aqueous sample or oil seal. Finally, we converged to a chamber where the sample was kept in place just by capillary forces, not touching the sides of the chamber, similar to [505]. An oil seal proved to be effective for minimizing evaporation, allowing us to perform measurements over several hours. In absence of oil, the GUVs did not only develop anomalous structures such as membrane tubes over time, but also we found the pressure to change drastically. Another solution for evaporation could be to increase the sample volume in the aspiration chamber, but one should keep in mind that a certain minimum density of GUVs is required, as aspiration measurements often rely on cherry picking the useful vesicles.

The microscope objective also affected pressure stability. Using an oil immersion objective resulted in bending of the thin glass bottom surface of the aspiration chamber. This problem was solved by switching to a water immersion objective. In fact, to our knowledge, all micropipette aspiration studies published have been performed with water immersion objectives.

It should be noted that most of the published protocols control aspiration pressure using a moving water bath. In fact, a pressure-based flow control system in principle provides more precise control of aspiration pressure, with the ability to quickly and automatically adjust pressure in case of drifts. However, a down-side of these systems is that they typically provide either a wide working range of pressures, or a small step size, but seldom combine both features (an example is the MFCS-EZ microfluidic pressure pump from Fluigent that we tested). For doing simultaneously bending and stretching measurements, a combination of small pressure increments and long working range is essential, which was the motivation to use a motorized translational stage for this work, with a pressure range of $300 mm$ H_2O and a minimal step size of $1 \mu m$ H_2O (2.9 kPa and 9.8 mPa, respectively).

In this work, we recorded vesicle deformation in aspiration assays by epifluorescence imaging. Although the signal in wide field fluorescence is blurred by out-of-focus light, an issue which is typically minimized by confocal imaging, we show that the wide field image can be reduced to a confocal-like signal by image post-processing, which has to our knowledge not been used for MPA analysis before. This enhances robustness in membrane detection, especially in the vesicle tongue, where out-of-focus fluorescence is relatively strong compared to the in-plane membrane signal.

In general, it should be noted that a membrane area increase can be measured more accurately for larger than for smaller GUVs, as similar relative strain values will give larger absolute increases in projection length. In this study, vesicles were typically sized $5-15 \mu m$ in radius, where we preferred to use GUVs with a radius between 10-15 μm. It can be seen from fig. 6.4d that initial increments in protrusion length are of the size of a pixel (108 nm). Resolution of our method is thus determined more by imaging and membrane detection, rather than by the resolution of the vertically moving water bath.

We have tried various pipette coating strategies to prevent membrane adhesion. We found the overnight coating procedure presented in [505], which we tried with a 1 mg/mL

β-casein solution, to be time-intensive and prone to error. While setting up the aspiration assay, multiple things can go wrong, such as the undesired introduction of a bubble in the pipette, clogging of the pipette, or encountering a pipette orifice that is not cut as blunt and straight as desired. In those cases, it is efficient if one can switch quickly to another pipette. A 30-minute pre-coating step with a concentrated β-casein solution (5 mg/mL) [483] proved to be more pragmatic. Note that addition of 10 mM Tris-HCl at pH 7.4 to the β-casein solution was essential to prevent aggregation of the protein, both in solution and on the pipette. Addition of the coating agent to the pipette interior as well as the sample chamber ensured a two-sided coating. For easier exchange of solution during the subsequent washing steps, it is desirable to have a chamber that is open from two sides. We also tried to circumvent the washing steps by adding 1 mg/mL β-casein solution directly to the experimental chamber together with the GUVs, but this was unsuccessful in preventing membrane adhesion. We emphasize that β-casein coating was only tested for neutral membranes at minimal salt concentrations. We also tried to aspirate DOPC membranes containing 20 % DOPS lipids (mol/mol) in a solution containing 100 mM KCl, but this resulted in adhesion of the membrane to the pipette. Thus, aspiration of charged membranes or membranes with bound proteins might require a different treatment. Possible other coating strategies include bovine serum albumin (BSA) [365, 506] fetal bovine serum (FBS) [507], polyethylene glycol (PLL-PEG) [507] or SurfaSil [57, 459, 508].

For elasticity measurements, a pre-stress step for several minutes at $2-5 mN/m$ is essential for removal of small membrane structures [56, 459, 501, 505]. While pre-stressing, we often noticed that vesicles burst at medium aspiration pressures. Following [459], we used an antistatic gun to remove any static charge from the pipette. Spontaneous rupture of vesicles was barely observed after introducing this. However, even with application of pre-stress, we consistently observed a hysteresis between forward and reverse stretch measurements. Although this contradicts other studies which report that compression is typically reversible once a pre-stress is applied[56, 459], exact levels of compressibility are usually not reported and therefore difficult to compare. In our experiments, pressure did not drift, an oil seal was placed successfully to prevent evaporation, and the membrane did not visibly adhere to the pipette. A potential explanation could be that the pre-stress that we applied was not sufficient, or that membrane structures were present in planes other than the recorded equatorial plane, even though vesicles were checked before aspiration. Alternatively, hysteresis could have been caused by residual hydrogel polymers in the membrane, which can incorporate when vesicles are formed by gel-assisted swelling. Polymer contaminations in the lipid membrane can have a mechanical effect[365], although to our knowledge no observations have been reported about hysteresis in aspiration measurements specifically. This could be easily checked by MPA measurements on electroformed vesicles.

PERFORMING VFA MEASUREMENTS

In case of VFA, image processing as well as mode selection influence bending rigidity outcomes. In fig. 6.7a we show that image smoothing mainly affects the fluctuations at shorter wavelengths. While smoothing can effectively reduce contour detection errors that are inherently linked to measurement noise (fig. 6.12), it thus also affects the fluctuation spectrum that is used for determination of κ. The experimenter has to find a

compromise between robustness in contour detection and maintaining the membrane's spatial profile. In addition to image processing, we have shown that the exact mode range chosen for fitting has an effect on the extracted bending rigidity. We present a way to minimize the subjectivity of mode selection by plotting κ versus q_{low}. For a good experiment, the outcome of κ should depend minimally on the selection of q_{low}, thus presenting a plateau in the plot of κ versus q_{low}. Comparison of the plateau width between different plots of κ versus q_{low}, generated with different experimental and analysis conditions, provides an objective approach for choosing the image processing settings and the lower cut-off mode. In general, it is advisable to compare data against internal standards such as DOPC vesicles that have been obtained with the same technique, environmental conditions and analysis procedure.

Faizi et al. [491] have convincingly shown that phase contrast and confocal fluorescence microscopy can both be used for fluctuation analysis of membranes. From an experimental point of view, it is pragmatic to have the freedom to choose between phase contrast and fluorescence imaging. Phase contrast imaging is strongly influenced by any particles that float around in the medium, while high LED intensities typically required for fluorescence imaging can inflict photodamage on the vesicle membrane and other internal structures. We thus compared both imaging types and we retrieved similar bending rigidities (fig. 6.8c).

Optical smearing of fast fluctuations due to non-zero camera acquisition times is a common concern for VFA measurements. Most research groups have tackled this issue by minimizing the illumination time of the membrane in each frame using microsecond stroboscopic illumination [471, 491]. We instead followed the approach presented by Pecreaux *et al.* [5], where data acquired with exposure times on the order of milliseconds can be analysed using a theoretical correction. Indeed, via this way we obtained values for κ that resembled literature values and that were independent of exposure time. We also tried analysis of our data neglecting the effect of exposure time, i.e. assuming $\tau = 0 ms$, but this resulted in substantially higher values for κ, on the order of 50 to $80 k_B T$ for POPC and DOPC membranes. Our work provides an extra proof that VFA can be performed without stroboscopic illumination, but that exposure time correction is required.

THE EFFECT OF VESICLE FORMATION METHOD ON MECHANICS

The large majority of literature data is based on measurements conducted on vesicles formed with electroformation. However, with all the possibilities that GUVs nowadays have to offer for biophysical research and complex reconstitution, the variety in GUV formation methods is increasing rapidly (reviewed in chapter 4 and [16, 509]). While there has been significant attention for how mechanical measurements are influenced by the measuring technique and vesicle medium used [52, 481], the effect of the vesicle formation method has received less attention. Here, we give an overview of published work on the effect of vesicle formation strategy on membrane mechanics.

In this project, we focused on vesicles produced by electroformation and gel-swelling. Electroformation has been the golden standard for GUV production since its first publication with neutral membranes and solution of low salinity in the 1980s [74]. Later, it was shown that electroformation parameters can be tuned to work for charged membranes and buffers of physiological ionic strength as well [354]. Even though electro-

formed membranes are typically clean from contaminations, lipids can get oxidized during electroformation due to high electric field intensities, which will depend on the lipid composition, buffer ionic strength and electric field parameters [283, 381].

Gel-based swelling, on the other hand, is a newer method with the advantage of being more robust and versatile with respect to different membrane compositions and solutions with varying ionic strength [76, 285]. However, for agarose-based swelling it was shown that the highly water-soluble agarose polymers can end up in the vesicle and the lipid membrane, thereby affecting vesicle mechanics [350]. A general scepticism of membrane cleanliness remained even when the gel-swelling protocol was adapted to other hydrogels, such as the less water-soluble PVA [76] and cross-linked hydrogels [286]. A comparison of stretch moduli of PVA-swollen vesicles and electroformed vesicles was done using the micropipette aspiration technique by Dao et al. [365]. Membranes made by PVA-swelling were notably easier to stretch than electroformed membranes (k_s= 90 mN/m versus 160 mN/m, respectively), a difference that was attributed to membrane contamination with PVA polymers. Interestingly, we report in this work that bending rigidities are similar for DOPC membranes formed by electroformation and gel-assisted swelling. To our knowledge, these are the first bending rigidity measurements on PVA-swollen vesicles, indicating that more research is required to explore how gel-assisted swelling can be used to create membranes for reliable mechanical measurements.

To create more complex cellular subsystems, emulsion-based vesicle formation is more suitable than the classic swelling methods [175]. Notwithstanding, a common concern with emulsion-based vesicle formation is that organic solvent molecules, initially used for lipid dispersion, can end up in the membrane. To test this concern, it is useful to compare mechanical properties of emulsion-based GUVs to model membranes formed by for example electroformation. Interestingly, while bending rigidity, a static property, was found to be unaffected by emulsion-based formation [328, 343], membrane dynamics were influenced by residual oil in the bilayer [510]. Since we demonstrated in chapter 4 that the emulsion-based method eDICE is of particular interest for bottom-up reconstitution, we employed VFA to measure bending rigidities of eDICE GUVs, which have to our knowledge not been reported before. Membrane fluctuations of eDICE GUVs were clearly visible for protein-free GUVs, for membranes decorated with streptavidin, and for membranes with an actin cortex nucleated by membrane-bound Arp2/3. However, quantitative VFA was often hindered by the presence of small membrane structures which interfered with contour detection. While in some cases it might be possible to get rid of membrane structures by fine-tuning the GUV formation protocol, sometimes the presence of these structures is intrinsically related to the reconstituted system, for example by protein-membrane interactions. For future studies, one could develop a more sophisticated contour detection algorithm that either excludes angular positions which exhibit excessive fluctuations, or that excludes angular positions based on discontinuity of the membrane contour, such as the tracking algorithm we propose in chapter 5. Otherwise, (fast) confocal microscopy might help to get rid of out-of-focus signals that impact contour detection.

6.3.1. CONCLUSION

Membrane deformation lies at the heart of many vital processes of eukaryotic cells, such as migration and cell division. As such, design of a membrane with the right mechanical properties is a key challenge in the construction of a synthetic cell and needs evaluation by mechanical probing assays on the way. In this chapter, we developed pipelines for two well-established membrane elasticity measurements: active deformation by micropipette aspiration (MPA) and passive observation by vesicle fluctuation analysis (VFA). We showed that pH control over the vesicle inner and outer solution is crucial to obtain fluctuating membranes devoid of membrane structures, which is essential for both assays. Being an active probing assay, MPA requires high control over applied aspiration pressures to deform membranes. After identification of the most important factors that influence pressure stability, we have proposed concrete design routes to minimize their effect. Additionally, we presented an image analysis pipeline useful for analysis of membrane deformations in MPA images taken in epifluorescence. For VFA, we developed an image analysis pipeline to extract bending rigidities from time-lapse videos of fluctuating membranes. We showed that the obtained bending rigidity is sensitive to image preprocessing parameters, and we presented an objective method to choose the best set of parameters. Furthermore, we showed that consistent bending rigidities were obtained, independent of the camera exposure time that was used. We validated our experimental and analysis pipelines for both MPA and VFA with a set of benchmark measurements on model membranes. Our results agreed well with literature values, for obtained bending rigidities (VFA and MPA) as well as for stretch moduli (MPA). After validation, we employed VFA measurements to show that vesicles produced by gel-assisted swelling displayed a similar bending rigidity as electroformed vesicles. This is in contrast to earlier studies which found that residual polymer can alter mechanical properties of GUV membranes [350, 365]. Furthermore, we tested the applicability of VFA to measure the bending stiffness of vesicles produced with eDICE, as a starting point for more complex reconstitution assays. Samples produced with eDICE were non-ideal, as small membrane structures interfered with contour detection and thereby hindered further quantitative analysis. This problem could in future be solved by development of more sophisticated contour tracking algorithms, which would improve robustness of the method and allow for more complex mechanical measurements, for example in presence of a non-homogeneous actin cortex. Altogether, we hope that our clear presentation of workflows for implementation of both VFA and MPA measurements will encourage researchers in the synthetic cell community to combine reconstitution assays with mechanical characterization.

6.4. MATERIALS AND METHODS

6.4.1. CHEMICALS

The lipids 1,2-dioleoyl-sn-glycero-3-phosphocholine (DOPC), 1-palmitoyl-2-oleoylphosphatidylcholine (POPC), egg-phosphocholine (EggPC), 1,2-dimyristoyl-sn-glycero-3-phosphocholine (DMPC) and 1,2-dioleoyl-sn-glycero-3-phosphoethanolamine-N-(lissamine rhodamine B sulfonyl) (Rhodamine DOPE) were ordered from Avanti (Alabaster, Alabama, US). The fluorescently tagged lipid ATTO 655 1,2-dioleoyl-sn-glycero-3-phosphoethanolamine (ATTO 655 DOPE) was obtained from ATTO-TEC (Siegen, Germany). All lipids were obtained in chloroform. Lipid solutions were

handled using Transferpettor pipettes (BRAND GMBH + CO KG, Wertheim, Germany) with glass tips, of volumes ranging from 10 to 50μL. All lipids were stored under argon at -20 °C.

Cholesterol, sucrose, glucose, Tris hydrochloride (Tris-HCl), β-casein (BioUltra, >98% purity), bovine serum albumin (BSA), light mineral oil (330779, 0.838 g/mL), heavy mineral oil (330760, 0.862 g/mL), and silicone oil (5 cSt) were ordered from Sigma Aldrich (St. Louis, Missouri, United States). Polyvinyl-alcohol (PVA, 145 kDa, 98% hydrolysed) was obtained from VWR (Amsterdam, the Netherlands).

6.4.2. GUV FORMATION

GUVs for mechanical measurements were either made by PVA-assisted swelling, using a protocol adapted from [76], or by electroformation of lipid films, adapted from its first publication [74] (see chapter 4). While gel-assisted swelling is a robust and versatile GUV formation method that can easily be used to form membranes of lipid different compositions including charged lipids, and in buffers with a range of pH and ionic conditions, there are concerns about residual polymer associated with the GUV membrane [350, 365]. We therefore used electroformation as a well-established standard for comparison.

For gel-swelling, first a 5% (w/v) PVA solution was prepared by adding PVA powder to a 200 mOsm sucrose solution in milliQ water. The solution was then heated to 90 °C on a hot plate while stirring continuously in order to dissolve the PVA powder. After a couple of hours, when the PVA powder was properly dissolved, the solution was cooled down to room temperature. The solution was then filtered with a 200 nm filter (25 mm diameter, polyethersulfone membrane, non-sterile, VWR) to remove any undissolved polymer. The resulting PVA solution could be used for months when stored in the fridge. To prepare a PVA gel for GUV swelling, a 24x24 mm coverslip (Menzel-Glaser) was first rinsed sequentially with ethanol, distilled water and ethanol and then blow-dried with nitrogen. The slide was then cleaned with a plasma cleaner (Plasma Prep III, SPI supplies, West Chester, PA, USA) for 30 seconds to ensure gel adhesion to the glass substrate. Then, 100 µL of PVA solution at room temperature was applied to the coverslip and spread by tilting the glass. Excess solution was removed with a tissue to minimize gel thickness. The slide was baked in an oven for 30 minutes at 50 °C, yielding a solid gel. Then, 10 µL of lipid solution in chloroform at a total lipid concentration of 1 mg/mL in chloroform was spread on top of the gel with a glass syringe (Hamilton) and dried for 1 hour in a vacuum dessiccator to remove any organic solvent. At lower lipid concentrations, GUV formation resulted in both a lower quality and lower yield of produced samples. In addition, a lipid concentration of 1 mg/mL was convenient as it was also found to work best for electroformation (see chapter 4). Afterwards, the coverslip was placed in a compartmentalised petri dish (4 compartments, VWR). 300 µL of swelling solution containing 200 mOsm sucrose and 10 mM Tris-HCl at pH 7.4 was carefully added on top of the gel. After swelling for 1 hour, vesicles were harvested by tilting the petri dish, carefully pipetting up the swelling solution with a 1 mL pipette tip, flushing it once over the gel to detach the vesicles, and then collecting it.

For electroformation of GUVs, we used custom-built electroformation chambers consisting of a teflon vial and a teflon cap with two platinum wires of 0.5 mm diameter inserted with about 3 mm spacing (see chapter 4). Both vial and cap contained screw thread for tight closure. The electroformation chambers were first cleaned by sonication for 15 minutes in water and then in ethanol. After blow-drying the electrodes with nitrogen, 5 µL lipids at a total lipid concentration of 1 mg/mL were spread over the two electrodes using a 5 µL Hamilton syringe. Spreading of the lipid solution over the wire was found to be essential for GUV formation. The electrodes were then dried for 30 minutes in a vacuum desiccator. The bottom part of the electroformation chamber was filled with 100 µL of swelling solution typically containing 200 mOsm sucrose and 10 mM Tris-HCl at pH 7.4. The electrodes were inserted in the solution and connected to a function generator

(Rigol DG1032). Electroformation was run by applying an alternating sinusoidal current of 300 Hz and 2 V_{pp} for 90 minutes. The effective voltage was measured with a multimeter (15XL, Wavetek Meterman, Everett, WA, USA) on the wire and adjusted if needed. After formation, the electroformation chamber was firmly tapped about 5 times on a lab bench to detach vesicles from the wire. While electroformation without Tris-HCl could be performed at 10 Hz and 2 V_{pp} (peak-to-peak voltage), addition of buffer required a higher frequency, consistent with published protocols at higher ionic strengths [340, 354] (see also chapter 4).

6.4.3. IMAGING SETUP

All VFA and MPA measurements in this chapter were performed on a Nikon Eclipse Ti microscope equipped with a confocal detector (Crest X-light), a digital camera (Orca-Flash 4.0, Hamamatsu) and monochromatic illumination with a LED light source (Spectra X, Lumencor). Aspiration experiments were conducted with a dedicated setup assembled on top of this microscope, whose basis was laid by a former PhD student in our lab, Yuval Mulla [511]. A micropipette was mounted on the setup using a pipette holder (Narishige). The holder could be clamped in a micromanipulator that was assembled on the microscope stage. The micromanipulator allowed for movement in x, y, z (sideways, in and out of the chamber, and up and down, respectively), as well as changing the out-of-plane insertion angle, to allow for insertion and precise positioning of the micropipette. The pressure in the micropipette was controlled using hydrostatic pressure with a vertically moving water bath. To this end, a 15 mL syringe without plunger was mounted on an up-right translational stage (range 30 cm, minimal step size 1 μm, LTS300, Thorlabs). The water bath was connected to the pipette holder via flexible tubing (C-Flex Clear tubing, ID 2.4 mm, OD 4 mm, Cole Parmer). Using a custom-built software written in C-sharp (developed by Brahim Ait Said from the AMOLF research institute, Amsterdam), we were able to execute automated protocols for pressure change and simultaneous imaging.

6.4.4. MICROPIPETTE ASPIRATION ELASTICITY MEASUREMENTS

We probed membrane elasticity by active deformation following the micropipette aspiration assay [7, 56]. In this assay, GUVs are aspirated with a glass micropipette by application of a suction pressure. By increasing the suction pressure, the GUV membrane tension is increased. By recording the resulting GUV deformation with an optical microscope, the strain can be calculated. For the calculation of the stress and strain, we follow the procedure described in detail in [7].

PREPARATION

Aspiration micropipettes with an orifice diameter of 5 to 8 µm were fabricated from borosilicate glass capillaries (Harvard Apparatus, inner diameter 0.58 mm and outer diameter 1.0 mm, length 100 mm) in a two-step process. First, two fine capillaries were pulled from a single wide capillary using a laser-heated pipette puller (Sutter Instruments Co Mode P-2000) using the instrument's pull settings: Heat 450, Filament 4, Velocity 50, Delay 255 and Pull 150. These pull settings yielded capillaries with long, almost parallel tips and closed ends. The capillary ends were opened using a microforge (Narishige MF-900) including a 35x magnification objective (Narishige), see fig. 6.14. The 35x magnification objective is essential to see if pipette ends are cut straight and if pipettes are free of dirt. The platinum heating filament (150 µm diameter, Narishige) of the microforge was bent into a U-shape in upright orientation. A bead of low-melting temperature glass (lead-free VPS, melting temperature ~600 °C, Ferro) was molten into the concave region. The low melting temperature glass was required as it can flow into the capillary, without melting the capillary, which is useful for making a clean cut. We opened the capillary by melting the closed tip to the glass bead, then letting the bead and filament cool down, after which the capillary was retracted backwards. Then, while heating the glass bead, we immersed the very tip of the open capillary in

the molten bead to let the low-melting temperature glass creep up into the pipette via capillary action. When the glass meniscus had flowed up in the pipette to reach the desired inner diameter of the final pipette opening, the system was cooled down to solidify. Upon retraction of the pipette, a clean cut perpendicular to the pipette walls was made.

For each aspiration experiment, an aspiration chamber was assembled for which we designed a special aluminum spacer of 3 mm thickness (see fig. 6.2d-e and fig. 6.15). The spacer was used to assemble a chamber with final dimensions of 40 x 12 x 1.5 mm (l x w x h). The spacer had slots on both sides to fit glass slides that would form the bottom and top of the chamber. Two glass coverslips (No. 1.5H, Thorlabs) were cut to 12 mm width with a glass cutter, cleaned with water and ethanol, and dried with a nitrogen gun. Next, the two glasses were mounted on the aluminium spacer from top and bottom sides by sticking them to the slots with vacuum grease (Beckman Coulter). The final chamber was thus closed from the bottom and top, and accessible from two sides. We found that in order to keep a constant pressure in the micropipette, the chamber had to be sufficiently spacious in length and width such that the sample could rest in the centre of the chamber without touching the sides. In addition, we noticed that it is important to prevent water evaporation from the chamber in order to maintain a constant pressure. For a more elaborate discussion on chamber design, see section 6.2.2.

Before the start of an experiment, the aspiration chamber and the pipette were pre-coated to prevent membrane adhesion. To this end, a droplet of 70 µL of a filtered β-casein solution (5 mg/mL β-casein, 200 mOsm glucose, 10 mM Tris-HCl pH 7.4) was placed in the middle of the aspiration chamber. We made sure that the droplet touched the bottom and top of the chamber, but not the glass edges or aluminium spacer. The micropipette was back-filled with the same β-casein solution using a thin pipette tip (Eppendorf GELloader, 20 µL), leaving a small meniscus at the pipettes' back end and leaving the front end empty. Before mounting the pipette into the pipette holder, any air bubbles in the water bath, tubing and holder were removed. Then, the pipette was mounted into the holder while applying a positive pressure to push out any remaining air. This was important to prevent the insertion of bubbles in the pipette. Finally, the β-casein solution was pushed to entirely fill the pipette, until a small droplet could be seen at the tip.

The pipette was inserted into the aspiration chamber under a small out-of-plane angle of about 5°. After bringing the pipette into focus on the microscope, we verified that the opening was clean and smooth and that the solution could freely flow in and out of the pipette. Then, the system was left to passivate for 30 minutes. The chamber was then washed twice with 80 µL aspiration buffer (200 mOsm glucose, 10 mM Tris-HCl pH 7.4) by carefully removing solution from the chamber with a tissue and filling it with a 200 µL pipette. During washing, we again made sure that solutions did not touch any of the sides of the chamber. Finally, the chamber was filled with 80 µL aspiration buffer to which we added 10 µL vesicle solution. The vesicles were left to sediment for 5 minutes. For aspiration, GUV membranes had to be slightly deflated. Therefore, the chamber was left open to allow solvent evaporation for about 10 minutes until a substantial fraction of vesicles visibly fluctuated. Then, the chamber was closed with an oil seal by carefully adding 200 µL of heavy mineral oil around the sample. By applying an oil seal, we prevented further water evaporation from the sample, which we found to be essential for maintaining a constant aspiration pressure. Furthermore, sealing the chamber prevented further deflation of vesicles, which allowed us to use the sample up to several hours. Before starting measurements, any static charge on the pipette was removed with an anti-static gun (Zerostat 3, Sigma Aldrich). Static charge on the pipette has been reported to lower the membrane lysis tension [459]. Preparation of the aspiration setup took about 1-1.5 hour, including a 30 minute waiting time for pipette passivation.

ASPIRATION PROTOCOL

For membrane elasticity measurements, we only selected vesicles that visibly fluctuated as these allowed for bending rigidity measurements, and ensured a visible aspiration into the pipette. Fur-

thermore, vesicles were only selected if they did not have tubes or other secondary membrane structures, were not sticking to other vesicles or the glass surface, and were sized between 10 and 30 µm diameter. For smaller vesicles, the area changes were too small to accurately detect in the pipette, while larger vesicles were visibly deformed by gravity outside the pipette. Before each measurement, the zero pressure was calibrated by moving the water bath up and down until no flow of naturally present small particles was seen in the pipette. The height of the water bath was in this way refined to a final precision of 10 µm H_2O as determined by digital read-out of the translational stage. Then, a vesicle of choice was aspirated with a water bath height of -50 mm (with respect to the zero pressure, typically corresponding to a moderate tension of $\sim 1 mN/m$). We lifted the pipette about twenty microns to isolate the vesicle in a focal plane slightly above the vesicles on the surface, and also moved the aspirated vesicle several hundreds of µm parallel to the glass surface to break any possible membrane tethers. Then, a pre-stress was applied by decreasing the water bath height to -200 mm for 3 minutes [56, 459, 501]. By applying a pre-stress, sub-visible membrane reservoirs, meaning membrane reservoirs with sizes smaller than the diffraction limit, are incorporated into the projected area and remain incorporated even when tension is decreased. After the pre-stress, the water bath height was decreased to -0.1 mm (with respect to the zero pressure height) to commence aspiration in the low-tension regime to measure the bending rigidity. The water bath height was decreased automatically from -0.1 to -2 mm in 20 steps, and then from -2 mm to -30 mm in 30 steps, typically corresponding to a total tension increase of about 1 mN/m. After 2 seconds equilibration time at each pressure, a fluorescence wide field image was taken with a 100 ms exposure time using a 60x long working distance water immersion objective (2.0 mm working distance, NA 1.0, Nikon), resulting in a final pixel size of 108 nm. Stretch modulus measurements were performed directly after the bending modulus measurement by further decreasing the water bath height from -30 mm to -250 mm in 50 steps, corresponding to a tension increase of about 4 to 8 mN/m. Epifluorescence images were again taken at each position after 2 seconds equilibration time. To test for hysteresis, we next performed a compression experiment by decreasing aspiration pressure, starting from a water bath height of -200 to a final height of -30 mm. Finally, the vesicle was pushed out of the pipette by applying a negative aspiration pressure. The total experiment took around 15 minutes per vesicle.

ANALYSIS OF ASPIRATION EXPERIMENTS

We wrote a Python program ($MPA\_analysis.py$) that implements the analysis described by Henriksen and Ipsen [7]. While we use the theoretical framework described in ref. [7], we propose a new image analysis method to obtain the vesicle shape parameters from epifluorescence images. Our refinements in the analysis are described in detail in section 6.2.2.

Starting from the epifluorescence image of an aspirated vesicle, we first created two smoothed images: I_{sm}, the working image, and I_{sub}, the image that is subtracted from I_{sm} to enhance the membrane signal. Smoothing was performed by convolution with a 2-dimensional Gaussian filter using the `gaussianblur` function from the `OpenCV` package. For I_{sm}, we used a small kernel size of 3x3 pixels to smoothen local random noise caused from the camera. For I_{sub}, we used a larger kernel size of 21x21 pixels to remove long-range noise caused by inhomogeneous illumination and out-of-plane fluorescence. Subtraction of I_{sub} from I_{sm}, followed by thresholding using a manually defined global intensity threshold, yielded an image containing a continuous membrane signal over a background set to zero. Image preprocessing constants could be kept constant for all GUVs analyzed. Since the membrane position corresponds to a maximum in fluorescence intensity, we applied a local maxima filter using the `peak_local_max` function from the `skimage` package to detect intensity peaks in the non-zero membrane signal, typically yielding a set of at least 50 membrane coordinates for the entire GUV. We then identified the tongue and vesicle body by fitting two circles to these coordinates using the RANSAC circle fitting algorithm from Python's `skimage` package with a minimum number of 5 inliers, yielding the relevant vesicle geometry: the

pipette radius R_p, vesicle radius R_v, tongue coordinates $(x,y)_p$ and vesicle coordinates $(x,y)_v$ (see fig. 6.3).

After performing circle detection for all the images, we calculated the time-average vesicle location, vesicle radius and tongue radius. We then determined the protrusion length for each image by taking an intensity profile along the x-axis at y_v. The membrane position in the front end of the tongue in the pipette was then defined as the maximum of the intensity profile. In further analysis we are only interested in the change of protrusion length for each step i in the aspiration pressure, that is $dL = L_p(i) - L_p(0)$. Then, via geometrical considerations, the change in membrane area dA for a change in protrusion length dL was calculated:

$$\mathrm{d}A = \frac{1}{2}\left(\left(\frac{R_p}{R_v}\right)^2 - \left(\frac{R_p}{R_v}\right)^3\right)\frac{\mathrm{d}L}{R_p} \tag{6.1}$$

The membrane tension σ was calculated via the Laplace's law from the vesicle geometry:

$$\sigma = P\frac{R_p}{2\left(1-\frac{R_p}{R_v}\right)} \tag{6.2}$$

At low membrane tensions, typically limited to 0.5 mN/m [7], the membrane deformation is dominated by bending, following:

$$\mathrm{d}A = \frac{1}{8\pi\kappa}\ln\left(\frac{\sigma}{\sigma_0}\right) \tag{6.3}$$

where κ is the bending rigidity. At tensions higher than 0.5 mN/m, the membrane deforms mainly by stretching with a stretch modulus k_s. For stretching deformations, the stress-strain relationship is given by:

$$\mathrm{d}A = \left(\frac{\sigma}{k_s}\right) \tag{6.4}$$

Thus, the obtained stress-strain data is divided into two regimes: a low-tension regime, up to $0.5 mN/m$, and a high-tension regime, from $0.5 mN/m$ and higher. By fitting eq. (6.3) to the low-tension regime, and eq. (6.4) to the high-tension regime of experimentally obtained values of stress and strain, the membrane's bending modulus κ and stretch modulus k_s were obtained. We fit these equations using the `scipy.linear_curve_fit` function. In the plots in this thesis, $\mathrm{d}A$ is given as a percentage rather than a fraction.

6.4.5. VESICLE FLUCTUATION ANALYSIS

As a complementary approach to probe membrane mechanics, we applied the established vesicle fluctuation analysis (VFA) technique [5, 341, 471]. In this method, we make use of the fact that lipid membranes spontaneously fluctuate when they are under low tension.

EXPERIMENT

First, imaging chambers were prepared as described in section 4.5.12 (small $20\mu L$ chambers). In short, an 8-well silicone gasket (8-6 mm diameter x 1 mm depth, Grace Bio-Labs) was placed on a cleaned glass coverslip (No. 1.5H, 24x50 mm, Thorlabs). To each well, 15 µL of β-casein solution (1 mg/mL β-casein, 10 mM Tris-HCl pH 7.4) was added and left for 15 minutes to passivate the glass surface. After 15 minutes, the solution was removed with a tissue and the chambers were blow-dried with nitrogen gas. To each well we added 15 µL of outer solution containing 200 mOsm glucose and 10 mM Tris-HCl pH 7.4 was. Then, 5 µL of vesicle solution in 200 mOsm sucrose and 10 mM Tris-HCl was added. Due to their higher mass density, vesicles sunk to the bottom of the

chamber which facilitated imaging. The chamber was then closed from the top, to prevent evaporation and minimize flow in the sample, with a glass slide (1 mm thickness, Thermo Scientific).

Vesicles were imaged using the microscope setup described in section 6.4.3 equipped with a 100x oil immersion objective (Nikon, N.A. 1.40). For fluctuation analysis, we selected vesicles with a radius larger than 5 µm but smaller than 20 µm, that were spatially separated from other vesicles, with membranes that were clearly fluctuating and that did not have secondary structures in the focal plane. This size criterium was important as for small vesicles, most fluctuations are too fast to resolve [5], while membrane contour fluctuations of larger vesicles are distorted by gravity effects [341]. Time-lapse movies of 2000 frames were recorded at the equatorial plane of the vesicle in epifluorescence mode at an excitation wavelength of 655 nm with 50% LED intensity and an exposure time between 2 and 10 ms

ANALYSIS

To analyse fluctuation recordings, we wrote a Python code that detects vesicle contours from either fluorescence or phase contrast time-lapse image series and finally extracts the bending rigidity and membrane tension. The analysis can be split up in four steps: contour detection, calculation of the fluctuation spectrum, mode selection, and fitting of the fluctuation spectrum. Figure 6.5 and fig. 6.6 give a visual representation of the analysis pipeline.

Unless specified otherwise, detection was done by first convolving the image with a small two-dimensional Gaussian smoothing filter using the `cv2.GaussianBlur` from the `OpenCV` package with a kernel size of 3 pixels and a standard deviation of 3 pixels. A set of 360 radial rays at an angular separation $d\theta = 1°$ was then created to extract radial fluorescence intensity profiles, starting from an initially guessed centre of the vesicle (x_m, y_m) and crossing the membrane along the entire contour. To minimise the computational cost, fluorescence intensities were analyzed only within a narrow ring around the membrane confined by an inner and outer radius r_{in} and r_{out}. The membrane position r_i at angle θ_i was defined as the maximum intensity of the smoothed signal. In some cases, as specified in the text, the one-dimensional intensity profile was smoothed with an additional one-dimensional Gaussian filter using `ndimage.filters.gaussian_filter1d` with a standard deviation of 3. This process was repeated for all 360 profiles to obtain $r_m(\theta)$. Using the angular profile of the radius, we updated the vesicle centre position by calculating the sum of the vectors $\mathbf{r}_i$ and adding this to the former centre:

$$\begin{aligned} \theta_m &= \tan^{-1}\left(\frac{\sum_i r_i \sin(\theta_i)}{\sum_i r_i \cos(\theta_i)}\right) \\ r_m &= \frac{\sum_i r_i \cos(\theta_i)}{\cos(\theta_i)} \end{aligned} \tag{6.5}$$

with the new centre coordinates (x_n, y_n) being:

$$\begin{aligned} x_n &= x_m + \cos(\theta_m) r_m \\ y_n &= y_m + \sin(\theta_m) r_m \end{aligned} \tag{6.6}$$

This process of membrane detection and centre refinement was repeated until the new centre position was less than one pixel separated from the previous one. Contour detection was repeated for all frames to yield $r(\theta, t)$. In addition, we calculated the vesicle contour length L_c for each frame as the sum of the Euclidian distances between all contour points:

$$L_c = \sum_i \sqrt{(x_{i+1} - x_i)^2 - (y_{i+1} - y_i)^2} \tag{6.7}$$

Videos with frames with a contour length deviating by more than 2% from the time-averaged contour length were ignored in the analysis.

After obtaining the vesicle contours, we performed a discrete spatial Fourier transformation. First, each point on the contour r_i was rescaled by the time-averaged radius $\langle R \rangle$. Then, the first 80 Fourier modes q of the contour were calculated as follows [471]:

$$a_q = \frac{1}{2\pi} \sum_i \{\cos(q\theta_i) + r_{i+1}\cos(q\theta_{i+1})\} (\theta_{i+1} - \theta_i) \tag{6.8}$$

$$b_q = \frac{1}{2\pi} \sum_i \{\sin(q\theta_i) + r_{i+1}\sin(q\theta_{i+1})\} (\theta_{i+1} - \theta_i) \tag{6.9}$$

Note that we use q to denote the mode number and $q_x = \frac{q}{\langle R \rangle}$ to denote the wave number (m^{-1}) belonging to q. For each mode, the Fourier amplitude was then calculated to yield the Fourier spectrum:

$$c_q = \sqrt{a_q^2 + b_q^2} \tag{6.10}$$

from which we finally derived the experimental fluctuation spectrum [5]:

$$\langle |\tilde{u}(q_{x,y=0})|^2 \rangle = \frac{\pi \langle R \rangle^3}{2} \left(\langle |c_q|^2 \rangle - \langle |c_q| \rangle^2 \right) \tag{6.11}$$

which we call $\langle |\tilde{u}_q|^2 \rangle$ henceforth.

To determine bending rigidity and tension from the experimental fluctuation spectrum, we follow the analysis outlined by Pecreaux et al. [5]. In their study, Pecreaux et al. have shown that although the vesicle fluctuates in spherical geometry, fluctuations can be described by equations valid for a planar membrane[5]. Errors due to curvature and closed topology of the membrane are significant only for the first modes[5], which are anyway not considered in the analysis because they are dominated by membrane tension (see below). The fluctuation spectrum for a planar membrane has been calculated by Helfrich and reads [4]:

$$\langle |u(\mathbf{q}_\perp)|^2 \rangle = \frac{k_B T}{\sigma q_\perp^2 + \kappa q_\perp^4} \tag{6.12}$$

Here, $u(\mathbf{r}_\perp)$ is the local displacement normal to the membrane with respect to the mean position. $\mathbf{q}_\perp = (q_x, q_y)$ is the wave vector corresponding to $\mathbf{r}_\perp = (x, y)$, the coordinates of a membrane point on the (x, y)-plane. σ and κ are the membrane tension and bending rigidity, T is the absolute temperature and k_B the Boltzmann constant. Since only fluctuations in the equatorial plane are captured with microscopy experiments, we measure:

$$\langle |u(q_{x,y=0})|^2 \rangle = \frac{k_B T}{2\sigma} \left[\frac{1}{q_x} - \frac{1}{\sqrt{\frac{\sigma}{\kappa} + q_x^2}} \right] \tag{6.13}$$

which is solely dependent on the wave number q_x. It should be noted that eq. (6.13) is the theoretical fluctuation spectrum. In our experiments, we used camera exposure times (or integration times) τ between 1 and 5 ms to record frames. This means that fluctuations with a lifetime shorter than the integration time cannot be resolved. Even at small wave vectors q_x, the spectrum is affected by this limitation. In our analysis, we follow the approach proposed by Pecreaux et al. [5] to account for the finite camera exposure time:

$$\langle |\tilde{u}(q_x)|^2 \rangle = \frac{1}{\pi} \int_{-\infty}^{\infty} \frac{kT}{4\eta q_\perp} \tau_m \frac{\tau_m^2(q_\perp)}{\tau^2} \times \left[\frac{\tau}{\tau_m(q_\perp)} + \exp\left(-\frac{\tau}{\tau_m(q_\perp)} \right) - 1 \right] \mathrm{d}q_y \tag{6.14}$$

where $q_\perp = ||\mathbf{q}_\perp||$, η is the medium viscosity and τ_m the fluctuation lifetime of a mode $\mathbf{q}_\perp$ given by [512]:

$$\tau_m(\mathbf{q}_\perp)^{-1} = \left(\frac{1}{4\eta q_\perp}\right)\left(\sigma q_\perp^2 + \kappa q_\perp^4\right) \tag{6.15}$$

Thus, by experimentally obtaining the vesicle fluctuation spectrum, we could fit eq. (6.14) to obtain the bending rigidity and tension of the membrane.

Due to experimental limitations, only a finite range of modes can be used to fit the fluctuation spectrum [5, 471]. Low q modes are statistically under-represented in the analysis as they have long fluctuation lifetimes and thus do not equilibrate on the time-scale of a typical VFA time-lapse video. In addition, deformations at low q are typically dominated by tension rather than by bending. High q modes are affected by two experimental limitations: the temporal resolution of the camera and the spatial resolution of the microscope. At intermediate modes, the variances scale as the inverse cube of the wave number q^{-3} (see fig. 6.7). By plotting $\langle|\tilde{u}_q|^2\rangle\, q_x^3$ versus q_x, the intermediate regime that is typically used to obtain the bending rigidity can be recognised as a plateau [471]. However, obtaining the exact mode cut-offs q_{high} and especially q_{low} from such a plot is subjective and can strongly influence the fit results.

Theoretical estimates help identifying the limiting modes. The cut-off between the bending- and tension-dominated regime is given by $q_b^c = R_0\sqrt{\sigma/\kappa}$ [5]. For a typical vesicle with $R_0 = 10\mu m$, $\kappa = 10^{-19}J$ and $\sigma = 10^{-8}mN/m$, we obtain a lower cut-off mode number $q_{low} = 3$. The higher mode cut-off set by the spatial resolution of the set-up, assuming a diffraction limit of $200nm$ and a vesicle radius of $10\mu m$, is $q_{high} = 50$. A temporal cut-off mode is set by the camera integration time, where fluctuations with a lifetime shorter than the integration time are not correctly fitted. The temporal cut-off mode number is given by [5]:

$$q_t^c = \sqrt[3]{\frac{4\eta}{\kappa\tau}} \tag{6.16}$$

Assuming $\tau = 5ms$, $\kappa = 10^{-19}J$ and a solution viscosity $\eta = 0.001kg/ms$, we obtain $q_t^c = 20$. Given that the spatial cut-off mode is higher than the temporal cut-off, we assumed $q_{high} = q_t^c$.

In practice, we fitted eq. (6.14) to measurements of $\langle|\tilde{u}_q|^2\rangle$ using `optimize.curve_fit` from Python's `scipy` package, which yielded values for κ and σ. As we found the exact choice of q_{low} to have a large impact on the fit outcomes, we repeated the fitting for a range of values of q_{low} as described in more detail in section 6.2.3. Plotting κ as a function of q_{low} typically showed a regime, often for q_{low} between 5 and 10, where κ minimally depended on q_{low}. We therefore based the final value for κ on the average of the values obtained within this regime. To obtain a value for the membrane tension σ, we fitted eq. (6.14) used the final κ and corresponding q_{low}. When contour detection was poor or when membranes were tense, we could not distinguish a plateau in the plot of $\langle|\tilde{u}_q|^2\rangle\, q_x^3$ versus q_x. These vesicles were excluded from analysis.

6.5. ACKNOWLEDGEMENTS

We thank Rumi Dimova, Rafael Lira, Patricia Bassereau, Feng Tsai, Stephanie Mangenot, Poul Martin Bendix, Guillermo Moreno-Pescador, Carlos Marques and Marjorie Longo for useful discussions and tutorials about MPA measurements. We thank George Dadunashvili, Timon Idema, Felix Frey, Hammad Faizi, and Petra Vlahovska for their help with VFA measurements. We thank Hammad Faizi for providing simulation data on membrane fluctuations to validate the VFA analysis script [491]. We thank C. Martinez-Torres for help with the image analysis. We thank Yuval Mulla and George Jenkinson for involve-

ment in early stages of building the aspiration setup and setting up data analysis. We thank the AMOLF software department and in particular Brahim Ait Said for programming of the aspiration measurement automation software. We thank Henk-Jan Boluijt (AMOLF design engineering), Tom Brouwer (AMOLF mechanical workshop), Dimitri Verhulst (TU Delft mechanical workshop) and Jan-Bonne Aans for assistance with development of the measurement set-up. We thank François Liénard for his help in testing VFA image analysis and implementation of the fitting procedures, Floris van Rooij for his help in VFA benchmarking experiments and Abel Hutten for his help in implementing an exposure-time corrected fitting procedure. We thank Sophie Sandy and Lucia Baldauf for providing fluctuation data on eDICE GUVs.

6.6. SUPPLEMENTARY FIGURES

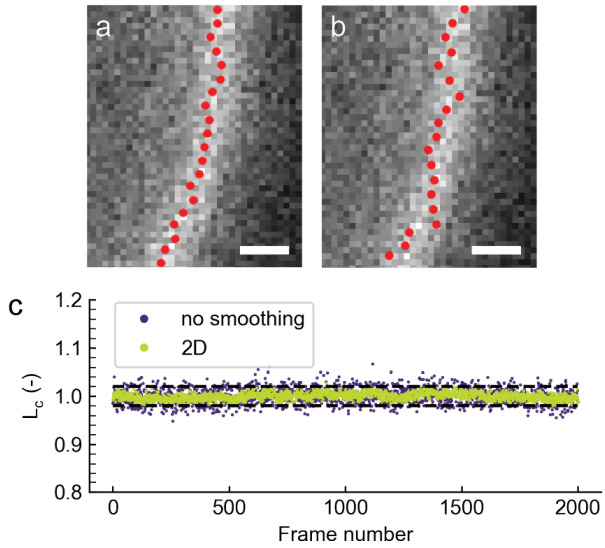

Figure 6.12: **VFA membrane detection results obtained with different image preprocessing options.** Image shown is a zoom-in on fig. 6.5. Scale bar is $5\mu m$ in both images. (a) Membrane detection with 2-dimensional smoothing only. (b) Membrane detection without smoothing applied. (c) Evolution of contour length (normalised by its time-average) without smoothing (purple) and with two-dimensional smoothing (yellow).

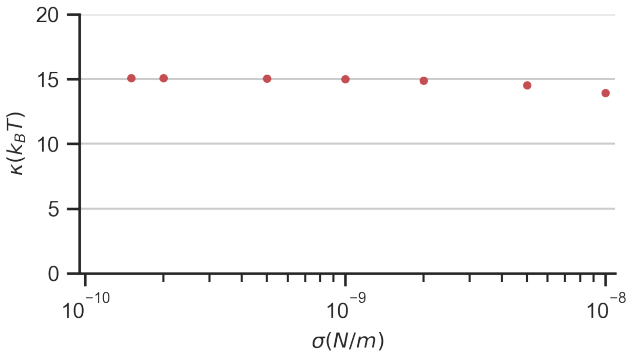

Figure 6.13: **Effect of membrane tension on the fitting of bending rigidity.** A theoretical fluctuation spectrum was calculated using $\kappa = 15k_BT$ and $\sigma = 10^{-9}N/m$. Fitting the spectrum using a range of fixed σ values resulted in bending rigidities close to $15k_BT$ (red dots), with at maximum $1k_BT$ difference.

Table 6.3: **Overview of VFA results.** Fitting results for κ and σ of all VFA measurements performed on DOPC and POPC membranes, with and without 30 % cholesterol (indicated by + and -, respectively), produced by gel swelling (GSW) or electroformation (EF). 'GUV no.' denote unique GUVs, 'exp no.' denote different time-lapses taken from individual GUVs, R denotes the vesicle radius.

GUV no.	Exp. no.	Lipid	Chol 30%	Form	R μm	κ k_BT	σ N/m
1	1	DOPC	+	GSW	6.9	14.6	8.3e-10
1	2	DOPC	+	GSW	6.9	12.8	2.2e-8
2	1	DOPC	+	GSW	10.8	19.6	1.2e-8
2	2	DOPC	+	GSW	10.9	17.9	1.7e-8
3	1	DOPC	-	GSW	7.8	15.6	5.9e-9
3	2	DOPC	-	GSW	7.8	15.0	7.4e-9
4	1	DOPC	-	GSW	9.6	19.5	2.6e-8
4	2	DOPC	-	GSW	9.6	18.2	3.2e-9
5	1	DOPC	-	GSW	8.9	16.4	3.1e-9
5	2	DOPC	-	GSW	9.0	15.0	5.7e-9
6	1	POPC	+	GSW	8.4	24.5	2.4e-9
6	2	POPC	+	GSW	8.4	23.9	3.2e-9
7	1	POPC	-	GSW	5.5	14.3	9.4e-10
8	1	POPC	-	GSW	7.0	18.5	9.2e-10
8	2	POPC	-	GSW	7.0	17.2	1.5e-10
9	1	DOPC	-	EF	8.7	20.0	2.7e-9
9	2	DOPC	-	EF	8.7	20.5	5.2e-9
10	1	DOPC	-	EF	6	15.9	1.1e-8
10	2	DOPC	-	EF	6	15.8	2.8e-9
11	1	DOPC	-	EF	8.2	19.2	5.8e-9
11	2	DOPC	-	EF	8.2	20.0	2.4e-8
12	1	DOPC	-	EF	7.5	17.4	3.4e-9
12	2	DOPC	-	EF	7.5	17.7	1.4e-9
13	1	DOPC	-	EF	7.9	19.6	2.0e-9
13	2	DOPC	-	EF	7.9	20.2	3.4e-9

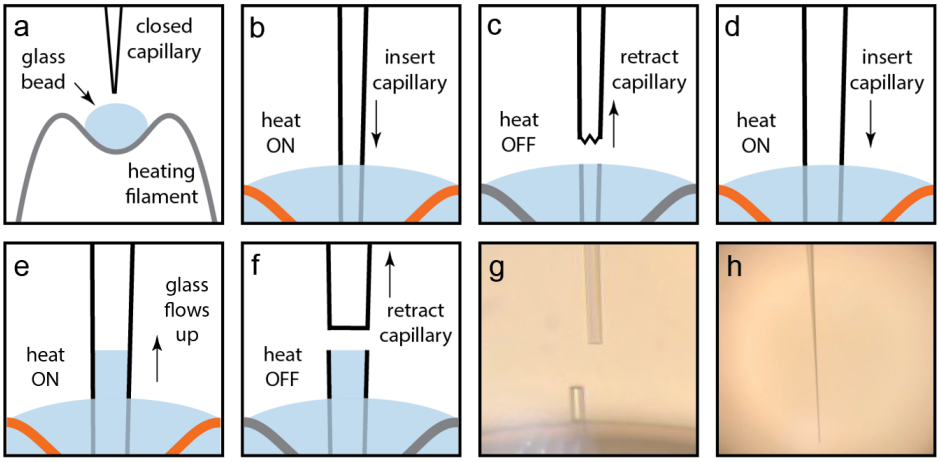

Figure 6.14: **Protocol for fabrication of micropipettes for aspiration measurements.** (a-h) Schematic overview of fabrication procedure. (a) A closed micropipette is brought close to the glass bead of the heating filament of the microforge. It is advised to use the 5x objective for a good overview of the system. (b) After switching to the 35x objective for precise control of the pipette tip, the heating filament is warmed up such that the glass bead melts. The micropipette tip is inserted in the molten bead. (c) The heat is switched off, after which the pipette can be retracted. The resulting pipette is open, but the cut is likely not straight. (d) Again, the glass is molten, and the pipette is inserted. (e) While the glass bead is heated, the glass will flow into the capillary. Once the glass reached the desired pipette orifice position, release your foot from the heating pedal. (f) After the glass solidifies, carefully retract the pipette to create a clean cut at the glass meniscus. Inspect the pipette opening: it should be straight and clean. (g) Image of successfully fabricated pipette as seen with 35x magnification. The cut tip can be seen frozen in the glass bead. (h) View of the pipette with 5x magnification.

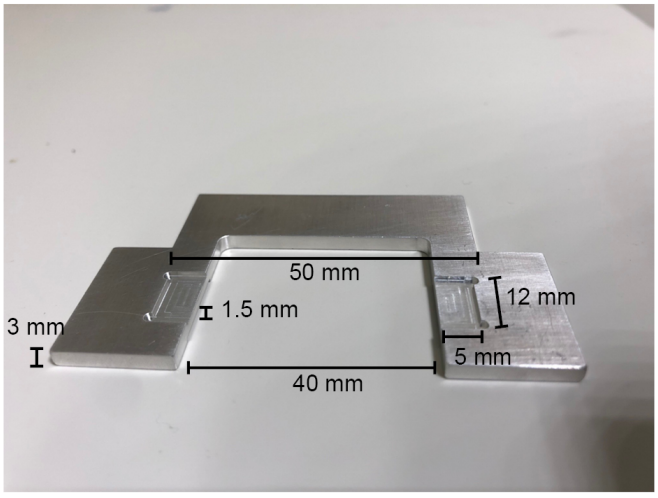

Figure 6.15: **Sample chamber for MPA measurements.** Aluminum spacer used for constructing micropipette aspiration chamber. Slots seen here on top are made to fit a glass slide, which serves as the top of the chamber. Similar slots are present on the bottom to insert the bottom coverslip.

7

IN VITRO LIPID MEMBRANE GROWTH BY FUSION

Generating membrane growth is a key challenge in building a synthetic cell from the bottom up. While previous reconstitution assays have demonstrated that lipids can be synthesized de novo in giant unilamellar vesicles (GUVs), surface area growth might be more easily realized by external feeding of smaller vesicles that incorporate in the GUV membrane by lipid bilayer fusion. A fusion mechanism based on hybridization of two complementary membrane-bound DNA linkers has been well-established for fusion between small vesicles and small vesicles with supported lipid bilayers in the past, but the requirements for efficient fusion of small vesicles with GUVs has been relatively unexplored. In this chapter, we characterize fusion between GUVs and hundred times smaller large unilamellar vesicles (LUVs) mediated by cholesterol-anchored single stranded DNA linkers. We perform fluorescence image analysis on a GUV population level to evaluate individual steps in the fusion process, being membrane incorporation of the DNA linker, binding between LUVs and GUV, and content mixing. We show that fusion is highly dependent on DNA linker concentration in a non-monotonic way, with a maximum fusion efficiency of 30% of the total number of GUVs. Furthermore, we show that this fusion mechanism is compatible with different GUV membrane compositions as well as with GUVs produced by emulsion Droplet Interface Crossing Encapsulation, thereby showcasing the potential of generating membrane growth in complex reconstitution assays. Altogether, DNA-mediated membrane fusion provides a facile yet effective way to generate growth of a synthetic cell membrane in vitro.

Experiments in this project were performed by Tom Aarts and analysed by Lennard van Buren. The project was executed under supervision of Lucia Baldauf and Lennard van Buren.

7.1. INTRODUCTION

A key goal in building a synthetic cell is to reconstitute its ability to grow and replicate. Fundamental to both of these processes is an increase in membrane area. To achieve volume homeostasis for division of a spherical vesicle, the membrane area has to grow by ~28% based on geometrical considerations [269]. Besides volume homeostasis, the ratio of membrane area to volume is important for control of cell shape and membrane tension, both of which play a major role in cytokinesis (see also chapter 2). For reconstitution of cellular growth and cytokinesis, we thus need a technique to generate extra membrane area for a pre-formed synthetic cell.

Living cells generate extra membrane area by synthesizing phospholipids in the endoplasmatic reticulum and Golgi apparatus (reviewed in ref. [500]). Membrane is then trafficked internally by means of endosomes from the ER and Golgi to merge with the plasma membrane by exocytosis. During cytokinesis, fusion of endosomes is targeted specifically to the cytokinetic furrow to cause local expansion of the membrane area [82]. Recapitulating this system in the synthetic cell would involve the reconstitution of internal metabolic and synthesis pathways, self-assembly of phospholipids into internal organelles, and finally fusion of internal vesicles with the synthetic external 'plasma' membrane, all processes controlled in space and time.

Such a reconstituted process would be closest to its biological counterpart and give the synthetic cell maximum autonomy. However, recreation of the full biological pathway imposes several challenges. First, the production capacity of *de novo* synthesis of phospholipids is limited to ~10% area increase in GUVs over the course of >5 hours when produced with genetically encoded enzymes [88]. Larger (relative) areal growth of 25-30% can be achieved by phospholipid biosynthesis using purified enzymes, but this has so far only been established in LUVs [87]. Reconstitution of a synthesis pathway for large increases in areal growth has yet to be established for GUVs. Second, temporal coordination of membrane growth and division is challenging, especially when time scales for phospholipid biosynthesis and furrow constriction do not match. Furthermore, lipid types can only be incorporated once their metabolic pathways have been successfully reconstituted. This potentially narrows down the compositional richness of membranes, and might for example be problematic when non-standard lipids such as PIP_2, a signalling lipid particularly relevant for cytokinesis *in vivo* [513], are required.

To construct a minimal synthetic cell, we may not need to reconstitute the full biological system. This is especially true when the goal of a reconstitution experiment is not membrane growth itself, but where membrane growth is a prerequisite, such as cell division. Therefore, synthetic cell research would benefit from an easy, supply-on-demand of excess membrane area, that can be used as an intermediate step on the roadmap of constructing a fully autonomous synthetic cell.

An intuitive and simple approach for membrane growth is to supply extra membrane area from the outside. Large unilamellar vesicles (LUVs, < 300 nm diameter) can be added to GUVs, and be designed to fuse with GUVs, thereby delivering their membrane area. The potential of LUV-GUV fusion has already been demonstrated in various studies [89–91, 514]. More general, membrane fusion has been studied extensively over the past decades because of the importance of this process in biological processes such as endo- and exocytosis and neuronal signalling (reviewed in [515, 516]). Although the exact path-

ways remain under debate and may depend on the fusion mechanism at play [517–519], two stages can generally be recognized in the process of membrane fusion [517]. First, the two opposite bilayers are brought in close proximity, which means that repulsive hydration forces between the lipid headgroups need to be overcome[520]. Second, destabilization of the lipid bilayers, either spontaneous or induced, leads to the opening of a fusion pore which can expand until the two membranes are fully fused. These events can proceed through or even be stalled at a hemi-fused intermediate [517, 519, 521], where the proximal outer leaflets have mixed, but not the inner ones.

Numerous mechanisms have been designed to induce membrane fusion. While all fusion mechanisms definitely lead to close apposition of the bilayers, some also promote further progression to hemifused and fused states. First, there are more generic mechanisms, based on size exclusion with polyethylene glycol (PEG) [522], electrostatic interactions with divalent cations such as Ca^{2+} [523], or electrostatic interactions generated by lipid composition [90]. These systems lack programmability and often require unphysiological conditions. To circumvent these problems, there is an increased focus on rational design of membrane-bound receptors which render membranes fusogenic via membrane surface recognition[8, 9, 271]. The design of most receptors is inspired by the soluble N-ethyl-maleimide-sensitive-factor attachment protein (SNARE) family which mediates vesicle fusion *in vivo* (reviewed in ref. [524]). In SNARE-mediated fusion, SNARE proteins anchored in the two opposite membranes bind, thereby forming a bridging complex between the membranes. As the bridge closes in a zipper-like mechanism, the two membranes are brought in close proximity and are finally fused. Although the exact mechanisms by which SNARE proteins mediate fusion are to date unknown, this biological machinery has inspired researchers to design simpler model systems that capture two essential features of SNARE: (1) two subunits that recognize and bind to each other, each of which is anchored in one of the opposing membranes, and (2) the subunits bind in a zipper-like manner, starting from the membrane-distal ends of the linkers. As such, several model systems have been developed, among which a peptide-mediated mechanism developed by the Kros group [271], and a mechanism based on hybridization of membrane-anchored DNA first reported by the Höök group [8]. While the peptides are synthesized in house by the research group involved, oligonucleotides for the DNA-based assay are readily available from commercial producers. This makes DNA-mediated fusion an excellent candidate for the development of a membrane fusion assay geared towards generating growth of a synthetic cell membrane.

Over the years, DNA-mediated fusion has been well characterized with fusion assays either involving fusion between small unilamellar vesicles (SUVs, diameter < 100 nm) or fusion of SUVs with supported lipid bilayers (SLBs). In particular, the influence of the size and molecular properties of the membrane anchor has been mapped [525, 526], as well as the length and composition of the nucleotide linker sequence [525, 527] and the membrane composition [8]. The results from these studies can however not be readily applied to LUV-GUV fusion. Fusion processes have been shown to depend on membrane geometry and tension, which differ significantly between the different model systems (reviewed in [528]). In this chapter, we therefore demonstrate the potential of DNA-programmable membrane fusion of large unilamellar vesicles (LUVs) with GUVs as a growth mechanism for artificial cells. For membrane growth in synthetic cells, fusion of

LUVs to GUVs is the most desirable process, as LUVs can efficiently increase the membrane area of micron-sized synthetic cells without significantly interfering with volume homeostasis.

Note that we while previous assays mostly worked with vesicles of 50 nm to 100 nm diameter, considered SUVs, we performed our assays with LUVs of a slightly larger diameter of 200 nm, because we found that the larger LUVs resulted in a higher detectable fusion efficiency. We performed quantitative image analysis of large GUV samples using the DisGUVery software introduced in chapter 5 to evaluate our fusion assay at the population level. In this way, we investigated the individual steps in the fusion process: membrane incorporation of the DNA linker, binding of LUVs to GUVs, and finally fusion. As a result, we provide a clear overview of the experimental parameters that are (or are not) crucial to establish fusion. We anticipate that our results will help synthetic cell engineers to employ DNA-based fusion for reconstituting membrane growth.

7.2. RESULTS

7.2.1. EXPERIMENTAL WORKFLOW AND ANALYSIS

In this chapter, we describe how we established an assay for DNA-mediated fusion between GUVs and LUVs based on membrane-anchored single stranded DNA-oligos, schematically illustrated in fig. 7.1. DNA-mediated fusion has been well established for SUV-SUV fusion [8, 9, 527] and SUV-SLB fusion [519], but has only recently been shown to be effective for GUV-LUV fusion [91]. In this study, we explored the potential of DNA-mediated fusion for *in vitro* growth of a synthetic cell membrane. To this end, we mapped the experimental design parameters influencing the three different steps in the fusion process: chol-DNA insertion in the membrane, LUV-GUV docking and fusion.

To ensure binding specificity between GUV and LUVs, one DNA strand (DNA1) was incorporated in the LUVs, and the complementary strand (DNA1′) in GUVs. Membrane incorporation was accomplished by using DNA-strands modified with a hydrophobic cholesterol moiety [8]. Previous studies have shown that the orientation of the DNA strands in the membrane greatly influences the success of fusion [9]. Only in antiparallel orientation, membrane fusion occurs due to a zipper-like binding mechanism between opposite membranes[9]. Therefore, we used a DNA1 strand that was modified with cholesterol on the 3′ end, while DNA1′contained a cholesterol moiety attached to its 5′ end. After incubation of the different vesicle populations with their respective chol-DNA strands, GUVs and LUVs were mixed to allow fusion to occur. Finally, fusion was monitored based on a content mixing assay (described under fig. 7.8). We examined all three steps in the fusion process individually by quantitative analysis of fluorescence microscopy images.

The results in this chapter are based on high-throughput fluorescence-based image analysis of large GUV populations. To obtain population characteristics from our experiments, we used our custom-written DisGUVery software (see chapter 5). The standardized analysis workflow is illustrated in fig. 7.2. GUVs were imaged in epifluorescence microscopy yielding images that typically contained several vesicles per field of view (fig. 7.2a). In general, for each condition we acquired at least ten images accounting to a minimum of hundred GUVs. Vesicle detection was performed in the appropriate chan-

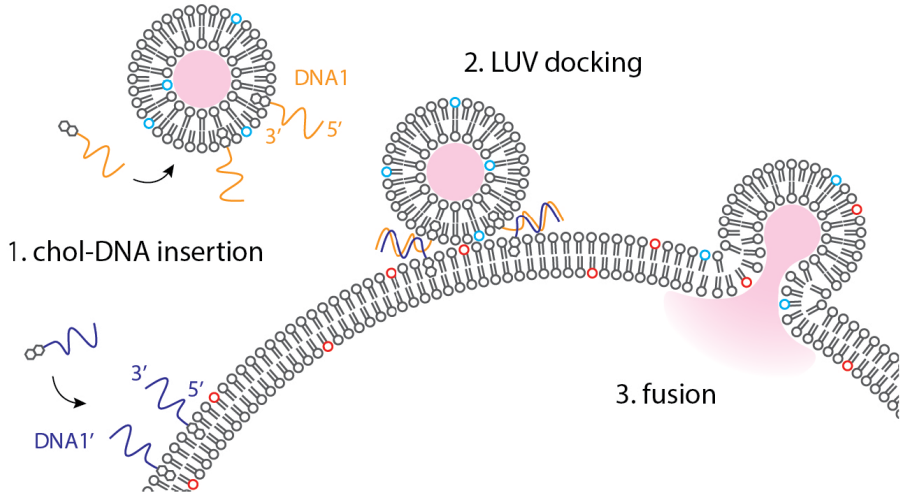

Figure 7.1: **Schematic illustration of the DNA-mediated fusion experiments.** GUV membranes consisting of DOPC with a small fraction of fluorescent lipids (red) are produced by gel-assisted swelling. DOPC LUVs doped with a small fraction of fluorescent lipids (cyan) and encapsulating a fluorescent dye (pink) are formed by extrusion with 200nm pore size. After formation, LUVs are incubated with 5′-DNA1-3′-cholesterol (orange). The complementary cholesterol-5′-DNA1′-3′(dark blue) is incorporated in the GUV membrane. When LUV and GUV approach each other, the complementary strands hybridize, leading to docking of the LUV on the GUV membrane. Due to their antiparallel orientation, binding of the DNA strands occurs in a zipper-like fashion, bringing LUV and GUV membrane close together. Once docked, the membranes can fuse, leading to lipid mixing as well as content mixing, and therefore to influx of the encapsulated dye into the GUV lumen.

nel, which was often a fluorescent lipid in the GUV membrane, after which further fluorescence analysis could be done in any other channel. After a membrane enhancement step (fig. 7.2b), vesicles were detected by means of the Circular Hough Transform (CHT) detection method (fig. 7.2c, see chapter 5 for more details). The CHT algorithm detects objects based on their circularity, making it suitable for these samples where the large majority of the vesicles was spherical. After successful detection, CHT yielded the coordinates of the vesicle centres together with the radii of the detected circles. Using these detection results, fluorescence analysis of the GUV membranes could be performed. To this end, angular and radial fluorescence profiles were extracted as follows (fig. 7.2d). Using the detected vesicle radius and centre from CHT detection, a 50-pixel wide ring was drawn centred around this radius to segment the membrane. This ring was divided in 72 angular slices (5° angular width), and from each slice the intensity maximum was obtained to generate the angular intensity profile (fig. 7.2e). The average signal was defined as the mean of all angular maxima (fig. 7.2e, dashed line). For the radial profile, the vesicle was divided into 5 pixel wide concentric rings up to the outer edge of the wide ring used for the angular profile (fig. 7.2d). In this way, radial intensities were computed as the mean of each ring from the vesicle interior up to the solution directly outside the GUV. To locally correct for background fluorescence, the signal at the outermost pixels of

the ROI was radially averaged, and was used as the local background signal just outside the GUV (fig. 7.2f). After subtraction of the background signal from the median angular signal, the average membrane intensity per vesicle was obtained.

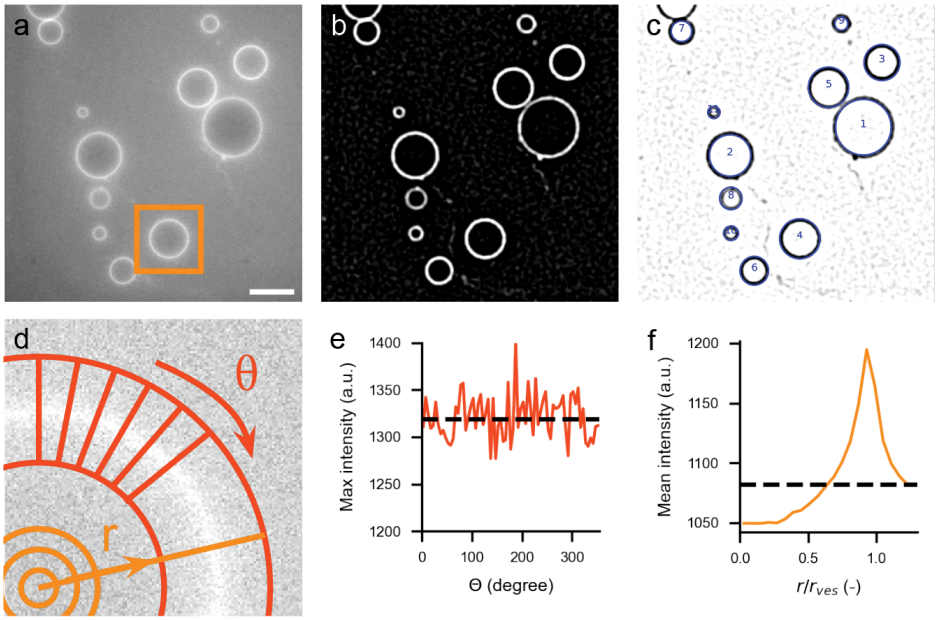

Figure 7.2: **Analysis workflow for membrane fluorescence measurements.** (a) Epifluorescence image of DOPC GUVs produced by gel-swelling. GUVs were incubated with $1\mu M$ chol-DNA1′and $1\mu M$ DNA1-Alex488 (see fig. 7.3). The orange box indicates the vesicle analysed in panel d-f. (b) Preprocessed image created by Gaussian smoothing and edge enhancement of the original image. (c) Results of Circular Hough Detection. Detected vesicles are indicated in blue. (d) Angular (dark orange) and radial (orange) intensity profiles were extracted from detected vesicles. (e) Angular intensity profile obtained with the maximum intensity of 72 angular slices. The dashed line indicates the median intensity. (f) Radial intensity profile obtained by calculating the mean of each radial ring. On the x-axis is plotted the radial distance to the vesicle centre normalized by the vesicle radius. The dashed line indicates the mean intensity at largest radial distance, which is the value used for background subtraction.)

7.2.2. DNA INCORPORATION

As the first step in DNA-mediated fusion, we investigated what determines the incorporation of chol-DNA into the GUV membrane. To this end, we incubated GUVs with chol-DNA1′, after which we added a fluorescently-tagged complementary strand of sequence 5′-DNA1-3′-Alexa488 (fig. 7.3a). Membrane incorporation of the cholesterol-DNA could then be assessed using fluorescence microscopy by measuring membrane co-localization of the fluorescent strand. We measured membrane incorporation over a range of DNA concentrations, from 0.25 to $5\mu M$, increasing both the concentration of chol-DNA as well as the fluorescent complementary strand. All concentrations are well below the critical micelle concentration of the oligonucleotides (above 10 μM) [529].

Over the entire range of concentrations, DNA-Alexa488 fluorescence was clearly enhanced at the GUV membrane (fig. 7.3b-c). We observed no non-specific binding in absence of chol-DNA. Furthermore, quantitative analysis of membrane fluorescence of GUV populations revealed that the average DNA intensity at the GUV membrane increased with DNA concentration over the entire range, indicating increased chol-DNA membrane binding (fig. 7.3d). Analysed GUV populations contained between 80 and 320 vesicles from 1 independent experiment, dependent on the condition (table 7.6). In addition to the absolute increase in intensity, also the variation in intensity increases with DNA concentration. The increasing variation is likely caused by the higher concentration of fluorescent DNA at higher cholesterol-DNA concentrations, thereby increasing background fluorescence and decreasing the signal-to-background (S/Bg) ratio. While at $0.25\mu M$ DNA the S/Bg is 1.26, at $5\mu M$ DNA the S/Bg is only 1.07. Besides providing a quantitative readout for DNA incorporation at different concentrations, population analysis shows that the DNA signal on the membrane was independent of vesicle size for GUV sizes larger than $1\mu m$ (fig. 7.3d). Since the DNA signal at a certain concentration is constant over a large range of GUV sizes, this also proves that there are no substantial size-dependent artefacts related to fluorescence imaging, nor any physical effects such as curvature on DNA insertion.

For each DNA concentration, we computed the population average of the DNA signal per vesicle (fig. 7.3e). This reveals that incorporation shows a logarithmic dependence on DNA concentration. We fitted the data using a simple Langmuir adsorption model of the form:

$$I_{\mathrm{DNA}} = \frac{I_{\mathrm{DNA,\,m}} K c_{\mathrm{DNA}}}{(1 + K c_{\mathrm{DNA}})} \tag{7.1}$$

where I_{DNA} is the DNA signal at the membrane, $I_{\mathrm{DNA,\,m}}$ is the DNA signal at the membrane for a monolayer of DNA molecules occupying the entire surface area, c_{DNA} the concentration of DNA in solution, and K is the equilibrium constant. Fitting eq. (7.1) to our data resulted in $K = 0.89\mu M^{-1}$ (fig. 7.3e, dashed line). In other words, at a DNA concentration of $1/K = 1.1\mu M$, half of the binding sites at the GUV membrane is occupied with DNA molecules. Qualitatively, the adsorption behaviour follows previous reports on chol-DNA binding to supported lipid bilayers (SLBs) measured by quartz-crystal microbalance with dissipation (QCM-D) [529, 530]. For monovalent binding with a single hydrophobic moiety, incorporation was found to be reversible and to follow a Langmuir-adsorption behaviour[529, 530]. However, quantitative QCM-D measurements have previously yielded an equilibrium concentration of $17nM$ [530]. Both in ref. [530] and in this work the DNA was of comparable length (20 bp vs 24 bp in this study), the incorporation was mediated by a single cholesterol anchor, and the lipid bilayer consisted of PC lipids (POPC in [530] vs DOPC in this study). A difference in adsorption behaviour could originate from the degree of mixing in the different systems. QCM-D experiments are performed under continuous inflow of fresh chol-DNA, thereby mixing the solution close to the lipid bilayer and ensuring a high concentration of chol-DNA adjacent to the membrane. In our optical microscopy experiments, GUVs and DNA are first mixed and then placed in a closed imaging chamber. Without further mixing, DNA binding will result in a local depletion of chol-DNA close to the membrane, resulting in a lower effective

concentration. In addition, equilibrium constants for bilayer incorporation of chol-DNA have to our knowledge only been determined for SLBs. Considering the effect that the solid support can have on bilayer properties [531–533], a question thus remains to which extent these results can be extrapolated to free-standing GUV membranes. Based on the equilibrium concentration obtained in our experiments, we chose to work with a DNA concentration of $1\mu M$ henceforth, as it ensures a high surface coverage while minimiz-

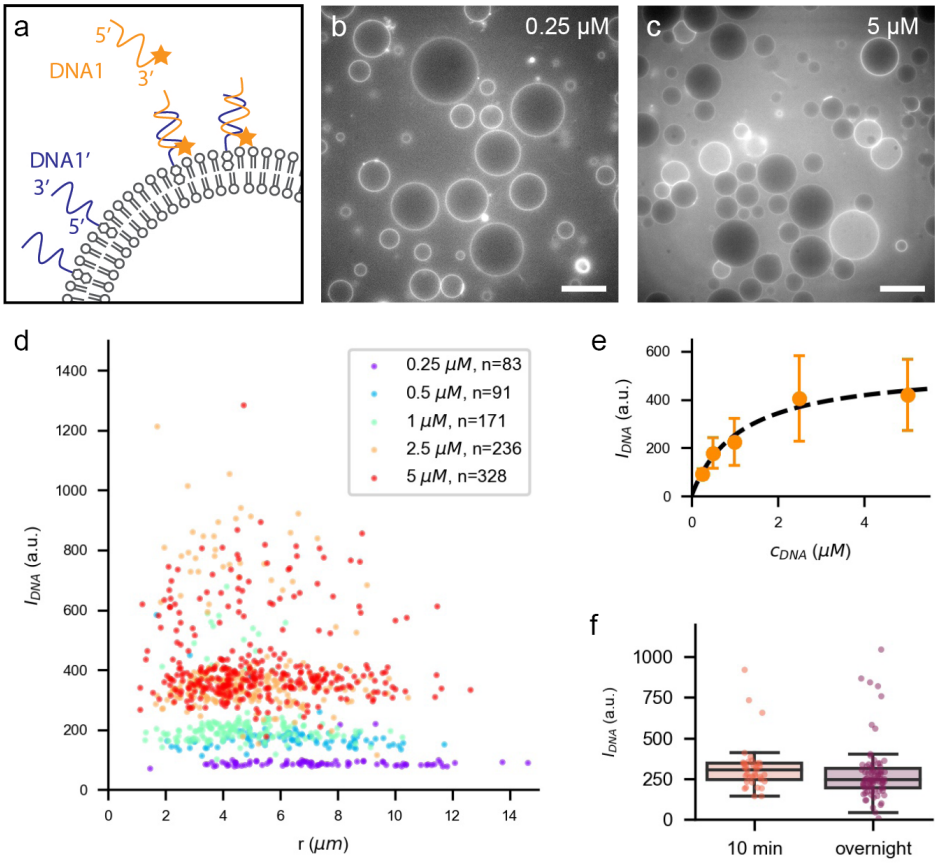

Figure 7.3: **Effect of DNA concentration on insertion in the GUV membrane.** (a) Schematic of the DNA incorporation experiment. GUVs were incubated with unlabelled chol-5′-DNA1′-3′(dark blue), after which membrane incorporation was visualized by introducing a complementary 5′-DNA1-3′-Alexa488 (orange) (b) Epifluorescence image of DOPC GUVs incubated with $0.25\mu M$ chol-DNA and DNA-Alexa488. Scale is $20\mu m$ (c) Epifluorescence image of DOPC GUVs incubated with $5\mu M$ chol-DNA and DNA-Alexa488. (d) Scatter plot of DNA intensity at the GUV membrane plotted against the GUV size. Each point represents a single vesicle. (e) Adsorption curve of chol-DNA, where the fluorescence intensity of DNA-Alexa488 at the membrane is plotted against the DNA concentration. Orange represents the population average of experimentally measured DNA intensities with standard deviation. The black dashed line is the fit of the Langmuir adsorption model, with equilibrium constant $K = 0.89\mu M^{-1}$. (f) DNA intensity measured at the GUV membrane 10 minutes after mixing (n=37) and after overnight incubation (n=91). Each point represents a single vesicle, the boxes represent quartiles of the dataset and the whiskers show the rest of the distribution.

ing the amount of free unbound DNA in solution.

Besides DNA concentration, we studied the effect of binding time. DNA incorporation was fast, showing no significant change in fluorescence when a sample was incubated overnight as compared to a 10 minutes incubation time at a concentration of $1\mu M$ (fig. 7.3f, p=0.39). For practical reasons, we therefore used an incorporation time of 70 minutes for further experiments.

Closer inspection of fig. 7.3c and fig. 7.3d shows that the distribution of fluorescence at high DNA concentrations is not uniform. Instead, two populations seem to be present: a large population of vesicles with lower membrane-localized DNA fluorescence (fig. 7.4a, orange arrow), and a smaller population of vesicles with higher DNA signal at the membrane (fig. 7.4a, dark orange arrow). Not only is the DNA signal at the membrane different between these populations, also the lumen intensity is higher for the GUVs with higher membrane-localized DNA fluorescence. For a concentration of $5\mu M$ DNA, a histogram of the DNA intensity distribution is given in fig. 7.4. The distribution shows two peaks, around $I_{\mathrm{DNA}} = 350$ and 700. Based on the fact that the high intensity GUVs have a brighter lumen than the majority of the GUV population, we hypothesize that DNA strands have permeated the membranes of these vesicles. Once DNA is present on both sides of the membrane, it can decorate both leaflets, in turn leading to the observed doubling of DNA signal at the membrane. We quantified the fraction of high intensity GUVs by calculating an intensity threshold to separate both populations using Otsu's method [534]. For a DNA concentration of $5\mu M$, the threshold is indicated in fig. 7.4b, separating the population in 80% low intensity GUVs and 20% high intensity GUVs. We computed the fraction of high intensity GUVs for all DNA concentrations fig. 7.4c, showing a clear increase with increasing DNA concentration. These results point in the direction of a DNA-induced permeabilization of the GUV membrane. This is in line with a previous study, which reported that insertion of a peptide into the membrane can result in packing defects, and in turn lead to increased membrane permeability [535]. Alternatively, local osmotic mismatches upon addition of DNA, which is dissolved in a solution of low osmolarity, might have resulted in enhanced membrane permeability. It should be noted that some GUVs with a higher DNA intensity did not have a brighter lumen, especially at lower DNA concentrations. This means that a part of the population displayed in fig. 7.4 are GUVs with a high DNA intensity that are not permeabilized. However, numbers of these GUVs with dark lumen and bright membrane signal were small and will not affect the qualitative outcome.

There is a body of work supporting that elevation of membrane tension enhances fusion [89, 536, 537]. Therefore, we examined if membrane tension can be used as a handle to boost DNA-mediated vesicle fusion. To investigate if membrane tension affected chol-DNA incorporation, we incubated GUVs with DNA at different osmotic mismatches with the outer solution, ranging from $-45 mOsm$ (hypotonic) to $+30 mOsm$ (hypertonic) (fig. 7.5a-c). In all osmotic conditions, GUVs were spherical and many showed small membrane structures, such as tubes or buds, pointing outwards. We did not see differences between samples in terms of GUV shape or membrane fluctuations. As can be seen from fig. 7.5a-c, chol-DNA successfully incorporated in the GUV membrane in all osmotic conditions. Population averages for between 50 and 100 GUVs per condition (see table 7.6 in SI for population sizes) showed no significant differences between any of

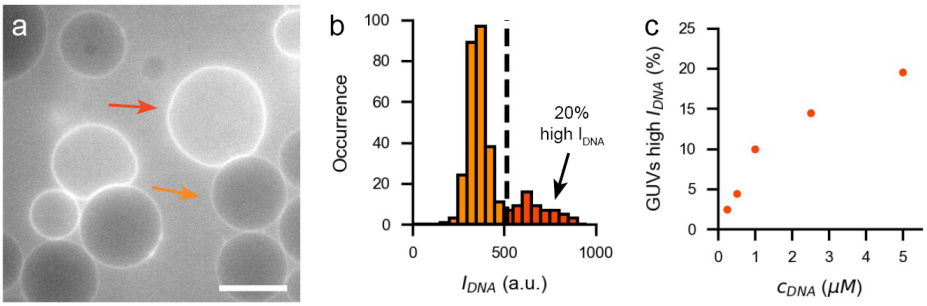

Figure 7.4: **Bimodal distribution of DNA signal on GUV membranes.** (a) Epifluorescence image of DOPC GUVs incubated with 5μM chol-DNA and DNA-Alexa488. Most GUVs have a dark lumen and low membrane signal (orange arrow), while for some GUVs both the lumen and the membrane show increased brightness (dark orange arrow. Scale bar is 10μm. (b) Distribution of membrane-bound DNA fluorescence for GUVs incubated with 5μM DNA. Dashed line represents the intensity threshold computed with the Otsu method. (c) Fraction of high intensity GUVs as a function of DNA concentration.

the conditions (p>0.1). These results show that DNA incorporation is feasible regardless of the osmotic conditions. However, the absence of membrane fluctuations in hypertonic solutions raises the question if it was really the membrane tension that was varied in these experiments. It is possible that the osmotic mismatches did not result in gentle deflation of the GUVs, but rather caused membranes to open up to quickly release osmotic stress, refolding the membrane into buds and tubes upon closing. However, this would be accompanied by temporal permeabilization of the GUV membrane, and therefore to influx of fluorescent DNA, which we did not observe. An alternative explanation for the absence of fluctuations might be found in spontaneous curvature effects. Since chol-DNA in principle only inserts in the outer leaflet, this leaflet will expand in area creating an asymmetry over the membrane. This, in turn, can give rise to the formation of membrane tubes and buds on the outside of the membrane [63, 64, 268] as we see in fig. 7.5. Such membrane deformations might be exaggerated upon GUV deflation, and will most likely reduce membrane area available for membrane fluctuations.

7.2.3. DOCKING

The next step in the fusion process is binding of LUVs to GUVs by hybridization of the complementary DNA-oligos (see fig. 7.1). To achieve docking, GUVs and LUVs were first incubated separately with chol-DNA1′and chol-DNA1, respectively. After incubation for 70 minutes, LUVs and GUVs were mixed and imaged. We first tested the influence of DNA concentration on GUV-LUV binding, by incubating GUVs and LUVs with their respective DNA strand at DNA concentrations from 0 to 5μM. LUVs comprised of DOPC lipids were produced by extrusion with a 200nm membrane, yielding LUVs around the size of the diffraction limit. Therefore, individual LUVs cannot be resolved in our optical microscopy assays. In absence of DNA, LUVs did not localize on the GUV membrane: instead, LUVs are visible as a speckled continuous signal only present in the solution surrounding the GUVs (fig. 7.6a). In stark contrast, we observed clear colocalization over

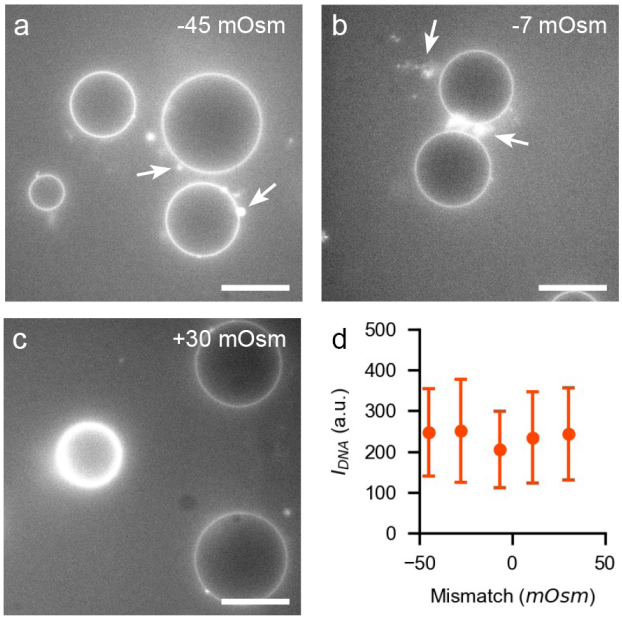

Figure 7.5: **DNA incorporation was successful at all osmotic conditions tested.** Scale bar is $10\mu m$ in all images. (a-c) Epifluorescence images of DOPC GUVs incubated with $1\mu M$ chol-DNA and DNA-Alexa488 in buffers of different osmolarity. In all images, outward-pointing membrane structures can be seen, such as tubes and buds. Structures are indicated with white arrows. (a) Outer buffer is $45mOsm$ lower in osmolarity compared to the inner buffer. (b) Outer buffer is $7mOsm$ lower in osmolarity. (c) Outer buffer is $30mOsm$ higher in osmolarity compared the the inner buffer. (d) Population average and standard deviation of DNA intensity at the GUV membrane for samples incubated at different osmotic conditions. All populations contain between 50 and 100 GUVs, exact population sizes can be found in table 7.6.

the entire range of $0.25\mu M$ to $5\mu M$ DNA (fig. 7.6b-d). Note that at $0.25\mu M$ DNA, the LUV signal on the GUV membranes is speckled, as is the LUV signal in the outer solution. At $1\mu M$ DNA, on the other hand, a homogenous LUV signal is observed on the GUV membrane, while the background signal appears dark and homogeneous. At a higher concentration of $5\mu M$, the background again showed a speckled signal.

Vesicle population analysis shows that the level of LUV binding depends substantially on the DNA concentration, as measured by LUV fluorescence on the membrane (fig. 7.6e). Furthermore, we confirmed that binding showed no clear dependence on GUV size (fig. 7.6e), and that LUV fluorescence was not influenced by spectral crosstalk from the GUV membrane dye (fig. 7.14). Interestingly, LUV binding first increases with DNA concentration, but then decreases from DNA concentrations higher than $1\mu M$ (fig. 7.6f). The initial increase in LUV binding can be explained by a higher DNA surface coverage on the GUV membrane at higher DNA concentrations, as discussed above. However, DNA surface coverage increases over the entire range from 0.25 to $5\mu M$ DNA (fig. 7.3), in contrast to LUV binding. A possible explanation for the apparent decrease in docking is that membrane-bound chol-DNA hybridizes with free chol-DNA that is not

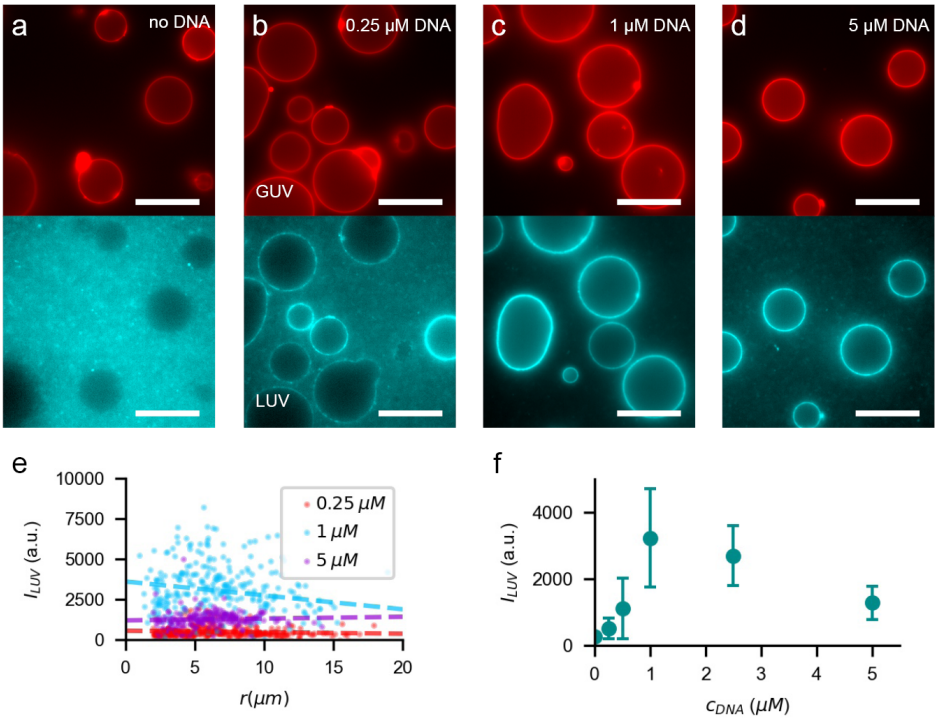

Figure 7.6: **LUV docking on GUVs is highly sensitive to chol-DNA concnetration.** (a-d) Epifluorescence images of DOPC GUVs (top) and DOPC LUVs (bottom) at varying DNA concentration. Scale bar is 20μm in all images. GUVs were labelled with 0.5% Atto 488 DOPE, LUVs were labelled with 0.05 % Atto 655 DOPE (a) No DNA. (b) 0.25μM DNA. (c) 1μM DNA. (d) 5μM DNA. (e) Distribution of LUV intensities on the GUV membranes plotted against GUV radius. Each point represents a single vesicle. Dashed lines are linear regression results with slopes (units a.u. per μm) -9 (0.25μM DNA), -86 (1μM DNA), and 11 (5μM DNA). (f) Population average and standard deviation of LUV intensity on the GUV membrane plotted against DNA concentration. All populations contained between 200 and 500 GUVs (table 7.7).

inserted in membranes. Given that we measured the equilibrium adsorption concentration to be around 1μM, this means that adsorption of chol-DNA becomes less efficient at higher concentrations. This results in more unbound chol-DNA in solution, which can hybridize with its complementary strand on either the GUV or LUV membrane. In turn, potential binding sites on GUV and LUV membranes are blocked by free chol-DNA, leading to a decreased level of LUV-GUV binding. However, others have found that a similar decrease in DNA-mediated binding can occur in a system where unbound DNA is washed out using a flow-channel (L. Laan, personal communication, December 2021). An alternative explanation is that a high DNA surface coverage induces steric hindrance between the linkers, thereby limiting binding. Such a decreased binding activity at high linker density has been reported for various systems [538, 539]. While we in principle do not expect self-dimerisation to decrease availability of linkers, because self-dimerisation interactions are weak for our linkers (see section 7.5), at high DNA surface densities even

a large number of interactions that are individually weak might have an impact on global linker availability.

Due to the reversibility of membrane adsorption of chol-DNA, mixing of GUVs and LUVs can lead to a redistribution of the DNA strands over the different vesicles. This, in turn, would cause a loss in binding specificity. Since LUV-GUV binding will fixate the strands involved in binding, it is important to consider the time-scales of LUV-GUV binding and chol-DNA adsorption. Comparing LUV-GUV binding at different times after mixing showed that docking was fast, with the LUV intensity on the GUV membrane not changing significantly between 10 minutes to 120 minutes after mixing (fig. 7.7a). In agreement with this, when LUVs were added in the direct vicinity of the GUVs by local injection with a micropipette, we saw that binding was almost instantaneous (see chapter 8). A previous QCM-D study on chol-DNA insertion in SLBs has shown that adsorption of chol-DNA is also fast, in their experiment rate-limited by transport rather than binding [529]. The precise time-scales of chol-DNA insertion and LUV-GUV binding have yet to be determined, but are in our experiment more likely dependent on mixing than binding.

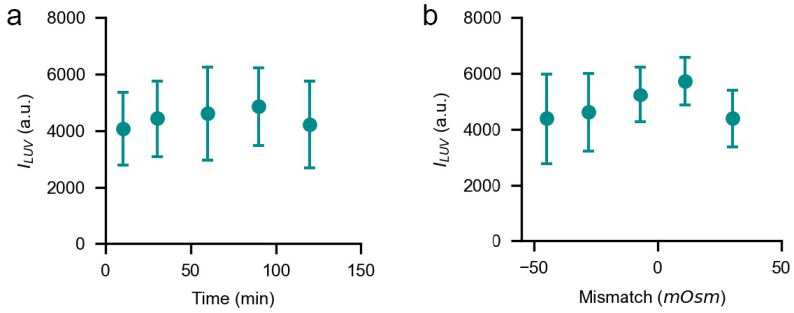

Figure 7.7: **LUV binding is fast and depends minimally on osmotic mismatch.** Data points represent population average with standard deviations. All populations constituted between 50 and 130 GUVs. The exact population sizes can be found in table 7.7. All experiments were performed by incubating LUVs and GUVs with $1\mu M$ DNA. (a) LUV intensity on the GUV membrane measured 10 to 120 minutes after mixing at an osmotic mismatch of $-30 mOsm$. (b) LUV binding to GUV membranes at different osmotic conditions after 2 hours incubation time. A negative mismatch means a hypotonic condition, a positive mismatch hypertonic.

Following up on our investigation of osmotic effects on DNA incorporation, we tested how osmolarity mismatches affected GUV-LUV binding. LUV binding efficiency was highest at -7 mOsm and 10 mOsm, and slightly decayed at higher osmotic mismatches in both directions ($p<0.05$, Tukey's test) (fig. 7.7). There is no trivial explanation for this non-monotonous effect, especially because we know that the density of binding sites does not vary with osmolarity (see fig. 7.5). Possible actors affecting LUV docking at different osmotic mismatches are spontaneous curvature effects, crowding of DNA linkers on the membrane, membrane dilation, membrane fluctuations, or a combination of those. Since differences are small, further experimentation is required to settle the extent of the osmotic effect and its possible causes. Despite the small differences across osmotic conditions, this experiment shows that there is strong LUV docking at all osmotic

mismatches, thereby opening up opportunities to use osmotic effects to tune membrane fusion.

7.2.4. FUSION

THE CONTENT MIXING ASSAY

Finally, we explored the potential of DNA-mediated binding for promoting LUV-GUV fusion. Fusion is generally thought to proceed through several stages [9, 517]. First, docking brings two membranes in close proximity. Then, merging of the membrane outer leaflets leads to a hemi-fused intermediate. Lastly, content mixing is achieved either via formation of transient pores, or complete merging of two membranes. Since we were interested in the final state of fusion, we set up a LUV-GUV content mixing assay based on the water-soluble fluorescent dye HPTS (fig. 7.8a). Comparable content mixing assays have been developed to demonstrate LUV-LUV fusion [9, 540] and to a lesser extent LUV-GUV fusion [514, 541, 542]. We encapsulated HPTS at high concentration (10 mM) in LUVs by extrusion, while GUVs were formed in absence of the dye. By itself, HPTS is not able to permeate the membrane, meaning it can not spontaneously enter the GUV. Only upon content exchange between LUVs and GUVs in the final state of membrane fusion, HPTS is transferred from the LUV to the GUV lumen. Thus, GUVs with an increased internal HPTS signal have undergone content mixing, and can be considered fused GUVs. To minimize background fluorescence coming from non-encapsulated HPTS, we introduced the quencher DPX to the aqueous solution surrounding the GUVs. In practice, LUVs with HPTS and GUVs were first incubated separately, each with one type of chol-DNA (the DNA incubation step). Then, LUVs and GUVs were mixed to allow for membrane fusion (the fusion step). Typically, the fusion step was performed at hypotonic conditions ($-25 mOsm$) since elevated membrane tension is supposed to promote membrane fusion [89]. We expect fusion to occur quickly after docking, typically within minutes [519]. After 70 minutes, the GUVs and LUVs were transferred to an observation buffer containing DPX, in which they were imaged by fluorescence microscopy (the imaging step).

To set up the content mixing assay, we first measured HTPS fluorescence as a function of concentration in a bulk assay (fig. 7.8b). HPTS signal increased up to a concentration of 1 mM, after which fluorescence levelled off and finally decreased due to self-quenching. In presence of 7.5 mM DPX, fluorescence of HPTS was greatly reduced at lower dye concentrations (fig. 7.8b). At 25 mM HPTS, fluorescence again increased substantially, indicating limited quenching efficiency. We therefore ensured that the DPX concentration was always higher than the HPTS concentration in the imaging chamber. An important consideration of this content mixing assay is that fusion is only detectable once the HPTS signal has sufficiently increased. This, in turn, may require numerous fusion events. From fig. 7.8b, we see that the HPTS signal is only higher than the quenched signal above a concentration of 0.01 mM. When an LUV of 200 nm diameter fuses with a GUV of $5 \mu m$ radius, its content is diluted 120000 times. Starting from an HPTS concentration of 10 mM, this means that over 100 fusion events are required before fusion is detectable.

In fig. 7.8c, an example content mixing experiment is illustrated. The HPTS signal is clearly enhanced in the GUV on the left, while the GUV on the right side of the image

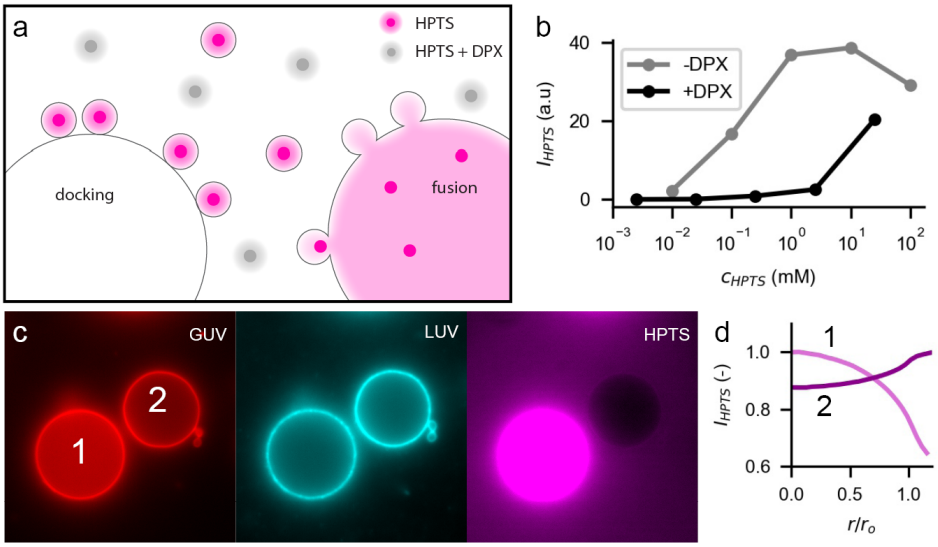

Figure 7.8: **Content mixing assay to detect membrane fusion.** Illustration of the content mixing assay to visualize GUV-LUV fusion. (a) Schematic representation of the assay. Fluorescent HPTS is encapsulated in LUVs, and only enters GUVs upon content mixing. HPTS in the outer solution is quenched by DPX. (b) Bulk fluorescence measurement of HTPS in $10mM$ HCl at pH 7.4 and $100mM$ KCl in presence (black) or absence (gray) of $7.5mM$ DPX. Curves represent averages of 6 measurements, standard deviations are smaller than the size of the data points. (c) Typical epifluorescence images used to analyse content mixing assays. Two DOPC GUVs (red) are shown with bound LUVs (cyan) using $1mM$ chol-DNA. Vesicle 1 has increased HPTS fluorescence (magenta), while vesicle 2 has a dark interior. (d) Radial HTPS intensity profiles for the vesicles shown in panel c. Intensity profiles have been normalized by their maximum intensity. The x-axis displays the radial distance from the vesicle centre r normalized by the vesicle radius r_0.

shows an interior that is darker than the background. To distinguish fused vesicles from non-fused vesicles in population analysis, we computed the radial profile of HPTS fluorescence in GUVs (fig. 7.8d). From the radial profile, we computed the ratio of HPTS signal inside the vesicle, $I_{\text{HPTS,in}}$, versus outside, $I_{\text{HPTS, out}}$, using the radial intensity average at the vesicle centre ($r/r_0 = 0$) and at the maximum radial distance ($r_{max}/r_0 > 1$). A ratio $I_{\text{HPTS, in}}/I_{\text{HPTS, out}} > 1$ thus indicated enhanced HPTS fluorescence, while a ratio smaller than 1 signified that the vesicle interior is darker than the surrounding solution. To exclude potential leaky GUVs, which would allow for spontaneous crossing of HPTS over the membrane and thus to an intensity ratio $I_{\text{HPTS, in}}/I_{\text{HPTS, out}} \simeq 1$, we only counted GUVs with a higher intensity ratio $I_{\text{HPTS, in}}/I_{\text{HPTS, out}} > 1.05$ as fused.

SUCCESSFUL LUV-GUV FUSION WITH DNA LINKERS

When GUVs and LUVs were incubated with $1\mu M$ chol-DNA, and then mixed at an osmolarity slightly less than the GUV interior ($-25mOsm$), a large fraction of GUVs showed an increased HPTS signal (fig. 7.9a). In line with our previous experiments, LUVs clearly localized on the GUV membrane. As a control, we tested to which extent spontaneous HPTS transfer over the membrane occurred in the fusion step by mixing GUVs and LUVs in absence of DNA (fig. 7.9b). As a second control, we examined if incorporation of chol-

DNA in the GUV membrane induced membrane permeability (fig. 7.9c). Both controls resulted in a substantially lower fraction of GUVs with enhanced HPTS, indicating that increased internal HPTS fluorescence is primarily a result of specific LUV-GUV binding and fusion. To quantify the fraction of fused GUVs, we analyzed a population of GUVs (DNA on both: n=250, no DNA: n=169, DNA on GUV only: n=235), extracting their size, LUV intensity at the membrane, and internal HPTS intensity. The resulting HPTS intensity ratio is plotted against LUV intensity at the membrane in fig. 7.9d. The dashed line separates GUVs we consider to be fused from non-fused GUVs. From this plot, it is immediately clear that LUV localization is stronger for the experiment where both DNA strands were used as compared to the controls. The final fraction of fused vesicles was substantially higher when both complementary DNA strands were used (30%, 76 fused GUVs) as compared to the use of no strands (3%, 5 fused GUVs) or only one strand for the GUV (6%, 13 fused GUVs). A closer inspection of the GUV population in the fusion experiments with both complementary DNA strands reveals a non-uniform distribution of HPTS ratios. Firstly, a large population of GUVs with an HPTS ratio centred around 0.9, being the non-fused population, and secondly a smaller population of fused GUVs with an increased intensity ratio. This non-uniform distribution reveals that fusion is not a simple stochastic process in which all bound LUVs have an equal fusion probability. Instead, fusion seems to be dependent on GUV properties as we further discuss in section 7.3. Interestingly, GUV fusion occurred over the entire range of LUV intensities, although at first sight the population of fused GUVs seems to be slightly shifted towards higher LUV intensities. Using a two-sided t-test to compare the LUV intensities of the fused GUVs to the entire population, however, revealed that the LUV intensities are not significantly different (p=0.1). We compared the described fusion outcomes where we applied a small osmotic shock to an experiment where GUVs and LUVs were mixed under isotonic conditions (fig. 7.9e). Including both DNA strands, the fraction of fused GUVs was lower in absence of osmotic shock (18%, 72 out of 422) as compared to the osmotic shock condition. In addition, the fraction of GUVs with increased HPTS due to non-specific processes also decreased with respect to the osmotic shock condition (1%, 3 out of 225 in absence of DNA; 1%, 4 out of 295 for only DNA strand on GUV). We conclude that the osmotic shock effectively leads to a higher fraction of fused GUVs as compared to fusion under isotonic conditions (30% vs. 18 %, respectively), but likely also somewhat increases the fraction of transiently permeabilized GUVs. In line with the results of Deshpande et al. [89], we thus found increased membrane tension to promote fusion.

In these experiments, controls using only one complementary strand showed that a maximum of 6% of the total GUV population had an increased internal HPTS signal as a result of non-specific transfer. This fraction is somewhat lower than what we saw for the DNA-dependent permeabilization, which for $1\mu M$ chol-DNA accounted for 10% of the GUVs fig. 7.4c). Interestingly, in the content mixing assay, non-specific transfer was dependent on the DNA concentration but also on the osmotic shock. Possibly, osmotic stresses give rise to the formation of temporary membrane pores, allowing non-specific transfer of the HPTS dye into GUVs in the fusion step when an osmotic shock is applied. Further studies will need to delineate these effects.

An interesting observation from the population analysis of the content mixing assay

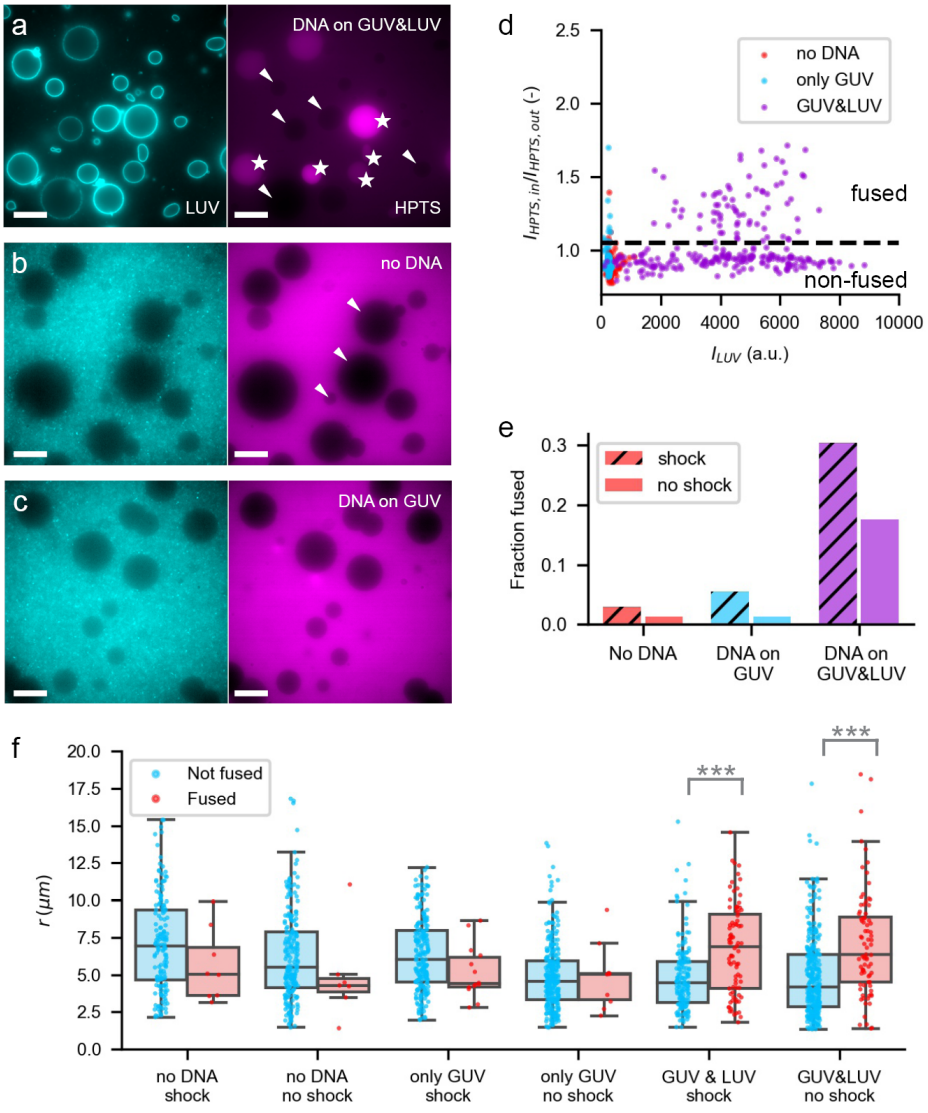
a
DNA on GUV&LUV
LUV
HPTS
b
no DNA
c
DNA on GUV
d
no DNA
only GUV
GUV&LUV
fused
non-fused
$I_{HPTS,in}/I_{HPTS,out}$ (-)
I_{LUV} (a.u.)
e
shock
no shock
Fraction fused
No DNA
DNA on GUV
DNA on GUV&LUV
f
Not fused
Fused
r (μm)
***
***
no DNA shock
no DNA no shock
only GUV shock
only GUV no shock
GUV & LUV shock
GUV&LUV no shock

is that for both experiments with and without osmotic shock, in case of using both DNA strands, fused GUVs were significantly larger than the population average (p<0.001, see fig. 7.9f). While the average GUV radius of the entire population was 5.5μm for both experiments with and without osmotic shock, fused vesicles had an average radius of 6.9μm (shock) and 7.5μm (no shock). This indicates that either GUV-LUV fusion is promoted for larger GUVs, or that GUV-LUV fusion has resulted in measurable GUV growth. Assuming an LUV diameter of 200nm and spherical geometry for both GUV and LUV, for a GUV to grow in surface area from a radius of 5.5μm to 7.5μm corresponds to 2600 fusion events. To calculate the total number of LUVs that can bind to a GUV membrane, we assume the GUV surface to be flat and a maximum surface packing density ρ of spherical LUVs (ρ= 0.9 for 2D packing of circles). For a GUV of 5.5μm radius, this amounts to ~ 10000 LUVs, which makes 2600 fusion events only one quarter of the maximal number of bound LUVs. This means that GUVs could have grown due to fusion events. For the controls, the population of GUVs with increased HPTS was too small to perform statistical analysis (less than 20 GUVs). All population sizes and statistical tests can be found in table 7.8.

FUSION DEPENDS ON DNA LINKER DENSITY

Given that membrane fusion has been reported to depend on linker density in LUV-LUV studies [9], we explored how fusion efficiency depended on DNA concentration. We therefore incubated GUVs and LUVs with chol-DNA at varying concentration, from 0 to 5μM DNA. Upon mixing GUVs and LUVs, we observed fusion at all concentrations (fig. 7.10a-c), but to varying extent. As with the experiment described in fig. 7.9, fusion was not clearly correlated to LUV intensity at the GUV membrane at a certain DNA concentration (fig. 7.10d). Comparing DNA concentrations, we see that the fraction of fused GUVs clearly depended on DNA concentration in a non-linear fashion (fig. 7.10e). In fact, the dependence is reminiscent of the LUV binding behaviour (fig. 7.6f): fusion first showed an increase up to a concentration of 1μM DNA, but then decreased for higher DNA concentrations. In this way, fusion appears to be tightly linked to LUV density. However, other effects could play a role as well. For example, an upper limit for linker density has been reported before [539]. As discussed for docking results (fig. 7.6), a high

Figure 7.9 *(preceding page)*: **Successful DNA-mediated LUV-GUV fusion.** Content mixing experiment with DOPC GUVs labelled with 0.5% Atto 488 DOPE and 200 nm DOPC LUVs labelled with 0.05% Atto 655 DOPE. (a-c) Epifluorescence images of LUVs (cyan) and HPTS (magenta) in content mixing experiments. Fused GUVs show an increased internal HPTS signal (indicated with stars), while non-fused GUVs have a lumen darker than the surrounding solution (indicated with triangles). GUVs were subjected to -25 mOsm osmotic shock during the fusion step. Scale bar is 20μm in all images. (a) Both LUVs and GUVs were incubated with 1μM of chol-DNA1′ and chol-DNA1, respectively. (b) Neither LUVs nor GUVs were incubated with DNA prior to the fusion step. (c) Only GUVs were incubated with 1μM of chol-DNA1 prior to fusion. (d) Population analysis of GUVs subjected to osmotic shock of -25 mOsm during fusion. Displayed is the HPTS intensity ratio (inside/outside) as a function of LUV intensity at the membrane for the experiment and both controls. Each point represents an individual GUV. The dashed line indicates threshold intensity ratio above which GUVs are annotated as fused. (e) Fraction of fused GUVs for the experiment and both controls when GUVs were subjected to a -25 mOsm osmotic shock during fusion (dashed bars) or when fusion was performed under isotonic conditions (solid bars). (f) GUV radii of fused (red) and non-fused (blue) populations, in absence and presence of DNA, and absence and presence of an osmotic shock. Each data point represents a single GUV. ***p<0.001

surface density of DNA oligos may cause steric repulsion between the two membranes. Compared to the steric hindrance effect on docking, the effect on fusion will be stronger. While docking can already occur with partial hybridization of the DNA strands, we expect fusion to require hybridization over a longer sequence, and in addition the attached LUV has to be pushed through the steric boundary. Similar to the experiment described under fig. 7.9, we observed a correlation between GUV size and vesicle fusion. In the experiments conducted with $0.5\mu M$ and $1\mu M$ DNA, fused vesicles were larger than the population average ($5.6\mu m$ to $6.9\mu m$ with p<0.001, and $6.7\mu m$ to $7.9\mu m$ with p<0.05, respectively, see fig. 7.16). We excluded GUV populations from other DNA concentrations from statistical analysis, since the population of fused GUVs was too small (less than 20). Note that the fused fraction at $1\mu M$ DNA is 18% in this experiment, while we measured a fraction of 30% under similar experimental conditions in fig. 7.9. This difference most likely resulted from a combination of day-to-day and batch-to-batch variability. To minimize the effects of experimental variability, we only compared results between experiments performed on the same day with the same batch of GUVs and LUVs.

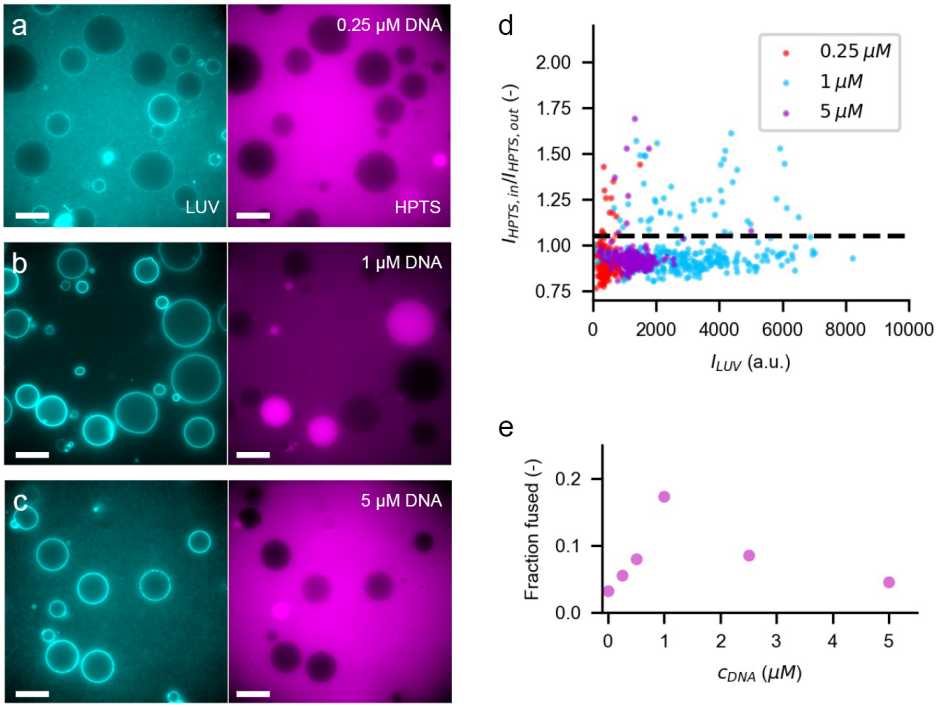

Figure 7.10: **DNA concentration strongly determines fusion efficiency.** Content mixing experiment with DOPC GUVs labelled with 0.5% Atto 488 DOPE and $200nm$ DOPC LUVs labelled with 0.05% Atto 655 DOPE. (a-c) Epifluorescence images of LUVs (cyan) and HPTS (magenta) in content mixing experiments. GUVs were subjected to $-25mOsm$ osmotic shock during the fusion step. Scale bar is $20\mu m$ in all images. (a) $0.25\mu M$ DNA. (b) $1\mu M$ DNA. (c) $5\mu M$ DNA. (d) HPTS intensity ratio of GUV populations plotted against the LUV intensity at the GUV membrane. Each point represents a single vesicle. Points above the dashed line are considered to be fused GUVs. (e) Fraction of fused GUVs calculated for each DNA concentration.

Our observation that fusion strongly depended on the DNA linker density is in line with the results presented by Chan et al. [9]. However, Chan et al. reported a monotonous increase of fusion with linker density, while our study shows a drop in fusion efficiency at higher DNA concentrations. It is important to take a note of the differences between the studies, all of which can affect the apparent qualitative dependence of fusion on linker density. The work done by Chan et al. [9] concerned LUV-LUV fusion, while we examined GUV-LUV fusion. Furthermore, their work was performed for DNA densities varying between 10 and 100 DNA molecules per LUV, where fusion appeared to reach saturation at around 100 DNA molecules per LUV. In our case, we do not exactly know the DNAs per LUV. For $200nm$ DOPC produced at $0.5mg/mL$, assuming an area per lipid of $0.6nm^2$ [543], we form $1.6pmol/L$ LUVs. These were incubated with $1\mu M$ DNA, meaning that we added ~ 600 DNA molecules per LUV. However, in our case, linkers are added in solution and incorporate in the membrane by equilibrium partitioning. In ref. [9] linkers are conjugated to a lipid molecule, which allows more precise control over the incorporated fraction. Additionally, the membrane anchor itself can affect fusion efficiency [525, 526].

As discussed above, we found DNA concentration to be determinant for DNA incorporation (fig. 7.3), for LUV docking (fig. 7.6), and for LUV-GUV fusion (fig. 7.10). There are several ways in which a higher DNA density (up to $1\mu M$) can promote membrane fusion. First, fusion could be enhanced by an increased number of LUVs bound to a GUV. If each LUV has a given probability to fuse with the GUV membrane, then a larger number of docked LUVs will naturally give rise to more fusion. However, our data suggests that the explanation might not be as trivial as this. While we do observe more fusion for samples with a higher LUV intensity (fig. 7.6, fig. 7.10), our data shows no correlation between fusion and LUV intensity within each sample. Fusion can occur for GUVs with any non-zero LUV intensity (fig. 7.10d), and statistical tests show no increased LUV intensity in the population of fused GUVs (see table 7.8). A second mechanism promoting membrane fusion at higher DNA concentrations could be found in an increased number of linkers involved per LUV-GUV interaction. It has been speculated that linkers do not only bring membranes in close proximity, but that hybridization also causes local disruption of the membrane [535]. Alternatively, docking between the two surfaces could lead to a local increase in membrane tension, which could in turn promote fusion [527]. In either case, a larger number of linkers involved in binding leads to increased destabilisation of the membrane, thereby promoting fusion. However, such an influence of DNA hybridization energy on fusion is contradicted by Van Lengerich et al., [519], who found the number of DNA linkers on an SUV not to impact the rate of the transition from hemifusion to fusion with an SLB. The authors explain the difference between their work and the LUV-LUV fusoin study of Chan et al. [9] by distinguishing docking from fusion. In the bulk experiment of Chan et al., docking and fusion could not be distinguished, and Van Lengerich et al. argue that Chan et al. actually observed a higher rate of docking, leading to a higher apparent fusion rate. A similar explanation does not hold for our experiments, as LUV intensity was in our study not correlated with fusion probability. These results have yet to be reconciled, and will require further investigation of the influence of at least system geometry and type of membrane anchor.

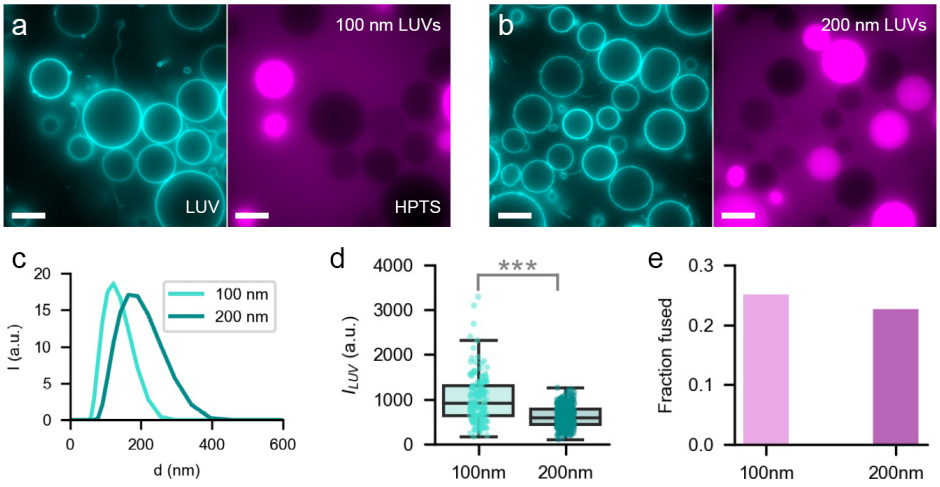

Figure 7.11: **Fusion assays using LUVs of different sizes.** Fusion was performed by pre-incubation with $1\mu M$ chol-DNA and at hypotonic conditions of $-25mOsm$. (a-b) Epifluorescence images of unlabelled DOPC GUVs incubated with LUVs labelled with 0.05 % Rhomadine DOPE (mol/mol). LUVs contained $10mM$ HPTS to visualize content mixing. Scale bar is $20\mu m$ in all images. (a) $100nm$ LUVs. (b) $200nm$ LUVs. (c) DLS results for DOPC LUVs produced by extrusion with a membrane pore size of either $100nm$ (cyan) or $200nm$ (dark cyan). Data presented is the intensity distribution of particle sizes. (d) Population analysis of LUV intensity on the GUV membrane (***p<0.001). Each point represents an individual GUV. (e) Fraction of fused GUVs calculated from the HPTS ratio inside versus outside GUVs.

7

SMALLER LUVS BOOST FUSION?

Previous studies have found that the fusogenicity of LUVs is dependent on their size [544–546] (although this vies is challenged in ref. [519]). We therefore investigated if we could boost vesicle fusion by using smaller LUVs produced by extrusion through a membrane of a pore size of 100 nm instead of 200 nm. We confirmed the smaller size of 100 nm LUVs by DLS measurements (fig. 7.11c). Indeed, the peak in the size histogram shifted towards 110 nm when using a 100 nm pore size membrane, versus 180 nm for LUVs extruded with a 200 nm membrane. These LUVs will be called 100 nm and 200 nm LUVs henceforth. Fluorescence images of fusion experiments showed no visible differences between using 100 nm and 200 nm LUVs (fig. 7.11a-b). Analysis of the intensity of bound LUVs showed increased brightness for 100 nm LUVs as compared to 200 nm LUVs (two-sided students t-test, p<0.001). Based on geometrical arguments, an intensity difference is not expected for different LUV sizes. The length of the DNA spacer is around 8 nm for a 24 base pair strand, thus being much smaller than the LUV size. As a result, LUV-GUV binding will occur in a monolayer-like manner. Again, approximating the GUV surface to be flat, and assuming a maximum surface packing density ρ of LUVs (ρ= 0.9 for two-dimensional packing of circles), the number of bound LUVs n per unit GUV membrane area depends on the LUV radius as $n \propto \frac{1}{r^2}$. The total membrane area of bound LUVs, A, is linearly correlated to the fluorescence intensity, since the LUVs are smaller than the diffraction limit. As $A \propto nr^2$, the size dependence is cancelled out. In

effect, an explanation for the intensity difference might be less trivial. Binding affinity could for example be dependent on LUV size, either via size-dependent incorporation of chol-DNA, or by a size-dependent number of linkers involved in binding. The observed fraction of fused GUVs is slightly higher with 100 nm LUVs than with 200 nm LUVs (0.25 versus 0.23, see fig. 7.11e). However, it is not trivial to make a direct comparison between fusion experiments conducted with different LUV sizes. Apart from a difference in fusogenicity, also the contact area between LUV and GUV will depend on LUV size, as well as the number of linkers involved in binding. Furthermore, our content mixing assay is based on dye transfer from LUVs to GUVs, which depends on LUV volume. Fusion of a 200 nm LUV leads to 8 times as much dye influx as compared to a 100 nm LUV. Since we apply the same threshold for labelling GUVs as fused in both experiments, and we know that dye signal increases roughly linearly in the concentration range we are working in, we need a substantial larger number (8-fold) of fusion events before we can detect fusion of 100 nm LUVs as compared to 200 nm LUVs. We can therefore conclude that the smaller LUVs are more fusogenic, although the exact origin of this difference remains unclear. Interestingly, while GUVs fused with 200 nm LUVs were larger than the population average, GUVs fused with 100 nm LUVs did not show a similar size increase. (see table 7.8).

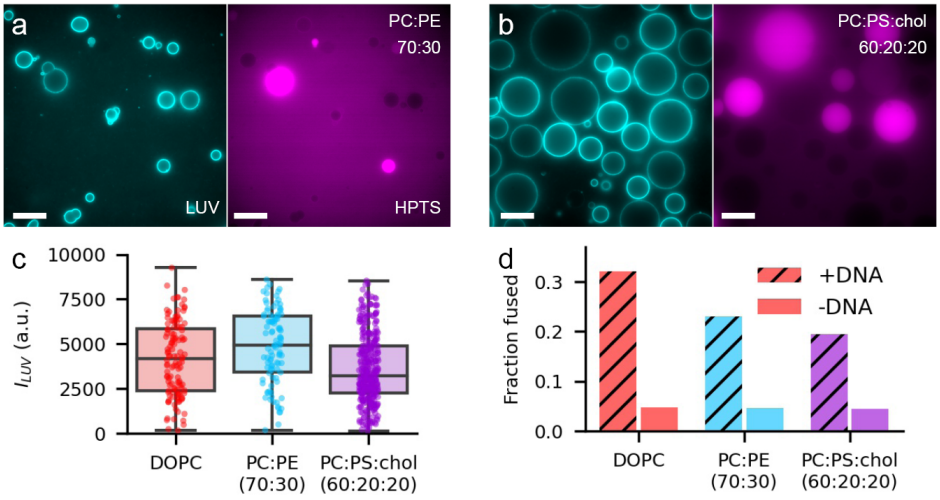

Figure 7.12: **Fusion using GUVs with different membrane compositions.** (a-b) Epifluorescence images of GUVs in content mixing assays. Both GUVs and 200 nm DOPC LUVs (cyan) were incubated with $1\mu m$ chol-DNA prior to the fusion step. LUVs encapsulated 10 mM HPTS (magenta) as an indicator for membrane fusion. Scale bar is $20\mu m$ in all images. (a) GUVs were produced from a lipid composition consisting of 69.5% DOPC, 30 % POPE and 0.5 % Atto 488 DOPE. (b) GUVs were formed from a lipid composition of 59.5 % DOPC, 20 % DOPS, 20% cholesterol and 0.5% Atto 488 DOPE. (c) LUV intensity measured on the GUV membrane. Each point represents an individual GUV. (d) Fraction of fused vesicles for different GUV membrane compositions tested. Dashed bars indicate experiments including an incubation step of $1\mu M$ chol-DNA for both GUVs and LUVs, plain bars represent a control experiment where no chol-DNA was added in the incubation step.

FUSION IS COMPATIBLE WITH MULTIPLE MEMBRANE COMPOSITIONS

So far, our fusion assays have been performed with DOPC membranes only. We extended our experiments to different membrane compositions for two reasons. First, vesicle fusogenicity is dependent on the type of lipids constituting the membrane [8], thereby providing a way to optimize fusion via membrane design. Second, for this fusion method to be applicable for more complex reconstitution assays, it is essential that the fusion method is robust towards varying membrane composition. To test if membrane fusion could be enhanced by changing GUV lipid composition, we doped the DOPC GUVs with 30% (mol/mol) of POPE lipids. POPE lipids have a small headgroup, and therefore a negative intrinsic curvature, which is known to boost membrane fusion [8, 547]. GUV formation with a lipid composition of PC:PE (70:30) yielded GUVs that were smaller than DOPC GUVs (average radius of 4.5μm vs 7.2μm, respectively) (fig. 7.12a). LUVs successfully bound to the DOPC:POPE membrane, with a higher intensity as compared to DOPC GUVs (p=0.02) as shown in fig. 7.12c. This possibly indicates that chol-DNA insertion depends on GUV membrane composition, where the presence of DOPE promotes adsorption of chol-DNA to the membrane. The fraction of fused GUVs, however, was smaller, being 23% for DOPC:POPE membranes (23 of 100 GUVs) versus 32% for GUVs containing only DOPC lipids (41 out of 128) (fig. 7.12d). This difference is unlikely to result from different membrane permeabilities, as control experiments without DNA yielded similar fractions of GUVs with increased HPTS (5% for both compositions). Another explanation could be that the affinity for the incorporation of chol-DNA depends on GUV membrane composition, as reported in [8], but this is in contrast with the higher binding affinity we see for membranes containing DOPE. It is important to note that most studies on the effect of DOPE on membrane fusion have been conducted with SUVs or LUVs rather than GUVs [547], raising the question how the interplay between membrane curvature and lipid intrinsic curvature modulates fusogenic properties.

To explore the potential of the DNA-mediated fusion assay for other membrane compositions, we produced GUVs from a lipid mix consisting of DOPC:DOPS:cholesterol (60:20:20). A fraction of 20% negatively charged DOPS lipids is typical for eukaryotic membranes, as are molar fractions up to 30% cholesterol [548, 549] (fig. 7.12). LUVs bound successfully but with lower intensity than to DOPC membranes (p<0.005) (fig. 7.12c). Since DNA is negatively charged, electrostatic repulsion by the presence of like-charged DOPS lipids likely decreases chol-DNA incorporation. Out of the 369 GUVs analysed in this experiment, 20% had fused with LUVs (72 GUVs), as compared to 4% in a control experiment without chol-DNA (fig. 7.12d). A lower fusion rate upon inclusion of negatively charged lipids compared to the fused fraction measured with DOPC membranes is in line with results from a peptide-mediated fusion study [535], but the exact effects may well depend on the interaction mechanism. Interestingly, non-specific content transfer was similar across all three membrane compositions tested, even though membrane permeability is known to depend on membrane composition [535]. Altogether, tuning membrane composition provides a wide parameter space that can be explored for a sweet spot combining minimal membrane leakiness with a maximized fusion rate.

Further inspection of the fused population shows that for none of the membrane compositions tested, there was a difference between the LUV intensity of fused vesicles

with respect to the entire population (p>0.05). However, in all samples including DNA, independent of membrane composition, the GUV radius of the fused fraction was significantly larger than the population average (p<0.01), again suggesting that either fusion is promoted for larger vesicles or sufficient LUVs fuse with the GUVs to result in membrane growth. All population statistics can be found in table 7.8. Statistical tests were not performed for the control experiments, as the number of GUVs with high HPTS in these experiments were too small (fewer than 10 in most cases).

SUCCESSFUL FUSION WITH EMULSION-FORMED GUVS

Finally, for compatibility of the fusion assay with complex reconstitution assays and synthetic cell engineering, fusion should not only be robust towards different membrane compositions but also towards GUV formation methods. All experiments discussed in this chapter thus far have been performed with GUVs that were produced by gel-assisted swelling. While gel swelling is a quick, easy and robust technique to produce lipid bilayer membranes, it offers limited control over encapsulation of proteins and other molecules which is essential for building synthetic cells of increasing complexity. Emulsion-based GUV formation methods, either being microfluidics, bulk assays or a hybrid between these two, provide much more control over the encapsulated content (see also chapter 4). One promising technique that combines experimental ease with robustness and control over encapsulation is eDICE, as discussed in chapter 4. We therefore investigated if our fusion assay is compatible with GUVs produced by eDICE, the preliminary data of which is shown below.

GUVs produced with eDICE were in this particular smaller than vesicles produced by gel swelling (radius of $3\mu m$ versus $7\mu m$, respectively). We observed a higher signal of bound LUVs for eDICE GUVs (two-sided t-test, $p < 0.001$), possibly signifying enhanced DNA incorporation in membranes produced with eDICE. Due to a poor Atto 488 DOPE signal of GUVs produced with eDICE in this sample (preliminary data), GUVs were detected in the LUV fluorescence channel. To prevent detection bias caused by LUV binding, we verified by eye that all GUVs were properly detected. Since LUVs did not localize on GUV membranes in the control sample, vesicle detection could not be run on the control, and these results were not included in the analysis. Of the 118 GUVs that were analysed, 11% (15 vesicles) were fused (fig. 7.13c). Although this is a smaller fraction than for DOPC GUVs produced by gel swelling (31%), our results demonstrate that the DNA-mediated fusion assay can be successfully employed for GUVs produced by emulsion-based methods. If higher fused fractions are required, there are still various ways to boost membrane fusion that are not yet explored in this study (see in section 7.3).

7.3. DISCUSSION

We established a robust protocol to fuse LUVs with GUVs based on specific interactions between membrane-anchored oligonucleotides. Based on a content mixing assay, we showed that fusion was detectable in up to 30 % of the GUVs, dependent on the experiment.

For a typical GUV with a radius of $5\mu m$, we estimate that fusion of 200 nm LUVs is detectable from a minimum of 100 fusion events (see text of fig. 7.8). At complete coverage of the GUV surface by LUVs, 10000 LUVs can be bound (see text accompanying fig. 7.11).

In this case, for fusion to be detectable, this means that only 1% of the bound LUVs need to be fused. Given that we see a large population of GUVs without increased HTPS, this means that for many GUVs, even fewer than 1% of the LUVs have fused. Please take note of two assumptions here, namely that (i) measurements of HPTS bulk fluorescence can be translated to semiquantitative fluorescence imaging of HPTS confined in GUVs, and (ii) the GUV surface is completely covered with LUVs at maximum 2D packing density.

Earlier studies have monitored individual LUV fusion events of DNA-mediated LUV-SLB fusion. They reported that fusion is a stochastic process: of all the docking events observed, only a small percentage (5% to 10%) resulted in fusion, from which a fusion probability was derived [519, 526, 550]. Of all the other docking events, most were arrested in a hemifused state, and a small fraction in the docked state. Direct comparison of the fused percentages is difficult, because SLBs properties are strongly influenced by their support (reviewed in [531]). Furthermore, different membrane anchors (lipid-anchored versus cholesterol-anchored) and LUV sizes (50nm versus 200nm in this study) were used. Despite these differences, the notion of fusion as a stochastic process with a single fusion probability for LUVs is interesting. Can the LUV-GUV fusion behaviour observed in our study be explained based on a similar fusion stochasticity?

To answer this question, we look into the distribution of the HPTS signal across GUVs.

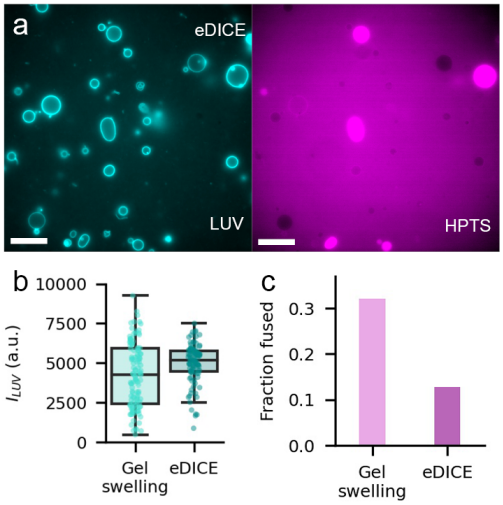

Figure 7.13: **Successful fusion with eDICE vesicles.** Membrane fusion of DOPC GUVs produced with different formation methods: gel-assisted swelling and eDICE. For both methods, GUVs were produced with a lipid composition of 99.5% DOPC and 0.5% Atto 488 DOPE, and with the same buffers except for the addition of 6.5% (v/v) optiprep for eDICE GUVs. (a) Epifluorescence images of GUVs produced with the eDICE technique in content mixing assays. Both GUVs and 200nm DOPC LUVs (cyan) were incubated with 1μM chol-DNA prior to the fusion step. LUVs encapsulated 10mM HPTS (magenta) as an indicator for membrane fusion. Scale bar is 20μm in both images. (b) LUV intensity measured on the GUV membrane for vesicles produced with gel swelling (n=128) and eDICE (n=118). Each data point represents an individual GUV. Data for DOPC membranes is the same as in fig. 7.12. (c) Fraction of fused vesicles for GUVs produced with different formation methods.

In a typical content mixing assay, we see a large population of GUVs with a dark HPTS interior, and a fraction of GUVs with a clearly increased HPTS signal (fig. 7.9d). If all LUV-GUV docking events result in fusion with the same fusion probability, then we would not expect a bimodal distribution. Instead, since the number of fusion events is large (of order 100), we would expect a unimodal distribution, where all GUVs have undergone fusion to some degree. The bimodal distribution thus suggests that the fusion probability is not uniform for all LUV-GUV docking events. Instead, the fusion probability depends on the GUV: in some GUVs, we see a large number of fusion events, while in other GUVs, there is minimal fusion.

A GUV-dependent fusion is in line with results of the SUV-GUV fusion study executed by Deshpande et al. [89]. In their study, SUVs were continuously supplied to GUVs in a microfluidic channel, while GUV size was recorded over time and used as a measure of fusion. Under increased GUV membrane tension, SUVs fused spontaneously through non-specific interactions with only a fraction of the GUVs, while the majority of the GUV population remained unchanged.

What causes the variability in fusogenicity between GUVs? We have shown that LUV intensity on the GUV membrane shows no correlation with fusion, thus excluding the LUV density on the membrane as a possible cause. While we did not see a correlation, we note that all our images were taken by epifluorescence microscopy. In epifluorescence imaging, all measured fluorescence intensities are affected by out-of-plane fluorescence. Imaging in confocal microscopy helps drastically to reduce this imaging artefact, and should be a next step towards more accurate quantitative image analysis. Another source of variation might be the DNA grafting density across GUVs in a population, which we cannot visualize in our fusion assays. However, indirect readouts from the complementary fluorescent strand and the signal of bound LUVs do not show a striking heterogeneity. Note that the exact effect of DNA linker density on fusion is still unclear (see fig. 7.10): a higher linker density might either promote fusion [9], have no effect [519], or even impede fusion [539], depending on the exact surface density and the geometry of the system involved.

Given the similarity of our results with the result of Deshpande et al. [89], which involved only non-specific interactions, other factors might be playing a role as well. Importantly, both our study and ref. [89] confirm the positive effect of GUV membrane tension on fusion. In both studies, membrane tension is controlled by supplying a solution of lower osmolarity to the GUVs. Consequently, tension will vary substantially between GUVs as it depends on excess area, which in turn depends on GUV formation history, temporary pore formation, and the presence of membrane reservoirs. Different fusion behaviours between GUVs might thus be explained by variation in membrane tension. Alternatively, fusion might be affected by contamination of the GUV membrane either by gel polymers originating from the PVA gel for gel-swollen vesicles [350, 365], or by residual oil for eDICE GUVs (or octanol in GUVs produced with microfluidics in ref. [89]). This explanation can be checked by performing fusion experiments with clean GUV membranes, produced for example by electroformation [74], spontaneous swelling [380], or swelling on a cross-linked hydrogel citeMora2014 (see chapter chapter 4). Furthermore, variation in fusion might be explained by naturally occurring lipid packing defects in GUV membranes [545].

Now, let us revisit the question that this chapter started with: can we employ DNA-mediated LUV-GUV fusion to grow the membrane area of synthetic cells, such that they can grow and divide? We have shown that our fusion protocol can be robustly used to generate fusion in up to 30% of the GUVs. However, for compatibility with synthetic cell membrane growth, higher fusion efficiencies might be desired. There are various routes to further boost the fusion efficiency, either via the DNA linker sequence, its membrane anchor, or by the LUV membrane composition.

First, the DNA linker sequence. In our study we erroneously used two strands taken from a previous study [91] that were not fully complementary on the membrane-proximal side (see section 7.5). As a result, the strands could not fully zip upon hybridization, effectively creating a 10 and 14 base pair spacer, corresponding to a spacer 4 to 5 nm on the LUV and GUV side, respectively (see fig. 7.15). Spacers in zipper-like DNA-mediated membrane fusion have been shown to decrease fusion [527]. Therefore, we expect that the use of two fully complementary 24 base pair strands (see table 7.5) will already substantially increase fusion. Compared to the non-repetitive sequences used in our study, repetitive poly-A/poly-T sequences have been shown to enhance fusion probabilities by releasing geometrical docking constraints [519, 527]. Whether the use of repetitive sequences will improve fusion in our system is not evident, since fusion in our assay does not appear to be docking-limited.

Second, the membrane anchor. We ensured DNA anchoring in the membrane using a single cholesterol tag, following ref. [91]. The chol-DNA was dispersed in the surrounding aqueous medium, after which it spontaneously incorporated in the membrane via hydrophobic interactions. Membrane incorporation with a single cholesterol anchor was previously shown to be reversible [529], meaning that linkers can desorb from the membrane after incorporation. This, in turn, can lead to redistribution of linkers among LUVs and GUVs, thereby impacting fusion specificity. Other anchoring methods can be considered to circumvent these problems. For example, coupling the DNA linker to a double instead of a single cholesterol anchor prevents the linker from desorbing from the membrane [529]. Additionally, a double anchor might be beneficial for fusion. It has been reported that the zipper-like binding even further promotes dissociation of single chol-DNA from the membrane, due to either drag or tilt of the cholesterol moieties imposed by stress build-up upon strand hybridization [525]. For double chol-DNA, the dissociation rate upon binding was much lower, meaning that the linker resides more stably in the membrane also after hybridization [525, 529]. Using DNA with a double anchor implies that the linker is partially double stranded on the anchor side, which effectively creates a spacer upon hybridization with the complementary strand on the opposite membrane. Nevertheless, doubly anchored DNA is more effective in fusion than singly anchored DNA [525]. Apart from cholesterol anchors, also lipids conjugated to oligonucleotides have been used extensively for anchoring DNA linkers in lipid bilayers [9, 519, 551]. The advantage of using DNA-lipid conjugates is that they will not partition into the aqueous medium, which allows for more precise control of grafting densities. However, lipid-DNA conjugates are not commercially available and thus have to be synthesized in-house, raising the threshold for their broad adoption. Furthermore, the length of the membrane anchor can affect fusion. In studies using DNA-lipid conjugates, it was shown that the majority of docking events was arrested in a hemifusion stalk

state, and thus did not result in fusion [519]. A reason for this is that the DNA-linker is only anchored in the outer leaflet. Upon mixing of the outer leaflets during hemifusion, the hybridized DNA linkers diffuse away from the contact area. By custom synthesis of a DNA linker conjugated to a longer anchor that spans both leaflets, Flavier et al. indeed managed to increase the fraction of full fusion events by two- to threefold [526]. While this is a promising strategy for increasing membrane fusion, accessibility of DNA conjugated to membrane-spanning anchors is still limited as these also require custom synthesis. It is interesting to note that the reversible nature of single chol-DNA anchors can be exploited for synthetic cell engineering. For example, after fusion and growth, anchors can be washed out, effectively 'resetting' the synthetic cell membrane after a cycle of growth and division. This allows for multiple cycles of DNA incorporation, growth and division, thereby enabling continued proliferation.

Third, fusion might be improved via changing the LUV membrane composition (reviewed in ref. [520, 552]). Fusogenicity may be boosted by established methods such as inclusion of cone-shaped lipids [8, 553] or by phase-separated lipid domain formation [91, 535]. Note that various lipids with negative intrinsic curvature, including PE, can also promote stalk formation, stalling the fusion process in the hemifused state [552]. Fusogenic mixtures are DOPC:DOPE:cholesterol (molar ratio 50:25:25) [8], DOPC:DOPE:sphingomyelin:cholesterol (molar ratio 35:30:15:20) [8, 554] and DOPC:DOPE:LPC (molar ratio 70:15:15) [89]. While we found the GUV membrane composition to minimally affect fusion, the larger curvature of LUVs will amplify packing defects generated by cone-shaped lipids. Therefore, fusion might better be tuned via the LUV membrane composition. Note that tuning membrane composition can affect membrane permeability, which also makes tuning the LUV composition more favourable.

A crucial question is still whether our assay successfully resulted in GUV membrane growth. By measuring vesicle sizes post-fusion, we indeed found that fused GUVs were significantly larger than the population average in all fusion experiments (table 7.8). It should be noted that size measurements were taken from single-plane epifluorescence images, and should therefore be considered rather an approximation than absolute sizes. Our results can indicate one of two things: either larger GUVs are more prone to fusion, or fusion has resulted in substantial GUV growth. The first seems rather unlikely. For a GUV increasing in radius from $5\mu m$ to $6\mu m$, membrane curvature changes minimally, as do curvature-dependent effects such as lipid packing. If the radius increase from $5\mu m$ to $6\mu m$ is indeed caused by fusion, this would signify a membrane area increase of 45%. To test if fusion results in membrane growth, there are various options. Here, we want to stress that typical quantitative membrane growth reporters from bulk SUV-SUV fusion studies cannot be directly translated to GUV-LUV membrane fusion. For example, the use of a self-quenching membrane dye which increases in fluorescence upon dilution, such as octadecyl rhodamine B, is very effective for SUV-SUV fusion studies[87]. Dye dilution upon fusion then leads to a moderate decrease (2-fold) in dye concentration, but a more substantial increase in light emission per dye molecule, and in turn to a net increase in fluorescence. On the contrary, for an LUV of $200nm$ diameter fusing with a GUV of radius $5\mu m$, the dye is either diluted 3000-fold (incorporated in the LUV) or 0.0003-fold (dye incorporated in GUV). In both cases, the effective change in quenching efficiency is not visible. As a better alternative, Förster

Resonance Energy Transmission (FRET) sensors can be used as a semi-quantitative fluorescence measurement[90, 514]. Otherwise, single-cell micromanipulation techniques can be used to measure area increase, such as electrodeformation [90] or micropipette aspiration [488].

7.4. CONCLUSION

To accommodate the needs for synthetic cell growth, we have established a facile membrane fusion assay that can be used to deliver LUV membrane area to GUVs. By using membrane-anchored DNA linkers, we showed that LUVs selectively bound to and fused with GUVs. By applying a quantitative imaging approach on large GUV population, we identified the crucial experimental input parameters in all three steps of the fusion process, being DNA incorporation, LUV-GUV docking, and fusion. Such a comprehensive overview of critical design parameters will aid in making membrane fusion an accessible tool in the field of synthetic cell engineering. We found the most important design parameter to be the DNA concentration, influencing all three steps of the process. In addition, osmotic pressure can be used to promote fusion. We demonstrated that this protocol is able to generate fusion in up to 30% of the GUVs. If required, further optimization can be performed with regards to the DNA linker sequence, its membrane anchor, or the LUV membrane composition. Importantly, we confirmed compatibility of this fusion protocol with the synthetic cell engineering field. First, this fusion protocol worked robustly with different GUV lipid compositions, allowing independent design of the GUV membrane. Second, we showed that fusion is compatible with emulsion-based GUV formation methods. While classical GUV swelling techniques are used ubiquitously in combination with the development of fusion assays, our study is to our knowledge the second study proving fusion of GUVs formed by emulsion-based techniques (next to ref. [89] which involved non-specific fusion). Finally, we want to stress that DNA-based fusion has a much wider potential than membrane growth alone. For example, fusogenic LUVs can be employed to deliver cargo to GUVs. In this way, temporal control can be obtained over GUVs even after their formation, an important challenge in synthetic cell design. As such, fusion can be used to trigger internal metabolic activity or to remodel cytoskeletal networks. Other than water-soluble cargo, also membrane-bound components can be delivered to GUVs, such as membrane proteins which are notoriously difficult to incorporate during GUV formation [419, 555, 556]. Next to synthetic cell engineering applications, programmability and biocompatibility make DNA-based fusion a versatile tool for development of targeted drug delivery systems, to study biological fusion mechanisms, or to guide protein delivery into live cells [557].

7.5. MATERIALS AND METHODS

7.5.1. CHEMICALS

The chemicals KCl, D-(+)-glucose, sucrose, Tris-HCl, 8-hydroxypyrene-1,3,6-trisulfonic acid trisodium salt (HPTS), p-xylene-bis-pyridinium bromide (DPX), and also cholesterol and β-casein were obtained from Sigma Aldrich. All non-fluorescent lipids 1,2-dioleoyl-sn-glycero-3-phosphocholine (DOPC), 1-palmitoyl-2-oleoyl-sn-glycero-3-phosphoethanolamine (POPE) and 1,2-dioleoyl-sn-glycero-3-phospho-L-serine (DOPS) were obtained from Avanti Polar Lipids. The fluorescent

lipids Atto 488 DOPE and Atto 655 DOPE were obtained from Atto-TEC, Germany.

7.5.2. GUV PREPARATION

GUVs were prepared by gel-assisted swelling [76], a facile and quick formation technique which successfully yields vesicles for a range of membrane lipid compositions and swelling solutions (see also chapter 4). In short, cover glasses (22 x 22 mm, No. 1.5H, Paul Marienfield GmbH & Co. KG) were first rinsed with ethanol and MilliQ water and dried under a stream of nitrogen. They were then plasma cleaned for 30 seconds (Plasma Prep III, SPI supplies), after which 100μL of a 5% (w/v) polyvinyl alcohol (PVA, 145 kDA, 98% hydrolysed, VWR, Amsterdam the Netherlands) solution in 200 mM sucrose at room temperature was spread over each coverslip. The gel was solidified by baking it in an oven for 30 minutes at 50 °C.

Then, 10μL of a lipid solution at a total lipid concentration of 1mg/mL in chloroform, typically consisting of DOPC:Atto 488 DOPE in a molar ratio of 99.5:0.5, was spread over the gel. The gel was placed in a vacuum desiccator for 30 minutes to ensure total evaporation of the organic solvent. The cover glasses were then placed in a compartmentalized petri dish (4 compartments, VWR), and to each gel we gently added 300μL of GUV swelling buffer containing 100 mOsm sucrose, 100 mM KCl and 10 mM Tris-HCl at pH 7.4. After swelling for one hour, GUVs were collected by taking the swelling solution with a pipette (1mL tip), flushing the solution again over the cover slip once to dislodge the GUVs, and pipetting it up again.

To compare the effect of GUV formation technique on fusion, we also produced GUVs with eDICE (see also chapter 4). eDICE vesicles were prepared with a membrane composition of DOPC:Atto 488 DOPE in a molar ratio of 99.5:0.5, and contained 100 mM KCl, 10 mM Tris pH 7.4, 6.5% (v/v) optiprep, and 52 mM sucrose in the IAS. They were spun into an outer aqueous solution of 310 mM MilliQ, and were diluted into a buffered solution immediately after formation. After this dilution step, the outer buffer components matched those of the gel swollen GUVs. All GUVs, formed by gel-swelling or eDICE, were stored in the fridge and used within two days after formation.

7.5.3. LUV PREPARATION

LUVs were prepared by extrusion. To this end, 5 ml glass tubes (Pyrex®) were first cleaned with tap water and soap, and then rinsed with demi water. After, the tubes were cleaned with ethanol, acetone and Milli-Q water, and then dried with nitrogen air. Once cleaned, the bottom of the glass tubes was filled with 200 μL chloroform to create volume for mixing. Lipids were then added to a total weight of 0.75 mg in a typical ratio of 29 μL DOPC at 25 mg/mL and 6.5-62 μL of fluorescently labelled lipids at 0.1 mg/mL depending on the final fraction of lipid dye in the vesicles. Lipids were mixed and then dried carefully under a stream of nitrogen, after which the tubes were placed in a vacuum desiccator for two hours. Then, 1.5 mL LUV swelling buffer containing 100 mM KCl, 10 mM Tris-HCl at pH 7.4, and, dependent on the experiment, 10 mM of the water soluble dye HPTS, was added to the tubes to obtain a final lipid concentration of 0.5 mg/mL. After a two minutes incubation time, the solution was vortexed for 30 seconds and put in a bath sonicator for 30 seconds (Branson 2510 Ultrasonic Cleaner, Marshall Scientific), resulting in the formation of small liposomes. To decrease the size polydispersity and promote unilamellarity, we extruded the produced liposomes 21 times through a polycarbonate filter (Nuclepore, Whatman) of a pore size 200 nm using the Avanti Mini Extruder (Avanti Polar Lipids, Inc), unless mentioned otherwise. The resulting LUV sample was stored at 4°C used within one week after formation.

LUV size distributions were characterized by dynamic light scattering (DLS) using a Zetasizer Nano ZS (Malvern Panalytical). For each measurement, 70μL of LUV sample was placed in a disposable cuvette (ZEN0040, Malvern Panalytical). Each sample was measured twice in a backscatter measurement at 25 °C, each measurement consisting of a minimum of 12 runs. The time-dependent raw scattering intensity was converted to the intensity autocorrelation function and

finally the particle size distribution using the commercial software.

7.5.4. DNA INCORPORATION

The sequences of single-stranded DNAs for fusion assays were adopted from Dreher et al. [91] and are shown in table 7.1. In this project, three different DNA strands were used. Two were used for fusion: chol-3′-DNA1-5′ and its complementary strand chol-5′-DNA1′-3′, called chol-DNA1 and chol-DNA1′ henceforth. In our fusion experiments, chol-DNA1 was inserted in LUV membranes, while chol-DNA1′ was used to functionalise GUV membranes. The strands chol-DNA1 and chol-DNA1′ have their cholesterol membrane anchor on opposite ends to allow antiparallel hybridization. This zipper-like binding has previously been shown to promote membrane fusion [9, 525]. Note that chol-DNA1 and chol-DNA1′ have a different number of base pairs and are therefore not fully overlapping, which we discovered in retrospect. This difference results from an erroneous display of one of the ssDNAs in ref. [91], and should be corrected for future studies[1]. The third strand, 5′-DNA1-3′-Alexa488, was only used to visualize incorporation of chol-DNA1′ in GUVs. All DNA strands arrived as powder and were dissolved and diluted to 100 mM DNA in MilliQ-water containing 10 mM Tris-HCl at pH 7.4. Dissolved DNA was stored at 4°C and could be used for months.

ssDNA name	DNA sequence	Used for	Base Pairs
chol-DNA1	5'-TGG ACA TCA GAA AGG CAC GAC GA-Cholesterol-TEG-3'	LUV	23
chol-DNA1′	5'-Cholesterol-TEG-TCC GTC GTG CCT TAT TTC TGA TGT CCA-3'	GUV	27
DNA1-Atto488	5'-TGG ACA TCA GAA AGG CAC GAC GA-Atto488-3'	Visualization	23

Table 7.1: **DNA linker sequences.** DNA sequences and number of bases of the ssDNAs used in the project.

Different DNA dimerisation modes were analysed by means of an open-source online analysis program (Integrated DNA Technologies, eu.idtdna.com/calc/analyzer). We tested (1) dimerisation between complementary strands, (2) self-dimerisation of the individual strands, and (3) the formation of hairpin structures due to self-binding. Hetero-dimerisation yielded two binding modes of comparable Gibbs energy: hybridisation of the 13 membrane-distal base pairs, or hybridisation of 11 base pairs on the membrane-proximal side (starting from base pair 2 and 3 for chol-DNA1 and chol-DNA1′, respectively, see fig. 7.15). The Gibbs energy for these two modes is -22 and $-23 kcal/mol$, or 37 and $39 k_B T$, respectively. Since the binding energy is much higher than the thermal energy, unbinding is very unlikely, meaning that once a strand hybridizes in one of the two modes, it is trapped in that configuration. As the membrane-distal sides of the strands have most freedom of movement, we expect binding to mainly happen at the far end. This effectively creates a sub-optimal zippering mechanism, leaving a spacer of 10 bp between the membrane and the hybridized strand. The DNA sequence error should be corrected in future studies. Two correct complementary strands that we intend to test in future are given in table 7.5. Analysis of self-dimerisation showed a maximum hybridisation length of 2 base pairs for both chol-DNA1 and chol-DNA1′. The corresponding Gibbs energy is about 10 times lower than the hetero-dimerisation energy, meaning that unbinding easily happens by thermal fluctuations. In effect, self-dimerisation is transient. The formation of hairpin structures due to self-binding was energetically unfavourable. In summary, although transient self-dimerisation might occur in our fusion experiments, we do not expect this to be limiting for hetero-dimerisation.

For fluorescence visualization of DNA incorporation, GUVs were incubated overnight in swel-

[1] K. Jahnke, personal communication, 2021

ling buffer with chol-5′-DNA1′-3′and 5′-DNA1-3′-Alexa488, both at $1\mu M$ unless specified otherwise. To test the effect of DNA concentration on incorporation, both ssDNA strands were added to different but equi-osmolar concentrations between 0 and $5\mu M$ DNA to unlabelled GUVs. To investigate the effect of osmotic conditions on DNA incorporation, $10\mu L$ GUVs in swelling buffer were mixed with $29.2\mu L$ observation buffer of varying glucose concentration. Osmolarities were measured with an osmometer (Osmomat 3000, Gonotec GmbH, Germany). To test the effect of incubation time, GUVs were incubated with both DNA strands and transferred to the imaging chamber either directly, and imaged after 10 minutes, or after overnight incubation in the fridge. Both osmotic effects and time effects were tested with GUVs labelled with 0.01% Atto 655 DOPE.

7.5.5. LUV BINDING

Binding of LUVs to GUVs was done by first incubating LUVs and GUVs with the appropriate chol-DNA strand. Therefore, LUVs were incubated with $1\mu M$ chol-DNA1, while GUVs were incubated separately with $1\mu M$ of chol-DNA1′. For all binding experiments, we used DOPC LUVs doped with 0.05% (mol/mol) Atto 655 DOPE. To induce GUV-LUV binding, $10\mu L$ GUVs with DNA and $10\mu L$ LUVs with DNA were added to $20\mu L$ quenching observation buffer containing $100mM$ KCl, $100mM$ glucose, $10mM$ Tris-HCl at pH 7.4 and $5mM$ DPX. Note that the LUV buffer is of lower osmolarity than the GUV swelling buffer and quenching observation buffer, resulting in an osmotic shock of about $30mOsm$ for the GUVs in the binding/fusion step. The sample was finally transferred to a large imaging chamber passivated with β-casein (for details, see section 4.5.12) to allow for epifluorescence imaging.

Experiment	GUV dye	LUV dye	DNA concentration (μM)	Incubation time DNA	Incubation time vesicles
DNA concentration	0.5% Atto488	0.05% Atto655	0 - 5	Overnight	60 min
Binding time	0.5% Atto488	0.05% Atto655	1	25 min.	10 min - 2 hr
Osmotic conditions	0.1% Atto488	0.05% Atto655	1	Overnight	2 hr

Table 7.2: **GUV-LUV binding experiments.** Overview of the conditions used for the different DNA-mediated GUV-LUV binding experiments. Overnight experiments were done in the fridge, binding time experiments at room temperature.

7.5.6. CONTENT MIXING

To visualize which GUVs had fused with LUVs, we performed content mixing experiments. To this end, we encapsulated the fluorescent dye HPTS at high concentration (10 mM) in LUVs by adding it to the LUV swelling buffer. GUVs and LUVs were first incubated with $1\mu M$ DNA as described above. After incubation, GUVs and LUVs were mixed 1:1 (vol/vol) in quenching observation buffer to a final concentration of dye and quencher of 2.5 mM HPTS and 2.5 mM DPX, respectively. Note that fusion occurs in the same step in the experimental protocol as binding. Like in the binding experiments, GUVs were subjected to a small osmotic shock in fusion experiments. The effect of this shock is discussed in section section 7.2. For the specific conditions used for fusion experiments, see table 7.3. It is important to note that the choice of lipid dye can affect fusion outcomes, as certain dyes can lead to non-specific lipid and content mixing [9, 527]. We therefore kept the choice of membrane dye consistent.

Experiment	GUV dye	LUV dye	DNA concentration (µM)	Incubation time DNA	Incubation time vesicles
Osmotic shock	0.5% Atto488	0.05% Atto655	1	15 min	70 min
DNA concentration	0.5% Atto488	0.05% Atto655	0-5	Overnight	60 min
LUV size	No label	0.05% Rhodamine PE	1	90 min	70 min
GUV membrane composition	0.5% Atto488	0.05% Atto655	1	15 min	70 min
GUV formation method	0.5% Atto488	0.05% Atto655	1	15 min	70 min

Table 7.3: **Overview of experimental conditions for content mixing experiments.** All content mixing experiments were performed at room temperature, except for the overnight DNA concentration experiment with overnight incubation which was done in the fridge.

7.5.7. IMAGING AND ANALYSIS

Fluorescence imaging of GUVs was done using the 200μL imaging chambers as described in section 4.5.12. Imaging was performed on an inverted microscope (Nikon Eclipse Ti) equipped with a digital camera (Orca-Flash 4.0, Hamamatsu), an LED light source for monochromatic illumination (Spectra X, Lumencor), and a 100x magnification oil immersion objective (CFI Plan Apochromat VC 100x oil, NA 1.4, Nikon). All images presented in this chapter were taken in epifluorescence mode with a defined set of imaging settings to allow comparison between samples (see table 7.4). Absence of spectral cross-talk between different colour channels was confirmed both by imaging unlabelled samples and by absence of any correlation between intensities from different dyes as obtained in population analysis (see below). Microscopy fluorescence images were analysed with a custom-written python-based software named DisGUVery (see chapter 5 for a detailed description and characterisation). The processing workflow is outlined in detail in section 7.2.1. Statistical tests that were performed with the analysis results were either two-sided students t-test in case of two conditions that were compared, or Tukey's tests in case we cross-compared multiple experimental conditions.

	Label	Wavelength	Intensity	Exposure time
GUV	0.5% Atto488	508 nm	20%	100 ms
LUV	0.05% Atto655	640 nm	40%	100 ms
content	HPTS	440 nm	1%	10 ms

Table 7.4: **Imaging settings.** Overview of imaging settings used for epifluorescence imaging throughout this chapter.

7.6. ACKNOWLEDGEMENTS

We thank Yannick Dreher, Kevin Jahnke and Kerstin Göpfrich for useful instructions for the experiments, Liedewij Laan, Christine Linne and Ali Azadbakht for useful discussions about DNA-mediated interactions, Tom Aarts for execution of all experiments presented in this chapter, and Marcos Arribas Perez and Lucia Baldauf for proofreading the chapter and useful discussions.

7.7. SUPPLEMENTARY DATA

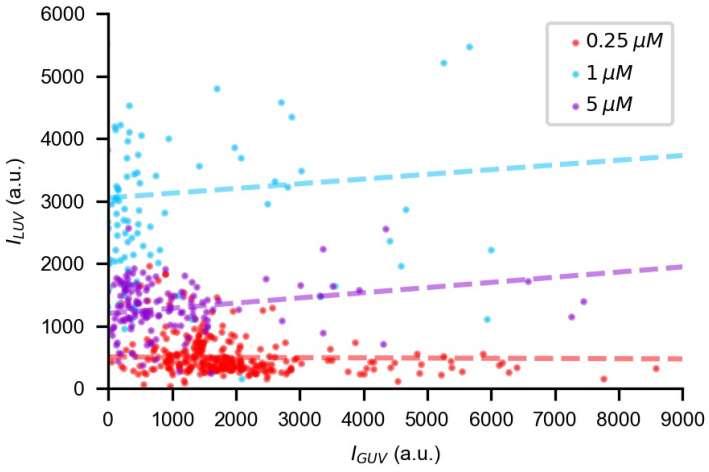

Figure 7.14: **No spectra cross-talk between GUV and LUV signal.** Population analysis shows that spectral crosstalk from GUV membrane fluorescence had a negligible influence on measured LUV intensities. GUVs were labelled with 0.5% Atto 488 DOPE, LUVs were labelled with 0.05% Atto 655 DOPE. Each data point represents the average intensity of both Atto 488 and Atto 655 fluorescence measured at the membrane of an individual GUV. Data was compiled from LUV binding experiments performed at different DNA concentrations of 0.25μM, 1μM, and 5μM DNA. Dashed lines are linear regression results with slopes -0.003 (0.25μM DNA), 0.075 (1μM DNA), and 0.083 (5μM DNA).

a

Membrane-proximal binding

Delta G = -23 kcal/mol Base Pairs: 11

```
DNA1    5′     TGGACATCAGAAAGGCACGACGA    chol
                  ::   :   ||||||||||||
DNA1′   3′ ACCTGTAGTCTTTATTCCGTGCTGCCT    chol
```

b

Membrane-distal binding

Delta G = -22 kcal/mol Base Pairs: 13

```
DNA1    5′ TGGACATCAGAAAGGCACGACGA        chol
           ||||||||||||||||       ::::
DNA1′   3′ ACCTGTAGTCTTTATTCCGTGCTGCCT    chol
```

Figure 7.15: **DNA binding strengths.** Analysis of hetero-dimerisation between DNA1 and DNA1′as used in this study. Analysis was performed by open-source commercial software of Integrated DNA Technologies (eu.idtdna.com). Delta G is the Gibbs energy calculated based on the longest stretch of complementary bases (solid lines). Additional complementary bases are indicated with dotted lines. (a) Dimerisation of the membrane-proximal ends. (b) Dimerisation of the membrane-distal ends.

ssDNA name	DNA sequence	Used for	Base Pairs
chol-DNA1	5'-TGG ACA TCA GAA AGG CAC GAC GA-Cholesterol-TEG-3'	LUV	23
chol-DNA1′	5'-Cholesterol-TEG-TCG TCG TGC CTT TCT GAT GTC CA- 3'	GUV	23
DNA1-Atto488	5'-TGG ACA TCA GAA AGG CAC GAC GA-Atto488-3'	Visualization	23

Table 7.5: **Correct DNA sequences.** Corrected DNA sequences and number of bases of the ssDNAs that should be used for future studies.

Experiment	Condition	n
DNA concentration fig. 7.3	$0.25\mu M$	83
	$0.5\mu M$	91
	$1\mu M$	171
	$2.5\mu M$	236
	$5\mu M$	328
Incubation time fig. 7.3f	10 min	37
	overnight	91
Osmolarity fig. 7.5	$-45mOsm$	66
	$-328mOsm$	81
	$-7mOsm$	90
	$11mOsm$	91
	$30mOsm$	72

Table 7.6: **Vesicle population sizes for the DNA incorporation experiments.**

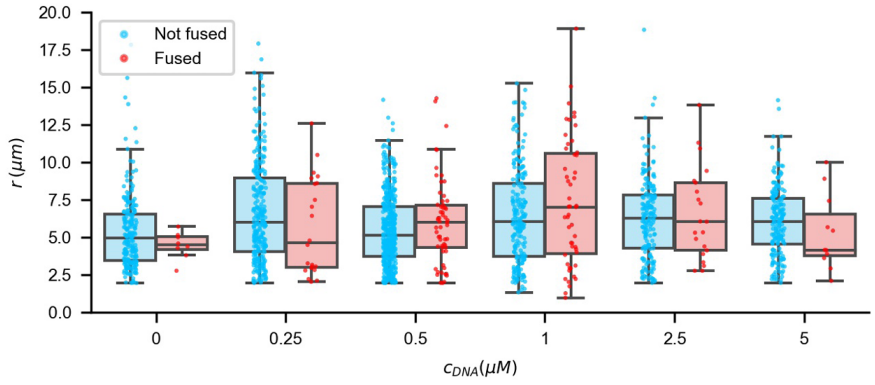

Figure 7.16: **GUV radii of fused and non-fused populations with varying DNA concentration.** GUV radii of fused and non-fused vesicles at different DNA concentrations as shown in fig. 7.3. GUVs are considered fused when the HPTS intensity ratio was larger than 1.05. Each data point represents an individual GUV.

Experiment	Condition	n
DNA concentration fig. 7.6	$0\mu M$	218
	$0.25\mu M$	307
	$0.5\mu M$	534
	$1\mu M$	271
	$2.5\mu M$	210
	$5\mu M$	197
Binding time fig. 7.7a	10 min	104
	30 min	91
	60 min	94
	90 min	57
	120 min	115
Osmolarity fig. 7.7b	$-45mOsm$	78
	$-28mOsm$	133
	$-7mOsm$	61
	$11mOsm$	70
	$30mOsm$	62

Table 7.7: **Vesicle population sizes for the LUV-GUV docking experiments.**

Experiment	Condition	n_{total}	n_{fused}	Fraction	$< r >$	$< r_{fused} >$	p	$I_{LUV,total}$	$I_{LUV,fused}$	p
Osmotic shock fig. 7.9	2x DNA, with shock	250	76	0.30	5.5	6.9	<0.001	4224	4633	0.097
	1x DNA, with shock	235	13	0.06	6.4	6.2	0.84	223	210	0.81
	0x DNA, with shock	169	5	0.03	7.1	5.0	0.16	282	261	0.88
	2x DNA, no shock	339	72	0.21	5.3	7.4	<0.001	4382	4490	0.65
	1x DNA, no shock	291	4	0.01	4.9	6.5	0.16	245	158	<0.001
	0x DNA, no shock	225	3	0.01	6.2	6.7	0.77	499	338	0.6
DNA concentration fig. 7.10	$0\mu M$	218	7	0.03	5.3	4.7	0.5	252	-309	<0.001
	$0.25\mu M$	307	17	0.06	6.8	7.5	0.33	497	433	0.45
	$0.5\mu M$	534	43	0.08	5.6	6.9	<0.001	1046	1220	0.26
	$1\mu M$	271	47	0.17	6.7	7.9	0.03	3031	2875	0.59
	$2.5\mu M$	210	18	0.09	6.3	6.4	0.87	2522	1718	0.005
	$5\mu M$	197	9	0.05	6.1	6.4	0.59	1270	1413	0.47
DNA concentration fig. 7.11	$100nm$	163	41	0.25	8.6	8.5	0.94	962	1096	0.21
	$200nm$	416	94	0.23	8.5	11.0	<0.001	595	613	0.5
Membrane composition fig. 7.12	DOPC +DNA	128	41	0.32	7.1	8.6	0.01	3930	4642	0.1
	DOPC -DNA	149	7	0.05	6.4	6.9	0.66	306	243	0.02
	PC:PE +DNA	100	23	0.23	4.5	6.4	<0.001	4732	5314	0.22
	PC:PE -DNA	152	7	0.05	4.9	3.9	0.22	312	280	0.01
	Phys +DNA	369	72	0.20	7.5	9.5	0	3264	301	0.52
	Phys -DNA	379	17	0.05	7.2	7.5	0.76	386	186	0.03
GUV formation method fig. 7.13	Gel swelling	128	41	0.32	7.1	8.6	0.01	3930	4642	0.1
	eDICE	118	15	0.13	3.0	3.1	0.6	4514	4798	0.57

Table 7.8: **Population info for the fusion experiments.** Reported p-values indicate results of two-sided student t-tests comparing the values from the fused population with the entire population.

8

OUTLOOK

Even though cells are the smallest entities that we consider alive, they still display an overwhelming complexity at the molecular level. In the past centuries, biological research has identified the rich arsenal of molecular components that constitute the cell, including proteins, metabolites, lipids, and many more. However, understanding how exactly these building blocks work together to form a living cell is difficult to unravel in the biological context. To acquire a mechanistic understanding, it is often more helpful to study the components of interest in an isolated system. In such a bottom-up reconstitution approach, cell functionalities are reconstituted with a minimal set of (biological) building blocks. The holy grail in this research is the eventual reconstruction of a minimal living cell from assembly of its components. However, the road to building a synthetic cell is unknown.

In this thesis, we focused mainly on the construction and shaping of the cell container, for which we decided to use Giant Unilamellar Vesicles (GUVs). As a key functionality of the cell container is its ability to divide, we discussed in chapter 2 strategies to divide a synthetic cell using the actomyosin division machinery found in eukaryotes. Next, we showed in chapter 3 how GUVs can be formed using the continuous Droplet Interface Crossing Encapsulation (cDICE) technique. We demonstrated how this technique can be used to encapsulate complex mixtures including proteins inside GUVs, because reliable encapsulation is crucial for building life-like functions. In chapter 4, we compared cDICE to other formation methods based on our own experiences. Importantly, we presented a simplified version of cDICE, which we called emulsion Droplet Interface Crossing Encapsulation (eDICE), which is easier and at the same time has greater potential for reconstitution experiments. With increasing complexity in bottom-up reconstitution assays, statistical analysis of GUV populations becomes crucial. We therefore introduced the GUV image analysis tool DisGUVery in chapter 5, which enabled us to perform high-throughput quantitative image analysis on large GUV populations.

The GUVs encapsulating a reconstituted septin cortex that are presented in this chapter were fabricated by Britta Bor under supervision by Gerard Castro Linares and Lennard van Buren. Local injection experiments were performed by Tom Aarts under supervision by Lucia Baldauf and Lennard van Buren.

As a basis for investigating the effect of cytoskeletal proteins on the mechanics of the synthetic cell, we presented in chapter 6 workflows for two techniques to probe cell mechanics: vesicle fluctuation analysis (VFA) and micropipette aspiration (MPA). Lastly, in chapter 7, we demonstrated how the synthetic cell container can be grown by fusion of externally added vesicles.

We anticipate that the work presented in this thesis expands the basis for bottom-up reconstitution of a synthetic cell. There are still many conceptual and experimental challenges ahead, which have been excellently reviewed by Olivi et al. [92]. We already presented a general outlook on actin-mediated GUV division chapter 2. In this chapter, we discuss the outlook on synthetic cell engineering endeavours specifically motivated by the work done in this thesis.

8.1. FOLLOW-UP WORK TO RECONSTITUTE ACTIN-DRIVEN SYNTHETIC CELL DIVISION

How can we use actin-mediated force generation to deform GUV membranes and finally to divide the synthetic cell? We extracted five (experimental) questions for which this work presents a basis for follow-up research.

1. How can we reconstitute actin networks in GUVs?
Reliable formation of vesicles and controlled encapsulation of solutes and proteins therein has presented a major hurdle for bottom-up synthetic biology. While the first proof-of-principle swelling-based encapsulation of actin in GUVs dates back more than thirty years [558], and the first emulsion-based encapsulation twenty years [75], the number of actin encapsulation studies has only been increasing rapidly in the past three years [112–114, 175, 294, 359]. Nowadays, a large fraction of actin encapsulation studies is being performed with continuous Droplet Interface Crossing Encapsulation (cDICE) [3]. In chapter 3, we showed how actin monomers can be encapsulated using cDICE, and also other systems including the In-Vitro Transcription Translation system PURE, DNA nanostars, and membrane-binding proteins. In chapter 4, we show how we invented emulsion Droplet Interface Crossing Encapsulation (eDICE) to extend the range of encapsulated proteins to include also the filamentous proteins actin and septin.

We believe that with the advent of cDICE and especially the invention of eDICE, this major hurdle of GUV production and encapsulation has been taken. These techniques form a solid basis for reconstitution experiments to engineer cell division. In chapter 4, we present several proof-of-concept experiments that demonstrate that actin cortices can now be reconstructed in GUVs in a variety of ways, including membrane-anchoring of prepolymerized filaments and growth of actin filaments from membrane-bound nucleators. From here, we can start exploring the wide parameter space of biological building blocks that govern actin network architecture and dynamics *in vivo*, such as bundling agents (fascin, anillin, septin), cross-linkers (alpha-actinin, plectin), motor proteins
(myosin), severing proteins (gelsolin), depolymerizing proteins (ADF/cofilin) and capping protein.

Besides demonstrating reconstitution pathways, we have also presented two main

routes for characterization of reconstituted networks. First, we have shown that the DisGUVery software that we developed (chapter 5) can be used to easily derive population characteristics from GUV microscopy images. This allows for high-throughput quantification of encapsulation, membrane deformation, and actin localization. In addition, DisGUVery lays a basis for fluorescence measurements of GUV membranes, which can be used to characterize incorporation of membrane building blocks that are required for reconstitution of cell division. For example, DOPS lipid incorporation can be probed on a population level by binding of a fluorescently labelled annexin [559]. As a second route to characterize reconstituted cortices in GUVs, we presented mechanical measurements in chapter 6. Together with these measurements, cortex reconstitution can be employed to disentangle the mechanical effects of cortex architecture (formin versus Arp2/3 nucleated), cross-linkers, membrane adhesion (see next paragraph) and cortical thickness.

Furthermore, using our membrane fusion assay (chapter 7) as a cargo delivery platform provides an alternative route to encapsulate molecules inside GUVs. This can be useful when components need to be added sequentially to a GUV, or when the encapsulation of a certain protein or solute interferes with the GUV formation process. Even multi-step fusion has been established with DNA-based fusion[560], opening up a wide design parameter space for addition of components post-formation. While sequential addition of components has been demonstrated in GUV formation before with sophisticated microfluidic platforms [79], we anticipate that membrane fusion provides an easier bulk assay as it only requires membrane-anchored DNA. If required, the cholesterol-anchored DNA can be washed out of the membrane after delivery [529].

2. How to adhere actin to the membrane?

Our current understanding of how the actin cortex is mechanically anchored to the plasma membrane is still minimal. While a number of proteins have been identified to play a role in adhesion, their exact function and molecular organization remain elusive. As we discussed in chapter 2, most reconstitution work has bypassed this knowledge gap by using engineered linking strategies for anchoring. As such, actin networks have mostly been bound to the membrane either by adhering pre-formed filaments using biotin-streptavidin links [113, 177, 237] or by growing actin filaments from His-tagged actin nucleators bound to nickelated lipids in the membrane [108, 112, 178, 238]. The binding strengths in these engineering approaches are so high, that bonds are virtually unbreakable. This is in stark contrast to biological systems, where actin-membrane adhesion is governed by many bonds which are individually much weaker [232]. Reconstitution of actin networks that are membrane-anchored with more physiological linkers, involving for example septins and ezrin(fig. 8.1a), is sparse and limited to 2D studies on supported bilayers[252–255]. Importantly, the exact requirements for the organization of the actin-membrane contact site are to date unknown. What is the role of density and strength of individual linkers? What are the requirements for lipid and/or linker diffusivity? These questions demand for a mechanical characterization of membrane-linker composites. Answering these questions will not only help us to reconstitute cytokinesis in GUVs, but also to understand the mysterious actin-membrane interface in cells.

In chapter 4, we demonstrated that we can encapsulate septin in GUVs, and that we can induce membrane localization of septin by addition of negatively charged DOPS

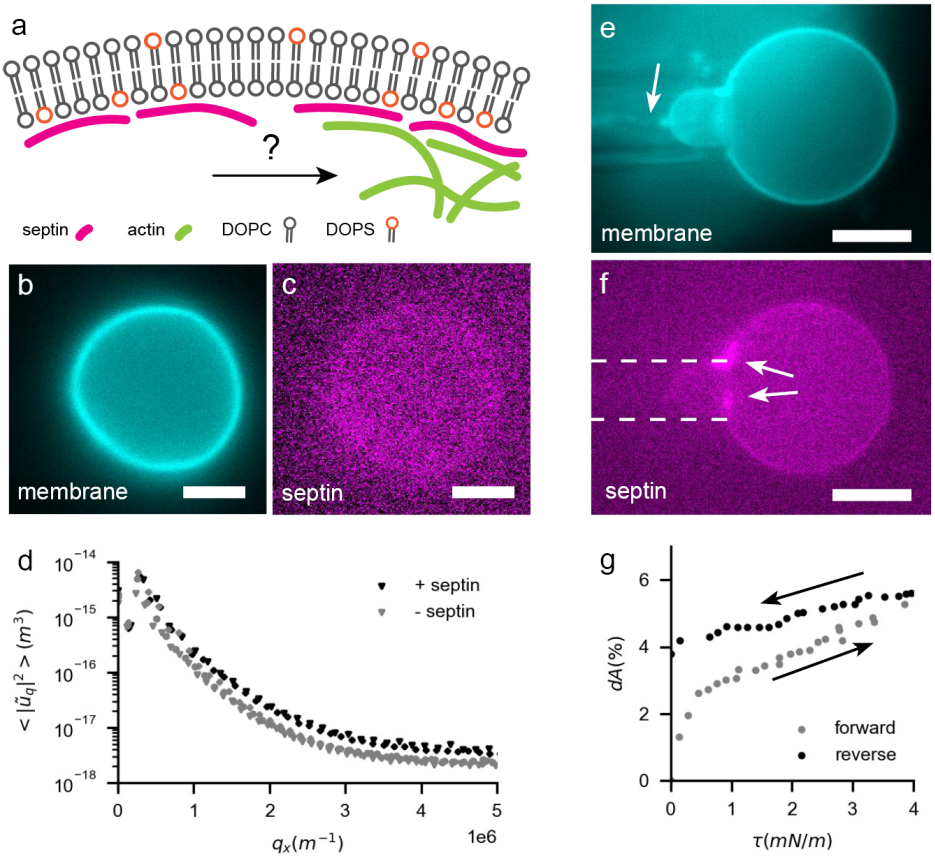

Figure 8.1: **Reconstruction of a septin cortex.** (a) Schematic of an internal membrane-bound septin cortex. (b-c) Epifluorescence image of a fluctuating GUV membrane (cyan) composed of DOPC:DOPS:Atto 655 DOPE (79.90:20:0.1) encapsulating $100nM$ septin hexamers (magenta) produced with eDICE. Scale bar is $5\mu m$. (d) Fluctuation spectra obtained from two GUVs as described in panel b and c (black), and for three DOPC GUVs produced with electroformation (grey). All fluctuation data was obtained using an exposure time of 2 ms from GUVs with radii between 6 and 9 μm. (e-f) Epifluorescence images of an aspirated GUV (DOPC:DOPS:Atto 655 DOPE in molar ratio 79.9:20:0.1) encapsulating septin hexamers at $300nM$. A membrane tube is seen in the pipette (panel e, arrow). Note that septin localizes at the neck region of the GUV where the curvature is negative (panel f, arrows). Dashed lines indicate pipette position. Scale bar is $10\mu m$. (g) Aspiration measurement performed on the vesicle described in panel e-f. A clear hysteresis is observed between the forward (grey) and reverse (black) measurements.

or PIP_2 lipids. Reconstruction of a septin cortex at the GUV inner leaflet is an important next step towards rebuilding a more physiological actin cortex. Moreover, these membranes can be used to measure physical properties of a membrane-bound layer of actin linkers in the cell-like configuration. In fig. 8.1, we show proof-of-principle experiments to probe the mechanical properties of GUVs with a septin cortex. At a nominal concentration of of $100nM$ septin hexamers, membranes enriched with septins were

clearly fluctuating (fig. 8.1b,c). This indicates that the membrane is still relatively soft at this septin concentration, with a bending modulus on the order of tens of k_BT. We employed vesicle fluctuation analysis (VFA) to obtain the fluctuation spectrum of these membranes (fig. 8.1d). Interestingly, septin-enriched membranes (DOPC:DOPS in a molar ratio of 80:20) showed a very comparable spectrum as compared to empty DOPC membranes, but with an enhanced fluctuation amplitude. Fitting the spectra yielded bending rigidities between 10.8 and 13.1 k_BT (n=4) in presence of septin (versus 17.4 to 20.5 k_BT for electroformed DOC membranes without septin, n=6). Likely, the higher apparent softness of the septin-decorated membranes is a result of a less robust contour detection in these vesicles as we also saw for actin-decorated GUVs (chapter 6). By contrast, at a higher nominal septin concentration of $300nM$, fluctuations were largely suppressed. In this regime, we set out to probe mechanics by active deformation of the septin-membrane composite using micropipette aspiration (MPA). Indeed, we successfully aspirated GUVs with septin-enriched membranes (fig. 8.1e,f). Interestingly, internal septin structures often colocalized at the pipette opening (fig. 8.1f), possibly indicating a preferential binding to negative curvature [222]. Forward aspiration typically led to a substantial jump in projected area initially, probably related to the presence of outwards membrane tubes that were seen on many GUVs (fig. 8.1e). Continued aspiration showed a linear increase in area with membrane tension, as typical for the stretching regime of naked membranes (chapter 6). Subsequent decrease of aspiration pressure showed a higher membrane compressibility, which could have resulted from a reconfiguration of the septin cortex, but also by membrane reservoirs that were incorporated by the initial stretching.

Further analysis of cortex elasticity should tell us more about the molecular organization of septin on the membrane, such as its polymerization state[561] and the number of stacked septin layers[255]. Besides VFA and MPA, tube-pulling measurements could be done to probe the cortex adhesion energy and dynamics [232, 261, 562]. Exciting novel techniques present themselves, such as aspiration based on optical interferometry which provides unmatched temporal and spatial resolution [457]. The system developed by Berardi et al. makes it possible to apply oscillatory stresses, and thus enable scientists to characterize the rheology of membrane-anchored networks even at small deformations. Of course, these methods are not limited to studying septin cortex formation alone, but can be extended to studies on membrane-binding proteins, actin-membrane linkers and reconstituted actin cortices. In turn, we anticipate that mechanical measurements on reconstituted cortices should grant us more insights about the biological system. We want to stress that mechanical measurements on cortex reconstructions in the inside orientation are only feasible once a reliable protein encapsulation platform is established. Since eDICE combines experimental ease with robustness and versatility in encapsulation, we believe that eDICE provides a crucial step forward in membrane-cortex studies. An essential challenge here is the quantification of encapsulated material inside GUVs. Only when the internal concentration is known, the body of experimental work on two-dimensional open systems can be reconciled with 3D measurements in GUVs.

3. How to trigger internal activity?
Once a membrane-bound actin network is formed, generation of contractile stresses in the network is required to reshape and finally divide the GUV. Timing is essential here: the actin network should first be formed and organized, before contraction starts. It is however not trivial to time internal processes post-formation, as the membrane imposes a barrier to any externally added solutes. As we discussed in chapter 2, myosin contractility can be controlled by light-based deactivation of the myosin inhibitor blebbistatin [158, 179, 180] or by optogenetics [181].

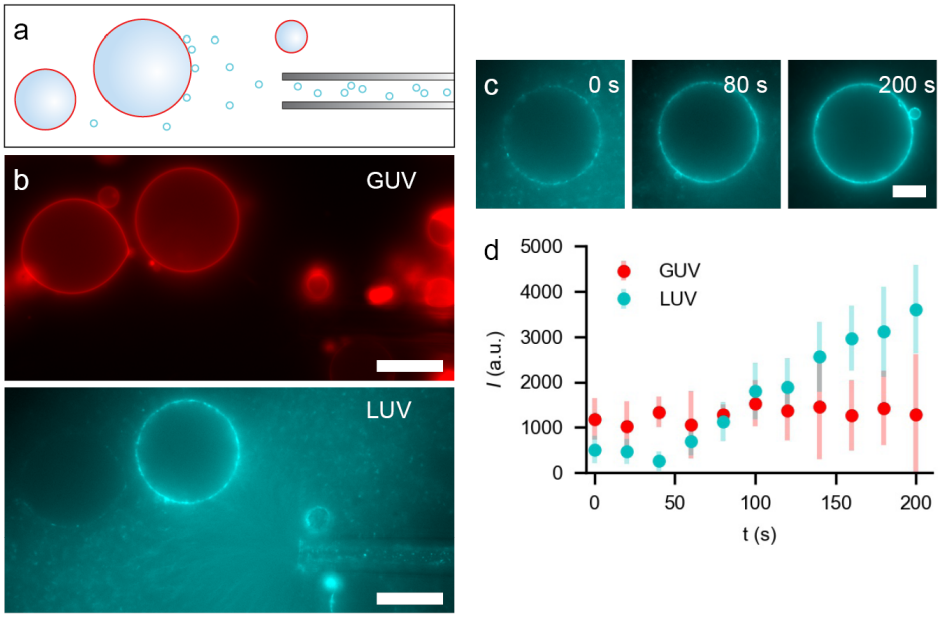

Figure 8.2: **Temporal control by local injection.** Using an injection micropipette, LUVs (cyan) can be added locally to the GUV (red) sample, as demonstrated here with a DNA-mediated binding experiment. (a) Schematic representation. (b) Epifluorescence images of a sample containing GUVs (top) to which LUVs (bottom) are locally added by micropipette injection. The pipette can be seen in the right bottom corner. Scale is $20\mu m$. (c) Epifluorescence time lapse images of the LUV fluorescence on a GUV membrane that is targeted by micropipette injection. Starting time (t = 0 s) corresponds to the onset of injection. Scale is $10\mu m$. (d) Evolution of the LUV signal on the membrane of a GUV (cyan) upon local injection of LUVs. The signal of the GUV membrane (red) is given as a reference. The membrane signals were obtained as described in chapter 7. Data points represent the angular average signal measured on a single GUV, error bars are standard deviation of the angular profile.

As an easier and more general alternative, vesicle fusion (see chapter 7) can be used to trigger internal processes, for example by delivery of solutes to the GUV interior. In the context of actomyosin-driven division, one could think of encapsulating ATP in LUVs, where actomyosin contraction in the GUV only starts upon delivery of ATP, which happens when LUVs fuse with the GUV. While a fusion-based triggering can in principle be performed in bulk, one ideally minimizes the time between addition and imaging in order to capture the entire deformation process. To combine temporal control with

immediate visualization, we implemented a local injection method, where a solution containing either proteins, LUVs or other components of interest can be locally added to the sample with the use of a micropipette [483, 563, 564]. We demonstrate the method by locally injecting LUVs close to GUVs with a small ($\sim 10\mu m$) micropipette (fig. 8.2a,b). Using membrane-anchored DNA linkers as described in chapter 7, we can trigger the fast binding processes by starting the injection (fig. 8.2c,d). As such, local injection provides a quick and easy way to control the timing of membrane-bound cellular processes. Combined with membrane fusion (chapter 7), cargo can be delivered inside the GUV with high temporal control, making LUV injection a powerful tool for reconstitution and visualization of time-dependent cellular processes. Alternatively, GUVs could be trapped in microfluidic channels[389, 565, 566], and LUVs of different types could be added sequentially in a multistep fusion process [567]. By using shape-imposing traps, mechanical shaping can be combined with fusion-triggered contraction [182, 196]. Because of its generality, we anticipate that fusion-based cargo delivery can be used as a common mechanism compatible with triggering a wide variety of internal processes.

4. How to break symmetry? Starting from typically spherical vesicles, symmetry breaking is an essential step in reconstitution of synthetic cell division. Ample strategies have been proposed to achieve this, which have been excellently reviewed by Olivi et al. [92]. In the specific context of an actin cortex-mediated division, symmetry can be broken by local modulation of the actomyosin network[158], by external mechanical deformation [182, 196], but also in the membrane. We highlight two membrane-based symmetry breaking mechanisms for which our work provides a basis for integration with other synthetic cell research.

First, macroscopic lipid-lipid phase separation can be employed to induce symmetry breaking [568]. The interfacial tension between the two phases, the line tension, can in turn result in a membrane deformation [569, 570] and even drive division [91]. By using a DNA-mediated fusion-based feeding mechanism, Dreher et al. managed to regenerate the two co-existing lipid phases after GUV division [91] making this a promising candidate for sustained synthetic cell division through multiple life cycles. In the context of actomyosin-driven division, we propose that symmetry breaking of a GUV bearing an actin cortex can be initiated by feeding LUVs with a membrane composition that drives phase separation of the GUV membrane. If followed by a slight osmotic deflation, a spherical symmetric phase-separated GUV can be deformed to a dumbbell-like shape[91]. A dumbbell shaped vesicle, in turn, provides an excellent template for shaping the cortex in a configuration corresponding to early cytokinesis. In this way, symmetry breaking is directly coupled to membrane growth. As a next step, loading added LUVs with ATP would serve as a way to trigger symmetry breaking, membrane growth and cortical activity simultaneously. It should be noted that the relation between actomyosin contractility and lipid domains has thus far been investigated on SLBs only [246, 248]. Futures studies should elucidate how an anchored cortex influences phase separation and resulting shape transformations in free-standing membranes. Alternatively, one could think of reversing the process. Instead of cortex formation followed by phase separation-mediated shaping, one could first create phase-separated dumbbell GUVs encapsulating cytosolic actin, and only later deliver membrane-binding or nucle-

ation factors by fusion.

Second, symmetry can be broken by spontaneous curvature effects, which in turn can lead to a wide range of shape transformations including dumbbell-shaped GUVs[571]. This effect has been put to work using a variety of mechanisms (see review [572]), including membrane-binding molecules (star-like oligonucleotides [220], proteins[64]) and triggered lipid asymmetries (thermal expansion [573], light-induced peroxidation [71]). In some cases, spontaneous curvature effects were sufficient to achieve full division[64, 71]. We propose that LUV-GUV fusion (chapter 7) can be employed as an alternative method to induce spontaneous curvature, by feeding LUVs with asymmetric lipid composition. In particular, delivery of lipids with negative curvature to the inner leaflet, and a positive curvature to the outer leaflet, should promote the formation of a furrow. Formation of asymmetric SUVs and LUVs has been demonstrated for a wide range of lipid mixtures[574–576], but their fusion to GUVs has not been explored yet. By coupling symmetry breaking with membrane growth, two essential steps in the division process are aligned. Moreover, generation of leaflet asymmetry captures a crucial feature of the biological plasma membrane[59, 577].

Altogether, there are plenty of membrane-based approaches that can be taken to induce symmetry breaking in GUVs. Important considerations are the cell surface rigidities and forces generated by the symmetry breaking mechanism and the contractile cortex. On the one hand, when the symmetry-breaking mechanism imposes a high stiffness, forces produced by the contractile cortex might not be sufficient to deform the GUV. On the other hand, small forces involved in symmetry breaking might not overcome the shape imposed by a pre-formed cortex. In the coming years, crucial challenges lie in the integration of symmetry-breaking methods with reconstitution of physiological division machineries.

5. How to generate membrane growth? Division of a spherical vesicle requires excess membrane area, which can be generated by a decrease of vesicle volume, or an increase in membrane area. While osmotic deflation is a simple and effective technique [578], it has a drastic impact on the chemical environment inside the cell container, thereby impeding the functionality of internal proteins and processes. Moreover, volume decrease does not contribute to the objective of a growing and dividing cell. Instead, novel research focuses on membrane growth, either by *de novo* (bio)synthesis of phospholipids inside vesicles[87, 88, 579, 580], or by external addition and fusion of vesicles [89–91, 514].

In chapter 7, we have elaborated on a DNA-mediated fusion assay for the growth of GUV membranes. While we found that fused vesicles were in general larger than non-fused GUVs, indicative of growth by fusion, an essential question remains to which extent the GUV membrane can increase in size with such an approach. Measuring the GUV membrane area during the fusion process would provide valuable insights. To investigate this, we propose a dual pipette experiment: while the GUV is aspirated at constant pressure with one micropipette, LUVs are added locally from a second pipette. Besides probing the extent of membrane growth, such an experiment can be employed to provide information about growth dynamics, the effect of tension, and the effect on membrane permeability.

While growing a synthetic cell membrane by external addition of LUVs might be a pragmatic way to by-pass outstanding reconstitution challenges, a fully autonomous cell should be able to synthesize lipids *in situ*. Micropipette aspiration can be used to control membrane tension on a single-vesicle level, thereby enabling the experimenter to control membrane tension and monitor area growth. In this way, we anticipate that single-vesicle micromanipulation can serve as a tool to investigate the biophysical cues involved in *in vitro* cellular growth. For example, aspiration can be employed to study how membrane tension affects synthesis of phospholipids in the membrane[87], or to drive membrane uptake of internal vesicles that are self-assembled from *de novo* synthesized lipids [580].

8.2. GENERAL RECOMMENDATIONS FOR GUV-BASED RECONSTITUTION

The above questions addressed specifically the future experimental challenges and research directions in actomyosin-driven division of synthetic cells. In addition, two other, more general challenges for the synthetic cell engineering field can be distilled from the work presented in this thesis.

6. GUV formation A technical challenge still lies in GUV fabrication and encapsulation of components. The formation of a viable synthetic cell relies heavily on the availability of a single production platform that can encapsulate all vital modules. Even though we showed that cDICE and eDICE are capable of encapsulating a wide range of subsystems, further investigation is required for several reasons.

First, the concentration of encapsulates is unknown and varying across the population of produced GUVs. This makes it difficult to extrapolate findings from bulk and open 2D studies to vesicles, both of which typically form a basis for GUV studies. Nowadays, the input parameter space often needs to be re-explored when findings are translated to vesicle formation, meaning that the input concentrations of encapsulates are varied until the desired behaviour is observed. This does not only become exponentially more time-consuming with the number of compounds involved, but not knowing the internal concentrations also prevents us from building a mechanistic understanding of the produced GUVs. The field needs to focus on reducing variability in encapsulation (see below), but also on quantitative reporting of solute concentration inside GUVs. Key in these developments is the availability of ready-to-use image analysis softwares, like DisGUVery we presented in chapter 5.

Second, the field still has minimal understanding of how (surface-active) solutes affect the vesicle formation process. We found that actin drastically impacts lipid monolayer formation in chapter 4, but the exact mechanism remains unknown. In general, studies focused on encapsulation issues are sparse [401] and continue to receive little attention, despite the growing attention for complex reconstitution experiments. While we showed that several tricks can be used to boost encapsulation[175], we believe that the field would benefit greatly from having an educated approach on how to encapsulate solutes - especially if you consider that even a simple synthetic cell will probably contain hundreds of different molecules, varying in size, charge, surface activity, and biochemi-

cal stability.

Third, more focus should be put on method comparison. Being able to make the right choice for a GUV fabrication technique can save years of synthetic cell research spent on implementation of different methods. Ideally, researchers should have a clear 'hand-book' on vesicle formation, guiding which method to use for which purpose. Besides literature reviews, which are being published increasingly [16, 355, 356], experimental comparisons should be made where single users or single labs evaluate the implementation of different techniques on a population level. Evaluation parameters should include yield, polydispersity, membrane lamellarity and cleanliness, encapsulation efficiency, and importantly, reproducibility. Such a method evaluation requires a characterization of GUV populations instead of individual GUV, which brings us to the next general challenge.

7. A population-level view

Synthetic cell research requires a paradigm shift from proof-of-concept experiments to quantitative population analysis. Reconstitution experiments become more and more complex, giving rise to a wider polydispersity in GUV populations. As a result, produced vesicles vary in size, morphology, concentration of encapsulated material and membrane localization of internal components, among others. A population level view is required to describe differences between or within such polydisperse population. Multiple studies already show the power of population-level analysis [89, 175, 328, 337, 377], but exciting prospects lie ahead in terms of high-throughput imaging and analysis.

Regarding analysis, we see the development of multiple freely available GUV analysis softwares [337, 427–429], including DisGUVery (chapter 5) which we specifically developed to have high versatility in use. The availability of ready-to-use analysis substantially lowers the threshold for data quantification. In addition, with the upcoming of machine learning (ML) it becomes possible to classify complex GUV populations without *a priori* knowledge of their appearance and properties. As such, GUV classification can be done either using GUV-specific ML applications [429] or using ML software from cell biology [581].

In concert with high-throughput analysis, also high-throughput imaging techniques are being developed. Researchers have used 96-well microtiter plates to couple GUV formation to automated imaging [328, 582]. In addition, GUVs can be fixed at pre-defined positions using microfluidic traps that can trap either single vesicles[389, 583] or large assemblies [566].

Finally, cell-based high-throughput imaging and analysis techniques have promising potential for GUV research. GUVs can be analyzed by flow cytometry [283, 434, 584, 585] or fluorescence-activated cell sorting (FACS) [307, 586, 587]. In combination with imaging on-the-fly and ML-based classification, automated cell sorting has unmatched potential for population-level analysis [587, 588].

BIBLIOGRAPHY

[1] R. Virchow, *Die Cellularpathologie in ihrer Begründung auf physiologische und pathologische Gewebelehre.* (Hirschwald, 1858).

[2] BaSyC - Building a Synthetic Cell, *www.basyc.nl,* .

[3] M. Abkarian, E. Loiseau, and G. Massiera, *Continuous droplet interface crossing encapsulation (cDICE) for high throughput monodisperse vesicle design,* Soft Matter **7**, 4610 (2011).

[4] W. Helfrich and R.-M. Servuss, *Undulations, steric interaction and cohesion of fluid membranes,* Il Nuovo Cimento D **3**, 137 (1984).

[5] J. Pécréaux, H. G. Döbereiner, J. Prost, J. F. Joanny, and P. Bassereau, *Refined contour analysis of giant unilamellar vesicles,* The European Physical Journal E **13**, 277 (2004).

[6] J. M. Mitchison and M. M. Swann, *The Mechanical Properties of the Cell Surface I. The Cell Elastimeter,* Journal of Experimental Biology **31**, 443 (1954).

[7] J. R. Henriksen and J. H. Ipsen, *Measurement of membrane elasticity by micropipette aspiration,* Eur. Phys. J. E **14**, 149 (2004).

[8] G. Stengel, R. Zahn, and F. Höök, *DNA-induced programmable fusion of phospholipid vesicles,* Journal of the American Chemical Society **129**, 9584 (2007).

[9] Y.-H. M. Chan, B. van Lengerich, and S. G. Boxer, *Lipid-anchored DNA mediates vesicle fusion as observed by lipid and content mixing,* Biointerphases **3**, FA17 (2008).

[10] A. P. Liu and D. A. Fletcher, *Biology under construction: in vitro reconstitution of cellular function,* Nature Reviews Molecular Cell Biology **10**, 644 (2009).

[11] I. Ezkurdia, D. Juan, J. M. Rodriguez, A. Frankish, M. Diekhans, J. Harrow, J. Vazquez, A. Valencia, and M. L. Tress, *Multiple evidence strands suggest that there may be as few as 19 000 human protein-coding genes,* Human Molecular Genetics **23**, 5866 (2014).

[12] R. Milo, *What is the total number of protein molecules per cell volume? A call to rethink some published values,* BioEssays **35**, 1050 (2013).

[13] S. Ausländer, D. Ausländer, and M. Fussenegger, *Synthetic Biology—The Synthesis of Biology,* Angewandte Chemie International Edition **56**, 6396 (2017).

[14] P. Schwille, *Bottom-up synthetic biology: Engineering in a Tinkerer's World,* Science **333**, 1252 (2011).

[15] H. Jia and P. Schwille, *Bottom-up synthetic biology: reconstitution in space and time,* Current Opinion in Biotechnology **60**, 179 (2019).

[16] Y. Mulla, A. Aufderhorst-Roberts, and G. H. Koenderink, *Shaping up synthetic cells,* Physical Biology **15**, 041001 (2018).

[17] P. Schwille, *Division in synthetic cells,* Emerging Topics in Life Sciences **3**, 551 (2019).

[18] P. Schwille, J. Spatz, K. Landfester, E. Bodenschatz, S. Herminghaus, V. Sourjik, T. J. Erb, P. Bastiaens, R. Lipowsky, A. Hyman, P. Dabrock, J. C. Baret, T. Vidakovic-Koch, P. Bieling, R. Dimova, H. Mutschler, T. Robinson, T. Y. Tang, S. Wegner, and K. Sundmacher, *MaxSynBio: Avenues Towards Creating Cells from the Bottom Up,* Angewandte Chemie **57**, 13382 (2018).

[19] B. a Cell, *www.buildacell.org,* .

[20] Synthetic Cell Initiative, *www.syntheticcell.eu,* .

[21] O. Staufer, J. A. De Lora, E. Bailoni, A. Bazrafshan, A. S. Benk, K. Jahnke, Z. A. Manzer, L. Otrin, T. Díez Pérez, J. Sharon, J. Steinkühler, K. P. Adamala, B. Jacobson, M. Dogterom, K. Göpfrich, D. Stefanovic, S. R. Atlas, M. Grunze, M. R. Lakin, A. P. Shreve, J. P. Spatz, and G. P. López, *Building a community to engineer synthetic cells and organelles from the bottom-up,* eLife **10** (2021).

[22] D. Fletcher, *Which biological systems should be engineered?* Nature **563**, 177 (2018).

[23] F. Lussier, O. Staufer, I. Platzman, and J. P. Spatz, *Can Bottom-Up Synthetic Biology Generate Advanced Drug-Delivery Systems?* Trends in Biotechnology **39**, 445 (2021).

[24] H. Zwart, *From primal scenes to synthetic cells,* eLife **8** (2019).

[25] D. G. Gibson, J. I. Glass, C. Lartigue, V. N. Noskov, R. Y. Chuang, M. A. Algire, G. A. Benders, M. G. Montague, L. Ma, M. M. Moodie, C. Merryman, S. Vashee, R. Krishnakumar, N. Assad-Garcia, C. Andrews-Pfannkoch, E. A. Denisova, L. Young, Z. N. Qi, T. H. Segall-Shapiro, C. H. Calvey, P. P. Parmar, C. A. Hutchison, H. O. Smith, and J. C. Venter, *Creation of a bacterial cell controlled by a chemically synthesized genome,* Science **329**, 52 (2010).

[26] J. F. Pelletier, L. Sun, K. S. Wise, N. Assad-Garcia, B. J. Karas, T. J. Deerinck, M. H. Ellisman, A. Mershin, N. Gershenfeld, R. Y. Chuang, J. I. Glass, and E. A. Strychalski, *Genetic requirements for cell division in a genomically minimal cell,* Cell **184**, 2430 (2021).

[27] M. Bedau, *Life after the synthetic cell,* Nature **465**, 422 (2010).

[28] W. K. Spoelstra, S. Deshpande, and C. Dekker, *Tailoring the appearance: what will synthetic cells look like?* Current Opinion in Biotechnology **51**, 47 (2018).

[29] E. Rideau, R. Dimova, P. Schwille, F. R. Wurm, and K. Landfester, *Liposomes and polymersomes: a comparative review towards cell mimicking,* Chemical Society Reviews **47**, 8572 (2018).

[30] M. H. van Stevendaal, L. Vasiukas, N. A. Yewdall, A. F. Mason, and J. C. van Hest, *Engineering of biocompatible coacervate-based synthetic cells,* ACS Applied Materials and Interfaces **13**, 7879 (2021).

[31] D. E. Discher and F. Ahmed, *Polymersomes,* Annual Review of Biomedical Engineering **8**, 323 (2006).

[32] M. Ugrinic, A. Zambrano, S. Berger, S. Mann, T. Y. Tang, and A. Demello, *Microfluidic formation of proteinosomes,* Chemical Communications **54**, 287 (2018).

[33] P. Walde, K. Cosentino, H. Engel, and P. Stano, *Giant Vesicles: Preparations and Applications,* ChemBioChem **11**, 848 (2010).

[34] A. O. Robinson, O. M. Venero, and K. P. Adamala, *Toward synthetic life: Biomimetic synthetic cell communication,* Current Opinion in Chemical Biology **64**, 165 (2021).

[35] M. Edidin, *Lipids on the frontier: a century of cell-membrane bilayers,* Nature Reviews Molecular Cell Biology **4**, 414 (2003).

[36] J. Lombard, P. López-García, and D. Moreira, *The early evolution of lipid membranes and the three domains of life,* Nature Reviews Microbiology **10**, 507 (2012).

[37] J. B. de la Serna, G. J. Schütz, C. Eggeling, and M. Cebecauer, *There is no simple model of the plasma membrane organization,* Frontiers in Cell and Developmental Biology **4**, 106 (2016).

[38] J. Zimmerberg and M. M. Kozlov, *How proteins produce cellular membrane curvature,* Nature Reviews Molecular Cell Biology **7**, 9 (2006).

[39] B. Kollmitzer, P. Heftberger, M. Rappolt, and G. Pabst, *Monolayer spontaneous curvature of raft-forming membrane lipids,* Soft matter **9**, 10877 (2013).

[40] D. W. Deamer and J. Bramhall, *Permeability of lipid bilayers to water and ionic solutes,* Chemistry and Physics of Lipids **40**, 167 (1986).

[41] E. Awoonor-Williams and C. N. Rowley, *Molecular simulation of nonfacilitated membrane permeation,* Biochimica et Biophysica Acta (BBA) - Biomembranes **1858**, 1672 (2016).

[42] B. Hille, *Ionic channels in excitable membranes. Current problems and biophysical approaches,* Biophysical Journal **22**, 283 (1978).

[43] S. Wilkens, *Structure and mechanism of ABC transporters,* F1000Prime Reports **7** (2015).

[44] P. F. Fahey, D. E. Koppel, L. S. Barak, D. E. Wolf, E. L. Elson, and W. W. Webb, *Lateral Diffusion in Planar Lipid Bilayers,* Science **195**, 305 (1977).

[45] S. J. Singer and G. L. Nicolson, *The Fluid Mosaic Model of the Structure of Cell Membranes,* Science **175**, 720 (1972).

[46] R. Macháň and M. Hof, *Lipid diffusion in planar membranes investigated by fluorescence correlation spectroscopy,* Biochimica et Biophysica Acta (BBA) - Biomembranes **1798**, 1377 (2010).

[47] W. Helfrich, *Elastic Properties of Lipid Bilayers: Theory and Possible Experiments,* Zeitschrift für Naturforschung C **28**, 693 (1973).

[48] A. Diz-Muñoz, D. A. Fletcher, and O. D. Weiner, *Use the force: Membrane tension as an organizer of cell shape and motility,* Trends in Cell Biology **23**, 47 (2013).

[49] E. Sitarska and A. Diz-Muñoz, *Pay attention to membrane tension: Mechanobiology of the cell surface,* Current Opinion in Cell Biology **66**, 11 (2020).

[50] K. Keren, *Cell motility: The integrating role of the plasma membrane,* European Biophysics Journal **40**, 1013 (2011).

[51] P. Bassereau, B. Sorre, and A. Lévy, *Bending lipid membranes: Experiments after W. Helfrich's model,* Advances in Colloid and Interface Science **208**, 47 (2014).

[52] J. F. Nagle, M. S. Jablin, S. Tristram-Nagle, and K. Akabori, *What are the true values of the bending modulus of simple lipid bilayers?* Chemistry and Physics of Lipids **185**, 3 (2015).

[53] B. A. Lewis and D. M. Engelman, *Lipid bilayer thickness varies linearly with acyl chain length in fluid phosphatidylcholine vesicles,* Journal of Molecular Biology **166**, 211 (1983).

[54] J. Dai and M. P. Sheetz, *Mechanical properties of neuronal growth cone membranes studied by tether formation with laser optical tweezers,* Biophysical Journal **68**, 988 (1995).

[55] M. Kaksonen and A. Roux, *Mechanisms of clathrin-mediated endocytosis,* Nature Reviews Molecular Cell Biology **19**, 313 (2018).

[56] W. Rawicz, K. C. Olbrich, T. McIntosh, D. Needham, and E. A. Evans, *Effect of Chain Length and Unsaturation on Elasticity of Lipid Bilayers,* Biophysical Journal **79**, 328 (2000).

[57] H. V. Ly and M. L. Longo, *The Influence of Short-Chain Alcohols on Interfacial Tension, Mechanical Properties, Area/Molecule, and Permeability of Fluid Lipid Bilayers,* Biophysical Journal **87**, 1013 (2004).

[58] K. Olbrich, W. Rawicz, D. Needham, and E. Evans, *Water Permeability and Mechanical Strength of Polyunsaturated Lipid Bilayers,* Biophysical Journal **79**, 321 (2000).

[59] M. Doktorova, J. L. Symons, and I. Levental, *Structural and functional consequences of reversible lipid asymmetry in living membranes,* Nature Chemical Biology **16**, 1321 (2020).

[60] N. Sapay, W. F. Bennett, and D. P. Tieleman, *Thermodynamics of flip-flop and desorption for a systematic series of phosphatidylcholine lipids,* Soft Matter **5**, 3295 (2009).

[61] J. Steinkühler, P. De Tillieux, R. L. Knorr, R. Lipowsky, and R. Dimova, *Charged giant unilamellar vesicles prepared by electroformation exhibit nanotubes and transbilayer lipid asymmetry,* Scientific Reports **8**, 1 (2018).

[62] H. G. Döbereiner, O. Selchow, and R. Lipowsky, *Spontaneous curvature of fluid vesicles induced by trans-bilayer sugar asymmetry,* European Biophysics Journal **28**, 174 (1999).

[63] M. Karimi, J. Steinkühler, D. Roy, R. Dasgupta, R. Lipowsky, and R. Dimova, *Asymmetric Ionic Conditions Generate Large Membrane Curvatures,* Nano Letters **18**, 7816 (2018).

[64] J. Steinkühler, R. L. Knorr, Z. Zhao, T. Bhatia, S. M. Bartelt, S. Wegner, R. Dimova, and R. Lipowsky, *Controlled division of cell-sized vesicles by low densities of membrane-bound proteins,* Nature Communications **11**, 1 (2020).

[65] A. Shevchenko and K. Simons, *Lipidomics: coming to grips with lipid diversity,* Nature Reviews Molecular Cell Biology **11**, 593 (2010).

[66] T. Harayama and H. Riezman, *Understanding the diversity of membrane lipid composition,* Nature Reviews Molecular Cell Biology (2018).

[67] S. M. Gruner, *Intrinsic curvature hypothesis for biomembrane lipid composition: a role for nonbilayer lipids,* Proceedings of the National Academy of Sciences of the United States of America **82**, 3665 (1985).

[68] D. Marsh, *Intrinsic curvature in normal and inverted lipid structures and in membranes,* Biophysical Journal **70**, 2248 (1996).

[69] Y. Barenholz, *Cholesterol and other membrane active sterols: from membrane evolution to "rafts",* Progress in Lipid Research **41**, 1 (2002).

[70] O. G. Mouritsen and M. J. Zuckermann, *What's so special about cholesterol?* Lipids **39**, 1101 (2004).

[71] Y. Dreher, K. Jahnke, M. Schröter, and K. Göpfrich, *Light-Triggered Cargo Loading and Division of DNA-Containing Giant Unilamellar Lipid Vesicles,* Nano Letters **21**, 5952 (2021).

[72] D. A. Fletcher and R. D. Mullins, *Cell mechanics and the cytoskeleton,* Nature **463**, 485 (2010).

[73] J. P. Reeves and R. M. Dowben, *Formation and properties of thin-walled phospholipid vesicles,* Journal of Cellular Physiology **73**, 49 (1969).

[74] M. I. Angelova, D. S. Dimitrov, M. I. Angelova, and D. S. Dimitrov, *Liposome electroformation,* Faraday Discussions of the Chemical Society **81**, 303 (1986).

[75] S. Pautot, B. J. Frisken, D. A. Weitz, W. D. Sophie Pautot, Barbara J. Frisken, S. Pautot, B. J. Frisken, and D. A. Weitz, *Production of Unilamellar Vesicles Using an Inverted Emulsion,* Langmuir **19**, 2870 (2003).

[76] A. Weinberger, F.-C. F. Tsai, G. H. G. Koenderink, T. Schmidt, R. Itri, W. Meier, T. Scmatko, A. Schröder, C. Marques, T. Schmatko, A. Schröder, and C. Marques, *Gel-assisted formation of giant unilamellar vesicles,* Biophysical journal **105**, 154 (2013).

[77] S. Deshpande, Y. Caspi, A. Meijering, and C. Dekker, *Octanol-assisted liposome assembly on chip.* Nature communications **7**, 10447 (2016).

[78] N. N. Deng, M. Yelleswarapu, and W. T. Huck, *Monodisperse Uni- and Multicompartment Liposomes,* Journal of the American Chemical Society **138**, 7584 (2016).

[79] M. Weiss, J. P. Frohnmayer, L. T. Benk, B. Haller, J. W. Janiesch, T. Heitkamp, M. Börsch, R. B. Lira, R. Dimova, R. Lipowsky, E. Bodenschatz, J. C. Baret, T. Vidakovic-Koch, K. Sundmacher, I. Platzman, and J. P. Spatz, *Sequential bottom-up assembly of mechanically stabilized synthetic cells by microfluidics,* Nature Materials **17**, 89 (2017).

[80] T. Litschel and P. Schwille, *Protein Reconstitution Inside Giant Unilamellar Vesicles,* Annual Review of Biophysics **50**, 525 (2021).

[81] A. Nohturfft and C. Z. Shao, *Coordination of Lipid Metabolism in Membrane Biogenesis,* Annual Review of Cell and Developmental Biology **25**, 539 (2009).

[82] C. B. Shuster and D. R. Burgess, *Targeted new membrane addition in the cleavage furrow is a late, separate event in cytokinesis,* Proceedings of the National Academy of Sciences **99**, 3633 (2002).

[83] M. Park, J. M. Salgado, L. Ostroff, T. D. Helton, C. G. Robinson, K. M. Harris, and M. D. Ehlers, *Plasticity-Induced Growth of Dendritic Spines by Exocytic Trafficking from Recycling Endosomes,* Neuron **52**, 817 (2006).

[84] K. Kurihara, M. Tamura, K. I. Shohda, T. Toyota, K. Suzuki, and T. Sugawara, *Self-reproduction of supramolecular giant vesicles combined with the amplification of encapsulated DNA,* Nature Chemistry **3**, 775 (2011).

[85] M. D. Hardy, J. Yang, J. Selimkhanov, C. M. Cole, L. S. Tsimring, N. K. Devaraj, and J. W. Szostak, *Self-reproducing catalyst drives repeated phospholipid synthesis and membrane growth,* Proceedings of the National Academy of Sciences of the United States of America **112**, 8187 (2015).

[86] R. Wick and P. L. Luisi, *Enzyme-containing liposomes can endogenously produce membrane-constituting lipids,* Chemistry & Biology **3**, 277 (1996).

[87] M. Exterkate, A. Caforio, M. C. Stuart, and A. J. Driessen, *Growing Membranes in Vitro by Continuous Phospholipid Biosynthesis from Free Fatty Acids,* ACS Synthetic Biology **7**, 153 (2018).

[88] D. Blanken, D. Foschepoth, A. C. Serrão, and C. Danelon, *Genetically controlled membrane synthesis in liposomes,* Nature Communications **11**, 1 (2020).

[89] S. Deshpande, S. Wunnava, D. Hueting, and C. Dekker, *Membrane Tension–Mediated Growth of Liposomes,* Small **15**, 1902898 (2019).

[90] R. B. Lira, T. Robinson, R. Dimova, and K. A. Riske, *Highly Efficient Protein-free Membrane Fusion: A Giant Vesicle Study,* Biophysical Journal **116**, 79 (2019).

[91] Y. Dreher, K. Jahnke, E. Bobkova, J. P. Spatz, and K. Göpfrich, *Division and Regrowth of Phase-Separated Giant Unilamellar Vesicles,* Angewandte Chemie **133**, 10756 (2021).

[92] L. Olivi, M. Berger, R. N. Creyghton, N. De Franceschi, C. Dekker, B. M. Mulder, N. J. Claassens, P. R. ten Wolde, and J. van der Oost, *Towards a synthetic cell cycle,* Nature communications **12** (2021).

[93] T. van der Heide, M. C. Stuart, and B. Poolman, *On the osmotic signal and osmosensing mechanism of an ABC transport system for glycine betaine,* The EMBO Journal **20**, 7022 (2001).

[94] J. Macía and R. V. Solé, *Protocell self-reproduction in a spatially extended metabolism–vesicle system,* Journal of Theoretical Biology **245**, 400 (2007).

[95] S. Kretschmer, K. A. Ganzinger, H. G. Franquelim, and P. Schwille, *Synthetic cell division via membrane-transforming molecular assemblies,* BMC Biology **17** (2019), 10.1186/s12915-019-0665-1.

[96] B. Mierzwa and D. W. Gerlich, *Cytokinetic Abscission: Molecular Mechanisms and Temporal Control,* Developmental Cell **31**, 525 (2014).

[97] A. Bertin, N. de Franceschi, E. de la Mora, S. Maiti, M. Alqabandi, N. Miguet, A. di Cicco, W. H. Roos, S. Mangenot, W. Weissenhorn, and P. Bassereau, *Human ESCRT-III polymers assemble on positively curved membranes and induce helical membrane tube formation,* Nature Communications **11**, 1 (2020).

[98] H. H. Low and J. Löwe, *A bacterial dynamin-like protein,* Nature **444**, 766 (2006).

[99] D. M. Faguy and W. F. Doolittle, *Cytoskeletal proteins: The evolution of cell division,* Current Biology **8**, R338 (1998).

[100] R. McQuillen and J. Xiao, *Insights into the Structure, Function, and Dynamics of the Bacterial Cytokinetic FtsZ-Ring,* Annual Review of Biophysics **49**, 309 (2020).

[101] A. C. Lindås, E. A. Karlsson, M. T. Lindgren, T. J. Ettema, and R. Bernander, *A unique cell division machinery in the Archaea,* Proceedings of the National Academy of Sciences **105**, 18942 (2008).

[102] Y. Caspi and C. Dekker, *Dividing the archaeal way: The ancient Cdv cell-division machinery,* Frontiers in Microbiology **9**, 174 (2018).

[103] A. Blanch Jover, N. D. Franceschi, D. Fenel, W. Weissenhorn, and C. Dekker, *The archaeal division protein CdvB1 assembles into polymers that are depolymerized by CdvC,* bioRxiv , 2021.10.07.463537 (2021).

[104] Y. W. Heng and C. G. Koh, *Actin cytoskeleton dynamics and the cell division cycle,* The International Journal of Biochemistry & Cell Biology **42**, 1622 (2010).

[105] P. Chugh and E. K. Paluch, *The actin cortex at a glance,* Journal of Cell Science **131** (2018).

[106] G. Salbreux, G. T. Charras, and E. K. Paluch, *Actin cortex mechanics and cellular morphogenesis,* Trends in Cell Biology **22**, 536 (2012).

[107] T. H. Cheffings, N. J. Burroughs, and M. K. Balasubramanian, *Actomyosin Ring Formation and Tension Generation in Eukaryotic Cytokinesis,* Current Biology **26**, R719 (2016).

[108] L. L. Pontani, J. Van Der Gucht, G. Salbreux, J. Heuvingh, J. F. Joanny, and C. Sykes, *Reconstitution of an actin cortex inside a liposome,* Biophysical Journal **96**, 192 (2009).

[109] F.-C. Tsai and G. Koenderink, *Shape control of lipid bilayer membranes by confined actin bundles,* Soft Matter **11**, 8834 (2015).

[110] Y. Bashirzadeh, N. H. Wubshet, and A. P. Liu, *Confinement Geometry Tunes Fascin-Actin Bundle Structures and Consequently the Shape of a Lipid Bilayer Vesicle,* Frontiers in Molecular Biosciences **7**, 337 (2020).

[111] Y. Bashirzadeh, S. A. Redford, C. Lorpaiboon, A. Groaz, H. Moghimianavval, T. Litschel, P. Schwille, G. M. Hocky, A. R. Dinner, and A. P. Liu, *Actin crosslinker competition and sorting drive emergent GUV size-dependent actin network architecture,* Communications Biology **4** (2021).

[112] K. Dürre, F. C. Keber, P. Bleicher, F. Brauns, C. J. Cyron, J. Faix, and A. R. Bausch, *Capping protein-controlled actin polymerization shapes lipid membranes,* Nature Communications **9**, 1 (2018).

[113] T. Litschel, C. F. Kelley, D. Holz, M. Adeli Koudehi, S. K. Vogel, L. Burbaum, N. Mizuno, D. Vavylonis, and P. Schwille, *Reconstitution of contractile actomyosin rings in vesicles,* Nature Communications **12**, 1 (2021).

[114] Y. Bashirzadeh, H. Moghimianavval, and A. Liu, *Encapsulated Actomyosin Patterns Drive Cell-Like Membrane Shape Changes,* SSRN Electronic Journal (2021).

[115] T. D. Pollard, *Nine unanswered questions about cytokinesis,* Journal of Cell Biology **216**, 3007 (2017).

[116] D. B. Cortes, A. Dawes, J. Liu, M. Nickaeen, W. Strychalski, and A. S. Maddox, *Unite to divide – How models and biological experimentation have come together to reveal mechanisms of cytokinesis,* Journal of Cell Science **131** (2018).

[117] K. Wang, H. Okada, and E. Bi, *Comparative Analysis of the Roles of Non-muscle Myosin-IIs in Cytokinesis in Budding Yeast, Fission Yeast, and Mammalian Cells,* Frontiers in Cell and Developmental Biology **8**, 1397 (2020).

[118] C. Addi, J. Bai, and A. Echard, *Actin, microtubule, septin and ESCRT filament remodeling during late steps of cytokinesis,* Current opinion in cell biology **50**, 27 (2018).

[119] L. Wolpert, *Experimental Cell Hesearch*, Tech. Rep. (1966).

[120] J. M. Arnold, *Cleavage furrow formation in a teoloecithal egg (Loligo Pealii) I. Filaments in Early Furrow Formation,* Journal of Cell Biology **41**, 894 (1969).

[121] T. E. Schroeder, *Preliminary notes: Cytokinesis: filaments in the cleavage furrow,* Experimental Cell Research **53**, 272 (1968).

[122] K. Kruse, J. F. Joanny, F. Jülicher, J. Prost, and K. Sekimoto, *Generic theory of active polar gels: A paradigm for cytoskeletal dynamics,* European Physical Journal E **16**, 5 (2005).

[123] G. Salbreux, J. Prost, and J. F. Joanny, *Hydrodynamics of cellular cortical flows and the formation of contractile rings,* Physical Review Letters **103** (2009).

[124] A. Zumdieck, M. C. Lagomarsino, C. Tanase, K. Kruse, B. Mulder, M. Dogterom, and F. Julicher, *Continuum description of the cytoskeleton: Ring formation in the cell cortex,* Physical Review Letters **95** (2005).

[125] H. Turlier, B. Audoly, J. Prost, and J.-F. F. Joanny, *Furrow constriction in animal cell cytokinesis,* Biophysical Journal **106**, 114 (2014).

[126] A.-C. Reymann, F. Staniscia, A. Erzberger, G. Salbreux, and S. W. Grill, *Cortical flow aligns actin filaments to form a furrow,* eLife (2016).

[127] J. G. White and G. G. Borisy, *J. theor. Biol*, Tech. Rep. (1983).

[128] T. Hiraiwa and G. Salbreux, *Role of Turnover in Active Stress Generation in a Filament Network,* Physical Review Letters **116** (2016).

[129] T. G. Chew, J. Huang, S. Palani, R. Sommese, A. Kamnev, T. Hatano, Y. Gu, S. Oliferenko, S. Sivaramakrishnan, and M. K. Balasubramanian, *Actin turnover maintains actin filament homeostasis during cytokinetic ring contraction,* Journal of Cell Biology **216**, 2657 (2017).

[130] M. M. Swann and J. M. Mitchison, *The mechanism of cleavage in animal cells,* Biological Reviews **33**, 103 (1958).

[131] J. C. Dan, *On the Mechanism of Astral Cleavage,* Physical Zoology **21**, 191 (1948).

[132] L. Wolpert, *The Mechanics and Mechanism of Cleavage,* International Review of Cytology **10** (1960).

[133] D. Marsland, *The mechanisms of cell division, temperature-pressure experiments on the cleaving eggs of arbacia punctulata,* Journal of Cellular and Comparative Physiology **36**, 205 (1950).

[134] M. Yoneda and K. Dan, *J. Exp. Biol*, Tech. Rep. (1972).

[135] R. A. Green, E. Paluch, and K. Oegema, *Cytokinesis in Animal Cells,* Annual Review of Cell and Developmental Biology **28**, 29 (2012).

[136] H. F. Gudejko, L. M. Alford, and D. R. Burgess, *Polar expansion during cytokinesis,* Cytoskeleton **69**, 1000 (2012).

[137] Y.-L. Wang, *The Mechanism of Cytokinesis: Reconsideration and Reconciliation,* Cell structure and function **26**, 633 (2001).

[138] J. Sedzinski, M. Biro, A. Oswald, J. Y. Tinevez, G. Salbreux, and E. Paluch, *Polar actomyosin contractility destabilizes the position of the cytokinetic furrow,* Nature **476**, 462 (2011).

[139] B. Sinha, D. Köster, R. Ruez, P. Gonnord, M. Bastiani, D. Abankwa, R. V. Stan, G. Butler-Browne, B. Vedie, L. Johannes, N. Morone, R. G. Parton, G. Raposo, P. Sens, C. Lamaze, and P. Nassoy, *Cells respond to mechanical stress by rapid disassembly of caveolae,* Cell **144**, 402 (2011).

[140] R. Albertson, B. Riggs, and W. Sullivan, *Membrane traffic: A driving force in cytokinesis,* Trends in Cell Biology **15**, 92 (2005).

[141] S. Asano, K. Hamao, and H. Hosoya, *Direct evidence for roles of phosphorylated regulatory light chain of myosin II in furrow ingression during cytokinesis in HeLa cells,* Genes to Cells **14**, 555 (2009).

[142] D. Bray and J. G. White, *Cortical flow in animal cells,* Science **239**, 883 (1988).

[143] G. H. Koenderink and E. K. Paluch, *Architecture shapes contractility in actomyosin networks,* Current Opinion in Cell Biology **50**, 79 (2018).

[144] I. Mendes Pinto, B. Y. Rubinstein, and R. Li, *Force to divide: Structural and mechanical requirements for actomyosin ring contraction,* Biophysical Journal **105**, 547 (2013).

[145] M. Murrell, P. W. Oakes, M. Lenz, and M. L. Gardel, *Forcing cells into shape: the mechanics of actomyosin contractility,* Nature Reviews Molecular Cell Biology **16**, 486 (2015).

[146] M. P. Murrell and M. L. Gardel, *F-actin buckling coordinates contractility and severing in a biomimetic actomyosin cortex,* Proceedings of the National Academy of Sciences of the United States of America **109**, 20820 (2012).

[147] M. Lenz, T. Thoresen, M. L. Gardel, and A. R. Dinner, *Contractile units in disordered actomyosin bundles arise from f-actin buckling,* Physical Review Letters **108** (2012).

[148] K. Kruse and F. Jülicher, *Actively Contracting Bundles of Polar Filaments,* Physical Review Letters **85**, 1778 (2000).

[149] V. Wollrab, J. M. Belmonte, L. Baldauf, M. Leptin, F. Nédeléc, and G. H. Koenderink, *Polarity sorting drives remodeling of actin-myosin networks,* Journal of Cell Science **132** (2019).

[150] M. Fritzsche, C. Erlenkämper, E. Moeendarbary, G. Charras, and K. Kruse, *Actin kinetics shapes cortical network structure and mechanics,* Science Advances **2** (2016).

[151] H. Berthoumieux, J. L. Maître, C. P. Heisenberg, E. K. Paluch, F. Jülicher, and G. Salbreux, *Active elastic thin shell theory for cellular deformations,* New Journal of Physics **16** (2014).

[152] M. Malik-Garbi, N. Ierushalmi, S. Jansen, E. Abu-Shah, B. L. Goode, A. Mogilner, and K. Keren, *Scaling behaviour in steady-state contracting actomyosin networks,* Nature Physics **15**, 509 (2019).

[153] Sonal, K. A. Ganzinger, S. K. Vogel, J. Mücksch, P. Blumhardt, and P. Schwille, *Myosin-II activity generates a dynamic steady state with continuous actin turnover in a minimal actin cortex,* Journal of Cell Science **132** (2019).

[154] M. Fritzsche, A. Lewalle, T. Duke, K. Kruse, and G. Charras, *Analysis of turnover dynamics of the submembranous actin cortex,* Molecular Biology of the Cell **24**, 757 (2013).

[155] F. B. Robin, W. M. McFadden, B. Yao, and E. M. Munro, *Single-molecule analysis of cell surface dynamics in Caenorhabditis elegans embryos,* Nature Methods **11**, 677 (2014).

[156] P. M. McCall, F. C. MacKintosh, D. R. Kovar, and M. L. Gardel, *Cofilin drives rapid turnover and fluidization of entangled F-actin,* Proceedings of the National Academy of Sciences of the United States of America **116**, 12629 (2019).

[157] S. Arzash, P. M. McCall, J. Feng, M. L. Gardel, and F. C. MacKintosh, *Stress relaxation in F-actin solutions by severing,* Soft Matter **15**, 6300 (2019).

[158] I. Linsmeier, S. Banerjee, P. W. Oakes, W. Jung, T. Kim, and M. P. Murrell, *Disordered actomyosin networks are sufficient to produce cooperative and telescopic contractility,* Nature Communications **7**, 1 (2016).

[159] M. Bovellan, Y. Romeo, M. Biro, A. Boden, P. Chugh, A. Yonis, M. Vaghela, M. Fritzsche, D. Moulding, R. Thorogate, A. Jégou, A. J. Thrasher, G. Romet-Lemonne, P. P. Roux, E. K. Paluch, and G. T. Charras, *Cellular control of cortical actin nucleation,* Current Biology **24**, 1628 (2014).

[160] L. Cao, A. Yonis, M. Vaghela, E. H. Barriga, P. Chugh, M. B. Smith, J. Maufront, G. Lavoie, A. Méant, E. Ferber, M. Bovellan, A. Alberts, A. Bertin, R. Mayor, E. K. Paluch, P. P. Roux, A. Jégou, G. Romet-Lemonne, and G. Charras, *SPIN90 associates with mDia1 and the Arp2/3 complex to regulate cortical actin organization,* Nature cell biology **22**, 803 (2020).

[161] D. Zimmermann, K. E. Homa, G. M. Hocky, L. W. Pollard, E. M. De La Cruz, G. A. Voth, K. M. Trybus, and D. R. Kovar, *Mechanoregulated inhibition of formin facilitates contractile actomyosin ring assembly,* Nature Communications **8**, 1 (2017).

[162] L. Cao, M. Kerleau, E. L. Suzuki, H. Wioland, S. Jouet, B. Guichard, M. Lenz, G. Romet-Lemonne, and A. Jegou, *Modulation of formin processivity by profilin and mechanical tension,* eLife **7**, 1 (2018).

[163] C. Suarez, R. T. Carroll, T. A. Burke, J. R. Christensen, A. J. Bestul, J. A. Sees, M. L. James, V. Sirotkin, and D. R. Kovar, *Profilin regulates F-Actin network homeostasis by favoring formin over Arp2/3 complex,* Developmental Cell **32**, 43 (2015).

[164] S. Shekhar, M. Kerleau, S. Kühn, J. Pernier, G. Romet-Lemonne, A. Jégou, and M. F. Carlier, *Formin and capping protein together embrace the actin filament in a ménage à trois,* Nature Communications **6** (2015).

[165] R. D. Mullins, J. F. Kelleher, J. Xu, and T. D. Pollard, *Arp2/3 complex from Acanthamoeba binds profilin and cross-links actin filaments,* Molecular Biology of the Cell **9**, 841 (1998).

[166] L. Blanchoin, T. D. Pollard, and R. D. Mullins, *Interactions of ADF/cofilin, Arp2/3 complex, capping protein and profilin in remodeling of branched actin filament networks,* Current Biology **10**, 1273 (2000).

[167] V. I. Risca, E. B. Wang, O. Chaudhuri, J. J. Chia, P. L. Geissler, and D. A. Fletcher, *Actin filament curvature biases branching direction,* Proceedings of the National Academy of Sciences of the United States of America **109**, 2913 (2012).

[168] J. V. Abella, C. Galloni, J. Pernier, D. J. Barry, S. Kjær, M. F. Carlier, and M. Way, *Isoform diversity in the Arp2/3 complex determines actin filament dynamics,* Nature Cell Biology **18**, 76 (2016).

[169] M. E. Quinlan, J. E. Heuser, E. Kerkhoff, and R. D. Mullins, *Drosophila Spire is an actin nucleation factor,* Nature **433**, 382 (2005).

[170] C. Chan, C. C. Beltzner, and T. D. Pollard, *Cofilin Dissociates Arp2/3 Complex and Branches from Actin Filaments,* Current Biology **19**, 537 (2009).

[171] T. Kotila, H. Wioland, G. Enkavi, K. Kogan, I. Vattulainen, A. Jégou, G. Romet-Lemonne, and P. Lappalainen, *Mechanism of synergistic actin filament pointed end depolymerization by cyclase-associated protein and cofilin,* Nature Communications **10**, 1 (2019).

[172] S. Jansen, A. Collins, L. Golden, O. Sokolova, and B. L. Goode, *Structure and mechanism of mouse cyclase-associated protein (CAP1) in regulating actin dynamics,* Journal of Biological Chemistry **289**, 30732 (2014).

[173] H. Wioland, A. Jegou, and G. Romet-Lemonne, *Torsional stress generated by ADF/cofilin on cross-linked actin filaments boosts their severing,* Proceedings of the National Academy of Sciences of the United States of America **116**, 2595 (2019).

[174] N. G. Pandit, W. Cao, J. Bibeau, E. M. Johnson-Chavarria, E. W. Taylor, T. D. Pollard, and E. M. De La Cruz, *Force and phosphate release from Arp2/3 complex promote dissociation of actin filament branches,* Proceedings of the National Academy of Sciences of the United States of America **117**, 13519 (2020).

[175] L. van de Cauter, F. Fanalista, L. van Buren, N. D. Franceschi, E. Godino, S. Bouw, C. Danelon, C. Dekker, G. H. Koenderink, and K. A. Ganzinger, *Optimized cDICE for Efficient Reconstitution of Biological Systems in Giant Unilamellar Vesicles,* ACS Synthetic Biology **10**, 1690 (2021).

[176] M. Murrell, L. L. Pontani, K. Guevorkian, D. Cuvelier, P. Nassoy, and C. Sykes, *Spreading dynamics of biomimetic actin cortices,* Biophysical Journal **100**, 1400 (2011).

[177] K. K. K. Carvalho, F.-C. C. Tsai, E. Lees, R. Voituriez, G. H. Koenderink, and C. Sykes, *Cell-sized liposomes reveal how actomyosin cortical tension drives shape change,* Proceedings of the National Academy of Sciences **110**, 16456 (2013).

[178] E. Loiseau, J. A. Schneider, F. C. Keber, C. Pelzl, G. Massiera, G. Salbreux, and A. R. Bausch, *Shape remodeling and blebbing of active cytoskeletal vesicles,* Science Advances **2** (2016).

[179] T. Sakamoto, J. Limouze, C. A. Combs, A. F. Straight, and J. R. Sellers, *Blebbistatin, a myosin II inhibitor, is photoinactivated by blue light,* Biochemistry **44**, 584 (2005).

[180] M. Schuppler, F. C. Keber, M. Krüger, and A. R. Bausch, *Boundaries steer the contraction of active gels,* Nature Communications **7**, 1 (2016).

[181] K. Yamamoto, H. Miura, M. Ishida, S. Sawai, Y. Kondo, and K. Aoki, *Optogenetic relaxation of actomyosin contractility uncovers mechanistic roles of cortical tension during cytokinesis,* bioRxiv , 2021.04.19.440549 (2021).

[182] F. Fanalista, A. Birnie, R. Maan, F. Burla, K. Charles, G. Pawlik, S. Deshpande, G. H. Koenderink, M. Dogterom, and C. Dekker, *Shape and Size Control of Artificial Cells for Bottom-Up Biology,* ACS Nano **13**, 5439 (2019).

[183] J. M. Barrows and E. D. Goley, *FtsZ dynamics in bacterial division: What, how, and why?* Current opinion in cell biology **68**, 163 (2021).

[184] A. W. Lau, A. Prasad, and Z. Dogic, *Condensation of isolated Semi-flexible filaments driven by depletion interactions,* Europhysics Letters **87** (2009).

[185] J. X. Tang, J. A. Käs, J. V. Shah, and P. A. Janmey, *Counterion-induced actin ring formation,* European Biophysics Journal **30**, 477 (2001).

[186] M. Mavrakis, Y. Azou-Gros, F.-C. C. Tsai, J. Alvarado, A. Bertin, F. Iv, A. Kress, S. Brasselet, G. H. Koenderink, and T. Lecuit, *Septins promote F-actin ring formation by crosslinking actin filaments into curved bundles,* Nature Cell Biology **16**, 322 (2014).

[187] M. Kinoshita, C. M. Field, M. L. Coughlin, A. F. Straight, and T. J. Mitchison, *Self- and actin-templated assembly of mammalian septins,* Developmental Cell **3**, 791 (2002).

[188] C. M. Field, M. Coughlin, S. Doberstein, T. Marty, and W. Sullivan, *Characterization of anillin mutants reveals essential roles in septin localization and plasma membrane integrity,* Development **132**, 2849 (2005).

[189] A. J. Piekny and M. Glotzer, *Anillin Is a Scaffold Protein That Links RhoA, Actin, and Myosin during Cytokinesis,* Current Biology **18**, 30 (2008).

[190] A. J. Piekny and A. S. Maddox, *The myriad roles of Anillin during cytokinesis,* Seminars in Cell and Developmental Biology **21**, 881 (2010).

[191] O. Kučera, D. Janda, V. Siahaan, S. H. Dijkstra, E. Pilátová, E. Zatecka, S. Diez, M. Braun, and Z. Lansky, *Anillin propels myosin-independent constriction of actin rings,* Nature Communications **12**, 1 (2021).

[192] S. Palani, S. Ghosh, E. Ivorra-Molla, S. Clarke, A. Suchenko, M. K. Balasubramanian, and D. V. Köster, *Calponin-homology domain mediated bending of membrane-associated actin filaments,* eLife **10**, 1 (2021).

[193] M. Biro, Y. Romeo, S. Kroschwald, M. Bovellan, A. Boden, J. Tcherkezian, P. P. Roux, G. Charras, and E. K. Paluch, *Cell cortex composition and homeostasis resolved by integrating proteomics and quantitative imaging,* Cytoskeleton **70**, 741 (2013).

[194] M. Miyazaki, M. Chiba, H. Eguchi, T. Ohki, and S. Ishiwata, *Cell-sized spherical confinement induces the spontaneous formation of contractile actomyosin rings in vitro,* Nature Cell Biology **17**, 480 (2015).

[195] A. A. Bridges, M. S. Jentzsch, P. W. Oakes, P. Occhipinti, and A. S. Gladfelter, *Micron-scale plasma membrane curvature is recognized by the septin cytoskeleton,* Journal of Cell Biology **213**, 23 (2016).

[196] K. A. Ganzinger, A. Merino-Salomón, D. A. García-Soriano, A. N. Butterfield, T. Litschel, F. Siedler, and P. Schwille, *FtsZ Reorganization Facilitates Deformation of Giant Vesicles in Microfluidic Traps**,* Angewandte Chemie **132**, 21556 (2020).

[197] G. Morrison and D. Thirumalai, *Semiflexible chains in confined spaces,* Physical Review E - Statistical, Nonlinear, and Soft Matter Physics **79**, 1 (2009).

[198] M. Soares E Silva, J. Alvarado, J. Nguyen, N. Georgoulia, B. M. Mulder, and G. H. Koenderink, *Self-organized patterns of actin filaments in cell-sized confinement,* Soft Matter **7**, 10631 (2011).

[199] M. M. Claessens, R. Tharmann, K. Kroy, and A. R. Bausch, *Microstructure and viscoelasticity of confined semiflexible polymer networks,* Nature Physics **2**, 186 (2006).

[200] L. Limozin and E. Sackmann, *Polymorphism of Cross-Linked Actin Networks in Giant Vesicles,* Physical Review Letters **89**, 14 (2002).

[201] M. Adeli Koudehi, D. M. Rutkowski, and D. Vavylonis, *Organization of associating or crosslinked actin filaments in confinement,* Cytoskeleton **76**, 532 (2019).

[202] T. E. Schroeder, *The contractile ring II. Determining its brief existence, volumetric changes, and vital role in cleaving arbacia eggs,* Journal of Cell Biology **53**, 419 (1972).

[203] X. Ma, M. Kovaćs, M. A. Conti, A. Wang, Y. Zhang, J. R. Sellers, and R. S. Adelstein, *Nonmuscle myosin II exerts tension but does not translocate actin in vertebrate cytokinesis,* Proceedings of the National Academy of Sciences of the United States of America **109**, 4509 (2012).

[204] E. M. Reichl, Y. Ren, M. K. Morphew, M. Delannoy, J. C. Effler, K. D. Girard, S. Divi, P. A. Iglesias, S. C. Kuo, and D. N. Robinson, *Interactions between Myosin and Actin Crosslinkers Control Cytokinesis Contractility Dynamics and Mechanics,* Current Biology **18**, 471 (2008).

[205] D. J. Fishkind and Y. L. Wang, *Orientation and three-dimensional organization of actin filaments in dividing cultured cells,* Journal of Cell Biology **123**, 837 (1993).

[206] A. M. Fenix, N. Taneja, C. A. Buttler, J. Lewis, S. B. Van Engelenburg, R. Ohi, and D. T. Burnette, *Expansion and concatenation of nonmuscle myosin IIA filaments drive cellular contractile system formation during interphase and mitosis,* Molecular Biology of the Cell **27**, 1465 (2016).

[207] J. H. Henson, C. E. Ditzler, A. Germain, P. M. Irwin, E. T. Vogt, S. Yang, X. Wu, and C. B. Shuster, *The ultrastructural organization of actin and myosin II filaments in the contractile ring: New support for an old model of cytokinesis,* Molecular Biology of the Cell **28**, 613 (2017).

[208] M. Lenz, *Geometrical origins of contractility in disordered actomyosin networks,* Physical Review X **4**, 041002 (2014).

[209] H. Ennomani, G. Letort, C. Guérin, J. L. Martiel, W. Cao, F. Nédélec, E. M. De La Cruz, M. Théry, L. Blancholn, L. Blanchoin, and L. Blancholn, *Architecture and Connectivity Govern Actin Network Contractility,* Current Biology **26**, 616 (2016).

[210] C. Schwayer, M. Sikora, J. Slováková, R. Kardos, and C. P. Heisenberg, *Actin Rings of Power,* Developmental Cell **37**, 493 (2016).

[211] D. J. Odde, *Mitosis, diffusible crosslinkers, and the ideal gas law,* Cell **160**, 1041 (2015).

[212] S. Chen, T. Markovich, and F. C. MacKintosh, *Motor-free Contractility in Active Gels,* arXiv preprint (2020).

[213] F. Rizzelli, M. G. Malabarba, S. Sigismund, and M. Mapelli, *The crosstalk between microtubules, actin and membranes shapes cell division,* Open biology **10** (2020).

[214] O. M. Lancaster and B. Baum, *Shaping up to divide: coordinating actin and microtubule cytoskeletal remodelling during mitosis,* Seminars in cell & developmental biology **34**, 109 (2014).

[215] F. C. Tsai, A. Bertin, H. Bousquet, J. Manzi, Y. Senju, M. C. Tsai, L. Picas, S. Miserey-Lenkei, P. Lappalainen, E. Lemichez, E. Coudrier, and P. Bassereau, *Ezrin enrichment on curved membranes requires a specific conformation or interaction with a curvature-sensitive partner,* eLife **7**, 1 (2018).

[216] G. A. Quinones, J. Jin, and A. E. Oro, *I-BAR protein antagonism of endocytosis mediates directional sensing during guided cell migration,* Journal of Cell Biology **189**, 353 (2010).

[217] W. Bae, S. Kocabey, and T. Liedl, *DNA nanostructures in vitro, in vivo and on membranes,* Nano Today **26**, 98 (2019).

[218] A. Czogalla, D. J. Kauert, H. G. Franquelim, V. Uzunova, Y. Zhang, R. Seidel, and P. Schwille, *Amphipathic DNA Origami Nanoparticles to Scaffold and Deform Lipid Membrane Vesicles,* Angewandte Chemie International Edition **54**, 6501 (2015).

[219] M. Mishra, J. Kashiwazaki, T. Takagi, R. Srinivasan, Y. Huang, M. K. Balasubramanian, and I. Mabuchi, *In vitro contraction of cytokinetic ring depends on myosin II but not on actin dynamics,* Nature Cell Biology **15**, 853 (2013).

[220] N. D. Franceschi, W. Pezeshkian, A. Fragasso, B. M. Bruininks, S. Tsai, S. J. Marrink, and C. Dekker, *A synthetic membrane shaper for controlled liposome deformation,* bioRxiv , 2021.12.22.473854 (2021).

[221] H. T. McMahon and E. Boucrot, *Membrane curvature at a glance,* Journal of cell science **128**, 1065 (2015).

[222] A. Beber, C. Taveneau, M. Nania, F. C. Tsai, A. Di Cicco, P. Bassereau, D. Lévy, J. T. Cabral, H. Isambert, S. Mangenot, and A. Bertin, *Membrane reshaping by micrometric curvature sensitive septin filaments,* Nature Communications **10**, 1 (2019).

[223] A. V. Taubenberger, B. Baum, and H. K. Matthews, *The Mechanics of Mitotic Cell Rounding,* Frontiers in cell and developmental biology **8** (2020).

[224] M. T. Prospéri, P. Lépine, F. Dingli, P. Paul-Gilloteaux, R. Martin, D. Loew, H. J. Knölker, and E. Coudrier, *Myosin 1b functions as an effector of EphB signaling to control cell repulsion,* The Journal of cell biology **210**, 347 (2015).

[225] G. Russo and M. Krauss, *Septin Remodeling During Mammalian Cytokinesis,* Frontiers in cell and developmental biology **9** (2021).

[226] K. A. Michie, A. Bermeister, N. O. Robertson, S. C. Goodchild, and P. M. Curmi, *Two Sides of the Coin: Ezrin/Radixin/Moesin and Merlin Control Membrane Structure and Contact Inhibition,* International journal of molecular sciences **20** (2019).

[227] M. P. Clausen, H. Colin-York, F. Schneider, C. Eggeling, and M. Fritzsche, *Dissecting the actin cortex density and membrane-cortex distance in living cells by super-resolution microscopy,* Journal of Physics D: Applied Physics **50**, 064002 (2017).

[228] M. T. Swulius, L. T. Nguyen, M. S. Ladinsky, D. R. Ortega, S. Aich, M. Mishra, and G. J. Jensen, *Structure of the fission yeast actomyosin ring during constriction,* Proceedings of the National Academy of Sciences of the United States of America **115**, E1455 (2018).

[229] N. A. McDonald, A. L. Lind, S. E. Smith, R. Li, and K. L. Gould, *Nanoscale architecture of the Schizosaccharomyces pombe contractile ring,* eLife **6** (2017).

[230] B. A. Truong Quang, R. Peters, D. A. Cassani, P. Chugh, A. G. Clark, M. Agnew, G. Charras, and E. K. Paluch, *Extent of myosin penetration within the actin cortex regulates cell surface mechanics,* Nature Communications **12**, 1 (2021).

[231] A. Das, A. Bhat, R. Sknepnek, D. Köster, S. Mayor, and M. Rao, *Stratification relieves constraints from steric hindrance in the generation of compact actomyosin asters at the membrane cortex,* Science Advances **6**, 6093 (2020).

[232] M. P. Sheetz, *Cell control by membrane-cytoskeleton adhesion,* Nature Reviews Molecular Cell Biology **2**, 392 (2001).

[233] A. Paraschiv, T. J. Lagny, C. V. Campos, E. Coudrier, P. Bassereau, and A. Šarić, *Influence of membrane-cortex linkers on the extrusion of membrane tubes,* Biophysical Journal **120**, 598 (2021).

[234] D. Raucher, T. Stauffer, W. Chen, K. Shen, S. Guo, J. D. York, M. P. Sheetz, and T. Meyer, *Phosphatidylinositol 4,5-bisphosphate functions as a second messenger that regulates cytoskeleton-plasma membrane adhesion,* Cell **100**, 221 (2000).

[235] P. A. Janmey, W. Xian, and L. A. Flanagan, *Controlling cytoskeleton structure by phosphoinositide-protein interactions: Phosphoinositide binding protein domains and effects of lipid packing,* Chemistry and Physics of Lipids **101**, 93 (1999).

[236] C. E. Snider, A. H. Willet, J. S. Chen, G. Arpag, M. Zanic, and K. L. Gould, *Phosphoinositide-mediated ring anchoring resists perpendicular forces to promote medial cytokinesis,* Journal of Cell Biology **216**, 3041 (2017).

[237] C. Simon, V. Caorsi, C. Campillo, and C. Sykes, *Interplay between membrane tension and the actin cytoskeleton determines shape changes,* Physical Biology **15** (2018).

[238] R. Shrivastava, D. Köster, S. Kalme, S. Mayor, and M. Neerathilingam, *Tailor-made ezrin actin binding domain to probe its interaction with actin in-vitro,* PLoS ONE **10**, e0123428 (2015).

[239] F. Rico, A. Russek, L. González, H. Grubmüller, and S. Scheuring, *Heterogeneous and rate-dependent streptavidin–biotin unbinding revealed by high-speed force spectroscopy and atomistic simulations,* Proceedings of the National Academy of Sciences of the United States of America **116**, 6594 (2019).

[240] J. A. Nye and J. T. Groves, *Kinetic control of histidine-tagged protein surface density on supported lipid bilayers,* Langmuir **24**, 4145 (2008).

[241] G. Raghunath and R. B. Dyer, *Kinetics of Histidine-Tagged Protein Association to Nickel-Decorated Liposome Surfaces,* Langmuir **35**, 12550 (2019).

[242] R. Grover, J. Fischer, F. W. Schwarz, W. J. Walter, P. Schwille, and S. Diez, *Transport efficiency of membrane-anchored kinesin-1 motors depends on motor density and diffusivity,* Proceedings of the National Academy of Sciences of the United States of America **113**, E7185 (2016).

[243] J. Pernier, R. Kusters, H. Bousquet, T. Lagny, A. Morchain, J. F. Joanny, P. Bassereau, and E. Coudrier, *Myosin 1b is an actin depolymerase,* Nature Communications **10**, 1 (2019).

[244] F. Schneider, D. Waithe, M. P. Clausen, S. Galiani, T. Koller, G. Ozhan, C. Eggeling, and E. Sezgin, *Diffusion of lipids and GPI-anchored proteins in actin-free plasma membrane vesicles measured by STED-FCS,* Molecular Biology of the Cell **28**, 1507 (2017).

[245] F. Heinemann, S. K. Vogel, and P. Schwille, *Lateral Membrane Diffusion Modulated by a Minimal Actin Cortex,* Biophysical Journal **104**, 1465 (2013).

[246] S. K. Vogel, F. Greiss, A. Khmelinskaia, and P. Schwille, *Control of lipid domain organization by a biomimetic contractile actomyosin cortex,* eLife **6** (2017).

[247] D. V. Köster, K. Husain, E. Iljazi, A. Bhat, P. Bieling, R. D. Mullins, M. Rao, and S. Mayor, *Actomyosin dynamics drive local membrane component organization in an in vitro active composite layer,* Proceedings of the National Academy of Sciences of the United States of America **113**, E1645 (2016).

[248] A. Honigmann, S. Sadeghi, J. Keller, S. W. Hell, C. Eggeling, and R. Vink, *A lipid bound actin meshwork organizes liquid phase separation in model membranes,* eLife **2014** (2014).

[249] M. Rao and S. Mayor, *Active organization of membrane constituents in living cells,* Current Opinion in Cell Biology **29**, 126 (2014).

[250] K. Gowrishankar, S. Ghosh, S. Saha, C. Rumamol, S. Mayor, and M. Rao, *Active remodeling of cortical actin regulates spatiotemporal organization of cell surface molecules,* Cell **149**, 1353 (2012).

[251] A. P. Liu and D. A. Fletcher, *Actin polymerization serves as a membrane domain switch in model lipid bilayers,* Biophysical Journal **91**, 4064 (2006).

[252] M. Schön, I. Mey, and C. Steinem, *Influence of cross-linkers on ezrin-bound minimal actin cortices,* Progress in Biophysics and Molecular Biology **144**, 91 (2019).

[253] H. Nöding, M. Schön, C. Reinermann, N. Dörrer, A. Kürschner, B. Geil, I. Mey, C. Heussinger, A. Janshoff, and C. Steinem, *Rheology of Membrane-Attached Minimal Actin Cortices,* Journal of Physical Chemistry B **122**, 4537 (2018).

[254] L. S. Mosby, N. Hundt, G. Young, A. Fineberg, M. Polin, S. Mayor, P. Kukura, and D. V. Köster, *Myosin II Filament Dynamics in Actin Networks Revealed with Interferometric Scattering Microscopy,* Biophysical Journal **118**, 1946 (2020).

[255] A. Szuba, F. Bano, G. Castro Linares, F. Iv, M. Mavrakis, R. P. Richter, A. Bertin, and G. H. Koenderink, *Membrane binding controls ordered self-assembly of animal septins,* eLife **10** (2021).

[256] K. S. Cannon, B. L. Woods, J. M. Crutchley, and A. S. Gladfelter, *An amphipathic helix enables septins to sense micrometer-scale membrane curvature,* Journal of Cell Biology **218**, 1128 (2019).

[257] L. Sun, R. Guan, I. J. Lee, Y. Liu, M. Chen, J. Wang, J. Q. Wu, and Z. Chen, *Mechanistic Insights into the Anchorage of the Contractile Ring by Anillin and Mid1,* Developmental Cell **33**, 413 (2015).

[258] C. F. Schroer, L. Baldauf, L. van Buren, T. A. Wassenaar, M. N. Melo, G. H. Koenderink, and S. J. Marrink, *Charge-dependent interactions of monomeric and filamentous actin with lipid bilayers,* Proceedings of the National Academy of Sciences of the United States of America **117**, 5861 (2020).

[259] S. H. Zigmond, *Formin-induced nucleation of actin filaments,* Current Opinion in Cell Biology **16**, 99 (2004).

[260] S. Romero, C. Le Clainche, D. Didry, C. Egile, D. Pantaloni, and M. F. Carlier, *Formin is a processive motor that requires profilin to accelerate actin assembly and associated ATP hydrolysis,* Cell **119**, 419 (2004).

[261] K. Guevorkian, J. Manzi, L. L. Pontani, F. Brochard-Wyart, and C. Sykes, *Mechanics of Biomimetic Liposomes Encapsulating an Actin Shell,* Biophysical Journal **109**, 2471 (2015).

[262] P. Bleicher, A. Sciortino, and A. R. Bausch, *The dynamics of actin network turnover is self-organized by a growth-depletion feedback,* Scientific Reports **10**, 1 (2020).

[263] M. M. Ng, F. Chang, and D. R. Burgess, *Movement of membrane domains and requirement of membrane signaling molecules for cytokinesis,* Developmental Cell **9**, 781 (2005).

[264] C. Cauvin and A. Echard, *Phosphoinositides: Lipids with informative heads and mastermind functions in cell division,* Biochimica et Biophysica Acta - Molecular and Cell Biology of Lipids **1851**, 832 (2015).

[265] M. R. Logan and C. A. Mandato, *Regulation of the actin cytoskeleton by PIP2 in cytokinesis,* Biology of the Cell **98**, 377 (2006).

[266] K. Emoto and M. Umeda, *Membrane Lipid Control of Cytokinesis,* Cell Structure and Function **26**, 659 (2001).

[267] P. Bassereau, R. Jin, T. Baumgart, M. Deserno, R. Dimova, V. A. Frolov, P. V. Bashkirov, H. Grubmüller, R. Jahn, H. J. Risselada, L. Johannes, M. M. Kozlov, R. Lipowsky, T. J. Pucadyil, W. F. Zeno, J. C. Stachowiak, D. Stamou, A. Breuer, L. Lauritsen, C. Simon, C. Sykes, G. A. Voth, and T. R. Weikl, *The 2018 biomembrane curvature and remodeling roadmap,* Journal of Physics D: Applied Physics **51**, 343001 (2018).

[268] R. Dasgupta, M. S. Miettinen, N. Fricke, R. Lipowsky, and R. Dimova, *The glycolipid GM1 reshapes asymmetric biomembranes and giant vesicles by curvature generation,* Proceedings of the National Academy of Sciences of the United States of America **115**, 5756 (2018).

[269] F. Frey and T. Idema, *More than just a barrier: using physical models to couple membrane shape to cell function,* Soft matter **17**, 3533 (2021).

[270] J. A. Schiel and R. Prekeris, *Membrane dynamics during cytokinesis,* Current Opinion in Cell Biology **25**, 92 (2013).

[271] H. R. Marsden, N. A. Elbers, P. H. H. Bomans, N. A. J. M. Sommerdijk, and A. Kros, *A Reduced SNARE Model for Membrane Fusion,* Angewandte Chemie **121**, 2366 (2009).

[272] T. E. Schroeder, *The origin of cleavage forces in dividing eggs: A mechanism in two steps,* Experimental Cell Research **134**, 231 (1981).

[273] G. K. Wong, P. G. Allen, and D. A. Begg, *Dynamics of filamentous actin organization in the sea urchin egg cortex during early cleavage divisions: Implications for the mechanism of cytokinesis,* Cytoskeleton **36**, 30 (1997).

[274] T. Bhatia, J. Agudo-Canalejo, R. Dimova, and R. Lipowsky, *Membrane Nanotubes Increase the Robustness of Giant Vesicles,* ACS Nano **12**, 4478 (2018).

[275] T. Bhatia, S. Christ, J. Steinkühler, R. Dimova, and R. Lipowsky, *Simple sugars shape giant vesicles into multispheres with many membrane necks,* Soft Matter **16**, 1246 (2020).

[276] K. A. Ganzinger and P. Schwille, *More from less – Bottom-up reconstitution of cell biology*, Journal of Cell Science **132** (2019).

[277] K. Göpfrich, I. Platzman, and J. P. Spatz, *Mastering Complexity: Towards Bottom-up Construction of Multifunctional Eukaryotic Synthetic Cells*, Trends in Biotechnology **36**, 938 (2018).

[278] T. J. Lagny and P. Bassereau, *Bioinspired membrane-based systems for a physical approach of cell organization and dynamics: usefulness and limitations*, Interface Focus **5** (2015).

[279] R. Dimova and C. Marques, *The Giant Vesicle Book*, 1st ed. (CRC Press, 2019).

[280] R. Dimova, *Giant Vesicles and Their Use in Assays for Assessing Membrane Phase State, Curvature, Mechanics, and Electrical Properties*, Annual Review of Biophysics **48**, 93 (2019).

[281] D. Papahadjopoulos and H. K. Kimelberg, *Phospholipid vesicles (liposomes) as models for biological membranes: Their properties and interactions with cholesterol and proteins*, Progress in Surface Science **4**, 141 (1974).

[282] L. R. Montes, A. Alonso, F. M. Goñi, and L. A. Bagatolli, *Giant Unilamellar Vesicles Electroformed from Native Membranes and Organic Lipid Mixtures under Physiological Conditions*, Biophysical Journal **93**, 3548 (2007).

[283] M. Breton, M. Amirkavei, and L. M. Mir, *Optimization of the Electroformation of Giant Unilamellar Vesicles (GUVs) with Unsaturated Phospholipids*, The Journal of Membrane Biology **248**, 827 (2015).

[284] R. Dimova, S. Aranda, N. Bezlyepkina, V. Nikolov, K. A. Riske, and R. Lipowsky, *A practical guide to giant vesicles. Probing the membrane nanoregime via optical microscopy*, Journal of Physics: Condensed Matter **18**, S1151 (2006).

[285] K. S. Horger, D. J. Estes, R. Capone, and M. Mayer, *Films of Agarose Enable Rapid Formation of Giant Liposomes in Solutions of Physiologic Ionic Strength*, Journal of the American Chemical Society **131**, 1810 (2009).

[286] N. L. Mora, J. S. Hansen, Y. Gao, A. A. Ronald, R. Kieltyka, N. Malmstadt, and A. Kros, *Preparation of size tunable giant vesicles from cross-linked dextran(ethylene glycol) hydrogels*, Chemical Communications **50**, 1953 (2014).

[287] P. Hu, S. Li, and N. Malmstadt, *Microfluidic fabrication of asymmetric giant lipid vesicles*, ACS applied materials & interfaces **3**, 1434 (2011).

[288] H. Ito, T. Yamanaka, S. Kato, T. Hamada, M. Takagi, M. Ichikawa, and K. Yoshikawa, *Dynamical formation of lipid bilayer vesicles from lipid-coated droplets across a planar monolayer at an oil/water interface*, Soft Matter **9**, 9539 (2013).

[289] D. Van Swaay and A. Demello, *Microfluidic methods for forming liposomes*, Lab on a Chip **13**, 752 (2013).

[290] K. Funakoshi, H. Suzuki, and S. Takeuchi, *Formation of giant lipid vesiclelike compartments from a planar lipid membrane by a pulsed jet flow,* Journal of the American Chemical Society **129**, 12608 (2007).

[291] J. C. Stachowiak, D. L. Richmond, T. H. Li, A. P. Liu, S. H. Parekh, and D. A. Fletcher, *Unilamellar vesicle formation and encapsulation by microfluidic jetting,* Proceedings of the National Academy of Sciences **105**, 4697 (2008).

[292] D. L. Richmond, E. M. Schmid, S. Martens, J. C. Stachowiak, N. Liska, and D. A. Fletcher, *Forming giant vesicles with controlled membrane composition, asymmetry, and contents,* Proceedings of the National Academy of Sciences of the United States of America **108**, 9431 (2011).

[293] M. C. Blosser, B. G. Horst, and S. L. Keller, *cDICE method produces giant lipid vesicles under physiological conditions of charged lipids and ionic solutions,* Soft Matter **12**, 7364 (2016).

[294] J. Deek, R. Maan, E. Loiseau, and A. R. Bausch, *Reconstitution of composite actin and keratin networks in vesicles,* Soft Matter **14**, 1897 (2018).

[295] F. Keber, E. Loiseau, T. Sanchez, S. DeCamp, L. Giomi, M. Bowick, M. Marchetti, Z. Dogic, and A. Bausch, *Topology and dynamics of active nematic vesicles,* Science **345** (2014).

[296] T. Litschel, B. Ramm, R. Maas, M. Heymann, and P. Schwille, *Beating Vesicles: Encapsulated Protein Oscillations Cause Dynamic Membrane Deformations,* Angewandte Chemie International Edition **57**, 16286 (2018).

[297] J. D. Berry, M. J. Neeson, R. R. Dagastine, D. Y. Chan, and R. F. Tabor, *Measurement of surface and interfacial tension using pendant drop tensiometry,* Journal of Colloid and Interface Science **454**, 226 (2015).

[298] *KNMI - Daggegevens van het weer in Nederland,* .

[299] K. Dürre and A. R. Bausch, *Formation of phase separated vesicles by double layer cDICE,* Soft Matter **15**, 9676 (2019).

[300] L. Song, M. R. Hobaugh, C. Shustak, S. Cheley, H. Bayley, and J. E. Gouaux, *Structure of Staphylococcal α-Hemolysin, a Heptameric Transmembrane Pore,* Science **274**, 1859 (1996).

[301] H. Ostolaza, B. Bartolomé, I. O. de Zárate, F. de la Cruz, and F. M. Goñi, *Release of lipid vesicle contents by the bacterial protein toxin α-haemolysin,* Biochimica et Biophysica Acta (BBA) - Biomembranes **1147**, 81 (1993).

[302] P. H. Kouwer, M. Koepf, V. A. Le Sage, M. Jaspers, A. M. Van Buul, Z. H. Eksteen-Akeroyd, T. Woltinge, E. Schwartz, H. J. Kitto, R. Hoogenboom, S. J. Picken, R. J. Nolte, E. Mendes, and A. E. Rowan, *Responsive biomimetic networks from polyisocyanopeptide hydrogels,* Nature **493**, 651 (2013).

[303] R. B. Lira, J. Steinkühler, R. L. Knorr, R. Dimova, and K. A. Riske, *Posing for a picture: vesicle immobilization in agarose gel,* Scientific Reports **6**, 25254 (2016).

[304] C. Claudet, M. In, and G. Massiera, *Method to disperse lipids as aggregates in oil for bilayers production,* Eur. Phys. J. E **39** (2016).

[305] A. Doerr, E. De Reus, P. Van Nies, M. Van Der Haar, K. Wei, J. Kattan, A. Wahl, and C. Danelon, *Modelling cell-free RNA and protein synthesis with minimal systems,* Physical Biology **16**, 025001 (2019).

[306] H. Saito, Y. Kato, M. Le Berre, A. Yamada, T. Inoue, K. Yosikawa, and D. Baigl, *Time-Resolved Tracking of a Minimum Gene Expression System Reconstituted in Giant Liposomes,* ChemBioChem **10**, 1640 (2009).

[307] T. Sunami, K. Sato, T. Matsuura, K. Tsukada, I. Urabe, and T. Yomo, *Femtoliter compartment in liposomes for in vitro selection of proteins,* Analytical Biochemistry **357**, 128 (2006).

[308] K. Hosoda, T. Sunami, Y. Kazuta, T. Matsuura, H. Suzuki, and T. Yomo, *Quantitative study of the structure of multilamellar giant liposomes as a container of protein synthesis reaction,* Langmuir **24**, 13540 (2008).

[309] S. Ota, S. Yoshizawa, and S. Takeuchi, *Microfluidic Formation of Monodisperse, Cell-Sized, and Unilamellar Vesicles,* Angewandte Chemie International Edition **48**, 6533 (2009).

[310] Y. Shimizu, A. Inoue, Y. Tomari, T. Suzuki, T. Yokogawa, K. Nishikawa, and T. Ueda, *Cell-free translation reconstituted with purified components,* Nature Biotechnology **19**, 751 (2001).

[311] F.-C. Tsai, B. Stuhrmann, and G. H. Koenderink, *Encapsulation of Active Cytoskeletal Protein Networks in Cell-Sized Liposomes,* Langmuir **27**, 10061 (2011).

[312] J. D. Castile and K. M. Taylor, *Factors affecting the size distribution of liposomes produced by freeze–thaw extrusion,* International Journal of Pharmaceutics **188**, 87 (1999).

[313] Y. Yamashita, M. Oka, T. Tanaka, and M. Yamazaki, *A new method for the preparation of giant liposomes in high salt concentrations and growth of protein microcrystals in them,* Biochimica et Biophysica Acta (BBA) - Biomembranes **1561**, 129 (2002).

[314] L. M. Machesky and K. L. Gould, *The Arp2/3 complex: A multifunctional actin organizer,* Current Opinion in Cell Biology **11**, 117 (1999).

[315] D. Pantaloni, R. Boujemaa, D. Didry, P. Gounon, and M. F. Carlier, *The Arp2/3 complex branches filament barbed ends: Functional antagonism with capping proteins,* Nature Cell Biology **2**, 385 (2000).

[316] D. M. Veltman and R. H. Insall, *WASP family proteins: their evolution and its physiological implications,* Molecular biology of the cell **21**, 2880 (2010).

[317] R. Wang and A. E. Carlsson, *How capping protein enhances actin filament growth and nucleation on biomimetic beads,* Physical Biology **12** (2015).

[318] O. Akin and R. D. Mullins, *Capping Protein Increases the Rate of Actin-Based Motility by Promoting Filament Nucleation by the Arp2/3 Complex,* Cell **133**, 841 (2008).

[319] B. J. Jeon, D. T. Nguyen, G. R. Abraham, N. Conrad, D. K. Fygenson, and O. A. Saleh, *Salt-dependent properties of a coacervate-like, self-assembled DNA liquid,* Soft Matter **14**, 7009 (2018).

[320] P.-Y. Bolinger, D. Stamou, and H. Vogel, *An Integrated Self-Assembled Nanofluidic System for Controlled Biological Chemistries,* Angewandte Chemie **120**, 5626 (2008).

[321] K. Y. Lee, S. J. Park, K. A. Lee, S. H. Kim, H. Kim, Y. Meroz, L. Mahadevan, K. H. Jung, T. K. Ahn, K. K. Parker, and K. Shin, *Photosynthetic artificial organelles sustain and control ATP-dependent reactions in a protocellular system,* Nature Biotechnology **36**, 530 (2018).

[322] J. W. Hindley, Y. Elani, C. M. McGilvery, S. Ali, C. L. Bevan, R. V. Law, and O. Ces, *Light-triggered enzymatic reactions in nested vesicle reactors,* Nature Communications **9**, 1 (2018).

[323] R. Phillips, J. Kondev, J. Theriot, H. G. Garcia, and N. Orme, *Physical Biology of the Cell,* Physical Biology of the Cell (2012).

[324] T. E. Miller, T. Beneyton, T. Schwander, C. Diehl, M. Girault, R. McLean, T. Chotel, P. Claus, N. S. Cortina, J. C. Baret, and T. J. Erb, *Light-powered CO2 fixation in a chloroplast mimic with natural and synthetic parts,* Science **368**, 649 (2020).

[325] O. P. Lehtinen, R. W. N. Nugroho, T. Lehtimaa, S. Vierros, P. Hiekkataipale, J. Ruokolainen, M. Sammalkorpi, and M. Österberg, *Effect of temperature, water content and free fatty acid on reverse micelle formation of phospholipids in vegetable oil,* Colloids and Surfaces B: Biointerfaces **160**, 355 (2017).

[326] R. Koynova and B. Tenchov, *Lipids: Phase Transitions,* Wiley Encyclopedia of Chemical Biology , 1 (2008).

[327] K. Karamdad, R. V. Law, J. M. Seddon, N. J. Brooks, and O. Ces, *Preparation and mechanical characterisation of giant unilamellar vesicles by a microfluidic method.* Lab on a chip **15**, 557 (2015).

[328] A. Moga, D. N. Yandrapalli, D. R. Dimova, D. T. Robinson, N. Yandrapalli, R. Dimova, and T. Robinson, *Optimization of the Inverted Emulsion Method for High-Yield Production of Biomimetic Giant Unilamellar Vesicles,* Chembiochem **20**, 2674 (2019).

[329] M. Schaich, D. Sobota, H. Sleath, J. Cama, and U. F. Keyser, *Characterization of lipid composition and diffusivity in OLA generated vesicles,* Biochimica et Biophysica Acta (BBA) - Biomembranes **1862**, 183359 (2020).

[330] D. Garenne, A. Libchaber, and V. Noireaux, *Membrane molecular crowding enhances MreB polymerization to shape synthetic cells from spheres to rods,* Proceedings of the National Academy of Sciences of the United States of America **117**, 1902 (2020).

[331] Rayleigh Lord VI., *On the Capillary Phenomena of Jets,* Proceedings of the Royal Society of London **117**, 1902 (1879).

[332] P. B. Stranges, M. Palla, S. Kalachikov, J. Nivala, M. Dorwart, A. Trans, S. Kumar, M. Porel, M. Chien, C. Tao, I. Morozova, Z. Li, S. Shi, A. Aberra, C. Arnold, A. Yang, A. Aguirre, E. T. Harada, D. Korenblum, J. Pollard, A. Bhat, D. Gremyachinskiy, A. Bibillo, R. Chen, R. Davis, J. J. Russo, C. W. Fuller, S. Roever, J. Ju, and G. M. Church, *Design and characterization of a nanopore-coupled polymerase for single-molecule DNA sequencing by synthesis on an electrode array,* Proceedings of the National Academy of Sciences of the United States of America **113**, E6749 (2016).

[333] J. Canny, *A Computational Approach to Edge Detection,* IEEE Transactions on Pattern Analysis and Machine Intelligence **PAMI-8**, 679 (1986).

[334] P. Virtanen, R. Gommers, T. E. Oliphant, M. Haberland, T. Reddy, D. Cournapeau, E. Burovski, P. Peterson, W. Weckesser, J. Bright, S. J. van der Walt, M. Brett, J. Wilson, K. J. Millman, N. Mayorov, A. R. Nelson, E. Jones, R. Kern, E. Larson, C. J. Carey, l. Polat, Y. Feng, E. W. Moore, J. VanderPlas, D. Laxalde, J. Perktold, R. Cimrman, I. Henriksen, E. A. Quintero, C. R. Harris, A. M. Archibald, A. H. Ribeiro, F. Pedregosa, P. van Mulbregt, A. Vijaykumar, A. P. Bardelli, A. Rothberg, A. Hilboll, A. Kloeckner, A. Scopatz, A. Lee, A. Rokem, C. N. Woods, C. Fulton, C. Masson, C. Häggström, C. Fitzgerald, D. A. Nicholson, D. R. Hagen, D. V. Pasechnik, E. Olivetti, E. Martin, E. Wieser, F. Silva, F. Lenders, F. Wilhelm, G. Young, G. A. Price, G. L. Ingold, G. E. Allen, G. R. Lee, H. Audren, I. Probst, J. P. Dietrich, J. Silterra, J. T. Webber, J. Slavič, J. Nothman, J. Buchner, J. Kulick, J. L. Schönberger, J. V. de Miranda Cardoso, J. Reimer, J. Harrington, J. L. C. Rodríguez, J. Nunez-Iglesias, J. Kuczynski, K. Tritz, M. Thoma, M. Newville, M. Kümmerer, M. Bolingbroke, M. Tartre, M. Pak, N. J. Smith, N. Nowaczyk, N. Shebanov, O. Pavlyk, P. A. Brodtkorb, P. Lee, R. T. McGibbon, R. Feldbauer, S. Lewis, S. Tygier, S. Sievert, S. Vigna, S. Peterson, S. More, T. Pudlik, T. Oshima, T. J. Pingel, T. P. Robitaille, T. Spura, T. R. Jones, T. Cera, T. Leslie, T. Zito, T. Krauss, U. Upadhyay, Y. O. Halchenko, and Y. Vázquez-Baeza, *SciPy 1.0: fundamental algorithms for scientific computing in Python,* Nature Methods **17**, 261 (2020).

[335] S. Van Der Walt, J. L. Schönberger, J. Nunez-Iglesias, F. Boulogne, J. D. Warner, N. Yager, E. Gouillart, and T. Yu, *Scikit-image: Image processing in python,* PeerJ **2014**, e453 (2014).

[336] P. Van Nies, A. S. Canton, Z. Nourian, and C. Danelon, *Monitoring mRNA and Protein Levels in Bulk and in Model Vesicle-Based Artificial Cells,* Methods in Enzymology **550**, 187 (2015).

[337] D. Blanken, P. Van Nies, and C. Danelon, *Quantitative imaging of gene-expressing liposomes reveals rare favorable phenotypes,* Physical Biology **16**, 045002 (2019).

[338] C. E. Aitken, R. A. Marshall, and J. D. Puglisi, *An oxygen scavenging system for improvement of dye stability in single-molecule fluorescence experiments,* Biophysical journal **94**, 1826 (2008).

[339] P. Méléard, L. A. Bagatolli, and T. Pott, *Giant Unilamellar Vesicle Electroformation: From Lipid Mixtures to Native Membranes Under Physiological Conditions,* Methods in Enzymology **465**, 161 (2009).

[340] Q. Li, X. Wang, S. Ma, Y. Zhang, and X. Han, *Electroformation of giant unilamellar vesicles in saline solution,* Colloids and Surfaces B: Biointerfaces **147**, 368 (2016).

[341] J. Henriksen, A. C. Rowat, and J. H. Ipsen, *Vesicle fluctuation analysis of the effects of sterols on membrane bending rigidity,* European Biophysics Journal **33**, 732 (2004).

[342] S. Pautot, B. Frisken, D. Weitz, and T. Lubensky, *Engineering asymmetric vesicles,* PNAS **100**, 10718 (2003).

[343] Y. Elani, S. Purushothaman, P. J. Booth, J. M. Seddon, N. J. Brooks, R. V. Law, and O. Ces, *Measurements of the effect of membrane asymmetry on the mechanical properties of lipid bilayers,* Chemical Communications **51**, 6976 (2015).

[344] S. L. Veatch and S. L. Keller, *Separation of Liquid Phases in Giant Vesicles of Ternary Mixtures of Phospholipids and Cholesterol,* Biophysical Journal **85**, 3074 (2003).

[345] K. Göpfrich, B. Haller, O. Staufer, Y. Dreher, U. Mersdorf, I. Platzman, and J. P. Spatz, *One-Pot Assembly of Complex Giant Unilamellar Vesicle-Based Synthetic Cells,* ACS Synthetic Biology **8**, 937 (2019).

[346] D. Needham and R. S. Nunn, *Elastic deformation and failure of lipid bilayer membranes containing cholesterol,* Biophysical Journal **58**, 997 (1990).

[347] D. Scherfeld, N. Kahya, and P. Schwille, *Lipid Dynamics and Domain Formation in Model Membranes Composed of Ternary Mixtures of Unsaturated and Saturated Phosphatidylcholines and Cholesterol,* Biophysical Journal **85**, 3758 (2003).

[348] P. Cicuta, S. L. Keller, and S. L. Veatch, *Diffusion of Liquid Domains in Lipid Bilayer Membranes,* Journal of Physical Chemistry B **111**, 3328 (2007).

[349] Y. Tamba and M. Yamazaki, *Single Giant Unilamellar Vesicle Method Reveals Effect of Antimicrobial Peptide Magainin 2 on Membrane Permeability,* Biochemistry **44**, 15823 (2005).

[350] R. B. Lira, R. Dimova, and K. A. Riske, *Giant Unilamellar Vesicles Formed by Hybrid Films of Agarose and Lipids Display Altered Mechanical Properties,* Biophysical Journal **107**, 1609 (2014).

[351] V. Girish, J. Pazzi, A. Li, and A. B. Subramaniam, *Fabrics of Diverse Chemistries Promote the Formation of Giant Vesicles from Phospholipids and Amphiphilic Block Copolymers,* Langmuir **35**, 9264 (2019).

[352] J. Pazzi, M. Xu, and A. B. Subramaniam, *Size Distributions and Yields of Giant Vesicles Assembled on Cellulose Papers and Cotton Fabric,* Langmuir **35**, 7798 (2019).

[353] J. Pazzi and A. B. Subramaniam, *Nanoscale Curvature Promotes High Yield Spontaneous Formation of Cell-Mimetic Giant Vesicles on Nanocellulose Paper,* ACS Applied Materials & Interfaces **12**, 56549 (2020).

[354] T. Pott, H. Bouvrais, and P. Méléard, *Giant unilamellar vesicle formation under physiologically relevant conditions,* Chemistry and Physics of Lipids **154**, 115 (2008).

[355] E. Rideau, F. R. Wurm, and K. Landfester, *Self-Assembly of Giant Unilamellar Vesicles by Film Hydration Methodologies,* Advanced Biosystems **3**, 1800324 (2019).

[356] G. Zhang and J. Sun, *Lipid in Chips: A Brief Review of Liposomes Formation by Microfluidics,* International Journal of Nanomedicine **16**, 7391 (2021).

[357] Y. Ai, R. Xie, J. Xiong, and Q. Liang, *Microfluidics for Biosynthesizing: from Droplets and Vesicles to Artificial Cells,* Small **16**, 1903940 (2020).

[358] P. Supramaniam, O. Ces, and A. Salehi-Reyhani, *Microfluidics for Artificial Life: Techniques for Bottom-Up Synthetic Biology,* Micromachines **10**, 299 (2019).

[359] N. H. Wubshet, Y. Bashirzadeh, and A. P. Liu, *Fascin-induced actin protrusions are suppressed by dendritic networks in giant unilamellar vesicles,* Molecular Biology of the Cell **32**, 1634 (2021).

[360] J. R. Silvius, *Thermotropic phase transitions of pure lipids in model membranes and their modifications by membrane proteins,* Lipid-protein interactions **2**, 239 (1982).

[361] Avanti Lipids, *Phospholipid profile,* .

[362] J. Steinkühler, J. Agudo-Canalejo, R. Lipowsky, and R. Dimova, *Modulating Vesicle Adhesion by Electric Fields,* Biophysical Journal **111**, 1454 (2016).

[363] H. Nakayama, T. Mitsui, M. Nishihara, and M. Kito, *Relation between growth temperature of E. coli and phase transition temperatures of its cytoplasmic and outer membranes,* Biochimica et Biophysica Acta (BBA) - Biomembranes **601**, 1 (1980).

[364] M. Souissi, J. Pernier, O. Rossier, G. Giannone, C. Le Clainche, E. Helfer, and K. Sengupta, *Integrin-Functionalised Giant Unilamellar Vesicles via Gel-Assisted Formation: Good Practices and Pitfalls,* International Journal of Molecular Sciences **22**, 6335 (2021).

[365] T. Dao, M. Fauquignon, F. Fernandes, E. Ibarboure, A. Vax, M. Prieto, and J. F. Le Meins, *Membrane properties of giant polymer and lipid vesicles obtained by electroformation and pva gel-assisted hydration methods,* Colloids and Surfaces A: Physicochemical and Engineering Aspects **533**, 347 (2017).

[366] B. L. Woods and A. S. Gladfelter, *The state of the septin cytoskeleton from assembly to function,* Current opinion in cell biology **68**, 105 (2021).

[367] E. T. Spiliotis and M. A. McMurray, *Masters of asymmetry - lessons and perspectives from 50 years of septins,* Molecular biology of the cell **31**, 2289 (2020).

[368] M. Kuzmić, G. Castro Linares, J. Leischner Fialová, F. Iv, D. Salaün, A. Llewellyn, M. Gomes, M. Belhabib, Y. Liu, K. Asano, M. Rodrigues, D. Isnardon, T. Tachibana, G. H. Koenderink, A. Badache, M. Mavrakis, and P. Verdier-Pinard, *Septin-microtubule association via a motif unique to isoform 1 of septin 9 tunes stress fibers,* Journal of Cell Science **135** (2022).

[369] D. Lobato-Márquez, J. Xu, G. Ö. Güler, A. Ojiakor, M. Pilhofer, and S. Mostowy, *Mechanistic insight into bacterial entrapment by septin cage reconstitution,* Nature communications **12** (2021).

[370] F. Iv, C. S. Martins, G. Castro-Linares, C. Taveneau, P. Barbier, P. Verdier-Pinard, L. Camoin, S. Audebert, F. C. Tsai, L. Ramond, A. Llewellyn, M. Belhabib, K. Nakazawa, A. Di Cicco, R. Vincentelli, J. Wenger, S. Cabantous, G. H. Koenderink, A. Bertin, and M. Mavrakis, *Insights into animal septins using recombinant human septin octamers with distinct SEPT9 isoforms,* Journal of cell science **134** (2021).

[371] M. Kelkar, P. Bohec, and G. Charras, *Mechanics of the cellular actin cortex: From signalling to shape change,* Current opinion in cell biology **66**, 69 (2020).

[372] J. Saarikangas, H. Zhao, and P. Lappalainen, *Regulation of the actin cytoskeleton-plasma membrane interplay by phosphoinositides,* Physiological reviews **90**, 259 (2010).

[373] J. A. Brill, R. Wong, and A. Wilde, *Phosphoinositide Function in Cytokinesis,* Current Biology **21**, R930 (2011).

[374] A. Beber, M. Alqabandi, C. Prévost, F. Viars, D. Lévy, P. Bassereau, A. Bertin, and S. Mangenot, *Septin-based readout of PI(4,5)P2 incorporation into membranes of giant unilamellar vesicles,* Cytoskeleton **76**, 92 (2019).

[375] C. F. Kelley, T. Litschel, S. Schumacher, D. Dedden, P. Schwille, and N. Mizuno, *Phosphoinositides regulate force-independent interactions between talin, vinculin, and actin,* eLife **9**, 1 (2020).

[376] S. Shukla, R. Jin, J. Robustelli, Z. E. Zimmerman, and T. Baumgart, *PIP2 Reshapes Membranes through Asymmetric Desorption,* Biophysical Journal **117**, 962 (2019).

[377] D. Drabik, J. Doskocz, and M. Przybyło, *Effects of electroformation protocol parameters on quality of homogeneous GUV populations,* Chemistry and Physics of Lipids **212**, 88 (2018).

[378] Z. Boban, I. M. Mardesic, W. K. Subczynski, M. Raguz, J. Koty´nska, K. Koty´nska, and M. Naumowicz, *Giant Unilamellar Vesicle Electroformation: What to Use, What to Avoid, and How to Quantify the Results,* Membranes **11**, 860 (2021).

[379] J. Peruzzi, M. G. Gutierrez, K. Mansfield, and N. Malmstadt, *Dynamics of Hydrogel-Assisted Giant Unilamellar Vesicle Formation from Unsaturated Lipid Systems,* Langmuir **32**, 12702 (2016).

[380] B. Kubsch, T. Robinson, J. Steinkühler, and R. Dimova, *Phase Behavior of Charged Vesicles Under Symmetric and Asymmetric Solution Conditions Monitored with Fluorescence Microscopy,* Journal of Visualized Experiments : JoVE **2017**, 56034 (2017).

[381] Y. Zhou, C. K. Berry, P. A. Storer, and R. M. Raphael, *Peroxidation of polyunsaturated phosphatidyl-choline lipids during electroformation,* Biomaterials **28**, 1298 (2007).

[382] E. Parigoris, D. L. Dunkelmann, A. Murphy, N. Wili, A. Kaech, C. Dumrese, N. Jimenez-Rojo, and U. Silvan, *Facile generation of giant unilamellar vesicles using polyacrylamide gels,* Scientific Reports **10**, 1 (2020).

[383] N. Dolder, P. Müller, and C. von Ballmoos, *Experimental platform for the functional investigation of membrane proteins in giant unilamellar vesicles,* bioRxiv , 2021.12.22.473796 (2021).

[384] M. Morita and N. Noda, *Membrane Shape Dynamics-Based Analysis of the Physical Properties of Giant Unilamellar Vesicles Prepared by Inverted Emulsion and Hydration Techniques,* Langmuir **37**, 2268 (2021).

[385] P. M. Shaklee, S. Semrau, M. Malkus, S. Kubick, M. Dogterom, and T. Schmidt, *Protein Incorporation in Giant Lipid Vesicles under Physiological Conditions,* ChemBioChem **11**, 175 (2010).

[386] L. M. Dominak and C. D. Keating, *Polymer encapsulation within giant lipid vesicles,* Langmuir **23**, 7148 (2007).

[387] L. M. Dominak and C. D. Keating, *Macromolecular crowding improves polymer encapsulation within giant lipid vesicles,* Langmuir **24**, 13565 (2008).

[388] D. J. Estes and M. Mayer, *Giant liposomes in physiological buffer using electroformation in a flow chamber,* Biochimica et Biophysica Acta (BBA) - Biomembranes **1712**, 152 (2005).

[389] T. Robinson, P. Kuhn, K. Eyer, and P. S. Dittrich, *Microfluidic trapping of giant unilamellar vesicles to study transport through a membrane pore,* Biomicrofluidics **7** (2013).

[390] N. Yandrapalli, J. Petit, O. Bäumchen, and T. Robinson, *Surfactant-free production of biomimetic giant unilamellar vesicles using PDMS-based microfluidics,* Communications Chemistry **4**, 1 (2021).

[391] M. Chiba, M. Miyazaki, and S. Ishiwata, *Quantitative Analysis of the Lamellarity of Giant Liposomes Prepared by the Inverted Emulsion Method,* Biophysical Journal **107**, 346 (2014).

[392] S. G. Baldursdottir, M. S. Fullerton, S. H. Nielsen, and L. Jorgensen, *Adsorption of proteins at the oil/water interface—Observation of protein adsorption by interfacial shear stress measurements,* Colloids and Surfaces B: Biointerfaces **79**, 41 (2010).

[393] D. E. Evans and M. C. Sheehan, *Don't Be Fobbed Off: The Substance of Beer Foam—A Review,* Journal of the American Society of Brewing Chemists **60**, 47 (2002).

[394] V. Mitropoulos, A. Mütze, and P. Fischer, *Mechanical properties of protein adsorption layers at the air/water and oil/water interface: A comparison in light of the thermodynamical stability of proteins,* Advances in Colloid and Interface Science **206**, 195 (2014).

[395] J. R. Lu, T. J. Su, and R. K. Thomas, *Structural Conformation of Bovine Serum Albumin Layers at the Air–Water Interface Studied by Neutron Reflection,* Journal of Colloid and Interface Science **213**, 426 (1999).

[396] C. Gicquaud, J. P. Chauvet, G. Grenier, P. Tancrède, and G. Coulombe, *Adsorption of actin at the air-water interface: a monolayer study,* Biopolymers **70**, 289 (2003).

[397] T. Le Bihan, D. Pelletier, P. Tancrède, B. Heppell, J. P. Chauvet, and C. R. Gicquaud, *Effect of the polar headgroup of phospholipids on their interaction with actin,* Journal of Colloid and Interface Science **288**, 88 (2005).

[398] C. Gicquaud, J. P. Chauvet, and P. Tancrède, *Surface film pressure of actin: interactions with lipids in mixed monolayers,* Biochemical and biophysical research communications **308**, 995 (2003).

[399] H. Du, P. Chandaroy, and S. W. Hui, *Grafted poly-(ethylene glycol) on lipid surfaces inhibits protein adsorption and cell adhesion,* Biochimica et Biophysica Acta (BBA) - Biomembranes **1326**, 236 (1997).

[400] A. Renault, P. F. Lenne, C. Zakri, A. Aradian, C. Vénien-Bryan, and F. Amblard, *Surface-Induced Polymerization of Actin,* Biophysical Journal **76**, 1580 (1999).

[401] P. Stano, T. de Souza, P. Carrara, E. Altamura, E. D'Aguanno, M. Caputo, P. Luisi, and F. Mavelli, *Recent Biophysical Issues About the Preparation of Solute-Filled Lipid Vesicles,* Mechanics of Advanced Materials and Structures **22**, 748 (2015).

[402] S. Deshpande and C. Dekker, *On-chip microfluidic production of cell-sized liposomes,* Nature Protocols **13**, 856 (2018).

[403] S. M. Koning, M. G. Elferink, W. N. Konings, and A. J. Driessen, *Cellobiose uptake in the hyperthermophilic archaeon Pyrococcus furiosus is mediated by an inducible, high-affinity ABC transporter,* Journal of Bacteriology **183**, 4979 (2001).

[404] D. Needham and E. Evans, *Structure and Mechanical Properties of Giant Lipid (DMPC) Vesicle Bilayers from 20 °C below to 10 °C above the Liquid Crystal-Crystalline Phase Transition at 24 °Ct,* Biochemistry **27**, 34 (1988).

[405] I. Rasnik, S. A. McKinney, and T. Ha, *Nonblinking and long-lasting single-molecule fluorescence imaging,* Nature Methods **3**, 891 (2006).

[406] B. S. Gentry, S. Van Der Meulen, P. Noguera, B. Alonso-Latorre, J. Plastino, and G. H. Koenderink, *Multiple actin binding domains of Ena/VASP proteins determine actin network stiffening,* European biophysics journal : EBJ **41**, 979 (2012).

[407] L. van Buren, G. H. Koenderink, and C. Martinez-Torres, *DisGUVery: a versatile open-source software for high-throughput image analysis of Giant Unilamellar Vesicles,* bioRxiv , 2022.01.25.477663 (2022).

[408] Q. Ruan, M. A. Cheng, M. Levi, E. Gratton, and W. W. Mantulin, *Spatial-Temporal Studies of Membrane Dynamics: Scanning Fluorescence Correlation Spectroscopy (SFCS),* Biophysical Journal **87**, 1260 (2004).

[409] H.-J. Kaiser, D. Lingwood, I. Levental, J. L. Sampaio, L. Kalvodova, L. Rajendran, and K. Simons, *Order of lipid phases in model and plasma membranes,* Proceedings of the National Academy of Sciences **106**, 16645 (2009).

[410] L. A. Bagatolli and E. Gratton, *A Correlation between Lipid Domain Shape and Binary Phospholipid Mixture Composition in Free Standing Bilayers: A Two-Photon Fluorescence Microscopy Study,* Biophysical Journal **79**, 434 (2000).

[411] P. Cicuta, S. L. Keller, and S. L. Veatch, *Diffusion of Liquid Domains in Lipid Bilayer Membranes,* Journal of Physical Chemistry B **111**, 3328 (2007).

[412] T. Wollert, C. Wunder, J. Lippincott-Schwartz, and J. H. Hurley, *Membrane scission by the ESCRT-III complex,* Nature **458**, 172 (2009).

[413] T. Tanaka and M. Yamazaki, *Membrane Fusion of Giant Unilamellar Vesicles of Neutral Phospholipid Membranes Induced by La3+,* Langmuir **20**, 5160 (2004).

[414] Z. Abil and C. Danelon, *Roadmap to Building a Cell: An Evolutionary Approach,* Frontiers in Bioengineering and Biotechnology **0**, 927 (2020).

[415] Z. Nourian, W. Roelofsen, and C. Danelon, *Triggered Gene Expression in Fed-Vesicle Microreactors with a Multifunctional Membrane,* Angewandte Chemie International Edition **51**, 3114 (2012).

[416] N.-N. Deng, M. A. Vibhute, L. Zheng, H. Zhao, M. Yelleswarapu, and W. T. S. Huck, *Macromolecularly Crowded Protocells from Reversibly Shrinking Monodisperse Liposomes,* Journal of the American Chemical Society **140**, 7399 (2018).

[417] S. Maktabi, J. W. Schertzer, and P. R. Chiarot, *Dewetting-induced formation and mechanical properties of synthetic bacterial outer membrane models (GUVs) with controlled inner-leaflet lipid composition,* Soft Matter **15**, 3938 (2019).

[418] K. Karamdad, R. V. Law, J. M. Seddon, N. J. Brooks, and O. Ces, *Studying the effects of asymmetry on the bending rigidity of lipid membranes formed by microfluidics,* Chemical Communications **52**, 5277 (2016).

[419] P. Girard, J. Pécréaux, G. Lenoir, P. Falson, J. L. Rigaud, and P. Bassereau, *A New Method for the Reconstitution of Membrane Proteins into Giant Unilamellar Vesicles,* Biophysical Journal **87**, 419 (2004).

[420] H. R. Vutukuri, M. Hoore, C. Abaurrea-Velasco, L. van Buren, A. Dutto, T. Auth, D. A. Fedosov, G. Gompper, and J. Vermant, *Active particles induce large shape deformations in giant lipid vesicles,* Nature **586**, 52 (2020).

[421] J. García-Calvo, J. Maillard, I. Fureraj, K. Strakova, A. Colom, V. Mercier, A. Roux, E. Vauthey, N. Sakai, A. Fürstenberg, and S. Matile, *Fluorescent Membrane Tension Probes for Super-Resolution Microscopy: Combining Mechanosensitive Cascade Switching with Dynamic-Covalent Ketone Chemistry,* Journal of the American Chemical Society **142**, 12034 (2020).

[422] K. Sato, K. Obinata, T. Sugawara, I. Urabe, and T. Yomo, *Quantification of structural properties of cell-sized individual liposomes by flow cytometry,* Journal of Bioscience and Bioengineering **102**, 171 (2006).

[423] M. V. Gudheti, M. Mlodzianoski, and S. T. Hess, *Imaging and Shape Analysis of GUVs as Model Plasma Membranes: Effect of Trans DOPC on Membrane Properties,* Biophysical Journal **93**, 2011 (2007).

[424] O. Staufer, S. Antona, D. Zhang, J. Csatári, M. Schröter, J. W. Janiesch, S. Fabritz, I. Berger, I. Platzman, and J. P. Spatz, *Microfluidic production and characterization of biofunctionalized giant unilamellar vesicles for targeted intracellular cargo delivery,* Biomaterials **264**, 120203 (2021).

[425] C. A. Schneider, W. S. Rasband, and K. W. Eliceiri, *NIH Image to ImageJ: 25 years of image analysis,* Nature Methods **9**, 671 (2012).

[426] C. McQuin, A. Goodman, V. Chernyshev, L. Kamentsky, B. A. Cimini, K. W. Karhohs, M. Doan, L. Ding, S. M. Rafelski, D. Thirstrup, W. Wiegraebe, S. Singh, T. Becker, J. C. Caicedo, and A. E. Carpenter, *CellProfiler 3.0: Next-generation image processing for biology,* PLoS Biology **16** (2018).

[427] E. Hermann, S. Bleicken, Y. Subburaj, and A. J. García-Sáez, *Automated analysis of giant unilamellar vesicles using circular Hough transformation,* Bioinformatics **30**, 1747 (2014).

[428] T. Sych, T. Schubert, R. Vauchelles, J. Madl, R. Omidvar, R. Thuenauer, L. Richert, Y. Mély, and W. Römer, *GUV-AP: multifunctional FIJI-based tool for quantitative image analysis of Giant Unilamellar Vesicles,* Bioinformatics **35**, 2340 (2019).

[429] I.-H. Lee, S. Passaro, S. Ozturk, and W. Wang, *Intelligent Fluorescence Image Analysis of Giant Unilamellar Vesicles and Protein Liquid Phase Droplets by Whole Z-stack Analysis,* Preprint, available at Research Square (2021).

[430] Y. F. Barooji, A. Rørvig-Lund, S. Semsey, S. N. S. Reihani, and P. M. Bendix, *Dynamics of membrane nanotubes coated with I-BAR,* Scientific Reports **6**, 1 (2016).

[431] K. R. Levental and I. Levental, *Giant Plasma Membrane Vesicles: Models for Understanding Membrane Organization,* Current Topics in Membranes **75**, 25 (2015).

[432] I. R. Sudji, Y. Subburaj, N. Frenkel, A. J. García-Sáez, and M. Wink, *Membrane Disintegration Caused by the Steroid Saponin Digitonin Is Related to the Presence of Cholesterol,* Molecules **20**, 20146 (2015).

[433] B. Mattei, R. B. Lira, K. R. Perez, and K. A. Riske, *Membrane permeabilization induced by Triton X-100: The role of membrane phase state and edge tension,* Chemistry and Physics of Lipids **202**, 28 (2017).

[434] K. Nishimura, T. Matsuura, K. Nishimura, T. Sunami, H. Suzuki, and T. Yomo, *Cell-free protein synthesis inside giant unilamellar vesicles analyzed by flow cytometry,* Langmuir **28**, 8426 (2012).

[435] R. O. Duda and P. E. Hart, *Use of the Hough transformation to detect lines and curves in pictures,* Communications of the ACM **15**, 11 (1972).

[436] R. Brunelli, *Template Matching Techniques in Computer Vision: Theory and Practice* (John Wiley and Sons, Ltd, 2009).

[437] J. D. Foley and A. Van Dam, *Fundamentals of interactive computer graphics* (Addison-Wesley Longman Publishing Co., Inc., 1982).

[438] N. Chinchor, *MUC-4 evaluation metrics,* 4th Message Understanding Conference, MUC 1992 - Proceedings , 22 (1992).

[439] D. Chicco and G. Jurman, *The advantages of the Matthews correlation coefficient (MCC) over F1 score and accuracy in binary classification evaluation,* BMC Genomics **21**, 1 (2020).

[440] S. M. Bartelt, E. Chervyachkova, J. Ricken, and S. V. Wegner, *Mimicking Adhesion in Minimal Synthetic Cells,* Advanced Biosystems **3**, 1800333 (2019).

[441] X. Wang, L. Tian, H. Du, M. Li, W. Mu, B. W. Drinkwater, X. Han, and S. Mann, *Chemical communication in spatially organized protocell colonies and protocell/living cell micro-arrays,* Chemical Science **10**, 9446 (2019).

[442] M. Sobrinos-Sanguino, S. Zorrilla, C. D. Keating, B. Monterroso, and G. Rivas, *Encapsulation of a compartmentalized cytoplasm mimic within a lipid membrane by microfluidics,* Chemical Communications **53**, 4775 (2017).

[443] D. A. Ramirez-Diaz, A. Merino-Salomón, F. Meyer, M. Heymann, G. Rivas, M. Bramkamp, and P. Schwille, *FtsZ induces membrane deformations via torsional stress upon GTP hydrolysis,* Nature Communications **12**, 1 (2021).

[444] A. P. Liu, D. L. Richmond, L. Maibaum, S. Pronk, P. L. Geissler, and D. A. Fletcher, *Membrane-induced bundling of actin filaments,* Nature Physics **4**, 789 (2008).

[445] M. Amaro, F. Reina, M. Hof, C. Eggeling, and E. Sezgin, *Laurdan and Di-4-ANEPPDHQ probe different properties of the membrane,* Journal of Physics D: Applied Physics **50**, 134004 (2017).

[446] C. Kimme, D. Ballard, and J. Sklansky, *Finding circles by an array of accumulators,* Communications of the ACM **18**, 120 (1975).

[447] G. Bradski, *The OpenCV Library,* Dr. Dobb's Journal of Software Tools (2000).

[448] C. Martinez-Torres, F. Burla, C. Alkemade, and G. H. Koenderink, *Revealing the assembly of filamentous proteins with scanning transmission electron microscopy,* PLOS ONE **14**, e0226277 (2019).

[449] C. E. Martinez-Torres, B. Laperrousaz, L. Berguiga, E. Boyer-Provera, J. Elezgaray, F. E. N. M.D., V. Maguer-Satta, A. Arneodo, and F. Argoul, *Deciphering the internal complexity of living cells with quantitative phase microscopy: a multiscale approach,* Journal of Biomedical Optics **20**, 096005 (2015).

[450] J. Alvarado and G. H. Koenderink, *Reconstituting cytoskeletal contraction events with biomimetic actin–myosin active gels,* Methods in Cell Biology **128**, 83 (2015).

[451] V. Srivastava, P. A. Iglesias, and D. N. Robinson, *Cytokinesis: Robust cell shape regulation,* Seminars in Cell & Developmental Biology **53**, 39 (2016).

[452] K. Rottner and M. Schaks, *Assembling actin filaments for protrusion,* Current Opinion in Cell Biology **56**, 53 (2019).

[453] A. Ponti, M. Machacek, S. L. Gupton, C. M. Waterman-Storer, and G. Danuser, *Two Distinct Actin Networks Drive the Protrusion of Migrating Cells,* Science **305**, 1782 (2004).

[454] K. Michel, *Das Phasenkontrastverfahren und seine Eignung für zytologische Untersuchungen,* Naturwissenschaften **3** (1950).

[455] P. Shchelokovskyy, S. Tristram-Nagle, and R. Dimova, *Effect of the HIV-1 fusion peptide on the mechanical properties and leaflet coupling of lipid bilayers,* New Journal of Physics **13**, 025004 (2011).

[456] R. M. Hochmuth, *Micropipette aspiration of living cells,* Journal of Biomechanics **33**, 15 (2000).

[457] M. Berardi, K. Bielawski, N. Rijnveld, G. Gruca, H. Aardema, L. van Tol, G. Wuite, and B. I. Akca, *Optical interferometry based micropipette aspiration provides real-time sub-nanometer spatial resolution,* Communications Biology **4**, 1 (2021).

[458] K. N. Dahl, A. J. Engler, J. D. Pajerowski, and D. E. Discher, *Power-Law Rheology of Isolated Nuclei with Deformation Mapping of Nuclear Substructures,* Biophysical Journal **89**, 2855 (2005).

[459] M. L. Longo and H. V. Ly, *Micropipet Aspiration for Measuring Elastic Properties of Lipid Bilayers,* From: Methods in Molecular Biology **400**, 421 (2007).

[460] J. Brugués, B. Maugis, J. Casademunt, P. Nassoy, F. Amblard, and P. Sens, *Dynamical organization of the cytoskeletal cortex probed by micropipette aspiration,* Proceedings of the National Academy of Sciences **107**, 15415 (2010).

[461] K. Sliogeryte, S. D. Thorpe, Z. Wang, C. L. Thompson, N. Gavara, and M. M. Knight, *Differential effects of LifeAct-GFP and actin-GFP on cell mechanics assessed using micropipette aspiration,* Journal of Biomechanics **49**, 310 (2016).

[462] L. M. Lee, J. W. Lee, D. Chase, D. Gebrezgiabhier, and A. P. Liu, *Development of an advanced microfluidic micropipette aspiration device for single cell mechanics studies,* Biomicrofluidics **10**, 054105 (2016).

[463] Q. Guo, S. Park, and H. Ma, *Microfluidic micropipette aspiration for measuring the deformability of single cells,* Lab on a Chip **12**, 2687 (2012).

[464] P. M. Davidson, G. R. Fedorchak, S. Mondésert-Deveraux, E. S. Bell, P. Isermann, D. Aubry, R. Allena, and J. Lammerding, *High-throughput microfluidic micropipette aspiration device to probe time-scale dependent nuclear mechanics in intact cells,* Lab on a Chip **19**, 3652 (2019).

[465] X. Liu, Y. Wang, and Y. Sun, *Cell contour tracking and data synchronization for real-time, high-accuracy micropipette aspiration,* IEEE Transactions on Automation Science and Engineering **6**, 536 (2009).

[466] E. Shojaei-Baghini, Y. Zheng, and Y. Sun, *Automated Micropipette Aspiration of Single Cells,* Annals of Biomedical Engineering **41**, 1208 (2013).

[467] J. F. Nagle and S. Tristram-Nagle, *Lipid bilayer structure,* Current Opinion in Structural Biology **10**, 474 (2000).

[468] T. Browicz, *Further observation of motion phenomena on red blood cells in pathological states,* Zbl. med. Wissen **28**, 625 (1890).

[469] H. A. Faizi, S. L. Frey, Jan Steinkühler, Rumiana Dimova, P. M. Vlahovska, H. A. Faizi, S. L. Frey, J. Steinkü, R. Dimova, and P. M. Vlahovska, *Bending rigidity of charged lipid bilayer membranes,* Soft Matter **15**, 6006 (2019).

[470] J. Steinkühler, E. Sezgin, I. Urbančič, C. Eggeling, and R. Dimova, *Mechanical properties of plasma membrane vesicles correlate with lipid order, viscosity and cell density,* Communications Biology **2**, 1 (2019).

[471] R. Serral Gracià, Natalya Bezlyepkina, R. L. Knorr, R. Lipowsky, and R. Dimova, *Effect of cholesterol on the rigidity of saturated and unsaturated membranes : fluctuation and electrodeformation analysis of giant vesicles,* Soft Matter **6**, 1472 (2010).

[472] N. Gov, A. G. Zilman, and S. Safran, *Cytoskeleton Confinement and Tension of Red Blood Cell Membranes,* Physical Review Letters **90**, 228101 (2003).

[473] J.-B. Fournier, D. Lacoste, and E. Raphaël, *Fluctuation Spectrum of Fluid Membranes Coupled to an Elastic Meshwork: Jump of the Effective Surface Tension at the Mesh Size,* Physical Review Letters **92**, 018102 (2004).

[474] L. Limozin, A. Roth, and E. Sackmann, *Microviscoelastic moduli of biomimetic cell envelopes,* Physical review letters **95** (2005).

[475] E. Schäfer, T. T. Kliesch, and A. Janshoff, *Mechanical properties of giant liposomes compressed between two parallel plates: impact of artificial actin shells,* Langmuir **29**, 10463 (2013).

[476] E. Schäfer, M. Vache, T. T. Kliesch, and A. Janshoff, *Mechanical response of adherent giant liposomes to indentation with a conical AFM-tip,* Soft matter **11**, 4487 (2015).

[477] E. Fischer-Friedrich, Y. Toyoda, C. J. Cattin, D. J. Müller, A. A. Hyman, and F. Jülicher, *Rheology of the Active Cell Cortex in Mitosis,* Biophysical journal **111**, 589 (2016).

[478] G. Fläschner, C. I. Roman, N. Strohmeyer, D. Martinez-Martin, and D. J. Müller, *Rheology of rounded mammalian cells over continuous high-frequencies,* Nature communications **12** (2021).

[479] E. Heifer, S. Harlepp, L. Bourdieu, J. Robert, F. C. MacKintosh, and D. Chatenay, *Viscoelastic properties of actin-coated membranes,* Physical review. E, Statistical, nonlinear, and soft matter physics **63**, 0219041 (2001).

[480] D. Mizuno, R. Bacabac, C. Tardin, D. Head, and C. F. Schmidt, *High-resolution probing of cellular force transmission,* Physical review letters **102** (2009).

[481] R. Dimova, *Recent developments in the field of bending rigidity measurements on membranes,* Advances in Colloid and Interface Science **208**, 225 (2014).

[482] A. Morshed, B. I. Karawdeniya, Y. M. D. Bandara, M. J. Kim, and P. Dutta, *Mechanical characterization of vesicles and cells: A review,* Electrophoresis **41**, 449 (2020).

[483] C. Prévost, F.-C. Tsai, P. Bassereau, and M. Simunovic, *Pulling Membrane Nanotubes from Giant Unilamellar Vesicles,* JoVE (Journal of Visualized Experiments) **2017**, e56086 (2017).

[484] J. Pan, S. Tristram-Nagle, N. Kučerka, and J. F. Nagle, *Temperature Dependence of Structure, Bending Rigidity, and Bilayer Interactions of Dioleoylphosphatidylcholine Bilayers,* Biophysical Journal **94**, 117 (2008).

[485] M. Doktorova, D. Harries, and G. Khelashvili, *Determination of bending rigidity and tilt modulus of lipid membranes from real-space fluctuation analysis of molecular dynamics simulations,* Physical Chemistry Chemical Physics **19**, 16806 (2017).

[486] S. Alex Rautu, D. Orsi, L. Di Michele, G. Rowlands, P. Cicuta, and M. S. Turner, *The role of optical projection in the analysis of membrane fluctuations,* Soft Matter **13**, 3480 (2017).

[487] D. Bochicchio and L. Monticelli, *The Membrane Bending Modulus in Experiments and Simulations: A Puzzling Picture,* Advances in Biomembranes and Lipid Self-Assembly **23**, 117 (2016).

[488] G. Weber, T. Charitat, S. Baptista, A. Uchoa, C. Pavani, H. C. Junqueira, Y. Guo, V. A. Baulin, R. Itri, C. M. Marques, and A. P. Schroder, *Lipid oxidation induces structural changes in biomimetic membranes,* Soft Matter **10**, 4241 (2014).

[489] D. Drabik, M. Przybyło, G. Chodaczek, A. Iglič, and M. Langner, *The modified fluorescence based vesicle fluctuation spectroscopy technique for determination of lipid bilayer bending properties,* Biochimica et Biophysica Acta (BBA) - Biomembranes **1858**, 244 (2016).

[490] J. Pan, S. Tristram-Nagle, and J. F. Nagle, *Effect of cholesterol on structural and mechanical properties of membranes depends on lipid chain saturation,* Physical Review E **80**, 021931 (2009).

[491] H. A. Faizi, C. J. Reeves, V. N. Georgiev, P. M. Vlahovska, and R. Dimova, *Fluctuation spectroscopy of giant unilamellar vesicles using confocal and phase contrast microscopy,* Soft Matter **16**, 8996 (2020).

[492] S. D. Shoemaker and T. K. Vanderlick, *Material Studies of Lipid Vesicles in the Lα and Lα-Gel Coexistence Regimes,* Biophysical Journal **84**, 998 (2003).

[493] K. A. Riske, T. P. Sudbrack, N. L. Archilha, A. F. Uchoa, A. P. Schroder, C. M. Marques, M. S. Baptista, and R. Itri, *Giant Vesicles under Oxidative Stress Induced by a Membrane-Anchored Photosensitizer,* Biophysical Journal **97**, 1362 (2009).

[494] J. F. Nagle, *Introductory Lecture: Basic quantities in model biomembranes,* Faraday Discussions **161**, 11 (2012).

[495] V. Vitkova, J. Genova, M. D. Mitov, and I. Bivas, *Sugars in the Aqueous Phase Change the Mechanical Properties of Lipid Mono- and Bilayers,* Molecular Crystals and Liquid Crystals **449**, 95 (2006).

[496] B. Sorre, A. Callan-Jones, J.-B. Manneville, P. Nassoy, J.-F. Joanny, J. Prost, B. Goud, and P. Bassereau, *Curvature-driven lipid sorting needs proximity to a demixing point and is aided by proteins,* Proceedings of the National Academy of Sciences **106**, 5622 (2009).

[497] S. Chakraborty, M. Doktorova, T. R. Molugu, F. A. Heberle, H. L. Scott, B. Dzikovski, M. Nagao, L.-R. Stingaciu, R. F. Standaert, F. N. Barrera, J. Katsaras, G. Khelashvili, M. F. Brown, and R. Ashkar, *How cholesterol stiffens unsaturated lipid membranes,* Proceedings of the National Academy of Sciences **117**, 21896 (2020).

[498] G. Khelashvili, N. Johner, G. Zhao, D. Harries, and H. L. Scott, *Molecular origins of bending rigidity in lipids with isolated and conjugated double bonds: The effect of cholesterol,* Chemistry and Physics of Lipids **178**, 18 (2014).

[499] L. R. Arriaga, I. López-Montero, F. Monroy, G. Orts-Gil, B. Farago, and T. Hellweg, *Stiffening Effect of Cholesterol on Disordered Lipid Phases: A Combined Neutron Spin Echo + Dynamic Light Scattering Analysis of the Bending Elasticity of Large Unilamellar Vesicles,* Biophysical Journal **96**, 3629 (2009).

[500] G. Van Meer, D. R. Voelker, and G. W. Feigenson, *Membrane lipids: where they are and how they behave,* Nature Reviews Molecular Cell Biology **9**, 112 (2008).

[501] J. Henriksen, A. C. Rowat, E. Brief, Y. W. Hsueh, J. L. Thewalt, M. J. Zuckermann, and J. H. Ipsen, *Universal Behavior of Membranes with Sterols,* Biophysical Journal **90**, 1639 (2006).

[502] J. F. Nagle, E. A. Evans, P. Bassereau, T. Baumgart, S. Tristram-Nagle, and R. Dimova, *A needless but interesting controversy,* Proceedings of the National Academy of Sciences **118** (2021).

[503] R. Ashkar, M. Doktorova, F. A. Heberle, H. L. Scott, F. N. Barrera, J. Katsaras, G. Khelashvili, and M. F. Brown, *Reply to Nagle et al.: The universal stiffening effects of cholesterol on lipid membranes,* Proceedings of the National Academy of Sciences **118**, 2102845118 (2021).

[504] R. Kwok and E. Evans, *Thermoelasticity of large lecithin bilayer vesicles,* Biophysical Journal **35**, 637 (1981).

[505] E. Ibarboure, M. Fauquignon, and J.-F. L. Meins, *Obtention of Giant Unilamellar Hybrid Vesicles by Electroformation and Measurement of their Mechanical Properties by Micropipette Aspiration,* JoVE (Journal of Visualized Experiments) **2020**, e60199 (2020).

[506] M. Fauquignon, E. Ibarboure, and J. F. Le Meins, *Membrane reinforcement in giant hybrid polymer lipid vesicles achieved by controlling the polymer architecture,* Soft Matter **17**, 83 (2021).

[507] K. Guevorkian and J. L. Maître, *Micropipette aspiration: A unique tool for exploring cell and tissue mechanics in vivo,* Methods in Cell Biology **139**, 187 (2017).

[508] O. A. Solis-Gonzalez, C. C. W. Tse, P. J. Smith, and J. P. A. Fairclough, *Preparation of Giant Polymersomes via Inkjet Printing and Confined Geometry Hydration Applied to Micropipette Aspiration Experiments,* Macromolecular Materials and Engineering **305**, 2000094 (2020).

[509] C. Has and P. Sunthar, *A comprehensive review on recent preparation techniques of liposomes,* Journal of Liposome Research **30**, 336 (2019).

[510] C. Campillo, P. Sens, D. Köster, L. L. Pontani, D. Lévy, P. Bassereau, P. Nassoy, and C. Sykes, *Unexpected Membrane Dynamics Unveiled by Membrane Nanotube Extrusion,* Biophysical Journal **104**, 1248 (2013).

[511] Y. Mulla, *The Cell: Strong, Soft Matter*, Ph.D. thesis (2018).

[512] S. Ramaswamy, *Equilibrium and non-equilibrium dynamics of the dilute lamellar phase,* Physica A: Statistical Mechanics and its Applications **186**, 154 (1992).

[513] A. Echard, *Phosphoinositides and cytokinesis: The "PIP" of the iceberg,* Cytoskeleton **69**, 893 (2012).

[514] N. L. Mora, A. L. Boyle, B. J. van Kolck, A. Rossen, S. Pokorná, A. Koukalová, R. Sachl, M. Hof, and A. Kros, *Controlled Peptide-Mediated Vesicle Fusion Assessed by Simultaneous Dual-Colour Time-Lapsed Fluorescence Microscopy,* Scientific Reports **10**, 1 (2020).

[515] R. Jahn and T. C. Südhof, *Membrane Fusion and Exocytosis,* Annual Review of Biochemistry **68**, 863 (1999).

[516] R. Jahn, *Principles of Exocytosis and Membrane Fusion,* Annals of the New York Academy of Sciences **1014**, 170 (2004).

[517] L. V. Chernomordik and M. M. Kozlov, *Mechanics of membrane fusion,* Nature Structural & Molecular Biology **15**, 675 (2008).

[518] T. Y. Yoon, B. Okumus, F. Zhang, Y. K. Shin, and T. Ha, *Multiple intermediates in SNARE-induced membrane fusion,* Proceedings of the National Academy of Sciences **103**, 19731 (2006).

[519] B. Van Lengerich, R. J. Rawle, P. M. Bendix, and S. G. Boxer, *Individual Vesicle Fusion Events Mediated by Lipid-Anchored DNA,* Biophysical Journal **105**, 409 (2013).

[520] L. K. Tamm, J. Crane, and V. Kiessling, *Membrane fusion: a structural perspective on the interplay of lipids and proteins,* Current Opinion in Structural Biology **13**, 453 (2003).

[521] M. M. Kozlov and V. S. Markin, *Possible mechanism of membrane fusion,* Biofizika **28**, 242 (1983).

[522] B. R. Lentz, *PEG as a tool to gain insight into membrane fusion,* European Biophysics Journal **36**, 315 (2007).

[523] J. Wilschut, N. Düzgüneş, R. Fraley, and D. Papahadjopoulos, *Studies on the mechanism of membrane fusion: kinetics of calcium ion induced fusion of phosphatidylserine vesicles followed by a new assay for mixing of aqueous vesicle contents,* Biochemistry **19**, 6011 (1980).

[524] Y. A. Chen and R. H. Scheller, *SNARE-mediated membrane fusion,* Nature Reviews Molecular Cell Biology **2**, 98 (2001).

[525] G. Stengel, L. Simonsson, R. A. Campbell, and F. Höök, *Determinants for Membrane Fusion Induced by Cholesterol-Modified DNA Zippers,* Journal of Physical Chemistry B **112**, 8264 (2008).

[526] K. M. Flavier and S. G. Boxer, *Vesicle Fusion Mediated by Solanesol-Anchored DNA,* Biophysical Journal **113**, 1260 (2017).

[527] Y. H. M. Chan, B. Van Lengerich, and S. G. Boxer, *Effects of linker sequences on vesicle fusion mediated by lipid-anchored DNA oligonucleotides,* Proceedings of the National Academy of Sciences **106**, 979 (2009).

[528] R. B. Lira and R. Dimova, *Fusion assays for model membranes: a critical review,* Advances in Biomembranes and Lipid Self-Assembly **30**, 229 (2019).

[529] S. A. Van Der Meulen, G. V. Dubacheva, M. Dogterom, R. P. Richter, and M. E. Leunissen, *Quartz crystal microbalance with dissipation monitoring and spectroscopic ellipsometry measurements of the phospholipid bilayer anchoring stability and kinetics of hydrophobically modified DNA oligonucleotides,* Langmuir **30**, 6525 (2014).

[530] I. Pfeiffer and F. Höök, *Quantification of Oligonucleotide Modifications of Small Unilamellar Lipid Vesicles,* Analytical Chemistry **78**, 7493 (2006).

[531] R. P. Richter, R. Bérat, and A. R. Brisson, *Formation of solid-supported lipid bilayers: An integrated view,* Langmuir **22**, 3497 (2006).

[532] M. Przybylo, J. Sýkora, J. Humpolíčová, A. Benda, A. Zan, and M. Hof, *Lipid diffusion in giant unilamellar vesicles is more than 2 times faster than in supported phospholipid bilayers under identical conditions,* Langmuir **22**, 9096 (2006).

[533] H. P. Wacklin, *Composition and asymmetry in supported membranes formed by vesicle fusion,* Langmuir **27**, 7698 (2011).

[534] N. Otsu, *A Threshold Selection Method from Gray-Level Histograms,* IEEE Trans Syst Man Cybern **SMC-9**, 62 (1979).

[535] Y. Gong, M. Ma, Y. Luo, and D. Bong, *Functional Determinants of a Synthetic Vesicle Fusion System,* Journal of the American Chemical Society **130**, 6196 (2008).

[536] M. M. Kozlov and L. V. Chernomordik, *Membrane tension and membrane fusion,* Current Opinion in Structural Biology **33**, 61 (2015).

[537] T. T. Kliesch, J. Dietz, L. Turco, P. Halder, E. Polo, M. Tarantola, R. Jahn, and A. Janshoff, *Membrane tension increases fusion efficiency of model membranes in the presence of SNAREs,* Scientific Reports **7**, 1 (2017).

[538] T. Porstmann and S. T. Kiessig, *Enzyme immunoassay techniques an overview,* Journal of Immunological Methods **150**, 5 (1992).

[539] L. Simonsson, P. Jönsson, G. Stengel, and F. Höök, *Site-specific DNA-controlled fusion of single lipid vesicles to supported lipid bilayers,* ChemPhysChem **11**, 1011 (2010).

[540] H. Ellens, J. Bentz, and F. C. Szoka, *Proton- and calcium-induced fusion and destabilization of liposomes,* Biochemistry **24**, 3099 (1985).

[541] N. Kahya, E. I. Pécheur, W. P. De Boeij, D. A. Wiersma, and D. Hoekstra, *Reconstitution of Membrane Proteins into Giant Unilamellar Vesicles via Peptide-Induced Fusion,* Biophysical Journal **81**, 1464 (2001).

[542] S. Trier, J. R. Henriksen, and T. L. Andresen, *Membrane fusion of pH-sensitive liposomes - A quantitative study using giant unilamellar vesicles,* Soft Matter **7**, 9027 (2011).

[543] M. C. Wiener and S. H. White, *Structure of a fluid dioleoylphosphatidylcholine bilayer determined by joint refinement of x-ray and neutron diffraction data. III. Complete structure,* Biophysical Journal **61**, 434 (1992).

[544] B. R. Lentz, G. F. Mcintyre, D. J. Parks, J. C. Yates, and D. Massenburg, *Bilayer Curvature and Certain Amphipaths Promote Poly(ethylene glycol)-Induced Fusion of Dipalmitoylphosphatidylcholine Unilamellar Vesicles,* Biochemistry **31**, 2643 (1992).

[545] J. K. Lee and B. R. Lentz, *Outer Leaflet-Packing Defects Promote Poly(ethylene glycol)-Mediated Fusion of Large Unilamellar Vesicles,* Biochemistry **36**, 421 (1997).

[546] V. S. Malinin and B. R. Lentz, *Energetics of Vesicle Fusion Intermediates: Comparison of Calculations with Observed Effects of Osmotic and Curvature Stresses,* Biophysical Journal **86**, 2951 (2004).

[547] M. Haque and B. R. Lentz, *Roles of Curvature and Hydrophobic Interstice Energy in Fusion: Studies of Lipid Perturbant Effects,* Biochemistry **43**, 3507 (2004).

[548] P. V. Escribá, X. Busquets, J. I. Inokuchi, G. Balogh, Z. Török, I. Horváth, J. L. Harwood, and L. Vígh, *Membrane lipid therapy: Modulation of the cell membrane composition and structure as a molecular base for drug discovery and new disease treatment,* Progress in Lipid Research **59**, 38 (2015).

[549] M. J. Gerl, J. L. Sampaio, S. Urban, L. Kalvodova, J. M. Verbavatz, B. Binnington, D. Lindemann, C. A. Lingwood, A. Shevchenko, C. Schroeder, and K. Simons, *Quantitative analysis of the lipidomes of the influenza virus envelope and MDCK cell apical membrane,* Journal of Cell Biology **196**, 213 (2012).

[550] R. J. Rawle, B. Van Lengerich, M. Chung, P. M. Bendix, and S. G. Boxer, *Vesicle Fusion Observed by Content Transfer across a Tethered Lipid Bilayer,* Biophysical Journal **101**, L37 (2011).

[551] Y. H. M. Chan, P. Lenz, and S. G. Boxer, *Kinetics of DNA-mediated docking reactions between vesicles tethered to supported lipid bilayers,* Proceedings of the National Academy of Sciences **104**, 18913 (2007).

[552] L. Chernomordik, *Non-bilayer lipids and biological fusion intermediates,* Chemistry and Physics of Lipids **81**, 203 (1996).

[553] H. A. Scheidt, K. Kolocaj, D. B. Konrad, J. A. Frank, D. Trauner, D. Langosch, and D. Huster, *Light-induced lipid mixing implies a causal role of lipid splay in membrane fusion,* Biochimica et Biophysica Acta (BBA) - Biomembranes **1862**, 183438 (2020).

[554] M. E. Haque, T. J. McIntosh, and B. R. Lentz, *Influence of Lipid Composition on Physical Properties and PEG-Mediated Fusion of Curved and Uncurved Model Membrane Vesicles: "Nature's Own" Fusogenic Lipid Bilayer,* Biochemistry **40**, 4340 (2001).

[555] M. Dezi, A. Di Cicco, P. Bassereau, and D. Levy, *Detergent-mediated incorporation of transmembrane proteins in giant unilamellar vesicles with controlled physiological contents,* Proceedings of the National Academy of Sciences of the United States of America **110**, 7276 (2013).

[556] M. A. Galkin, A. N. Russell, S. B. Vik, R. M. Berry, and R. R. Ishmukhametov, *Detergent-free Ultrafast Reconstitution of Membrane Proteins into Lipid Bilayers Using Fusogenic Complementary-charged Proteoliposomes,* Journal of visualized experiments **2018** (2018).

[557] L. Sun, Y. Gao, Y. Wang, Q. Wei, J. Shi, N. Chen, D. Li, and C. Fan, *Guiding protein delivery into live cells using DNA-programmed membrane fusion,* Chemical Science **9**, 5967 (2018).

[558] J. D. Cortese, B. Schwab, C. Frieden, and E. L. Elson, *Actin polymerization induces a shape change in actin-containing vesicles,* Proceedings of the National Academy of Sciences **86**, 5773 (1989).

[559] S. Majd, D. J. Estes, and M. Mayer, *Assays for Studying Annexin Binding to Artificial Bilayers,* Calcium Binding Proteins **1** (2006).

[560] P. M. Löffler, A. H. Hansen, O. Ries, U. Jakobsen, A. Rabe, K. T. Sørensen, K. Glud, and S. Vogel, *Lipidated Polyaza Crown Ethers as Membrane Anchors for DNA-Controlled Content Mixing between Liposomes,* Scientific Reports **9**, 1 (2019).

[561] M. Kinoshita, *Diversity of septin scaffolds,* Current Opinion in Cell Biology **18**, 54 (2006).

[562] B. Gumí-Audenis, L. Costa, L. Ferrer-Tasies, I. Ratera, N. Ventosa, F. Sanz, and M. I. Giannotti, *Pulling lipid tubes from supported bilayers unveils the underlying substrate contribution to the membrane mechanics,* Nanoscale **10**, 14763 (2018).

[563] A. Roux, G. Koster, M. Lenz, B. Sorre, J. B. Manneville, P. Nassoy, and P. Bassereau, *Membrane curvature controls dynamin polymerization,* Proceedings of the National Academy of Sciences **107**, 4141 (2010).

[564] A. F. Bitbol, N. Puff, Y. Sakuma, M. Imai, J. B. Fournier, and M. I. Angelova, *Lipid membrane deformation in response to a local pH modification: theory and experiments,* Soft Matter **8**, 6073 (2012).

[565] A. Yamada, S. Lee, P. Bassereau, and C. N. Baroud, *Trapping and release of giant unilamellar vesicles in microfluidic wells,* Soft Matter **10**, 5878 (2014).

[566] N. Yandrapalli and T. Robinson, *Ultra-high capacity microfluidic trapping of giant vesicles for high-throughput membrane studies,* Lab on a Chip **19**, 626 (2019).

[567] P. M. Löffler, O. Ries, A. Rabe, A. H. Okholm, R. P. Thomsen, J. Kjems, and S. Vogel, *A DNA-Programmed Liposome Fusion Cascade,* Angewandte Chemie International Edition **56**, 13228 (2017).

[568] S. F. Shimobayashi, M. Ichikawa, and T. Taniguchi, *Direct observations of transition dynamics from macro- to micro-phase separation in asymmetric lipid bilayers induced by externally added glycolipids,* Europhysics Letters **113**, 56005 (2016).

[569] K. Bacia, P. Schwille, and T. Kurzchalia, *Sterol structure determines the separation of phases and the curvature of the liquid-ordered phase in model membranes,* Proceedings of the National Academy of Sciences **102**, 3272 (2005).

[570] T. Baumgart, S. Hess, and W. Webb, *Imaging coexisting fluid domains in biomembrane models coupling curvature and line tension,* Nature **425**, 821 (2003).

[571] U. Seifert, K. Berndl, and R. Lipowsky, *Shape transformations of vesicles: Phase diagram for spontaneous- curvature and bilayer-coupling models,* Physical Review A **44**, 1182 (1991).

[572] R. Lipowsky and R. Dimova, *Introduction to remodeling of biomembranes,* Soft Matter **17**, 214 (2021).

[573] T. Jimbo, Y. Sakuma, N. Urakami, P. Ziherl, and M. Imai, *Role of Inverse-Cone-Shape Lipids in Temperature-Controlled Self-Reproduction of Binary Vesicles,* Biophysical Journal **110**, 1551 (2016).

[574] H. T. Cheng, Megha, and E. London, *Preparation and properties of asymmetric vesicles that mimic cell membranes. Effect upon lipid raft formation and transmembrane helix orientation,* Journal of Biological Chemistry **284**, 6079 (2009).

[575] H. T. Cheng and E. London, *Preparation and properties of asymmetric large unilamellar vesicles: interleaflet coupling in asymmetric vesicles is dependent on temperature but not curvature,* Biophysical journal **100**, 2671 (2011).

[576] M. Doktorova, F. A. Heberle, B. Eicher, R. F. Standaert, J. Katsaras, E. London, G. Pabst, and D. Marquardt, *Preparation of asymmetric phospholipid vesicles for use as cell membrane models,* Nature protocols **13**, 2086 (2018).

[577] J. H. Lorent, K. R. Levental, L. Ganesan, G. Rivera-Longsworth, E. Sezgin, M. Doktorova, E. Lyman, and I. Levental, *Plasma membranes are asymmetric in lipid unsaturation, packing and protein shape,* Nature Chemical Biology **16**, 644 (2020).

[578] Y. Caspi and C. Dekker, *Divided we stand: splitting synthetic cells for their proliferation,* Systems and Synthetic Biology **8**, 249 (2014).

[579] M. Exterkate and A. J. Driessen, *Synthetic Minimal Cell: Self-Reproduction of the Boundary Layer,* ACS Omega **4**, 5293 (2019).

[580] A. Bhattacharya, R. J. Brea, H. Niederholtmeyer, and N. K. Devaraj, *A minimal biochemical route towards de novo formation of synthetic phospholipid membranes,* Nature Communications **10**, 1 (2019).

[581] S. Berg, D. Kutra, T. Kroeger, C. N. Straehle, B. X. Kausler, C. Haubold, M. Schiegg, J. Ales, T. Beier, M. Rudy, K. Eren, J. I. Cervantes, B. Xu, F. Beuttenmueller, A. Wolny, C. Zhang, U. Koethe, F. A. Hamprecht, and A. Kreshuk, *ilastik: interactive machine learning for (bio)image analysis,* Nature Methods 2019 **16**, 1226 (2019).

[582] T. Litschel, K. A. Ganzinger, T. Movinkel, M. Heymann, T. Robinson, H. Mutschler, and P. Schwille, *Freeze-thaw cycles induce content exchange between cell-sized lipid vesicles,* New Journal of Physics **20**, 055008 (2018).

[583] K. Al Nahas, J. Cama, M. Schaich, K. Hammond, S. Deshpande, C. Dekker, M. G. Ryadnov, and U. F. Keyser, *A microfluidic platform for the characterisation of membrane active antimicrobials,* Lab on a Chip **19**, 837 (2019).

[584] K. Nishimura, T. Hosoi, T. Sunami, T. Toyota, M. Fujinami, K. Oguma, T. Matsuura, H. Suzuki, and T. Yomo, *Population analysis of structural properties of giant liposomes by flow cytometry,* Langmuir **25**, 10439 (2009).

[585] N. Wichmann, P. M. Lund, M. B. Hansen, C. U. Hjørringgaard, J. B. Larsen, K. Kristensen, T. L. Andresen, and J. B. Simonsen, *Applying flow cytometry to identify the modes of action of membrane-active peptides in a label-free and high-throughput fashion,* Biochimica et Biophysica Acta (BBA) - Biomembranes **1864**, 183820 (2022).

[586] K. Sato, K. Obinata, T. Sugawara, I. Urabe, and T. Yomo, *Quantification of structural properties of cell-sized individual liposomes by flow cytometry,* Journal of Bioscience and Bioengineering **102**, 171 (2006).

[587] A. Isozaki, H. Mikami, H. Tezuka, H. Matsumura, K. Huang, M. Akamine, K. Hiramatsu, T. Iino, T. Ito, H. Karakawa, Y. Kasai, Y. Li, Y. Nakagawa, S. Ohnuki, T. Ota, Y. Qian, S. Sakuma, T. Sekiya, Y. Shirasaki, N. Suzuki, E. Tayyabi, T. Wakamiya, M. Xu, M. Yamagishi, H. Yan, Q. Yu, S. Yan, D. Yuan, W. Zhang, Y. Zhao, F. Arai, R. E. Campbell, C. Danelon, D. Di Carlo, K. Hiraki, Y. Hoshino, Y. Hosokawa, M. Inaba, A. Nakagawa, Y. Ohya, M. Oikawa, S. Uemura, Y. Ozeki, T. Sugimura, N. Nitta, and K. Goda, *Intelligent image-activated cell sorting 2.0,* Lab on a Chip **20**, 2263 (2020).

[588] A. Isozaki, H. Mikami, K. Hiramatsu, S. Sakuma, Y. Kasai, T. Iino, T. Yamano, A. Yasumoto, Y. Oguchi, N. Suzuki, Y. Shirasaki, T. Endo, T. Ito, K. Hiraki, M. Yamada, S. Matsusaka, T. Hayakawa, H. Fukuzawa, Y. Yatomi, F. Arai, D. Di Carlo, A. Nakagawa, Y. Hoshino, Y. Hosokawa, S. Uemura, T. Sugimura, Y. Ozeki, N. Nitta, and K. Goda, *A practical guide to intelligent image-activated cell sorting,* Nature Protocols **14**, 2370 (2019).

LIST OF PUBLICATIONS

Publications covered in this thesis:

2. **Lennard van Buren**, G. H. Koenderink, C. Martinez-Torres, *DisGUVery: a versatile open-source software for high-throughput image analysis of Giant Unilamellar Vesicles*, bioRxiv, (2022)

1. L. van de Cauter, F. Fanalista, **Lennard van Buren**, N. De Franceschi, E. Godino, S. Bouw, C. Danelon, C. Dekker, G. H. Koenderink, K. A. Ganzinger, ACS Synthetic Biology **10** (2021)

Other publications:

4. C. J. Moll, G. Giubertoni, **Lennard van Buren**, J. Versluis, G. H. Koenderink, H. J. Bakker, *Molecular Structure and Surface Accumulation Dynamics of Hyaluronan at the Water–Air Interface*, Macromolecules, **54**, 18 (2021)

3. C. Schroer, L. Baldauf, **Lennard van Buren**, T. A. Wassenaar, M. N. Melo, G. H. Koenderink, S. J. Marrink, *Charge-dependent interactions of monomeric and filamentous actin with lipid bilayers*, PNAS, **11**, 117 (2020)

2. H. R. Vutukuri, M. Hoore, C. Abaurrea-Velasco, **Lennard van Buren**, A. Dutto, T. Auth, D. A. Fedosov, G. Gomppher, J. Vermant, *Active particles induce large shape deformations in giant lipid vesicles*, Nature, **586**, 52-56 (2020)

1. T. De Mooij, Z. Rajabali Nejad, **Lennard van Buren**, R. H. Wijffels, M. Janssen, *Effect of photoacclimation on microalgae mass culture productivity*, Algal Research, **22**, 56-67 (2017)